COUPLED LUMINESCENCE CENTRES IN ERBIUM-DOPED SILICON RICH SILICON OXIDE THIN FILMS DEPOSITED BY ECR-PECVD

Coupled Luminescence Centres in Erbium-Doped Silicon Rich Silicon Oxide Thin Films Deposited by ECR-PECVD

by

DARREN EARL BLAKIE

B.Sc., rmc (Royal Military College of Canada) 2004

A Thesis
Submitted to the School of Graduate Studies
in Partial Fulfilment of the Requirements
for the Degree
Master of Applied Science

McMaster University

MASTER OF APPLIED SCIENCE (2006) **McMASTER UNIVERSITY**

(Department of Engineering Physics) **Hamilton, Ontario**

TITLE: Coupled Luminescence Centres in Erbium-Doped Silicon Rich Silicon Oxide Thin Films Deposited by ECR-PECVD

AUTHOR: Darren Earl Blakie, B.Sc., rmc (Royal Military College of Canada)

THESIS SUPERVISORS: Dr. Peter Mascher and Dr. Andrew P. Knights

NUMBER OF PAGES: xix, 341

Abstract

Silicon has been the mainstay of the microelectroncs industry for over four decades. There is no material which can match the balance it affords between cost-benefit, mass consumability, process versatility, and nano-scale electron device performance. It is, therefore, the logical (and perhaps inevitable) platform for the development of integrated opto-electronics – a technology that is being aggressively developed to meet the next generation of bandwidth demands that are already beginning to strain interconnect architectures all the way down to the intra-chip level. While silicon-based materials already provide a variety of passive optical functionalities, the success of a genuine silicon-based opto-electronics will depend upon the ability of engineers to overcome those limitations in the optical properties of bulk silicon that occur at critical junctions in device requirements (eg. modulator and laser). Such solutions must not render the device processing incompatible with CMOS, for then the "silicon advantage" is lost. Achieving reliable and efficient electroluminescence in silicon remains the most intractable of these problems to date.

Reliability problems in recently developed light emitting devices operating near a wavelength of 1.54 μm, based on the thermally induced formation of silicon nano-clusters in erbium-doped silicon rich silicon oxide thin films, has re-inforced the need for a further understanding of the luminescence mechanisms in this material. Indeed, the efficient and stable sensitized photoluminescence from Er^{3+} ions (near the telecom wavelength), embedded in an oxide matrix, based on a quasi-resonant energy transfer from nanostructured silicon, has the potential to make possible compact waveguide amplifiers and thin film electroluminescence.

This thesis represents a study into the luminescence mechanisms in erbium-doped silicon oxide (SiO_x, $x \leq 2$) thin films grown by electron cyclotron resonance plasma enhanced chemical vapour deposition. Importantly, the film

growth relies on in-situ erbium doping through the cracking of a volatile organo-lanthanide $Er(tmhd)_3$ source. Rutherford backscattering spectroscopy has been used to map the film composition space generated from an ECR-PECVD parameter subspace consisting of precursor gas flow rates and the erbium precursor temperature. The response of the film photoluminescence spectra in both visible and infrared bands consistenly reveals three classes of luminescence centres, whose relative ability to emit light is shown in this study to exhibit a considerable degree of variability through the control of the film composition, subsequent thermal anneal temperature, duration, and process ambient. These three classes consist of optically active Er^{3+} ions, silicon nano-clusters phase separated during thermal annealing, and oxide-based defects (which may additionally include organic chromophores). The latter two of these species show the ability to sensitize the Er^{3+} luminescence. In fact, sensitization by intrinsically luminescent defects is a rarely studied phenomenon, which seems to be an important phenomenon in the present films owing to a potentially unique Er incorporation complex. To further investigate the ability of the oxide defects in this regard, an optimally luminescent film has been subject to a damaging ion irradiation to induce a photoluminescence quenching. The subsequent recovery of this luminescence with stepwise isochronous annealing has been correlated with Doppler broadening positron annihilation spectroscopy measurements made with a slow positron beam. Irradiation to a sufficiently high fluence has demonstrated a unique ability to de-couple luminescent sensitizers and Er^{3+} ions, producing enhanced blue and violet emissions.

Acknowledgements

I would like to thank my supervisors, Professor Peter Mascher and Professor Andrew Knights, for granting the opportunity to work on this project. They allowed me a significant degree of freedom to determine the particular aspects of focus for the research work according to my own interests. I have learned, from their example, a good deal about leadership in research groups.

A special thanks must be given to Dr. Othman Zalloum who not only worked patiently with me on measurements that took dozens of hours but also served as a research mentor and good friend who taught and encouraged me in many areas of pursuit. He exercises resolute precision in experimental work and is a first class professional and expert; his example would serve any student well.

I express a sincere thanks to Dr. Jacek Wojcik, not least for his persistent willingness to help me with film depositions and everything to do with thin film processing but also his patience and enthusiasm in explaining the technical operation of the ECR-PECVD system and other equipment. His interest in making me aware of all of the military applications of my research work has been enlightening and will certainly come in handy in the future.

Various staff of the Centre for Emerging Device Technologies provided invaluable assistance throughout this project. Dr. Brad Robinson helped with the set-up of the Rapid Thermal Annealer – particularly by translating the intricacies of French engineering into "military terms". Mr. Graham Pearson also provided a great deal of timely assistance and advice with the set-up of the RTA, as well as training and access to a variety of equipment. Ms. Doris Stevanovic provided laboratory training – including ten hours of clean room processing in a single day, only one of which was spent looking for a sample after it "disappeared" on the optical microscope. Mr. Jim Garrett from the Brockhouse Institute for Materials Research provided an annealing facility, several times on short notice, as well as

the timely repair of nearly $1500 in sheathed thermocouples that were broken by French-engineered RTAs. It should also be mentioned that the help of Mr. Peter Jonasson of the McMaster Department of Engineering Physics was very much appreciated.

Ion beam analysis was carried out with the assistance of Dr. Willy Lennard, Mr. Jack Hendricks, and Mr. Andrew Todd of Interface Science Western, at the University of Western Ontario. Positron annihilation measurements were graciously made by Dr. Peter Simpson of the University of Western Ontario Department of Physics and Astronomy. Dr. Dominic Ryan of McGill University has enthusiastically entered into collaboration with us to investigate thulium Mössbauer spectroscopy in our films.

Thank you to the various members (past and present) of the silicon photonics research group at McMaster University for their friendship, assistance and advice: Dr. David Comedi (XEOL measurements at the Canadian Light Source), Jonathan Doylend, Joel Milgram, Tyler Roschuk, Evguenyi Chelomentsev, Dr. Michael Flynn, Ed Irving (film depositions), Phil Foster, Jon Bradley, Dr. Xiaodong Pi, and Dr. Chenglin Heng, Steve Gou and Jon Lannan.

On a different note, I must express a deep gratitude to my parents, who provided me with a wonderful home and so much encouragement. Your example of hard-work and patience were critical aspects of this project. Similarly, Scott, Alix, and Eric, with your varied talents, your varied humour, and your increasingly sophisticated questions, I have drawn more enjoyment and inspiration from all of you than you can probably know.

Finally, for my loving wife, Janis and our two fine young sons Andrew and Ethan, it would be a grievous understatement to say that you have sacrificed freely and greatly to make this research and this thesis possible. Janis, for every ounce of work that I put into this project, I fear that you have contributed two. Know that I will be forever grateful for what you have given me. *This thesis is dedicated to you.*

Contents

Abstract iii

Acknowledgements v

List of Figures xii

List of Tables xviii

1 Introduction 1

1.1 Silicon Photonics and Optical Interconnect 1

1.2 The Engineering of Silicon-based Light Sources 7

1.2.1 Current Status 7

1.2.2 Thin Film Luminescence in Er-doped SiO_x ($x \leq 2$) 9

1.3 Thesis Outline 12

2 ECR-PECVD System and Deposition Chemistry 17

2.1 Plasma Generation by ECR 19

2.2 ECR-PECVD System Description 21

2.3 Structure Physics and Deposition Chemistry of SiO_x 30

2.4 Erbium Chemistry 30

2.4.1 Er^{3+} Bonding Requirements 30

2.4.2 Experimental Determination of the Er^{3+} Site in SiO_2 32

2.4.3 Er^{3+} Site in Si-rich SiO_x 34
2.5 In-situ Erbium Doping by ECR-PECVD 39

3 Luminescence Theory for SiO_x:Er ($x \leq 2$) Thin Films 43
3.1 Basic Luminescence Theory 45
3.1.1 Quantum Mechanical Description 45
3.1.2 Luminescence of Er Ions 49
3.1.3 Luminescence in Silicon 53
3.1.4 Luminescent Electronic Defects in SiO_2 56
3.2 Fundamentals of Quantum Confinement Theory 61
3.2.1 Quantum Confinement in Nanoclusters: Brus Model . . . 61
3.2.2 Quantum Size Effects and Luminescence 64
3.3 Luminescence of Si Nano-clusters in SiO_x ($x \leq 2$) 67
3.3.1 Current Model 67
3.3.2 Implications of the Si Nano-cluster Luminescence Mechanism 76
3.4 Luminescence of Nano-structured SiO_x:Er ($x \leq 2$) 84
3.4.1 Er^{3+} Luminescence near 1.54 μm. 84
3.4.2 Energy Transfer From Si Nano-clusters to Er^{3+} Ions 93

4 Structural Description and Thermal Evolution of SiO_x:Er ($x \leq 2$) Thin Films 107
4.1 Chemical Bonding Structure of SiO_x ($x \leq 2$) 107
4.2 Annealing-Induced Changes in the Bond Structure 112
4.2.1 Phase Separation of the SiO_x Structure 112
4.2.2 Formation of Erbium Complexes 114
4.2.3 Release of Gaseous Impurities from the Film (Outgassing) 115
4.3 Annealing-Induce Phase Separation Mechanisms 118
4.4 Impact of the Anneal Parameters on the Film Structure 126

4.4.1 Input and Output Variables in Anneal Processing 126
4.4.2 Anneal Temperature 128
4.4.3 Silicon Supersaturation Relative to SiO_2 132
4.4.4 Anneal Duration 133
4.4.5 Anneal Ambient Gas 133
4.5 Description of a Silicon Nano-Cluster 135

5 Experimental Details and Process Control Issues 137
5.1 ECR-PECVD Deposition Parameters 138
5.2 Post Deposition Thermal Processing 146
5.2.1 Conventional Furnace Annealing 146
5.2.2 JetFirst 100 RTA Annealing and Calibration 148
5.3 Photoluminescence Characterization 158
5.3.1 Infrared Photoluminescence Measurement 159
5.3.2 Visible Photoluminescence Measurement 161
5.3.3 Optical-Geometrical Effects in Photoluminescence Spectroscopy 165
5.4 Ion Irradiation Study 170
5.4.1 Pre-irradiation Sample Preparation 170
5.4.2 Ion Irradiation at the University of Western Ontario 170
5.4.3 Beam-based Variable Energy Positron Annihilation Spectroscopy 171
5.4.4 Post-irradiation annealing and Photoluminescence Spectroscopy 172

6 Parameter Space Map and Luminescence Optimization 173
6.1 Er^{3+} Luminescence Line-Shape of the $^4I_{1/32} \rightarrow {}^4I_{15/2}$ Transition . . 175
6.2 Summary of SiO_x:Er Film Composition and Thickness Characterization 178

6.3 Evolution of Er^{3+} Infrared PL with Nitrogen Annealing 182
6.3.1 Oxygen-Rich Films 184
6.3.2 Silicon-Rich Films 187
6.3.3 Effect of Long Duration Annealing on PL at 1.54 μm . . . 193
6.3.4 Isolation of the Optimum Composition for PL at 1.54 μm . 196
6.3.5 Sensitizing Defects at the Optimum Anneal Temperature . 197
6.4 Thermal Evolution of the Intrinsic Luminescence Emission of Erbium Sensitizers 199
6.4.1 Oxygen-Rich and Near Zero Excess Silicon Samples . . . 201
6.4.2 Silicon-Rich Films 204
6.4.3 Effect of Annealing Duration on PL in the 350-1000 nm Band 208
6.5 Silicon Nano-cluster/crystal PL and Sensitizing Functions in the Presence of Low Er Concentrations 213
6.6 Defect PL and Other Er-Sensitizing Centres 222
6.6.1 Characteristic Spectral Forms 222
6.6.2 Visible Er Luminescence 226
6.6.3 Spectral Decomposition and Identification of Radiative Defects 227
6.7 Isolation of the Optimum Compositions for PL from Silicon Nano-Clusters and Defect Centres 232
6.8 Coupling of Radiative Defects to Silicon Nano-Clusters 233
6.9 Hydrogenation Annealing 235
6.10 Oxidation Annealing 238

7 Response of the Luminescence and Structural Properties to High Energy Ion Beam Irradiation 245
7.1 The interaction of Ion Beams with Solid Matter 246
7.2 Simulation of Ion Irradiation Damage 250

7.3 Characterization of both the Irradiation Damage and Subsequent Thermal Repair by Photoluminescence and Positron Annihilation Spectroscopies 254
7.3.1 Sample Er149 As-irradiated 254
7.3.2 Annealing-induced Changes in Irradiated Films 262

8 Conclusions and Future Work **277**
8.1 Summary of the Thesis 277
8.2 Review of Results and Conclusions 277
8.3 Suggestions for Improvements to the ECR-PECVD System 280
8.4 Future Work 281
8.4.1 Continued Materials Characterization 281
8.4.2 Electroluminescent Devices 285
8.5 Final Remarks 288

A Basic Physical Theory of Quantum Confinement **291**

B Er^{3+} 4f Electron Energy Levels **299**

C Positron Annihilation Spectroscopy **301**

D List of Publications and Presentations **307**
D.1 Journal Publications 307
D.2 Conference Proceedings and Oral Presentations 307
D.3 Conference Poster Presentations 308

References **309**

List of Figures

1.1 Interconnect delay versus transistor gate delay at successive processing nodes 3

2.1 Resolution of forces on a charged particle in a converging magnetic field 20
2.2 Schematic of the McMaster ECR-PECVD system 22
2.3 Schematic of a 6-fold oxygen-coordinated Er^{3+} site in SiO_2 35
2.4 Schematic of the 12-fold silicon-coordinated Er site in $ErSi_2$. . . . 38
2.5 Bond diagram for the $Er(tmhd)_3$ molecule 39

3.1 General configurational coordinate diagram 48
3.2 4f electron energy level splitting in an Er^{3+} ion 51
3.3 Quantum confinement of semiconductor band edge and gap states. 65
3.4 Si nano-crystal energy levels for Si–H and Si=O surface passivetion as a function of size 75
3.5 Configurational coordinate diagram for 4-level model of optical gain in Si nano-crystals 77
3.6 Schematic of the Si nano-cluster to Er^{3+} ion energy transfer 87
3.7 Schematic of non-radiative relaxation processes in Er^{3+} ions and coupling effects leading to energy transfer between Er^{3+} ions . . . 89
3.8 Schematic of multiple Er-sensitization pathways in a Si-rich SiO_x ($x \leq 2$) host 104

4.1 Schematic diagrams of the random bonding and random mixture models of SiO_x ($x \leq 2$) 108
4.2 Photoluminescence from Si nano-clusters in two films as-deposited corresponding to different excess Si concentrations 110
4.3 Scanning electron micrograph of thermally-induced blister formations at the surface of a heavily doped O-rich SiO_x film 117
4.4 Schematic comparison of the spinodal decomposition and nucleation and cluster growth phase transformation processes 119
4.5 Schematic of the diffusion fields in the cluster growth process which illustrates the concept of the equilibrium cluster size 120
4.6 Flow chart illustrating the sequence of phase separation mechanisms and their experimental manifestations in Si-rich SiO_x 122
4.7 Plasmon loss EFTEM images of the phase separation process in Si-rich SiO_x subjected to various anneal temperatures 124
4.8 Kinetic three-dimensional lattice Monte Carlo simulations of the phase separation in Si-rich SiO_x 125
4.9 Flow chart illustrating the relationship between annealing input parameters and the responding variables for the SiO_x system. . . . 127
4.10 Diffusion length of Si in SiO_2 as a function of temperature/time . . 130
4.11 Graph of the number of Si atoms comprising a nano-cluster as a function of the cluster diameter 136

5.1 Schematic of the Jipelec JetFirst 100 rapid thermal annealer 149
5.2 Flow chart illustrating the [closed loop] temperature control feedback loop on the JetFirst 100 RTA 152
5.3 Depiction of the temperature offset in the JetFirst 100 RTA 153
5.4 Determination of the temperature offset in the JetFirst 100 RTA by comparison with common models for the thermal oxidation of Si . 157
5.5 Schematic of the experimental setup for photoluminescence spec-

troscopy characterization 160
5.6 Comparison of a Si nano-cluster PL spectrum in units of spectral power density and normalized photon flux 164
5.7 Comparison of corrected and un-corrected visible PL spectra for two types of luminescence centres 165
5.8 Depiction of the surface blister geometry in sample Er118 168
5.9 Representative PL spectrum for sample Er118 in the context of microcavity interference effects 169

6.1 Engineering cycle for optimizing luminescence in SiO_x:Er 174
6.2 Examples of the luminescence lineshape of the Er^{3+} $^4I_{13/2} \rightarrow$ $^4I_{15/2}$ transition observed for various film preparation conditions . . 175
6.3 Ellipsometry measurements showing the densification of thin film sample Er149 as a function of annealing 180
6.4 Anneal-PL correlation in the 1400-1650 nm emission band over all compositions (annealed under N_2 ambient). 183
6.5 PL intensity in the 1400-1650 nm band as a function of Er content in films with no excess Si 185
6.6 Anneal-PL correlation in the 1400-1650 nm emission band for various films annealed at long duration (3 hours) 195
6.7 Three-dimenional plot of the PL near 1.54 μm designed for the isolation of the optimum film composition 196
6.8 Pacifici et. al., PL near 1.54 μm as a function of anneal temperature 198
6.9 PL excitation spectra at 1.54 μm for various pre-doping anneal temperatures with normalization to show defect absorption 198
6.10 Representative PL spectra in the 350-1000 nm band 200
6.11 Anneal-PL curves in the 350-1000 nm band for films that do not contain excess Si (annealed under N_2 ambient) 201
6.12 PL intensity in the 350-1000 nm band as a function of Er content

in films with no excess Si 203
6.13 Anneal-PL curves in the 350-1000 nm band for films that contain moderate excess Si concentrations (annealed under N_2 ambient) . . 205
6.14 Anneal-PL curves in the 350-1000 nm band for Si-rich films having extreme compositions 207
6.15 Anneal-PL correlation in the 350-1000 nm emission band for various films annealed at long duration (3 hours) 209
6.16 Impact of rapid thermal annealing on Si nano-cluster PL at 1100 °C relative to a one hour anneal 211
6.17 Comparison of PL spectra for visible and infrared emission bands at various anneal temperatures in Si-rich SiO_x with low Er content . . 215
6.18 Effect of hydrogenation on the visible PL in film Da9 217
6.19 Red-shifting of the apparent Si nano-cluster PL emission with increasing excess Si content for low temperature formation 217
6.20 Si nano-cluster PL peak wavelength shift as a function of excess Si content for films annealed at 1100 °C 218
6.21 Gaussian fit of a sample Si nano-cluster PL emission band 219
6.22 Linear fit of the Si nano-cluster PL emission band full-width-at-half maximum as a function of excess Si content 220
6.23 Lorentzian composition dependence of both the Si nano-cluster and Er^{3+} PL in samples with low Er content annealed at 1100 °C. . . . 221
6.24 Characteristic spectral forms for 350-850 nm band defect PL . . . 224
6.25 Defect PL in the 350-850 nm band at various anneal temperatures. 225
6.26 Co-operative up-conversion luminescence from Er^{3+} in Si-rich SiO_x 227
6.27 Fitting by Gaussian de-convolution of the visible defect PL in representative spectra 228
6.28 Fitting by Gaussian de-convolution of the visible defect PL spectrum in thermally grown SiO_2 229

6.29 Fitting by Gaussian de-convolution of PL spectrum in sample Er118 230

6.30 Three-dimenional plot of the PL in the 350-850 nm band as a function of composition for an anneal temperature of 800 °C 232
6.31 Relationship between the defect PL and that at 1.54 μm 234
6.32 Comparison of PL in both visible and infrared emission bands for annealing under N_2 or (Ar + 5% H_2) gas 236
6.33 Comparison of PL in the 350-850 nm band for a highly Si-rich film annealed at 800 °C under N_2 or O_2 ambient gas 239
6.34 Effects on the visible PL emission of annealing under O_2 gas in films containing either zero or non-zero excess Si content 240
6.35 Comparison of PL in the 350-850 nm band for moderately Si-rich films annealed at 800 °C under N_2 or O_2 ambient gas 242

7.1 TRIM simulations of irradiation damage cascades and ion ranges . 251
7.2 TRIM simulations of target vacancies by element in sample Er149 following exposure to a 1 MeV Si^+ ion beam 252
7.3 Logarithmic plot of the PL intensity in the as-irradiated film as a function of ion fluence 255
7.4 Full positron annihilation S and W spectra as a function of ion fluence in films as-irradiated 256
7.5 Positron annihilation S and W parameters within the film as a function of ion fluence in films as-irradiated 259
7.6 Gamma ray photopeak difference spectra indicating formation of *p*-Ps for various fluences in as-irradiated films 261
7.7 Representative recovery curves for the PL intensity in all visible and infrared emission bands as a function anneal temperature 262
7.8 Ratio of the blue-violet PL peak to the broad red emission as a func-

tion of post-irradation anneal temperature for different ion fluences 265
7.9 (PART 1) Integrated PL intensity recovery in each emission band as a function of post-irradiation anneal temperature (all fluences) . . . 266
(PART 2) Visible and infrared band PL intensity plotted simultaneously for each individual irradiation fluence 267
7.10 Integrated infrared PL intensity recovery plotted alongside the positron annihilation S-parameter recovery as a function of the annneal temperature 272
7.11 Gamma ray photopeak difference spectra indicating formation of *p*-Ps at various film temperatures and irradiation fluences. 273
7.12 Positron annihilation S and W parameter spectra as a function of the post irradiation anneal temperature for the highest ion fluence . . . 275

8.1 X-ray excited PL from film Er149 excited at the oxygen K electron-shell absorption edge 282
8.2 ^{169}Tm Mössbauer spectrum for film Er147 and Tm-based standards 284

A.1 Representation of dimensions in nano-structures 291
A.2 One-dimensional quantum confined wave functions and energies . 293
A.3 Density of states function for 0D, 1D, 2D, and 3D solids 296
A.4 Energy levels at the band edges of a quantum confined solid film . 297

C.1 Markhovian distribution for positron implantation into SiO_2 at an energy of 2 keV 303

List of Tables

2.1 Classifcation of critical deposition parameters in ECR-PECVD . . 27

3.1 Multi-phonon decay rates for a series of higher-lying transitions in the Er^{3+} ion 93

4.1 Experimentally verified relationships between annealing parameters and Si nano-cluster distribution characteristics 128

5.1 Summary of ECR-PECVD deposition parameters and specifications for all of the films grown as part of this study 141

5.2 Calculation of the surface dome height in sample Er118 as determined by the photoluminescence fine structure under the assumption of interference modulation 169

5.3 List of ion irradiation parameters for sample Er149 171

6.1 Complete listing of the composition, thickness, and refractive index for all films deposited as part of the thesis research 179

7.1 Vacancy concentration by element following irradiation of sample Er149 to various fluences with a 1 MeV Si^{+} ion beam 253

B.1 Er^{3+} 4f energy levels and term symbols 299

C.1 Positron annihilation processes and characteristic liftetimes 304

Chapter 1

Introduction

1.1 Silicon Photonics and Optical Interconnect

High speed communication is a classic self-motivating technology whose advancement relies on *synchronous* improvements to component technologies. Like the flow of an incompressible fluid through a closed loop, this paradigm for the transfer of information breaks down when asynchronous advancement of the sub-technologies leads to information 'pile-up' at the slowest component. Optical fibres, for example, rescued long-haul data transfer from performance-crippling attenuation losses in metallic electrical transmission lines when computer performance – in conjunction with the demand for information prompted by the internet – drove bandwidth demand into the GHz regime.[1] Within the last ten years an analogous situation has arisen at the micro-processor level wherein four decades of the pursuit of Moore's Law has finally led to computer chips which can process information faster than they can transmit and receive it. As a fabrication-for-speed performance paradigm, Moore's law is based on the decrease of transistor gate time-delay with decreasing device size, allowing the chip to operate at ever-higher clock speeds. This has led to modern-day computer chips with bizarre device-packing densities reaching over one billion transistors

[1] While optical fibre was introduced to address attenuation problems, their potential bandwidth is currently nowhere near being fully exploited. A single optical fibre can, in theory, be made to transmit 150 trillion bits per second.

per square centimetre and blinding clock speeds expected to hit 14 GHz by 2009.[2] Connecting these *nano*-transistors to the outside world gives rise to an increasingly complex interconnect[3] in which kilometres of metal channelling (per chip) is processed into nano-spaced lines and layers with a required exactitude measured by the clean distribution of GHz clock signals. However, unlike transistors, interconnect speed *decreases* as the wire cross-section shrinks, increasing the parasitic resistive-capacitive (RC) coupling delay[4,5] – directly contradicting the need to operate at high clock speed. Today, the 'interconnect bottleneck' *is* the limiting factor in chip-speed performance; interconnect cannot keep up with Moore's law.[6] This is powerfully illustrated in Figure 1.1.

Under the *Manhattan* interconnect paradigm [1], the problems extend to include cross-talk between adjacent wires,[7] severe power consumption (which raises thermal dissipation concerns[8]), electromigration in the inter-metal dielectric, and low tolerance to signal noise.[9] The replacement of individual metallic wire interconnect with dielectric optical wave-guide interconnect would solve the problems that the former has under both dense line packing *and* high

---

[2] Instead of slowing down, this trend is accelerating. Multi-core processors are coming online. Terahertz transistors are set for production at the 65 nm processing node and prototype transistors were demonstrated at the 22 nm node (with 10 nm gate length and less than 0.1 ps gate delay). Interestingly, this has largely been achievable with nano- and materials engineering (eg. strained Si channels by embedded SiGe layers in the source/drain, silicon-on-insulator, NiSi gates, high k gate dielectrics, etc.) without resorting to radical re-engineering of the device architecture (although this is now being seriously explored with devices such as the Intel Tri-Gate transistor).

[3] This includes both high intra-layer interconnect density and an increasing number of layers to minimize area and wire cross-talk. Such complex interconnect decreases device processing yields.

[4] Clock speeds are actually reaching the point at which RLC delay becomes a factor; in conjunction, they are driving the 'R' higher because of increasingly severe skin effect.

[5] Furthermore, interconnect latency is proportional to the square of the wire length. Not only is this being exacerbated by a trend of increasing chip die size but it limits inter-chip links; chip-chip interconnect beyond 20 inches will not handle 10 Gbps of data transfer without significant effort.

[6] Significantly more time and money must now be invested to yield progressively smaller performance gains.

[7] This problem is particularly acute for local and intermediate interconnect.

[8] Current power densities in micro-processors are similar to that in a rocket nozzle (~kW/cm^2). Ironically, the necessary use of low k inter-metal dielectric to reduce capacitance (wire cross-talk) also tends to reduce its thermal/electromigration stability. The further the interconnect lines from the substrate (a good thermal conductor) the worse they dissipate heat because the dielectric matrix is thermally insulating (therefore heating at the device gates is less of an issue).

[9] This problem is exacerbated by the continuous reduction in transistor operating voltages

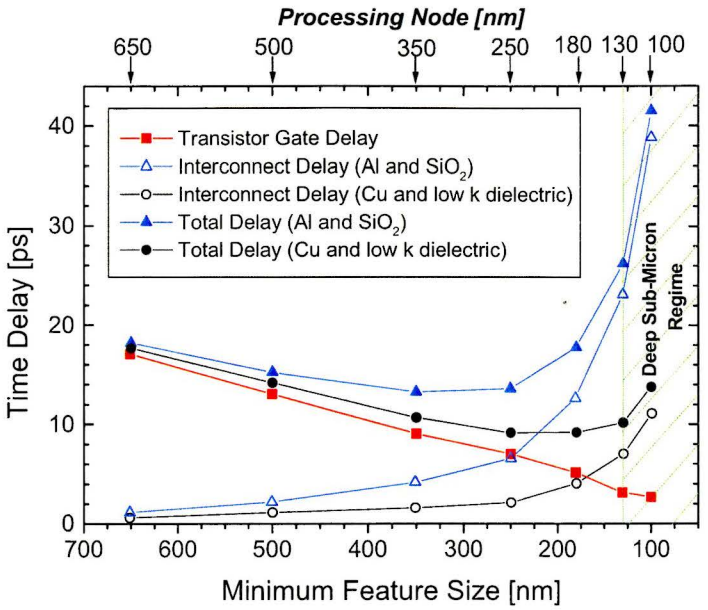

Figure 1.1: Shift of the micro-processor speed 'performance bottleneck' from the transistor gate to the interconnect [2]; materials engineering of the line and dielectric has rescued electrical interconnect so far: Al/SiO_2 was replaced at the 180 nm node by Al/SiOF, which was replaced by Cu/SiOF at 130 nm and finally by Cu/SiOC at 90 nm.

frequency operation.[10] The associated move to an optical frequency carrier would provide many advantages relevant to chip interconnect. [11] Clock distribution, which is carried by *global interconnect*, would be the first chip-level implementation; it is the highest bandwidth interconnect function (and power consumer) on a chip and so is increasingly subject to skew and jitter – that are already exacerbated by the broad fan-out of global interconnect. Multiplexing clock and data signals would simultaneously reduce clock distortion[12] and the required I/O pin density [3].

---

[10] This is because the former guide waves through a free carrier-mediated conduction mechanism (this is *impractically inefficient* when the electric-field oscillates beyond 10^{11} Hz) while the latter involves no free carriers (this becomes *practical to implement* once the frequency is ~10^{14} Hz).

[11] These include much larger potential information capacity (bandwidth; >Tb/s estimated for CMOS opto-electronic interconnect), low-attenuation transmission, no RC coupling delay, dense wavelength division multi-plexing capability, reduced signal cross-talk, robust signal (against RF interference), transmissible through free space, negligible heating, etc.

[12] Note also that optical signals can be split without introducing clock skew.

Unfortunately, the shift to an optical interconnect paradigm, as epitomized by the long-haul optical fibre, does not easily translate into the ULSI environment of Si-CMOS micro-electronics; the comparatively huge size of current photonic devices, their low processing yields and problematic integration onto a single chip are the biggest obstacles. Furthermore, today's photonic devices are dominated by exotic III/V semi-conductors, which are prohibitively expensive for chips intended for mass-marketing, and which are not even immediately compatible, from a fabrication perspective, with Si or CMOS. Any optical interconnect solution that is to be cost-effective for a major computer chip manufacturer (and therefore of any practical interest) will have to be integrable into the Si-CMOS back-end process-flow *and* monolithically integrated on a single Si substrate.[13] This leaves two options[14]: develop a cost-effective method for CMOS-compatible hybrid-integration of III/V photonic components on a Si substrate, or engineer the required photonic devices directly from Si or specific Si-based materials. The former solution solves the integration issue, in principle, but does not solve the device size problem, and is plagued by processing complexities[15] and probable device alignment issues – all driving up cost.[16] In comparison, the integrated 'all-silicon solution', beyond offering apparent ease of processing and a proven capability in nano-scale devices, promises to make opto-electronics 'cheap'. Indeed, it has a *huge* cost-beneft in the ability to leverage the decades of experience gained in the field of Si processing as well as a hundred billion dollars in research and Si-CMOS fabrication infrastructure. Such is the interest, that an entire field of '*silicon [micro]-photonics*' has rapidly taken shape [4], which

---

[13] In particular, rising chip costs associated with packaging and the increasing I/O pin density among other issues, provide a very strong motivation for monolithic integration. Assembly of optical devices can account for up to *a third* of the cost of the finished product today. Integration would save huge amounts of money since optical devices would not have to be packaged individually.

[14] This does not include free-space optical interconnect schemes.

[15] This would include exotic epitaxial re-growths which would likely destroy chip yields.

[16] Some of the most advanced opto-electronic integration to date has been achieved by Infinera Inc., which has built extremely competitive WDM systems in InP.

seeks to transform Si micro-electronics into Si-*opto*-micro-electronics – and seize an industry worth nearly 200 billion dollars in the process [1,5].

While a marketable rendition of Si-photonic *chip-level* interconnect is likely 10-15 years away, the interim implementation still promises ulta-fast inter-rack/board and perhaps inter-chip optical networking.[17] Furthermore, it could permit optical 'fibre-to-the-home' (FTTH[18]), which has thus far been prevented by the high cost of [III/V] photonic components.[19] The coupling of the optical fibre directly on to the micro-processor is also envisioned. One immediate push for these types of technologies is based on the anticipated explosion of data transfer between billions of connected digital media devices [6]. At the current time, most companies pursuing Si photonics are focusing on the computer chip market, which is much larger than the telecoms market [7]; there is an historical irony to this given that the concept of photonic integration was a product of the telecoms boom in the late 1990s – the idea was scrapped when the market ran into problems.

The realization of monolithic Si-CMOS opto-electronics requires the development of four main devices (these form the standard operating basis set for all integrated optical circuits).

Light Source

The source converts electrons to photons; configured differently, it could provide light amplification. For short-distance interconnect, an incoherent (LED) source would be sufficient, while long distance fibre applications would require a laser. The source should ideally be electroluminescent (ie. electrically pumped). While not strictly necessary, the option of direct (drive current-mediated) high-speed (GHz) modulation of the electroluminescence (EL) is preferable. The wavelength would ideally be below the Si band gap (~1.1 μm). For fibre-optic applications,

[17] This would represent a huge improvement over current copper-clogged rack and blade servers.
[18] Optical fibre communication is still limited by the 'last mile' of copper line to individual homes.
[19] In this application, the often mentioned problem of the lack of speed in Si-photonic components would not be an issue since MHz signalling would be adequate for an individual household.

the wavelength should be near 1.55 μm, which corresponds to the [C-band] ultra low-loss propagation window (1.45-1.60 μm) in SiO_2-based optical fibres. The most practical laser in Si to date seems to be a hybrid Si evanescent laser; the optically pumped – though potentially electroluminescent – device uses offset AlGaInAs quantum wells bonded to a Si waveguide in Si-on-insulator (SOI) and emits at 1568 nm [8].

Modulator

The modulator encodes information on the photon stream and can be configured to provide optical switching. Chip-based optical interconnect requires a GHz modulator. Optical modulation in Si is difficult because its crystal does not exhibit any Pockel's electro-optic effect (for electric dipole transitions). A weak free carrier dispersion effect (also known as plasma dispersion or the Drude effect) is the only available practical means of controlling the refractive index and is usually limited to tens of MHz. Nonetheless, Intel's Photonics Technology Lab (which is devoting a major research effort to Si photonics) recently developed a plasma dispersion modulator in silicon-on-insulator (SOI) [9]. The device uses a Mach-Zehnder wave-guide geometry with the source-drain current of an integrated field effect transistor to inject carriers. Operation at 1 GHz has been demonstrated; the device later demonstrated a data transmission rate of 10 Gb/s.[20]

Waveguide Devices

Waveguides perform various functions including the guiding, coupling, splitting, and combining of various streams of photons. They refer to an array of passive devices including point-to-point links, various opto-couplers,[21] beam splitters, and

---

[20] Luxtera Inc. (a start-up company from CalTech) claims to have produced a 10-Gbit/s CMOS modulator operating at 1550 nm that is superior to Intel's device. They are currently developing a 40-Gbit/s interface for DWDM by integrating the devices in at attempt to gain a foothold in the computer chip market, while leaving their options for telecoms open.

[21] Fibre-to-waveguide coupling for Si photonics is a perplexing problem because of the large mode mismatch. See (J. K. Doylend, et. al., Proc. SPIE **5970**, 59700G (2005)).

even waveguide gratings. These have been well-demonstrated in Si, SiO_2, and SOI for a range of geometries, particularly for 1.55 μm light [1,5]. The high index mismatch between Si (3.52) and SiO_2 (1.46) makes for tight confinement and reduced bend losses. Ion implantation-induced defect engineering has been used to enhance mode confinement and provide optical isolation between adjacent waveguides [10].

Photo-detector

The photo-detector converts photons to electrons and can be configured to provide power monitoring. Although this is easily achieved in Si for most visible wavelengths, the problem is much more difficult for sub-band gap photons – such as 1.55 μm. Band-gap engineering with SiGe alloys provide one solution [1]. A more novel solution relies on the introduction of divacancy defects in crystalline Si by irradiation with protons; these mid-gap charged defects strongly absorb 1.55 μm photons. Incorporation of a rib waveguide on SOI into a *p-i-n* diode has permitted MHz photo-detection in an unoptimized device [11]. To date, the low conversion efficiency limits their use to optical power monitors; however this is expected to improve.

1.2 The Engineering of Silicon-Based Light Sources

1.2.1 Current Status

Of the aforementioned photonic devices, a reliable and efficient Si-based EL device remains the major stumbling block towards the full realization of the basic infrastructure for Si optoelectronics.[22] To date, all of the required photonic

[22] While the basic Si photonic infrastructure may be nearly in place, little research effort has actually been invested into device integration. Current thought in the field seems to be dominated by individual device engineering. The assumption seems to have been made, by default, that integration will prove less of an engineering problem than that of the basic device physics so that the two can be handled sequentially. However, because Si photonics is such a disruptive technology, it will not be easy to bring it online with current micro-processor technology

components have been simply demonstrated in Si-based materials (with effectively CMOS compatible processing) *except* an electrically pumped Si laser.

Silicon Laser

Although Si is fundamentally a poor light emitter because it has an indirect band gap, there are two particular gain limiting mechanisms which specifically hinder lasing in Si [1,12]. The first is free carrier absorption, in which a free electron or hole absorbs a photon. The second is non-radiative three-particle Auger recombination, in which an electron-hole pair recombines by non-radiatively transferring energy to a free carrier,[23] exciting it higher into the excited band. Because both of these mechanisms are exacerbated by anything that populates the conduction band (including the intrinsic carrier generation at room temperature) they inhibit population inversion by definition. It was hoped that quantum confined Si nano-structures would resolve these issues. Indeed, gain was observed in the system of Si nano-crystals embedded in SiO_2 under optical pumping [13,14]. However, a corresponding injection laser has remained elusive owing to the problem of efficient electrical injection through the semi-insulating oxide (and oxide-based cavity mirrors).

Only partially satisfying was the development, by Intel, of an optically pumped continuous wave Raman laser *in Si*, which relies on the huge stimulated Raman scattering coefficient in pure Si. The device integrates a *p-i-n* diode structure across the gain-active rib waveguide in order to sweep out free carriers generated by two-photon absorption (which limited early prototypes to pulsed

---

advancing as fast as it is. It has even been suggested that the integration problem might prove fatal to Si-CMOS optical interconnect *even if* every individual device is successfully developed. The fact that a device is Si-based does not, in any case, necessarily mean it is compatible with CMOS processing. For example, Si *p-i-n* photo-detectors are not CMOS compatible because of the required intrinsic layer. In this way, Si photonics may be relegated to its own isolated systems.

[23] Er-doped Si exhibits Auger transfer to bound carriers as well, however the Auger coefficient with free carriers is two orders of magnitude higher (See: Priolo, et. al., Phys. Rev. B **57**, 4443 (1998)).

operation) [15]. Evidently, an injection laser is not an option with this mechanism.

Light Emitting Diodes

In general, there have been approximately six main approaches to attaining EL from Si [1]. These are as follows (italics in parentheses indicate examples): bulk Si systems attempting to eliminate non-radiative defects or decrease the free carrier diffusion length (*ultra-pure Si with careful surface passivation and texturing; implant-induced dislocation loops*), band structure engineering via alloying to create a "more direct" band gap ($Si_{1-x}Ge_x$ *or* $Si_{1-x-y}Ge_xC_y$ *multi-layer films*), quantum confined structures that attempt to force electron-hole localization with wave function overlap (*porous Si; Si nano-clusters in Si-rich* SiO_x*; nanocrystalline Si*), introduction of impurity luminescence centres (*iso-electronic impurity complexes in Si or a SiGe alloy; rare-earth doping of Si or* SiO_x *with nano-clusters*), relying on intra-band transitions so that the indirect band gap is irrelevant (*Si/Ge quantum cascade structures*), and polymers containing Si which display a direct band gap (*siloxene or polysilane and its polymer derivatives*).

1.2.2 Thin Film Luminescence in Er-doped SiO_x ($x \leq 2$)

In terms of achieving light emission near 1.55 μm[24] without a wavelength converter, the simplest approach employs Er doping, which coincidentally exhibits a metastable optical transition in this vicinity.[25] While Er doping of bulk Si is the logical and simple choice for fabricating EL devices, the emission is plagued by severe temperature quenching.[26] Furthermore, the EL is dominated by

---

[24] The 1.55 μm wavelength is not necessarily essential if one is uses it only for chip level interconnect.

[25] This makes it well suited for achieving population inversion and optical gain, and has now been exploited for 15 years in fibre amplifiers for long-haul telecommunication signal regeneration.

[26] Another advantage of Er-doped crystalline Si is the huge optical absorption cross-section of the Er ion (~$2\text{-}8\times10^{-12}$ cm^2 at 488 nm) – to be compared with Er in SiO_2 (<8.0×10^{-21} cm^2). See page 230 of A. J. Kenyon, Prog. Quan. Elec. **26**, 225 (2002).

hot electron impact excitation of the Er itself rather than a soft excitation by energy transfer from carrier recombination. In order to avoid these problems, attention has largely shifted to Er doped [Si-rich] SiO_x ($x<2$). The Si-rich SiO_x material system has been well researched within the last ten years owing to the luminescent Si quantum dot-like nano-clusters that form upon high temperature annealing. This system was hailed as a chemically and structurally stable[27] alternative to porous Si [16].[28] While the intense photoluminescence (PL) exhibited minimal temperature quenching, the emission was, however, exceedingly broad and peaked at 850 nm. It was found that Er doping of the material could effectively tune the emission to 1.54 μm, with significantly enhanced PL response over Er doped SiO_2 (a common material for fibre amplifiers) at non-resonant pump wavelengths as a result of an efficient energy transfer from the broad-band absorbing Si nano-clusters to surrounding Er^{3+} ions. The structurally disordered Si-rich SiO_x host matrix had the added advantage, over both bulk Si and SiO_2, of being able to incorporate a larger amount of optically active Er. Furthermore, it easily incorporates into a waveguide structure, can be optimally processed below 900 °C, and lends itself well to opto-isolation. For example, multiple circuits built in the same chip could be electrically isolated from each other by insulating SiO_2 but could communicate via optical signals. In an effort to maximize the energy transfer to the Er dopant, refinement of the film deposition methods has allowed Er-doped Si-rich SiO_x materials to be fabricated in superlattice structures with size-controlled Si nano-cluster distributions and precise control of the Er location [17]. As a photoluminescent material, this system shows great promise for planar optical amplifiers.

LEDs based on the SiO_x:Er system have shown significant promise, with the most advanced device being a MOS capacitor-like structure created by ST Microelectronics claiming a 10% external quantum efficiency [18,19]. However,

---

[27] In particular, this sytem is stable against room temperature oxidation, UV light and some ionizing radiation, as well as surface contact and light abrasion.

[28] The discovery of luminescent porous Si in 1991 sparked the current interest into Si-based light emitters for optoelectronics.

the mechanism of Er (and Si nano-cluster) excitation under current injection has universally been found to be dominated by hot electron impact excitation of the Er itself, with a seeming inability to leverage the nano-cluster sensitization mechanism so effective in the PL regime [20]. This is due to the insulating behaviour of the host, through which current injection occurs predominantly by a Fowler-Nordheim tunnelling mechanism [21]. This means that high electric fields (reverse bias conditions) are necessary to inject non-negligible carrier concentrations into the oxide and these carriers propagate through the material via the conduction band of the [wide band gap] SiO_x. This quickly leads to impact ionization and dielectric breakdown of the oxide, rendering the device useless. The fundamental problem here is that the devices rely on unipolar injection into the nano-clusters. More effective and efficient photo-excitation is based on an effective bipolar injection. Five years ago, this seemed to be a minor problem that could be fixed though the combined optimization of the device structure, current spreading in the contacts and film quality. A rash of devices produced by a dozen research groups around the world seems to be proving otherwise. The best devices do not last more than a few days. The paradigm of the pure engineering guess-and-test approach without full understanding of the physics of the material structure and luminescence mechanism, while often of use in quickly developing marketable devices, seems unworkable in this instance. Stagnation in the literature with respect to EL devices, not one of which demonstrates anything novel with respect to its predecessors, suggests that the field needs somewhat of a re-think in its approach. *This material system does not need any more 'proof of concept' MOS capacitor EL devices.* Fundamentally, this material system (and perhaps the associated deposition technologies) needs a fully developed *physical and chemical model* so that properly rigorous optimization can be undertaken and device engineering can be sensibly pursued with a real chance of success. Alternatively, EL device structures need to be re-engineered with serious attention

paid to novel current injection schemes – particularly those aimed at bipolar injection. Funding and research projects should shift to reflect this need.

In principle, such a re-evaluation may be starting to take shape. Experiments on this material system are becoming much more sophisticated. Furthermore, the first radical departure in EL device geometry, specifically aimed at resolving oxide reliability issues appeared in 2005 [22]. This device uses a field-effect EL mechanism in a Si nano-cluster floating gate transistor to achieve bipolar injection into the nano-clusters. The carriers sequentially tunnel (by *controlled* Fowler-Nordheim tunnelling) into the clusters from the source-drain channel, which reverses polarity at kHz frequencies. The device has exhibited stability over more than 5 billion cycles. The field-effect LED has not yet been applied to Er-doped SiO_x.

1.3 Thesis Outline

The current thesis is guided by this context of a requirement to understand the luminescence mechanisms and material structure of SiO_x:Er. Specifically, this work focuses on two issues. The first addresses the multiplicity of luminescence centres in Er-doped SiO_x ($x \leq 2$) thin films and how they couple to each other to influence Er-ion emission near 1.54 μm. Within the framework of these luminescence centres, the second issue addresses how the emission from the various centres depends on processing variables as pertaining to a plasma-based film deposition and subsequent thermal treatment. All depositions were based on SiH_4/Ar and O_2/Ar precursor gas mixtures and were carried out on a *electron cyclotron resonance plasma enhanced chemical vapour deposition* (ECR-PECVD) system with a specially engineered in-situ Er-doping capability relying on the metalorganic $Er(tmhd)_3$ precursor. A discussion of the ECR-PECVD system and associated deposition physics and chemistry is given in Chapter 2. Special attention is paid therein to Er chemistry and its incorporation in Si-oxides. In-situ Er doping of Si-rich SiO_x thin films is not common but is carried out

predominantly with two alternative techniques. The first is co-sputtering of Er or Er_2O_3 targets alongside Si/SiO_2 or SiO_x targets [23,24]. This permits reasonably high dopant concentrations up to a few atomic percent but raises concerns about film sputtering and ion bombardment damage. The second technique, as in the present study, relies on metal-organic CVD employing any of the numerous volatile Er precursors [25,26,27]. This technique also pemits high doping concentrations but results in carbon and orangic ligand contamination of the films. A semi-remote ECR-PECVD technique using concurrent sputtering of a metallic Er target in the glow discharge represents a hybrid technique intended to resolve both problems, however, it is not clear that Er sputters effectively in an oxygen-based ECR plasma (possibly since Er reacts vigorously with O) [28].

Chapter 3 gives a summary review of the fundamentals of luminescence theory, particularly in the context of rare-earth ions, silicon, and oxide point defects. Basic quantum confinement theory is reviewed and followed by a detailed application to semiconductor nano-clusters according to the Brus model [29]. Finally, a coherent treatise on Si nano-cluster luminescence along with the associated sensitization of optically active Er is presented based on the current understanding and literature.

Chapter 4 provides a detailed review of the thermo-chemical properties of the as-deposited thin films and their subsequent evolution under thermal annealing. Particular attention is paid to the evolution of the SiO_x phase; both spinodal decomposition and classical cluster nucleation and growth models are considered. The role of the Er and C-based impurity doping is discussed.

Chapter 5 reviews a selection of the post-deposition processing and experimental systems used in this study.[29] A number of recommendations are put

[29] Rutherford backscattering spectrometry (RBS) was an important composition measurement and profiling technique employed in this study, however it is not discussed in this thesis. Nonetheless, a major component of this work focused on enhancing the use of RBS as a characterization tool for these films; novel methods were found for extracting compositional information obscured in the RBS spectra as a result of the use of Si substrates. Two major software packages for analysing RBS data were compared (*Qualitative Analysis of Rutherford Kinemetics* (QUARK) deveoped at the University of Western Ontario, and the *RBS DataFurnace* developed at the Surrey Centre for

forth for enhancing process control on the ECR-PECVD system. The calibration and optimization of a rapid thermal processor, which formed a part of the current project, are discussed. Luminescence characterization in this study was carried out with single wavelength laser photoluminescence (PL) spectroscopy. The collection of both infrared and visible band PL is described along with common critical errors associated with this type of measurement as pertaining to experimental geometry and micro-cavity effects.

Chapter 6 presents a PL study of the deposition parameter space map for the ECR-PECVD system. A large number of films were studied with a range of both excess Si and Er concentrations. The major luminescent centres in the film were identified and classified into those resulting from the incorporation of the excess Si and those resulting from the incorporation of the Er. The coupling relationships between these centres, as well as their ability to enhance the Er-related PL at 1.54 μm, were probed through the evolution of their luminescence properties with annealing and over a range of annealing conditions. The results were connected with probable structural changes occurring in the films upon annealing. This information was used to identify the optimum composition and thermal treatment for maximizing the PL from the various luminescent centres. It was also used to assess the impact of deposition parameters on the film structures.

Chapter 7 investigates, more specifically, the role of luminescent oxide defects in the sensitization of Er luminescence. A film with optimized PL was intentionally damaged by Si^+ ion irradiation to induce a quenching of the PL signal. The subsequent recovery of the PL (corresponding individually to the different luminescent centres) with step-wise annealing was tracked and concurrently characterized by thin film positron annihilation spectroscopy using the slow positron beam at the University of Western Ontario.

Chapter 8 presents the final conclusions from the study relating to luminescence optimization and mechanisms. The impact of these conclusions on

---

Research in Ion Beam Analysis (SCRIBA)); the utility of fitting versus simulation routines was analyzed.

general EL device engineering is discussed. Suggestions for future work are identified both for further material structure characterization and EL device fabrication based specifically on films from the ECR-PECVD system.

Chapter 2

ECR-PECVD System and Deposition Chemistry

It has become common in Si CMOS processing to deposit dielectric thin films, particularly SiO_2 by chemical vapour deposition (CVD). CVD refers to an entire class of thin film deposition techniques, in which selected precursor gases (dependent on the desired film) are supplied to a substrate whereupon they are made to chemically react with each other. Certain of the reaction products chemisorb on the surface to form the desired film while the remainder desorb and are removed from the system. With properly engineered reaction chemistry, the film stoichiometry and bond structure can be precisely and repeatably controlled with a minimum incorporation of impuiry elements. The various methods by which the energy is supplied to drive the necessary chemical reactions define the specific types of CVD. Thermal CVD, wherein the reaction is enabled by substrate and gas heating, is inherently simple but is often not practical for the deposition of dielectric films (such as SiO_2) required in back-end CMOS or optoelectronic integrated circuit fabrication.[30] A major effort in process engineering has historically been devoted to the development of low temperature thin film deposition systems – particularly those for depositing SiO_2 – which can duplicate the excellent quality and film uniformity of thermal CVD (such as the

[30] The high temperatures typically required are prohibitive from a processing perspective as they can cause unwanted dopant diffusion or damage device structures.

themal oxidation of Si). Plasmas provide a means of achieving both objectives because they can simultaneously contain high energy particles but maintain a low overall temperature. The extremely high energy electrons in a plasma can be used to supply the thermal energy necessary to drive the reaction, while low temperatures can be maintained in the deposition chamber and at the substrate.[31] The use of a plasma to "enhance" the rate of chemical reaction of the precursor gases in CVD is referred to as plasma enhanced CVD (PECVD). There are various types of PECVD, each defined by a different method for generating the plasma. The most common is radio frequency (RF) PECVD (or often simply designated 'direct PECVD') which has an inherently simple implementation in the form of parallel electrodes between which a standard capacitive plasma is generated. The geometry of such an electrode system, however, necessitates that the substrate and therefore the film is submerged directly in the glow discharge of the plasma. The bombardment of the films by ions and other energetic particles present in the glow discharge can lead to both radiation and sputtering related damage to the film and incorporation of unintended products. Furthermore, the fact that all of the precursor gases are flowed through the plasma means that one has little control over the reaction pathways that lead to film deposition [30].[24] A partial solution to these issues is to design a 'remote' deposition system, in which the substrates are located a distance from the plasma, and in which precursors can be introduced at different locations in the reactor chamber. This usually necessitates a new technique for generating the plasma such as electron cyclotron resonance (ECR). In fact, ECR-PECVD (electron cyclotron resonance plasma enhanced chemical vapour deposition) has become popular in the deposition of numerous different dielectric optical coatings having demanding quality and uniformity requirements.

---

[31] Contrary to thermal formation of a thin film, this technique effectively forms a film by 'quenching'. The plasma cracking of the precursor gases produces highly reactive species which are thermodynamically only attainable at *much* higher temperatures. Forcing these species instantly onto a comparatively cold substrate results in rapid quenching which forms the film.

2.1 Plasma Generation by ECR

A magnetic field of flux density B exerts a force on a particle of charge e, which is directed along the cross product $e\boldsymbol{v}\times\boldsymbol{B}$ where $\boldsymbol{v}$ is the instantaneous particle velocity. Provided $\boldsymbol{v}$ is not parallel to $\boldsymbol{B}$, continual exposure to the field forces the charged particle to execute a circular motion.[32] The angular frequency of gyration (cyclotron frequency) ω_c and the radius of the trajectory r_L (Larmour radius) are constant for non-relativistic particles and can be determined classically by balancing the magnetic and centripetal forces:

$$\omega_c = \frac{eB}{m_e} \tag{2.1}$$

and

$$r_L = \frac{v_{perpendicular}}{\omega_c} \tag{2.2}$$

where m_e is the mass of the particle and $v_{perpendicular}$ is the velocity component perpendicular to the applied magnetic field. ECR refers to the condition whereby an electron undergoing such a motion will resonantly absorb circularly polarized electromagnetic radiation, whose wave vector is directed along the applied magnetic field, *at the cyclotron frequency* ω_c.[33] The electron continuously gains energy from the electric field, increasing r_L accordingly.[34]

ECR can be used to generate a stable plasma since the resonant effect quickly (and stochastically) generates electrons with sufficient energy to ionize neutral gas atoms/molecules through inelastic collisions, liberating further electrons which then undergo ECR themselves – creating an avalanche effect.

---

[32] The path is actually helical when there is a drift velocity component. This helical path is advantageous because it increases the effective path length of an electron within the plasma (before being lost at a chamber wall) thereby increasing its probability of ionizing a gas atom.

[33] The driving frequency must be greater than the plasma frequency.

[34] How much energy is gained by an electron for each pass through the ECR zone is a very complicated subject because the electron velocity distribution is a function of its instantaneous orientation relative to the applied magnetic field. Thus, the phase of the electron, as it passes through the resonance zone, relative to the electric field affects how much energy it absorbs from the electric field.

Plasma process gases vary in their ability to absorb energy from electron impact and dissipate it through non-ionizing interactions (molecular or atomic vibronic states for example). Furthermore, the ioniziation energy itself is a strong function of the species of gas atom/ion and its charge state (if any). This means that the ability to produce a stable plasma, the plasma density itself, and the charge states of the species present are sensitive to the species of gas used.

It is common to confine plasmas using magnetic fields established by a solenoid (and occasionally a hexapole) field. The field geometry and intensity can be tuned by the current through the coils, allowing the ECR region to be set inside a 'magnetic mirror' region. The non-uniform magnetic field (illustrated in Figure 2.1) produces a force $-\mu \vec{\nabla} \boldsymbol{B}_{//}$ (where μ is the gyrating particle's magnetic moment and is invariant) which acts in the opposite direction to that of increasing field flux. This progressively transfers energy from the drift motion v_{drift} to the ECR motion v_{ecr} as the electron moves into a progressively higher field.

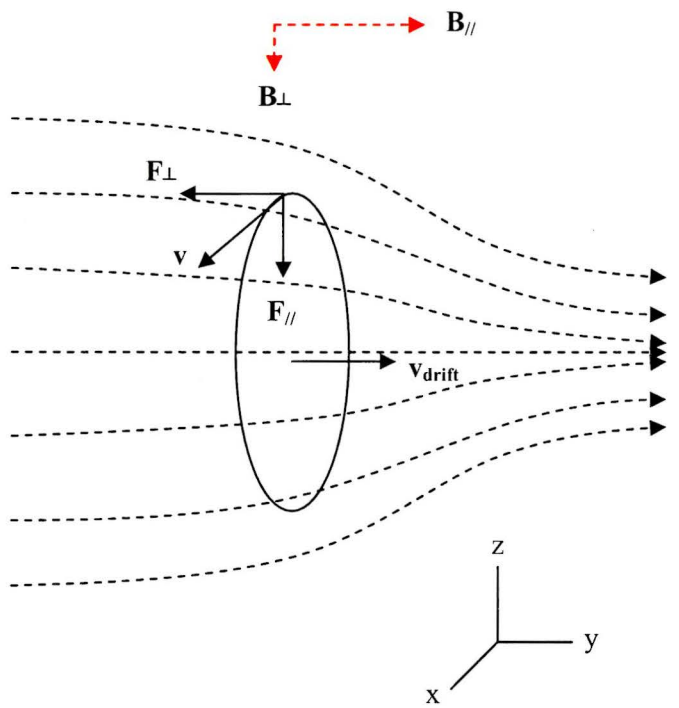

Figure 2.1: Resolution of the forces exerted by a converging magnetic field which attempt to reflect an electron drifting into the region of higher field strength. Adapted from [31].

Electron heating by the applied electric field tends to increase electron confinement because the cyclotron velocity increases without an increase in drift velocity. The magnetic field configuration, however, produces a loss cone in velocity space for the charged particles, which can be tuned to alter the number of escaping particles and their maximum energy (this is not clearly depicted in Figure 2.1) [31]. The escaped particles are accelerated towards the substrate by the divergent magnetic field which produces a force ($-\mu \vec{\nabla} \boldsymbol{B}_{//}$) [32].

2.2 ECR-PECVD System Description

The McMaster ECR-PECVD system is depicted in Figure 2.2 [31]. A magnetron head generates microwaves at a frequency of 2.45 GHz.[35] It is desirable to maximize efficient power delivery to the plasma, so an optical circulator (wavelength selection device) and directional coupler (couples radiation between two parallel waveguides) measure and limit the reflected power seen by the magnetron. The microwaves pass from the directional coupler through an impedance matching waveguide relying on three manually adjustable stub tuners. The microwaves continue through an apparatus known collectively as the symmetric plasma coupler. Within this system, the microwave energy proceeds through an aperture coupled cylindrical microwave cavity at the end of which it impinges on a quartz coupling window through which it passes into the ECR region of the plasma chamber.[36,37]

The next section of the ECR-PECVD consists of the plasma generation chamber. It is defined vertically by upper and lower solenoid electromagnets. Typically, the upper electromagnet carries a higher current than the lower

---

[35] The International Telecommunications Union specifies an operating frequency of 2.45 GHz for exciting microwave energy. This corresponds to an ECR magnetic flux density of 875 Gauss.

[36] The aperture contains a cylindrical tube antenna which ensures that a more uniform electric field impinges on the quartz window.

[37] The quartz window allows the microwaves to pass into the region where the plasma will be generated while preventing the plasma products from streaming back into the waveguiding.

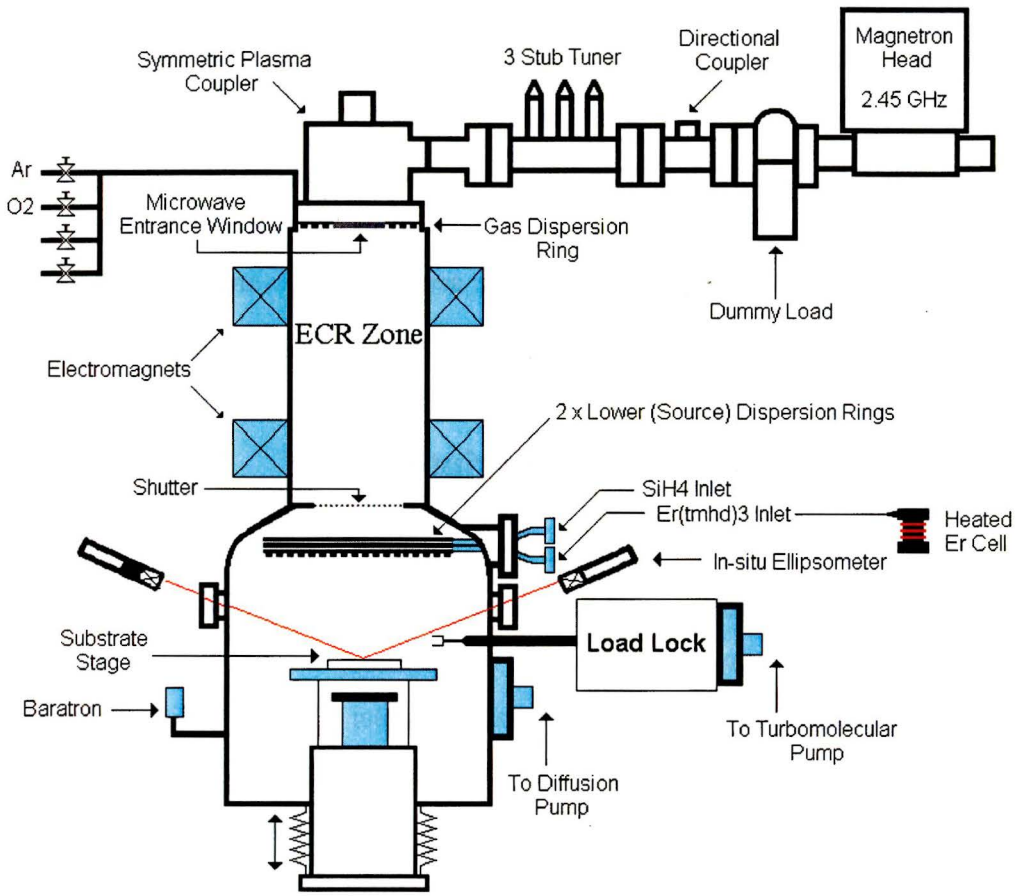

Figure 2.2: Schematic diagram of the McMaster ECR-PECVD system.

electromagnet and is primarily responsible for locating the ECR zone, which occurs in the region just below the quartz window. The lower magnet is primarily responsible for tuning the magnetic field profile in the chamber so as to confine charged particles near the ECR region. Because the current to the magnets is not equal, the magnetic field produced in the plasma generation chamber is asymmetric. This gives rise to the loss cone associated with the magnetic field profile *near the lower electromagnet* through which charged particles from the main body of the plasma can escape. In this way, energetic particles from the plasma can be extracted as necessary for the purposes of efficient CVD without locating the substrate directly in the glow discharge. The tuning of the plasma

confinement profile by adjustment of the lower magnet current provides some control over the ion flux reaching the film surface since the energies of the escaping particles depend upon the diverging magnetic field in the loss cone.

The plasma generation chamber contains a *gas dispersion ring* located around the quartz coupling window that supplies the gases from which the plasma is generated. All depositions in the present study simultaneously employ two plasma gases: Ar and O.[38] Gas flows are regulated by mass flow controllers.

The final section of the ECR-PECVD system consists of the reaction (deposition or processing) chamber. At the top of the reaction chamber is a second dispersion ring, which delivers the Si precursor gas, and a third (differently constructured) dispersion ring which is heated and delivers the Er precursor. The Er line leading into the dispersion ring connects, on the other end, to a small cell which is heated to sublime the precursor therein; an Ar carrier gas is used to transport the precursor down a heated line to the dispersion ring [33]. At the current time, the Si source is silane gas (SiH_4), the simplest gaseous Si compound. The Si precursor is therefore never introduced into the main body of the plasma, as in a direct PECVD system. In the ECR-PECVD system, energetic particles of Ar and O (as well as electrons), which are streaming from the magnetic loss cone of the plasma generation chamber, collide with the SiH_4 molecules to create several highly reactive chemical species. These species then proceed downward through the reaction chamber toward the substrate.[39] The SiH_4 dispersion ring is carefully engineered to deliver the gas uniformly to the substrate. This is essential for achieving compositional and morphological uniformity of the growing film.

The substrate stage is located near the very centre of the reaction chamber and is adjustable along the vertical direction. During deposition, it is typically placed approximately 15 centimeters below the SiH_4 dispersion ring. The

[38] It is possible to deposit *a*-Si by using only Ar as the plasma gas. SiO_xN_y may be deposited by adding N into the plasma chamber along with the Ar and O.

[39] The path of the cracked SiH_4 species from the dispersion ring to the substrate is fairly straight because there are actually relatively few activating collisions with plasma generated ions.

substrate stage is connected to a resistive heating element to allow temperature control (up to 800° C) of the substrate during deposition. The stage is also configured to apply an electrical potential to adjust the floating potential of the substrate. The ions bombarding the substrate will have energy proportional to the difference between the plasma potential and the floating potential. Finally, the substrate is rotated during deposition at frequencies of about 20 revolutions per minute to increase film uniformity. The reaction chamber can be isolated from the plasma generation chamber by a shutter, which allows the plasma to be initiated and stabilized before the substrate is exposed. This makes the deposition of multi-layer films and superlattices possible. Film thickness can be monitored throughout the growth by an in-situ ellipsometer operating at a single wavelength of 632.8 nm.

The ECR-PECVD system also contains a vacuum pumping system. The reaction chamber is pumped by a diffusion pump which is backed by a mechanical rotary vane pump. The system has a base pressure of about 10^{-7} Torr prior to deposition.[40] Samples are loaded through a load lock chamber, which is isolated from the reaction chamber during sample loading/unloading by a gate valve. To prevent the entrance of water vapour into the load lock during the loading/unloading, a N_2 gas overpressure flow is maintained. The sample is transferred from the load lock to the reaction chamber on a retractable fork. The load lock is pumped by a turbomolecular pump for which roughing and backing is carried out using the same rotary vane mechanical pump as for the diffusion pump. Typical pressures in the reaction chamber *during deposition* are kept to approximately 2 to 5 milli-Torr because the chamber is continually pumped by the diffusion pump; this is considered to be a very low pressure for a CVD process and contributes to the film quality.

[40] This greatly reduces the flux of contaminants to the film surface before and during the deposition.

Advantages of ECR-PECVD

There are several characteristic features of ECR plasmas. These include, but are not limited to, the following:

- generation of a dense plasma (electron density of 10^{10} to 10^{12} cm^{-3})[41]
- generation of a highly ionized plasma (10^{10} to 10^{11} $ions/cm^3$)[42]
- the ions leaving the ECR zone exhibit minimal energy dispersion
- a highly activated plasma (high density of charged species) is easily obtained at low gas pressures[43]
- Charged species escape the plasma through a moderately diverging magnetic field; the substrate/plasma potential difference accelerates the ions, which impinge on the substrate with energies as low as 20-30 eV. Within the magnetic bottle, the most energetic particles are reflected back into the ECR zone (the [average] ion temperature is likely a few eV in the ECR region). This avoids damaging of the substrate by those energetic ions, which in direct PECVD systems can be as high as 1 keV [31]. In ECR plasmas these more energetic particles dissipate this excess energy through ionizing collisions thereby increasing the ion density of the plasma
- high quality thin films can be deposited at low temperature (also a characteristic of PECVD in general)

The high density plasma (HDP) generated by ECR is very effective at exciting, ionizing and dissociation precursor gas molecules. In fact, the plasma

---

[41] Like most technological plasmas, the ECR-PECVD plasma is weakly ionized and fairly "cold" having a typical electron temperature (approximately equal to the thermal kinetic energy per particle) near 5 eV (though it is a function of the microwave power, gas pressure, magnetic field, etc.). The electrons should be nearly in thermal equilibrium with each other – a state which they reach relatively quickly – despite having a non-Maxwellian energy distribution. The ion/neutral temperature is likely much lower than this since the plasma gases are at low pressure. Therefore, because very little energy is transferred from electrons to ions/neutrals in elastic collisions, the ions/neutrals will not come into thermal equilibrium with the electrons on the time scale of a deposition.

[42] This usually represents only a few atomic percent of the instantaneous total number of atoms of the particular gas in the chamber (ie. most of the gas atoms remain as neutrals).

[43] The low pressure of ECR plasmas means that there is a greater propensity to form multiply charged ions since there is a lower proability of charge exchange between ions and neutrals.

densities stated above reflect an atomic ionization ratio of 10^{-3} to 10^{-1}, which is two to four orders of magnitude larger than typical direct RF-PECVD systems.[44] This higher ionization efficiency results in a greater production of reactive species at lower temperature, which tends to mean less contamination of the film due to the incorporation of improperly excited species. Furthermore, the presence of two dispersion rings in the reactor design is useful because the dissociation and activation of multiple precursors can be independently controlled for multiple precursor gases. For example, molecules which are more difficult to dissociate can be injected in the ECR region while other molecules can be injected downstream. This resolves the problem of microwave power flowing predominantly into the species which more easily dissociates.[45]

The Er-doping capability on the McMaster ECR-PECVD system presents some unique advantages over the more common ion implantation technique. First, it easily permits high doping concentrations which would otherwise require huge, costly industrial scale implanters. Second, it produces uniform doping throughout a film of arbitrary thickness, removing the uncertainty of Gaussian dopant profiles and the requirement for multiple implant steps to achieve the necessary overlap between the Er and excess Si concentration profiles. Third, 'soft' doping reduces the damage introduced into the film by ions implanted at MeV energies. Finally, metal-organic rare earth doping, in general, can easily be adapted to incorporate multiple rare earth elements [34].

---

[44] Different gases have different ionization potentials (with each subsequent ionization requiring more energy) and so ionize with differing efficiency. This partly reflects their ability to dissipate energy through non-ionizing channels such as vibrational or rotational modes.

[45] One important disadvantage of ECR plasmas relates to the propagation of the microwaves through the plasma. Once a plasma exists in the chamber, the electric field coming from the cylindrical cavity is resolved into right and left circularly polarized waves (RCP and LCP). (The propagation of electromagnetic (EM) waves in a magnetoplasma is a complicated subject and is discussed in [30].) In normal operating mode, the RCP wave propagates through the ECR region in the whistler mode, while the LCP wave reflects back to the stub tuners to be returned to the chamber as a RCP wave. However, the magnetic fields in the plasma complicate the EM field propagation. It is possible to have a circumstance whereby the LCP wave also propagates, causing hysteretic behaviour and plasma conditions which cannot be reproduced.

Deposition Parameter Space

ECR-PECVD presents at least 20 variable global parameters through which to control the deposition. These are expressed in Table 2.1; only two parameters were varied in this study and they are highlighted in the table. In principle, the parameters can be grouped into those which control the flux *and* energy of the impinging ions, and those that control chemical kinetics at the growth surface. Together, these determine the composition and micro-structure down to the atomic level as well as the micro-chemistry of the as-deposited film [35]. These, in turn, determine the film's physical properties. Low energy ion bombardment

Kinetic Parameters →	*precursor/plasma/carrier gases, absolute and* ***relative mass flow rates*** *and pressures, solid Er precursor,* ***Er cell temperature****/geometry, gas delivery location*
Electrical Parameters →	*excitation frequency, discharge/microwave power*
Magnetic Parameters →	*confining magnetic field geometry, electromagnet current*
Surface and Substrate Parameters →	*material/doping/crystallinity/orientation of substrate, pre-deposition surface cleaning procedure, temperature, floating potential, position relative to ECR zone, chamber pressure during deposition, chamber vacuum prior to deposition*

Table 2.1: Selection of the primary processing and deposition parameters and variables in ECR-PECVD. This table is adapted from reference [36].

of the growth surface such as that occurring during ECR-PECVD has three primary effects[46]:

1) Provide the activation energy leading to the dissociation of adsorbed molecules.

[46] See reference [35] page 69.

2) Create surface defect sites which have reduced activation energies for the occurrence of dissociative chemisorption or for the formation of a solid compound
3) Remove (by sputtering) foreign species from a surface. Such species may interfere with the dissociative chemisorption of a preferred species

All things being equal, the parameter which is most easily varied to adjust the plasma density and impinging ion energy[47] and flux is the microwave discharge power. Sputtering of Er from the film surface appears to be significant for depositions carried out at 800 W in the ECR-PECVD system in comparison with 500 W [37]. Insufficient microwave power prevents efficient cracking of the precursor in a way that would lead to effective incorporation into the growing film. There is thus an optimum power for maximizing Er incorporation; it has been identified through previous work on the system though its value is classified.

Similarly, the parameter which is most easily varied to adjust the growth kinetics at the film surface is the substrate temperature. In particular, the sticking coefficient of the impinging species (as affecting their adsorption and desorption rates) as well as their ability to diffuse on the growth surface are strongly temperature dependent and affect the film micro-structure and growth mode[48] as well as the overall film uniformity. Thermal activation of chemical reactions and phase transformations is strongly dependent on the surface temperature, however as noted above, activation energy for these processes is also provided by the inherent energy of the impinging ions.

Considering all other parameters as controlled, the film composition is largely a function of the gas mass flow ratios, while the deposition rate is

[47] The electric potential difference between the substrate and plasma is also a critical parameter for controlling the energy of the impinging ions since it constitutes an accelerating voltage.
[48] For example: layer-by-layer (Frank-van der Mewe), island (Volmer-Weber) or layer plus island (Stranski-Krastanov) modes.

determined by their absolute values.[49] It is important to remember, however that in the same wasy that many of the above deposition parameters are strongly coupled to each other, the same is true of the gas flow ratios. For example, it has been found that the Er incorporation can be highly dependent on the O_2 precursor mass flow rate [37].[50] Perhaps more subtly, the gas flow rates largely determine the deposition chamber pressure during film growth. This affects the 'residence time' of each species in the chamber during a deposition. There is evidence that the residence time can significantly alter the film bond structure by altering the type of radicals present in the chamber [38].

It should be noted that precise stoichiometric control can be difficult with CVD techniques; this is often simply the result of the presence of bonded hydrogen within the films – a certainty with a SiH_4 precusor. Because thin film growth is inherently a non-equilibrium process, thermodynamically unfavourable compositions and bond structures can be deposited. This is particularly true of low temperature depositions where thermal quenching plays an important role in the film growth. However, it is this very fact that allows the growth of Si-rich SiO_x films such as those of this study, as well as those containing higher amounts of Er than would be possible from melt glasses such as might occur in fibre-optic fabrication. Unfortunately, however, the luminescence properties of these films can be as sensitive to composition as the composition is to the limitations in the control of the deposition parameters and their various coupling effects. This was a challenging aspect in the present study and must be borne in mind when carrying out future work or considering future structural modifications to the ECR-PECVD system. Proper characterization of the plasma and its influence on the micro-structure and chemistry of the films (in addition to the overall

---

[49] In the deposition of ultra-thin layers, as might be necessary for superlattice structured films, the process should be calibrated to be carried out at much lower gas flow ratios than those of this study. Without such calibration, deposition repeatability and layer uniformity would be dubious.

[50] The higher Er incorporation at higher O_2 flow rates was explained on the basis of the lower vapour pressure of Er_2O_3 compound at the film surface relative to pure Er, leading to a higher desorption rate of the latter.

stoichiometry) is paramount if this issue is to be brought under tighter control. This has been most effectively achieved in the literature by the use of optical emission and/or absorption spectroscopy and quadrupole mass spectroscopy [39].

2.3 Structure Physics and Deposition Chemistry of SiO_x

Both the chemical and electronic structure of CVD and thermal SiO_2 as well as the associated deposition chemistry of SiO_x thin films in ECR plasmas from SiH_4 precursor have been extremely well developed in the literature and to a lesser extent in previous theses based on the McMaster ECR-PECVD system[30,40,41,42,43,44,45,46,47,48,49,50,51,52]. There are literally hundreds of gas phase *and* surface reactions (involving dozens of species) that occur during the plasma deposition of SiO_2 based films and it is difficult to usefully outline in a summary fashion.[51,52] For this reason and in the interest of space, these issues will not be addressed here at all. The reader will refer to the listed references.

2.4 Erbium Chemistry

2.4.1 Er^{3+} Bonding Requirements

Because Er doping represents the novel aspect of this study and the crucial luminescent species, it is of considerable value to understand, in detail, aspects of

---

[51] The variety of highly reactive radicals in a plasma discharge and the varied reactions that they undergo often causes stoichiometry problems in PECVD SiO_2 (ULSI Technology, Ed. C.Y. Chang and S.M. Sze, McGraw Hill Inc.: New York, p. 244 (1996)).

[52] One can get a sense for the complexity of the process by considering the various types of gas phase reactions: i) electron impact reactions (*electronic excitation, vibronic excitation, ionization, dissociation, attachment*), ii) reactions among neutral species (*atom transfer, metathesis reactions, dissociation, recombination*), iii) ion-ion neutralization, iv) ion-neutral reactions, v) charge exchange reactions, vi) ion-collision induced atom-transfer reactions. In addition to this, there are the surface reactions. One model (E. Meeks, et. al., J. Vac. Sci. Technol. A **16**, 544 (1998)) has isolated 167 different gas phase reactions involving 33 gas phase neutral species, 11 charged species, and two metastable species. They have also included 96 different surface reactions involving 13 different surface species, each of which is centered on a single Si atom.

rare-earth chemistry as pertaining to Er complexing in thin films and how this might be optimized in the deposition process.[53]

Er exhibits low solubility in SiO_2 and Si and so tends to precipitate (or at least cluster) at concentrations above 10^{19} cm^{-3} leading to severe luminescence quenching. This is a crippling problem for Er-doped micro-photonic devices and so motivates a detailed understanding of the Er environment in various host materials and the driving forces for precipitation.[54]

As a preface to the discussion, it should be noted that the typically accepted ionic radius of the Er^{3+} ion is 0.88 Å (considerably smaller than Er^0), while for Si^{4+} the value is 0.4 Å and for O^{2-} the value is 1.4 Å. The Si and O atoms in SiO_x are not exactly in these respective ionic states but such values are useful first-order approximations. Preliminary thermodynamic data on Er–Er, Er–Si, Er–N, Er–O and Si–Si bonding can be found in reference [53].

The Er^{3+} ion has very high cationic field strength[55] and requires a *significant anionic coordination* in order to screen its electric field (charge). The non-bridging oxygen (NBO) atom point defect[56] is the most electronegative species native to the SiO_x network[57] and constitutes the most effective coordinating anion for Er dopant.[58] However, the amorphous SiO_2 network is

---

[53] The chemistry of rare earth elements has historically been well-researched owing to their useful optical properties (as exploited in luminescent phosphors and numerous glass and crystal lasers) as well as their many unique magnetic properties (including an accessible antiferromagnetic transition).

[54] Given the necessity of minimizing Er clustering effects in fibre amplifiers, it might be expected that the diffusion kinetics for Er in SiO_2 would be well characterized. To the contrary, there is virtually no literature addressing this. Work on single crystal Si hosts has revealed that both Er and O are highly mobile at anneal temperatures as low as 400 °C – a temperature which might be used to eliminate implant damage. Activation energies relevant to diffusion are ~2 eV.

[55] This is defined to be the valence of the cation (in this case +3) divided by the ionic radius (typically equal to 0.88 Å for Er^{3+}).

[56] Perfectly stoichiometric SiO_2 contains no (uncompensated) NBOs. That is, unless each NBO is compensated by an O-vacancy (in the form of a Frenkel pair) the network will be oxygen rich. A large O surplus is not thermodynamically stable at room temperature.

[57] Er-Er and Er-Si compounds are both metallic. Pauling electronegativities: Er(1.24), Si(1.90).

[58] A bridging oxygen (BO) has a much lower ability to screen positive charge than a NBO. Er/O pair distribution functions produced with Molecular Dynamics simulations have confirmed that an increase of the total coordination number around Er^{3+} in SiO_2 is accomplished by an increase of the NBO contribution and a decrease in that of BOs.

characterized by strong Si–O covalent bonding so that the structure is not only rigid (contains very few NBOs[59] [54]) but contains low (four-fold) coordination throughout. The network is thus largely incompatible with Er^{3+} coordinating requirements and does not readily deform itself to accommodate. Simulations have shown [55] that as the Er concentration in SiO_2 increases, more Er ions formed clusters so as to share their NBOs and expel BOs out of the nearest neighbour shell. Insufficiently coordinated Er atoms experience significant forces from the surrounding Si–O bonds such that structural relaxation occurs most naturally through the mutual increase of coordination number that they achieve by clustering. This constitutes the driving force for Er clustering. Increasing the Er concentration inevitably increases the number of Er ions in clusters.[60] The problem with clustering is not necessarily that it takes the Er out of the optically active 3+ valence state (although Er^{2+} is thought to be optically inactive [56]). The problem is that the clusters place the Er^{3+} ions in close proximity to one another (about 2 Å in the case of an Er–Er pair, which is comparable to the Er ion diameter) so that parasitic ion-ion interactions dominate the optical properties, significantly enhancing non-radiative losses from the luminescent $^4I_{13/2}$ manifold.

2.4.2 Experimental Determination of the Er^{3+} Site in SiO_2

The most useful experimental techniques for the investigation of the Er environment in solids seems to be extended x-ray absorption fine structure (EXAFS) and electron paramagnetic (spin) resonance (EPR)[61] [56].[62] EXAFS at

---

[59] The number of NBOs per SiO_4 tetrahedral bonding unit forms a statistical distribution which measures the *connectivity* of the network. Fewer NBOs means that the network is highly *connected* and is therefore structurally rigid.

[60] The use of the word 'clustering', which is common in the literature, as in this case, refers to the formation of an Er/O nano/micro-cluster – which might be expected to contain some direct Er–Er bonding at sufficiently high Er concentrations. The formation of pure metallic Er inclusions should be termed "precipitation", and usually requires the application of temperatures high enough to drive the dissociation of Er-O centres.

[61] The EPR technique can also differentiate between the presence of Er^{2+} and Er^{3+} (See: Carey, et. al., Phys. Rev. B **59**, 2773 (1999)).

the Er L_{III} absorption edge (near 8.36 keV) using synchrotron radiation yields precise coordination numbers as well as the relevant bond lengths. Powdered samples of crystalline Er oxide (Er_2O_3), Er metal, and Er disilicide ($ErSi_2$) are often measured in conjuction to provide a comparison with well-characterized materials which might be expected to exhibit similar Er siting to the films [57,58,59]. Molecular Dynamics simulations have been effective in modeling the cluster formation dynamics and agree well with the EXAFS results [54,55].[63,64]

The EXAFS studies have confirmed that Er is preferentially coordinated by oxygen in SiO_x hosts (and even single-crystal Si hosts containing small amounts of residual impurity oxygen). The exact number of coordinating oxygen atoms has been found to be dependent on the preparation conditions. A study of SiO_2 doped with Er by ion implantation to a concentration of 1 atomic percent, revealed a first neighbour shell consisting of 5.5 oxygen atoms, at a distance of 2.25 Å. This sample showed a second-neighbour Er–Si shell at 3.11 Å [58].

Figure 2.3 represents an attempt to depict the Er^{3+} ion bonded in the three-dimensional SiO_2 network with six-fold oxygen coordination (adapted from E. Desurvire [60]). While the simplest six-fold geometry with the highest symmetry is an octahedron, the crystal field of such a structure does not exhibit sufficient asymmetry to form the electronic states necessary for the intra-4f optical transitions. The inherent asymmetry of the SiO_2 network contributes to the

---

[62] The Stark splitting of the $^4I_{13/2}$ to $^4I_{15/2}$ luminescent transition, which can usually be resolved with a PL measurement at cryogenic temperatures, is often used to draw comparative conclusions about changes to the Er environment in different host solids. This is usually plagued with ambiguity, however, owing to vibronic splitting and mixed symmetries.

[63] Electron paramagnetic (spin) resonance (EPR or ESR) has been used to study Er doped *c*-Si. Because the Er^{3+} ion has an odd number of electrons, the Zeeman splitting of the unpaired electron energy levels in a strong magnetic field can be probed by resonant absorption of microwaves. This yields information about the electronic structure of the Er^{3+} since the Zeeman splitting is also affected by *local* magnetic fields in the material. This allows the differentiation of specific Er site symmetries as well as the Er charge state.

[64] Emission Mössbauer spectroscopy (based on the recoil-less emission of Gamma rays) has been successfully used to measure the splitting of the nuclear energy levels of Er doped *a*-Si. In particular, the superposition of a singlet and quadrupole doublet has been ascribed to specific oxygen and Si coordinated Er sites respectively. See Chapter 8 for an experimental description. The technique has apparently never been applied to the SiO_x:Er system.

deviation from a perfect octahedral symmetry of the coordinating oxygen anions; the tapered axes in Figure 2.3 indicate the distortion into three-fold D_3 symmetry.[65] An examination of Figure 2.3 reveals that there is a charge compensation problem with this structure if one considers the Er–O bonds to be fully ionic. The Er^{3+} ion provides three electrons, whereas the six coordinating oxygen atoms would require an additional three electrons to fully meet their valence requirement. This could be provided by one nearby triply ionized ion (such as Al^{3+}) or three singly charged ions (such as Na^{+}) – or another Er^{3+} ion forming a clustered pair.[66]

2.4.3 Er^{3+} Site in Si-rich SiO_x

The only major study of Er doped Si-rich SiO_x containing Si nano-clusters used the EXAFS technique. This study [57] considered two samples, both annealed at high temperature (1250 °C) to produce Si nano-crystals; each was implanted with Er. Sample *A* contained $5.4x10^{19}$ Er/cm^3 while sample *B* contained $2.1x10^{20}$ Er/cm^3. Both received a post-implant anneal of 900 °C for 1 hour in N_2

---

[65] D_3 is the Schönflies notation for the point group having a 3-fold rotation axis plus a two-fold axis perpendicular to that axis.

[66] As a result, co-doping of SiO_2:Er with sodium or aluminum is a common technique for significantly enhancing the Er solubility. In practice, the co-doping is typically achieved by adding compounds such as Na_2O or Al_2O_3. The action of the extra oxygen from the co-dopant breaks up the SiO_2 network by forming singly bonded oxygens (NBOs) that do not participate in the network (the network *connectivity* is reduced because the NBO concentration increases). These co-dopants are therefore called *network modifiers* (to be compared with *network formers* which are the cations, such as Si^{4+}, forming the tetrahedral bonding units of the network). This creates exactly those conditions required to increase the Er solubility and allow the relaxation of the ErO_6 complex: charge compensating cations, NBOs and an open network. From a conceptual point of view, the modifying cations and extra oxygens form a solvation shell around the Er which is itself, soluble in the SiO_2 network. The Er^{3+} ions themselves are generally considered to be *network modifiers* in SiO_2 because they generate NBOs as a result of the large ionicity of the Er–O bond (to be discussed below). However, in some multi-component glasses, the Er^{3+} ion can actually be a *network former* because its six-fold coordination actually corresponds to the coordination of the basic bonding units in the glass. The more open structure of such glasses is, in any case, more favourable to Er solubility. It is interesting to note that while co-doping techniques allow a much higher concentration of optically active Er that is more randomly dispersed, ion-ion interactions are still found to be prevalent owing to the ability of the Er^{3+} ions to couple over distances seemingly well beyond 1 nm.

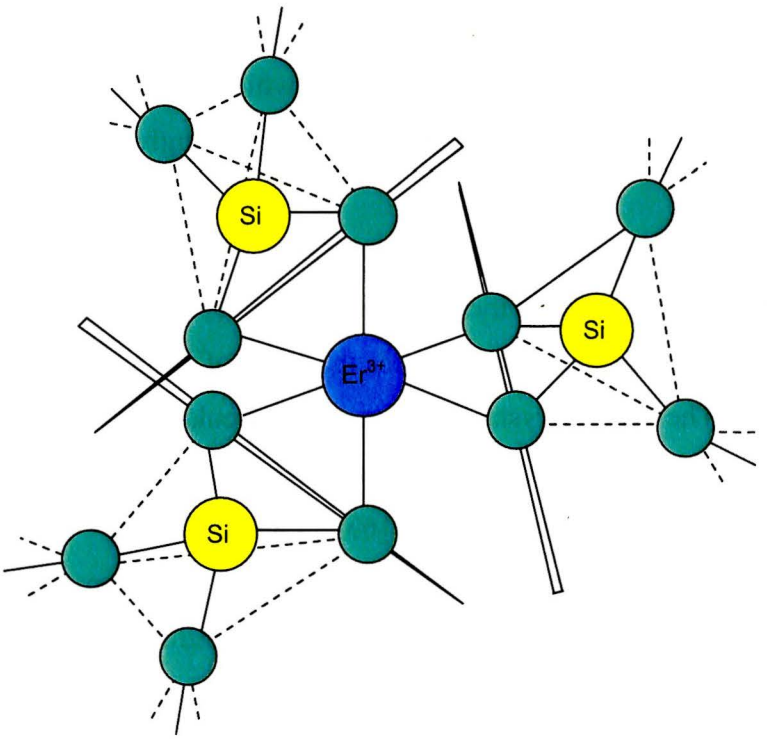

Figure 2.3: The Er^{3+} site in SiO_2 depicted with a six-fold [non-bridging] oxygen-coordinated shell in a distorted octahedral geometry. The SiO_4 tetrahedral units of the SiO_2 network are depicted. Adapted from [60].

gas. Sample *A* was found to have an average Er coordination of four O atoms at a distance of 2.09 Å, while sample *B* showed a first shell of about seven O atoms at a distance of 2.16 Å. The Debye-Waller factor in both cases indicated a broad distribution of Er–O bond lengths in the samples. The difference in the Er environment based on the implant fluence was ascribed to the difference in implant damage. The higher coordinated Er is the more stable complex. Thus, similar to the Er doped SiO_2 system described above, the limiting factor in the Er complex is the availability of O. While it is difficult to liberate O atoms from the strong Si–O bond, the implant step does just this. The higher implant fluence breaks more such bonds and avails more O atoms. Once available, they will likely have a stronger propensity to bond with the Er than with the Si; this has been demonstrated by oxidation studies on thin Er and Si layers on SiO_2 (see

[61,62]). Beyond the first neighbour O shell, the EXAFS data were inconclusive. However, there appeared to be a shell at 3 Å which might be ascribed to a Si shell from the SiO_2 matrix or a Si nano-cluster. Interestingly, no Er–Er bonding was detected.

The distribution of electronic charge in the Er complexes identified with the experimental techniques mentioned above has been found to be very similar to that of crystalline Er_2O_3. This includes the cases of Er in *c*-Si, *a*-Si, SiO_2 and Si-rich SiO_x. The Er_2O_3 crystal has sixteen molecular units in the unit cell and belongs to space group T_h^7.[67] There are two inequivalent Er sites, both of which are six-fold coordinated with oxygen [63]. Twenty four Er^{3+} ions occupy sites of C_2 symmetry[68] and eight occupy sites of C_{3i} (S_6) point symmetry[69]. These are both distorted cubic symmetries. This six-fold coordination is similar to the site observed in the SiO_x ($x \leq 2$) matrix, however the EXAFS data of crystalline Er_2O_3 suggest a narrower distribution of bond lengths than those of the Si-rich host.[70]

Molecular orbital calculations have been designed to simulate and predict the local distortion in an ErO_6 cluster such as is evidenced to occur in the SiO_x host. These have revealed that Er and O form a highly stable ionic bond when the Er^{3+} is shifted by 0.1 Å from the true octahedral centre to produce a structure with C_{4v} symmetry [64]. Such a structure optimizes the ionicity of the Er–O bond by preventing electron transfer from O^{2-} to Er^{3+}.[71] The structure represents an optimization over octahedra with either of C_{2v} or C_{3v} symmetry.[72]

---

[67] In the Schönflies notation, T indicates that the *point group* has the symmetry of a tetrahedron (excluding improper operations – which are those that change handedness) and T_h is T with the addition of an inversion; the superscript 7 is an index used to categorize distinct space groups that share major symmetry properties.

[68] In the Schönflies notation, C_2 indicates that the point group has a 2-fold rotation axis.

[69] In the Schönflies notation, C_{3i} indicates that the point group has a 3-fold rotation axis and an inversion; S_6 denotes a point group that contains a 6-fold rotation-reflection axis.

[70] The seemingly simultaneous use of the terms 'cubic' and 'octahedral' to describe Er symmetries should be clarified. The cube is dual to the octahedron, meaning that the vertices of one correspond to the faces of the other. Therefore, the cube has octahedral symmetry.

[71] This has to do with the rotation of an oxygen 2p orbital due to Er 5d translation which allows the formation of a special bond between these two orbitals.

[72] In the Schönflies notation, C_{2v} indicates that the point group has a 2-fold rotation axis with the addition of a mirror plane parallel to the axis of rotation.

Separate simulations involving density-functional theory with ultra-soft pseudopotentials have been applied to $Er_2Si_2O_7$ clusters in order to analyze the effect of the Er on the Si–O bond in the vicinity of six-fold oxygen coordinated Er [64]. This scheme actually treated the Er 4f states as a partially occupied core shell. The resulting calculated density of states and electronic charge distribution indicated that the presence of the Er tended to increase the covalency of neighbouring Si–O bonds. This occurs because the Er and Si energy levels are such that the Er–O bond is more ionic than the Si–O bond (recall that the Si–O bond in SiO_2 is about fifty percent ionic and fifty percent covalent). However, because the total charge transfer to the oxygen is similar in SiO_2 and $Er_2Si_2O_7$ the O has less capacity to accept electronic charge from the Si atom.

Regarding Er-Si complexes, Er forms various metallic alloys with Si, including $ErSi_2$ and Er_5Si_3. The most prominent example of Er-Si bonding seems to occur in Er-doped float zone Si, where the extreme high purity of the Si provides insufficient O atoms for gettering by the Er. EXAFS data suggests that the Er site in float zone Si is that of $ErSi_2$ [59]. The Er atom is twelve-fold coordinated in $ErSi_2$ with a Si–Er bond length of 3.00 Å, as shown in Figure 2.4 [65]. This coordination number is extreme. In order to reconcile this with a reasonable Er valence (it would have to be 5 for the isolated site), it is thought that the EXAFS data is actually referring to a precipitate of bulk metallic $ErSi_2$ [65]. The resulting centre is highly symmetric and does not provide sufficient mixing of electronic states to achieve efficient intra-4f luminescence. This optical inactivity of Er-Si complexes is a key factor that limits Er luminescence in high purity float zone Si -- aside from the extremely low solubility of Er in pure, single crystal Si.[73] The effects of Er-Si complexing may become increasingly significant in Si-rich SiO_x as one increases the Si excess to high concentration.

---

[73] This is principally due to the lack of anions and the regular sp^3 bonding of Si, which is not compatible with the coordination requirements of the Er and leads to ion clustering. There is also a size mismatch between the Er^{3+} ion and the crystalline Si lattice. The greater structural disorder found in amorphous Si makes this a better host, but this is also due, in part, to the greater tendency to have residual O impurities in amorphous Si.

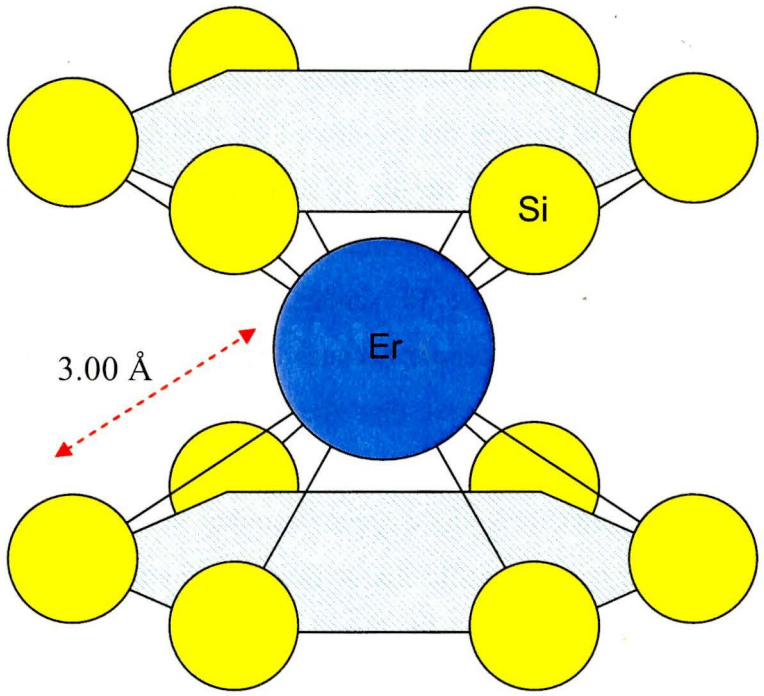

Figure 2.4: Illustration of the Er site in $ErSi_2$ metal showing a central Er ion with 12-fold Si coordination. The hexagonal planes have been drawn to guide the eye and emphasize the correct bonding alignment.

As with Er-doped SiO_2, the preparation technique for Si-rich SiO_x can significantly affect the tendency for Er clustering and the propensity to form certain Er complexes. Increasing the amount of excess Si alone can be significant because it reduces the overall concentration of O. For example, in SiO_x hosts with x in the range 0.002 to 0.076, the O-coordination was found to range from 2.0 to 3.6 respectively with bond lengths of about 2.1 Å [66]. Futhermore, it has been suggested that the presence of excess Si inhibits Er clustering in comparison with SiO_2 (similar to the implantation related damage as previously noted) [67]. SiO_2 grown by PECVD is also thought to incorporate higher amounts of unclustered Er as a result of reduced dopant diffusion in the matrix [68]. Contrarily, co-sputtered Er-doped Al_2O_3 films have been found to contain higher amounts of clustered Er via a spatially inhomogeneous distribution of Er relative to their implant-doped counterparts (evidenced by enhanced cooperative

upconversion luminescence in the former) owing to a greater tendency for non-uniformity in plasma processed films [69].

2.5 In-Situ Erbium Doping by ECR-PECVD

The ECR-PECVD system can, in principle, use any volatile metal-organic (MO) Er precursor.[74] The solid powder compound *tris(2,2,6,6-tetramethyl-3,5-heptanedionato)erbium(III)* or $Er(tmhd)_3$ was selected because it is thermally stable, exhibits considerable volatility at an accessibly low temperature [70] (melting point of 180 °C) and because it is already coordinated to six O atoms in the molecule.[75] The main unit in the molecular structure is depicted in Figure 2.5:

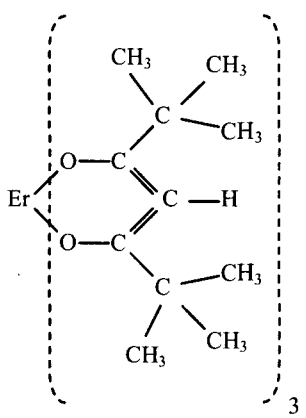

Figure 2.5: Bond diagram of the metalorganic Er precursor $Er(tmhd)_3$.

It would be desirable if the plasma cracked this molecule at the first O–C bond and allowed the Er-O complex to incorporate into the film while the ligand was pumped away. Mass spectrometry of the reactant stream in an ECR-PECVD

---

[74] The engineering of new MO rare-earth precursors which are optimized to incorporate optically active lanthanide centres is an ongoing effort. See: D. Pfeiffer, et. al., *Inorganic Chemistry 38, 4539 (1999).*

[75] The β-diketonate ligand actually forms analogous thermally stable, volatile organic chelates with all of the rare-earth metals. They are thus very useful precursors for metal-organic CVD. The six-fold O-coordination produces a distorted octahedral cage around the Er^{3+} because the O-bonds are not equivalent.

similar to that at McMaster, during growth of Er doped epitaxial Si with $Er(tmhd)_3$ showed that the Er–O bonds broke more easily and left the $C_{11}H_{19}O_2$ ligands intact; furthermore, H in the chamber was contributing strongly to the dissociation [27,71]. (The films of the present study *do* reveal significant C contamination; this is always a problem in MOCVD but is often tolerable.) When comparing various MO Er precursors, the previous study [27] found that the bonding arrangement of C within the MO molecule was an important factor in how it incorporated into a film and to what extent. It also showed that the C had a propensity to substitute for Si in the lattice.

The actual behaviour of $Er(tmhd)_3$ in the films of the present study has not been specifically investigated, however several observations should be made:

1) The Er could possibly incorporate *along with* an oxygen coordination shell from the $Er(tmhd)_3$ precursor or from the formation of Er-O complexes in the plasma itself.[76] Indeed, in-situ doping of *a*-Si:H with $Er(tmhd)_3$ has been seen to leave the molecule largely intact, reproducing an Er environement in the film similar to that in the precursor [25]. This would be tantamount to doping the SiO_x ($x \leq 2$) with Er_2O_3 or ErO_6, for example, and would therefore reduce the competition for NBOs (as discussed in the context of network modifier doping of SiO_2). This would reduce the driving force for clustering and would effectively depress the expected excess Si concentration. This does indeed seem to be supported by RBS data, which found that increasing the Er content in those depositions which could *not* incorporate excess Si, actually produced an O-rich SiO_x with the O surplus increasing with Er content. The O may well be bonded to Er because it does not seem to release from the film during annealing, which it should if the matrix is SiO_x. Furthermore, Si-rich SiO_x films grown at a given O_2/SiH_4 flow ratio reveal that the excess Si content falls with increasing Er.

[76] The growth temperature in the present study is low enough to leave undissociated $Er(tmhd)_3$ molecules intact.

2) The Er may be able to getter residual oxygen, including NBOs resulting from imperfect bonding, in the film during growth since the host matrix is actually forming at the same time as the Er is incorporating; this contrasts with the more common sequential process involving ion implantation.
3) The *tmhd* ligand on the precursor introduces carbon into the films. With respect to the Er, this could certainly be bonding directly to the Er and contributing to the nearest neighbour shell along with the oxygens – in fact reducing the requirement for NBOs. Carbon is thought to form a ligand capable of resulting in optically active Er [68]. The carbon could also affect the Er diffusion kinetics by altering the Si-O bond network much like a network modifier. It is unclear how much C is outgassing during annealing.
4) The presence of hydrogen within the film could affect the Er coordination by bonding to NBOs. Furthermore, some of the hydrogen will leave the film upon annealing. This hydrogen effusion can create voids within the film which increase the mobility of oxygen atoms.
5) Rutherford backscattering spectrometry (RBS) has revealed that Er-doped films from the ECR-PECVD system almost always exhibit an Er-rich layer corresponding to the first 10-50 nm of the deposition. The layer contains up to 25% more Er than the remainder of the film. This 'spike' in the doping is likely the result of a build-up of Ar/Er(tmhd)$_3$ over-pressure in the dopant delivery line in the minutes prior to deposition. The precursor has been sublimating for some time before the deposition begins and probably fills the line with an excess of precursor vapour. It takes a few minutes of deposition time before this has been exhausted and an equilibrium mass flow results. One possible solution to this problem would be to install a shutter at the top of the Er heating cell so that the Er(tmhd)$_3$ vapour does not prematurely penetrate into the carrier line. The shutter could then be opened simultaneously with – or perhaps a few seconds prior to – the opening of the main shutter in the reaction chamber.

Chapter 3

Luminescence Theory for SiO_x:Er ($x \leq 2$) Thin Films

Luminescence refers to the general property of the emission of visible and/or infrared electromagnetic radiation, beyond thermal radiation (incandescence),[77] occurring when an electron in an excited state relaxes to a lower energy level by creating a photon; such electronic transitions are characteristic of a material.

Luminescence theory is well developed within quantum electrodynamics and extends to address each material system and excitation mechanism individually. Semiconductor optoelectronic device applications are most often concerned with doped III/V semiconductor and glassy materials with the most important excitation/emission mechanisms being photoluminescence and electroluminescence. Broadly speaking, photoluminescence refers to the excitation of luminescence by the application of electromagnetic radiation (particularly at ultra-violet, visible, and IR energies), while electroluminescence refers to excitation by the applications of an electric field or voltage.

On an atomic level, luminescent transitions are, in effect, the result of temporal fluctuations of the electric and magnetic field produced by specific classes of oscillation of an electronic charge distribution. The electron distribution in question may be that of a single atom or molecule (as in a rarefied

[77] Incandescence occurs in heated materials and increases with temperature. "Cold" luminescence, by contrast, usually becomes more efficient with decreasing temperature.

gas), or of a macroscopic aggregate of atoms, as in a solid. Knowledge of the electron's full time-dependent wave function (or at least the energy level structure including excited states), is a pre-requisite to first principles modeling of luminescent transitions in a material system. The inverse problem, which seeks to elicit the electronic energy structure by measuring transition energies, is investigated with optical or electronic spectroscopies. A specific luminescence mechanism may be delocalized in the sense that it can occur almost anywhere within a material, as in band-edge electron-hole pair recombination, or it may be localized to a specific atomic site or defect giving rise to a *luminescent centre.* Because luminescent transitions in solids are complicated by the interactions with surrounding atoms (as opposed to a rarefied gas), much work in the field is invested in the study of the coupling of luminescence mechanisms or between luminescent centers, as well as the effect of the vibrations of neighbouring atoms.

A particular field of research which has gained considerable interest as of late, has been the luminescence properties (and optical properties in general) of quantum confined structures. Quantum confinement can distort the electronic distributions in a material such that they are quite different from that of the corresponding bulk material. This inevitably changes the way in which the material interacts with electromagnetic fields and gives rise to various useful non-linear optical properties as well as entirely new absorption and luminescent transitions. The ability to generate and manipulate materials in the quantum confinement regime allows many materials to exhibit properties which they would not otherwise exhibit in bulk form. This can permit the engineering of photonic devices of small size, which could help to overcome the device integration problems associated with the typically large size of photonic components. On a more exotic level, quantum confined structures may even allow the engineering of photonic devices from materials which have historically been considered useless for such an application. Silicon is one such example, which in this study, is

shown to be potentially useful as a light emitter when processed into a nano-structured configuration.

3.1 Basic Luminescence Theory

3.1.1 Quantum Mechanical Description

Quantum mechanically, the action of emission or absorption of a photon by a distribution of electronic charge places the system into a mixed state (time-varying superposition of two stationary states) [72]. Physically, this corresponds to an oscillation in the charge distribution. To emit or absorb radiation this oscillation must possess a *time-varying* net moment. For example, a spherically symmetric oscillation of an arbitrary charge distribution cannot emit net radiation because it has zero net fluctuating moment [73,74]. The time-varying electric and magnetic field originating from an arbitrarily complex fluctuating charge distribution can be mathematically expressed and conveniently conceptualized according to a multi-polar expansion. Successively higher moments (terms) in the expansion make a successively smaller contribution to the net field because they exert a progressively shorter-range influence. The largest non-spherical (zero moment) component of the field of an electronic charge distribution is the electric dipole moment. From a radiation emission perspective, a time-varying distribution having a fluctuating electric dipole moment will radiate intensely, dominated by the high efficiency of the radiating dipole, with the higher order moments making comparatively negligible contribution. From a radiation absorption perspective, electric dipole oscillations can be strongly driven by the electric field of an incident electromagnetic wave. If the fluctuating charge distribution does not have a fluctuating electric dipole moment, than radiation and absorption can only occur through the weaker oscillation of the higher order moments of the electric or magnetic fields. The next strongest coupling to electromagnetic radiation, beyond the fluctuating electric dipole moment, occurs

through the electric quadrupole moment, followed by the magnetic dipole moment (which is much weaker since the charge distribution is now coupling to the magnetic field of the electromagnetic wave), etc.

The transition probability, for a luminescent centre, from state ψ_i to state ψ_f, involving *absorption of a photon* of energy $\hbar\omega$ is [75]:

$$P_{if} = \frac{2\pi}{\hbar}\left|V_{fi}\right|\delta(E_f - E_i - \hbar\omega) \tag{3.1}$$

V_{fi} is the matrix element, $<\psi_f|V|\psi_i>$, and V is the operator corresponding to the interaction energy of the luminescent centre with the radiation (the electron-photon interaction), which is a function of the relevant field moments discussed above [76]. This same matrix element appears in the equation for the probability (per unit time) that *spontaneous emission of a photon* will occur from the excited state. This quantity is known as the Einstein spontaneous transition probability. In this way, this matrix element connects the symmetry of the wave function (and therefore the electronic charge distribution/orbitals) to the transition probability; the probabilities are then grouped into likely and unlikely events by the so-called selection rules.[78]

It is difficult to excite an electronic charge distribution into an excited state by photon absorption along a probabilistically inhibited path, that is, one which violates a selection rule. Furthermore, when an electronic charge distribution is excited into a state from which its only [radiative] decay modes are the inhibited paths of low probability, the state is so-called metastable. This excited state could persist for a significant amount of time (on the order of milliseconds or longer) if non-radiative decay modes are suppressed. It is evident

[78] The wave function symmetry is often discussed in term of parity and the selection rules can be cast in the language of momentum. Taking the potential seen by the electrons to be approximately spherically symmetric, the parity of their wave functions is strictly dependent on their orbital angular momentum number (identified as s, p, d, and f in spectroscopic notation). The transition which does not change the parity of the wave function does not induce an adequate change in the angular momentum of the electrons to compensate for the momentum transferred to the photon and symmetry is violated.

from the time-energy form of the Heisenberg uncertainty principle that such transitions should exhibit reduced lifetime broadening and therefore potentially narrow transition linewidths. It is possible for specific vibrations of the ions within a solid to disrupt the orbital symmetry, that is responsible for preventing the dipole transition, and thereby increase the transition probabilities.

An important phenomenon in luminescence theory is the extent of the coupling between the particular luminescent electronic charge distribution and the surrounding ion cores in the solid. The coupling determines the extent to which phonons can alter the transition energies and even non-radiative relaxation probabilities. Conceptually, the lattice vibrations "frequency modulate" the optical transition, thereby introducing side-bands (which appear as broadening) on the lifetime-broadened pure electronic transition [75]. The coupling is assumedly too strong for perturbation theory methods. Modelling is complicated by the fact that the electronic state of the luminescent ion affects the vibrational frequencies of the surrounding ions, which changes the crystal-field at the erbium site, which in turn modulates the electronic energy of the luminescent ion. The solution to the problem therefore relies on two assumptions:

1) Born-Oppenheimer approximation: the vibrational motion of the ion is much slower than the electronic motion
2) Only the 'breathing mode' of vibration of the neighbouring ions is considered. Under this assumption, the ions pulsate in and out around the luminescent ion via simple harmonic oscillation. The only spatial coordinate needed to describe the oscillation is the *configuration coordinate*, Q, which is the average distance from the luminescent ion to the nearest neighbours.

Within this model, the electronic and lattice states can be depicted on a single energy level diagram based on the configurational coordinate (Figure 3.1). The vibrational energy levels are a parabolic function of the configuration coordinate

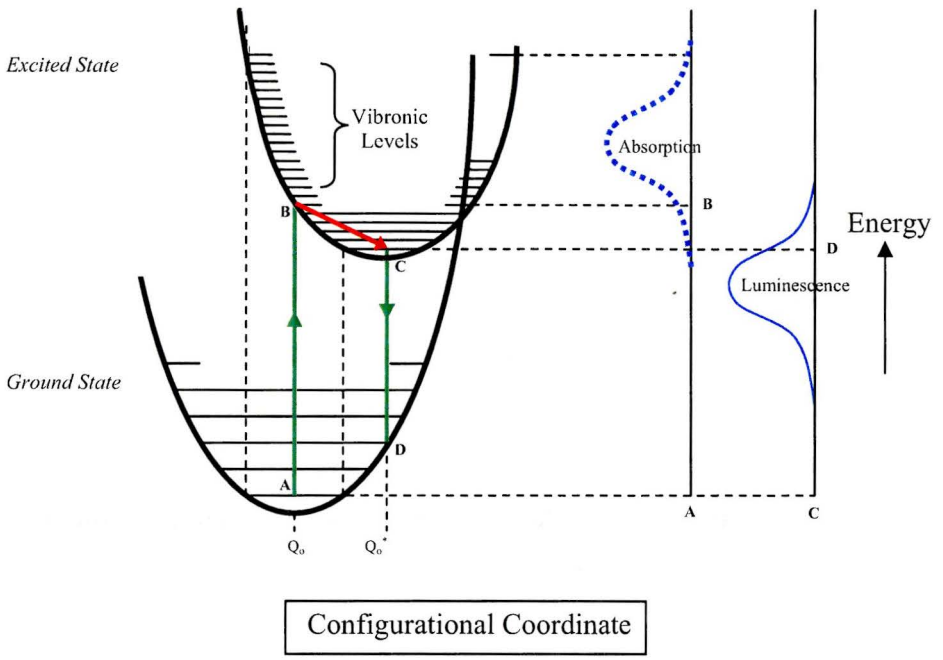

Figure 3.1: Configurational coordinate diagram depicting the vibronic energy levels at two different electronic states and the resulting Stokes shift and optical absorption/emission band widths. Adapted from [75].

(standard for the harmonic oscillator) for each electronic state of the centre.[79] This gives the energy states of the complete system (luminescent centre plus surroundings). The vibrational broadening into bands of what would otherwise be the sharp atomic-like transition lines of isolated luminescent centres is apparent since there are a myriad of possible transitions all with characteristic probabilities. Consistent with the Born-Oppenheimer assumption, the transition lines are depicted as vertical on the diagram suggesting that the electronic configuration re-arranges instantly as a function of the configuration coordinate (in the context of the diagram this is referred to as the Franck-Condon principle).

It is clear that there is a red-shift between the absorption and emission band as a result of the relaxation (by phonon emission) to the lowest vibronic

[79] If one were to take into account other modes of vibration and/or anharmonic effects, the parabolic shape would be distorted

level in the excited electronic state. This shift is referred to as the Stokes shift. The Stokes shift becomes more severe as the coupling to the surrounding ions increases. Note that an overlap of the emission and absorption bands is indicative of zero-phonon transitions, which can permit the re-absorption of luminescence emitted in the material.

The lateral separation between the two parabolas, ΔQ is quantified by the Huang-Rhys parameter S defined by:

$$\frac{1}{2}M\omega^2(\Delta Q)^2 = S\hbar\omega \tag{3.2}$$

where M is the equivalent ionic mass engaged in the vibration of angular frequency ω, and $\hbar$ is the Dirac constant. The Stokes shift ΔE_S can be expressed in terms of the Huang-Rhys parameter:

$$\Delta E_S = (2S-1)\hbar\omega \tag{3.3}$$

3.1.2 Luminscence of Er Ions

The rare-earths (lanthanide series) consist of fourteen elements in the sixth row of the periodic table, beginning with cerium (Ce, atomic number 57) and ending with ytterbium (Yb, atomic number 70). In their pure form, lanthanides are all metals, they are all characteristically unstable. They comprise the first subset of the f-block elements and are generated by the filling of the electronic 4f orbitals. In fact, the energies of the 4f, 5d, and 6s orbitals are comparable over much of the sixth period, so that the order of electron filling throughout this block is erratic [77]. These elements almost invariably incorporate in solid hosts as a 3+ ion (even Er metal is thought to be composed of Er^{3+} ion cores); the 2+ and 4+ charge states are much less common.[80,81] Rare earth ions are all characterized by the

[80] The 3+ valence state of rare-earth incorporation in semiconductors also has a firm theoretical basis (see C. Delerue, et. al., Phys. Rev. Lett. **67**, 3006 (1991)).

partially filled 4f shell which gives rise to low energy electronic states, some of which are optically active. This partially filled 4f shell is electrostatically shielded from external electric fields, such as the crystal field in a solid,[82] by the 5s and 5p electrons, which are located farther from the nucleus; the 4f electrons do not participate in bonding. For this reason, the energy levels of lanthanide ions are largely insensitive to their local field environments and therefore to the particular host solid in which they are incorporated.[83]

Er in its ground state has the electron configuration $[Xe]4f^{12}6s^2$. In the trivalent state, it takes the form: $[Xe]4f^{11}$ with the eleven 4f electrons shielded by the $5s^2$ and $5p^6$ electrons. Theoretical calculation of the energy levels indicates that the splitting, due to spin-orbit and spin-spin coupling, of the unperturbed levels of the free ion is much wider than the Stark splitting introduced by the host matrix. The latter is actually a fine-splitting in which the degeneracy of the energy levels of isolated Er^{3+} is lifted according to the symmetry of the coordinating ions.[84] This concurs with the experimental observation that different host materials change only the width of the energy manifolds while leaving their positions relatively unchanged. Within a manifold, the levels are closely spaced, however, and exhibit a strong thermal coupling. Increasing thermal population of levels within a manifold along with the inelastic/elastic collision broadening of those levels with increasing temperature effectively blurs each manifold into a quasi-continuous band.

---

[81] Theoretical calculations of the energy levels of divalent and tetravalent Er are extremely rare. The only example which the author has found can be found at: Charles W. Thiel, "Energies of rare-earth ion states relative to host bands in optical materials from electron photoemission spectroscopy", PhD thesis, Montana State University, Bozeman, Montana, 2003.

[82] The crystal field is due to the local electric field experienced by the Er^{3+} ion in a solid matrix from the charge density of all surrounding atoms, and particularly nearest neighbour anions.

[83] This unique phenomenon is not observed in transition metals, however it is partially observed in actinide series ions where the 7s electrons shield the 5f shell.

[84] For cubic (or lower symmetries) the number of Stark components for the $^4I_{15/2}$ level is 5 or 8, while that for $^4I_{13/2}$ is 5 or 7 as determined using group theory. This gives rise to 8x7=56 transitions between the Stark manifolds giving rise to the 1.54 μm.

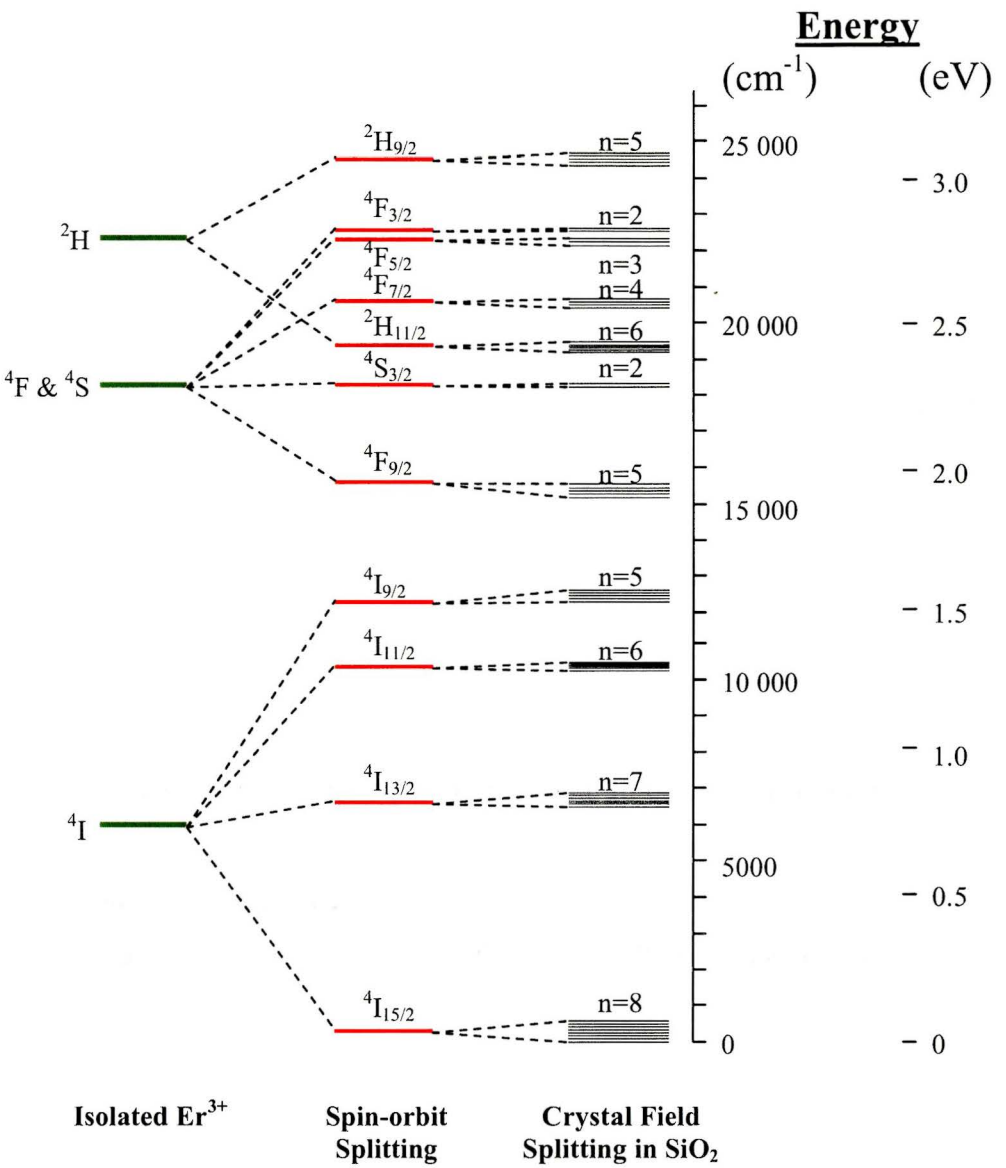

Figure 3.2: Energy level splitting of the Er^{3+} ion resulting from spin-orbit coupling and an applied electric field (Stark effect) in a solid. Adapted from [68].

It will be immediately apparent, given the previous discussion on electric dipole transitions and selection rules that intra-4f shell transitions in the free Er^{3+} ion are dipole forbidden (or parity forbidden depending on the preferred perspective). Evaluation of equation 3.1 yields zero because of the symmetry of

the 4f wave functions.[85] The solid host matrix plays an important role here. A crystal field that is non-centrosymmetric (lacks inversion symmetry) at the Er site enables a small amount of mixing of the $4f^{11}$ states with the $4f^{10}5d$ states. This makes the above transitions *weakly* dipole allowed. The effect is weakest for the low lying states, which is why only the lowest lying state of Er^{3+}, corresponding to the 1.54 μm transition, is metastable. Because all of the transitions are at least partly inhibited, even the higher lying excited states are characterized by rather long lifetimes – on the order of 1-100 micro-seconds – and correspondingly narrow linewidths, along with small direct optical absorption cross-sections (approximately 10^{-21} cm^2 for Er^{3+} in SiO_2). For this reason, direct optical pumping by resonant absorption is not an effective way to excite Er.

The coupling of the Er^{3+} ion to its host network arises through the modulation of the crystal field by vibrations of the network atoms. In amorphous SiO_2, the oscillations of the nearest neighbour network forming SiO_4 polyhedra are of primary importance; and of these vibrations, coupling to the highest energy vibrations dominates the phonon relaxation. In amorphous materials, it is not uncommon for vibrations to be much more localized than in crystals. The coupling of the 4f electrons to the surrounding ions is weak. This suggests, on the basis of the configuration coordinate model, that the excited state parabolas will be broad and not widely separated; in fact the Huang-Rhys parameter is near zero. As a result, the Stokes shift between luminescence and absorption bands in Er is small so that most of the transition energy is associated with the zero-phonon line; the Debye-Waller factor, which indicates the fractional intensity in the zero-phonon line, is experimentally found to be near unity. This supports the fact that there is little phonon broadening.[86] Despite the shielded 4f shell, one should remember that the higher the electronic energy level being considered, the greater

[85] The Er $4f^{11}$ configuration is the same for states up to about 6 eV, beyond which the opposite parity $4f^{10}5d$ states become active.

[86] This is somewhat tempered however, on the macroscopic scale in real systems (especially those that are glassy), because of the inhomogeneous broadening resulting from the existence of multiple non-equivalent Er sites, each subject to different crystal field symmetries and strength.

will be the involvement of the Er 5d orbitals in the excited state. The 5d orbitals are strongly affected by the surrounding ions and will therefore give rise to broader transitions. Further discussion of the phonon relaxation properties of Er^{3+} ions will be taken up in section 3.4.1.

3.1.3 Luminescence in Silicon

Luminescence in undoped semiconductors commonly occurs through electron-hole recombination across the band gap typically giving band edge emission or, at low temperatures, excitonic emission. The energy level structure of a bulk solid is more complicated than that of a single luminescence centre because the individual electronic states are, in principle, delocalized over the entire body of the solid and the Pauli Exclusion Principle is operating on a semi-infinite number of electrons. The electron energy is a function of its wave vector $k=2\pi/\lambda$ which determines its crystal momentum. The $E(k)$ function is highly complex (requiring four dimensions to fully visualize) and is referred to as the band structure.

Selection rules for band edge luminescence proceed from the same basic multi-polar transition physics as described above. A simplified tight-binding picture of the wave functions is useful in visualizing this [78]. The electron wave functions in the semiconductor are a linear combination of atomic-like orbitals multiplied by a phase factor in between unit cells. When adjacent cells are in phase, the wave vector $k=0$; when adjacent cells are out of phase, k is a maximum of π/a. In bulk Si, the valence band can be considered (in the simplified model) to arise from Si 3p orbitals. The maximum of the valence band (highest occupied molecular orbital – HOMO) occurs when these 3p orbitals are arranged to give σ antibonding (and π bonding). This requires that the 3p orbitals be in phase between unit cells, which means that the top of the valence band occurs at $k=0$. The conduction band can also be considered to arise from Si 3p orbitals. The minimum of the conduction band (lowest unoccupied molecular orbital – LUMO) occurs when these 3p orbitals are arranged to give σ bonding. This requires that

the 3p orbitals be out of phase between unit cells, which means that the bottom of the conduction band occurs at $k=\pi/a$. Thus, the HOMO and LUMO occur at different k values, a condition which is referred to as an *indirect band gap*. Within a unit cell, the HOMO and LUMO are aligned to yield a net dipole moment. However, the phasing of the molecular orbitals between unit cells points adjacent dipole moment in different directions, causing them to cancel. The wavelength of light, being long compared with the unit cell dimension, does not see a sufficient net electric dipole moment with which to couple. Radiative transition across the indirect band gap requires a temporary vibration that can appropriately alter the lattice symmetry. Electron-hole recombination is therefore a three-body process involving a phonon (although multi-phonon mediation is possible as a still higher order effect). The radiative rate now depends on the product of the matrix elements for electron-phonon scattering *and* the electron-photon interaction. As a result, the transition probability is low – typically 1000 times less than for a dipole allowed transition in a direct band gap material. In real crystalline Si (*c*-Si), the valence band maximum lies at the centre of the Brillouin zone or Γ point ($k=0$) while the conduction band minimum (Δ minimum) lies near the X point. The TO phonon at Δ minima ($E_{\Delta(TO)}$) is 57 meV; the optical phonon energy of Si at the Γ point ($E_{\Gamma(O)}$) is 64 meV. The dominant optical transition across the indirect gap in bulk Si occurs with the participation of a transverse optical (TO) phonon at 57 meV [79].[87]

Being weakly allowed vibronically means that the excited state lifetime of electron-hole pairs near the indirect band gap is very long – on the order of milliseconds, due to the low transition probability. This means that the diffusion length of these carriers (which have a high mobility in Si) can be very long, which increases the probability that the carriers will encounter a fast non-radiative defect or interface. In this way, even in highly pure single crystal Si, the efficiency of

[87] One can also view the phonon as a momentum conserving entity since a photon does not involve sufficient momentum to bridge the difference in momentum between an electron and hole across the indirect band gap.

band edge luminescence is extremely low. In principle, if one could eliminate all of the defects in the Si lattice, the indirect band gap would not necessarily be detrimental. One can pre-suppose that well-passivated Si quantum dots might provide a more attainable alternative in this regard, since the small volume of pure Si should make it possible to be entirely free of defects.

In a direct band gap semiconductor, the top of the valence band and the bottom of the conduction band occur at the *same k value* (often *k=0*). This means that the LUMO and HOMO both involve molecular orbitals which are in phase between unit cells, thereby removing the requirement for a momentum conserving phonon.[88] Radiative recombination across a direct band gap is typically very fast.

The high degree of disorder and disruption of translational symmetry in amorphous Si (*a*-Si) tends to increase the probability of radiative recombination relative to single-crystal Si. The difficulty, however, is that *a*-Si tends to possess large numbers of localized states owing to dangling bonds and other geometric defects – which are sensitive to the material preparation process. These defects can act both as non-radiative recombination centres and as charge traps. They appear in the band structure primarily as a region of localized states above and below which one gradually has the usual extended valence and conduction band-like states respectively; this structure gives rise to the so-called Urbach region in which the optical absorption coefficient has an exponential dependence on the energy for photons of energy less than 1000 cm^{-1}. The concept of an 'electrical' band gap in *a*-Si is thus ill-defined owing to the rather diffuse band edges and one speaks more typically of a *mobility gap* E_μ at the centre of which are defects localized neat the Fermi level. Nonetheless, it is not uncommon to define an *optical gap* based on the absorption coefficient; however such a definition is not unique. The most commonly accepted definition of the optical gap extrapolates

[88] This does not necessarily guarantee that the unit cell will possess a net dipole moment. It is possible to have a dipole forbidden direct band gap (eg. Cu_2O), although the most technologically important direct band gap semiconductors are those which are highly luminescent owing to their *dipole allowed* direct band gap.

the absorption coefficient to define a quantity called the *Tauc gap* [80].[89] The Tauc gap (denoted E_{Tauc}) is typically larger than the band gap of crystalline Si by 0.3-0.7 eV depending on the material preparation technique and the extent of hydrogenation. The large number of dangling bond defects makes the properties of *a*-Si highly sensitive to hydrogen. Hydrogenated *a*-Si (*a*-Si:H) has the advantage that the defects can be largely passivated (and therefore eliminated from the mobility gap).[90]

3.1.4 Luminescent Electronic Defects in SiO_2

There are a significant number of radiative defects which commonly occur in amorphous SiO_2 (*a*-SiO_2) since the lack of conduction band electrons at room temperature can stabilize most electronic defects (unlike pure Si). These radiative defects provide useful clues about the bond structures in SiO_2 thin films (an often difficult material to understand) and have been well researched. Their number, type and lineshape are extremely sensitive to their local environment as affected by film preparation conditions and heat treatments as well as the presence of impurities; in this regard, they serve an important characterization purpose.[91]

Most of the luminescent centers to be discussed here would be classified as point defects (ie. they are localized) so that their excited state wave functions for energy levels that are well below the host oxide band gap should be correspondingly localized [81]. The most important experimental tool for investigation of the defects is electron spin/paramagnetic resonance (EPR) and positron annihilation spectroscopy; photoluminescence (especially using UV

---

[89] Other definitions of the optical gap include the iso-absorption gap (denoted E_{04} and defined as the energy at which the absorption coefficient is 10^4 cm^{-1}) and a variation of the Tauc gap (E_3).

[90] However, it has been found that the hydrogen passivation can break down under prolonged exposure to infrared radiation – a phenomenon known as the Staebler-Wronski effect. This has proven a limiting factor in *a*-Si solar cell technology.

[91] Much of the research effort has been driven by the utility of these defects in the micro-structural characterization and optimization of SiO_2 films for micro and opto-electronics. Radiation damage characterization and structural optimization of thin MOSFET gate oxides, particularly in the context of defect-mediated breakdown, have been the primary motivating factors.

excitation) and cathodoluminescence [82] have been the most common optical characterization techniques.

Non-bridging oxygen hole centre (NBOHC): typically luminescent in the range 620-650 nm; 1.9-2.0 eV

$$\equiv Si–O\uparrow$$

The ≡Si notation refers to a Si atom singly bonded to three other atoms (not a Si atom triply bonded to another single atom). The ↑ on the oxygen atom refers to an unpaired electron (sometimes in the literature this is specified as a single dot, Si·). In other words, this defect is paramagnetic and would typically be an SiO_4 tetrahedron in which one of the corner oxygen atoms does not bridge to an adjacent tetrahedron. A possible precursor of the NBOHC could be the peroxy linkage or radical (see below). It has been proposed that there are two types of NBOHC, each from a different precursor [83]. The first results from a strained Si–O bond, which cleaves to produce a NBOHC emitting at 1.91 eV (FWHM of 0.2 eV) and an E' centre (see below).[92] The second is thought to originate from the removal of a hydrogen atom from a hydroxyl (OH^-) passivated Si bond, Si–OH to yield the NBOHC and atomic hydrogen; this centre emits at 1.95 eV with FWHM of 0.42 eV [84]. The emission energy differs from the previous NBOHC since it is not necessarily in an environment of strain bonds. Clearly, the presence and thermal evolution of hydrogen will influence the formation/elimination of this defect.

Neutral oxygen vacancy (NOV): typically luminescent in the range 450-470 nm; 2.64-2.76 eV

$$\equiv Si–Si\equiv$$

This is the most common example of an oxygen deficient centre. A typical example in SiO_2 would be $O_3\equiv Si–Si\equiv O_3$. This is a diamagnetic defect and has a

[92] This particular emission might also be associated with a Si_3^- defect (see for example: Kenyon, et. al., J. Appl. Phys. **79**, 9291 (1996)).

vacuum ultra-violet (VUV) absorption band near 7.6 eV (163 nm). It has been shown that this absorption can, in some cases, lead to a conversion of the NOV into a divalent Si defect (which is alternately viewed as a conversion from a relaxed to an un-relaxed form of an oxygen vacancy) from which fast (nano-second scale) 4.4 eV PL emission has been observed; non-radiative decay to two E' centers is also thought possible. A competing pathway from this excitation, however, is 2.7 eV PL. The 2.7 eV PL is due to the $S_o \rightarrow T_1$ (singlet to first triplet state) transition of the NOV. The 2.7 eV PL has shown a decay time of 10.2 milli-seconds and a linewidth in the range of 35-50 nm. This centre also seems to have an absorption band at 5.8 eV (214 nm) resulting from photo-ionization of the defect – which usually results in the formation of E' centers. This centre is sometimes referred to as oxygen deficient centre I: ODC(I) [85].

Two-fold coordinated (divalent) Si: typically luminescent near 285 nm (4.4 eV) [86]

$$=Si:$$

This is another type of oxygen deficient centre.[93] It has been suggested that three E' centres can combine to yield a divalent Si [87]. Common examples of this defect would be –O–Si–O– and –O–Si–C–. It has VUV absorption bands at 5.0 eV (248 nm) and 6.9 eV (180 nm). This centre may also be excited at 7.6 eV (163 nm) by a NOV (see above). The divalent Si defect is sometimes referred to, in this context, as oxygen deficient centre II: ODC(II) [85]. It should be noted that one of the divalent Si or NOV defects may also have a luminescent transition near 400 nm (3.1 eV) [88].[94] A possible luminescent triplet-to-singlet transition in divalent Si has been calculated at 2.5 eV (496 nm) and 2.84-3.2 eV (387-437 nm) [89].

---

[93] SiO_2 has an optical absorption band at 5.0 eV called the B_2 band. The defect giving rise to it is disputed but is referred to as the B_2 centre. The B_2 centre has been ascribed to divalent Si in the case where it is regarded as the un-relaxed form of a NOV; the form B_2(Si) is sometimes used.

[94] Alternately, this transition may simply be a perturbation of the NOV 2.7 eV transition by common inevitable impurities in the SiO_2 network.

Weak oxygen bond (WOB): typically luminescent near 415 nm (2.99 eV)

O–O

This is different from standard molecular O_2 which involves two sigma bonds and one pi bond. The precursor of the weak oxygen bond is interstitial oxygen atoms, such as might effectively be introduced by energetic collision damage during ion irradiation.[95]

E_δ' centre: typically luminescent in the range 520-550 nm; 2.25-2.38 eV

Si↑Si≡Si

This defect is often thought to be the precursor to a Si nano-cluster, being effectively a paramagnetic state of a small Si cluster [90]. In some of the literature, it has been ascribed to a five-centre tetrahedral Si cluster with the unpaired spin delocalized over the four Si–Si bonds; the FWHM and luminescence lifetime of this centre have been measured to be 0.44 eV and 20-30 ns respectively. However, recent theoretical work [91,92] has suggested that the defect is more likely to be a structurally relaxed Si dimer (oxygen monovacancy) with the unpaired spin localized on the dimer regardless of the cluster size; that is, regardless of the atoms which satisfy the rest of the bonds on the dimer (for example O_3≡Si↑Si≡O_3; note that the dimer does not involve a Si–Si bond). In principle, the E' centers define a class of paramagnetic defects, all positively charged oxygen vacancies, denoted E_α', E_β', E_γ', and E_δ'. The basis of all of these centers is a Si dangling bond (sp^3 orbital) with an unpaired electron, ≡Si↑. The different versions arise from different complexes in which this Si dangling bond structure exists. It is thought possible for E' centers to form by hole capture at a NOV to form, for example, O_3≡Si·$^+$Si≡O_3

[95] It should be noted that the observation of luminescence near 2.93 eV (423 nm) has also been ascribed either to a WOB or possibly a carbon related impurity (M. A. Stevens Kalceff and M. R. Phillips, Phys. Rev. B **52**, 3122 (1995)).

Other luminescent defects which occur in Si-rich SiO_x include the $-SiO_3$ group bonded at the interface of a Si nano-cluster (thought to be luminescent near 370 nm (3.35 eV)); a double peak emission at 417 nm (2.97 eV) and 436 nm (2.84 eV) has been proposed to originate from states produced in the band gap by vacancies in Si nanocrystals.

There are also a number of defect centers which are typically found to be non-radiative. However, it should be noted that in the quantum confinement regime (or maybe even in a network filled with impurity atoms) it is feasible that some of these centers might become radiative as a result of perturbations to their bulk charge distributions.

E' centre $\equiv Si\uparrow$

This general class of defects has been discussed above. An example of this would be $O_3{\equiv}Si\uparrow$. These have been assigned an absorption band at 5.8 eV.

Peroxy radical $O_3{\equiv}Si{-}O{-}O\uparrow$

A closely related defect is the peroxy linkage ($O_3{\equiv}Si{-}O{-}O{-}Si{\equiv}O3$). The peroxy linkage is effectively the Frenkel counterpart of the neutral oxygen vacancy and is thought to have an absorption band near 3.8 eV (325 nm). It is characteristic of oxygen rich SiO_x or even oxygen-rich regions within SiO_2. There has been some speculation [93] that a closely related defect, the *small peroxy radical* (SPR) can actually emit luminescence in oxygen-deficient SiO_2 at 550 nm (2.25 eV) with a FWHM of 0.2 eV and a lifetime of 300 ns (as distinct from the E_δ' centre. The SPR has the following structure:

$$O_3 \equiv Si - \overset{\overset{O\uparrow}{|}}{O} - Si \equiv O_3$$

D centre $(Si_3{\equiv}Si\uparrow)_n$

This is a Si dangling bond in pure Si. For example, such a defect is extremely common in *a*-Si.

P_b centre

This defect is located at a Si/SiO_2 interface and consists of a Si atom which is three-fold coordinated with other Si atoms and has a dangling bond that points into void space in the SiO_2 matrix [94]. It is distinct from the E' centre and is detectable by EPR.

It has been noted that the presence of impurity atoms in the network can perturb the defect site simply by altering the arrangment of the neighbouring atoms. This can influence the energy level structure of the defect without the impurity actually participating in the defect. Impurities may also favour the formation of oxygen vacancies by changing the thermochemical conditions during film growth and annealing [95].

One additional aspect of luminescence in Si-oxides which should be kept in mind (because it can be confused with the intrinsic electronic defect luminescence) is that there are hundreds of stable organosilane compounds which can potentially emit blue/green PL; the emission typically has broad FWHM and lifetimes in the ns regime [81]. This is an important consideration in SiO_x films deposited by PECVD using any sort of organic precursors.[96]

3.2 Fundamentals of Quantum Confinement Theory

3.2.1 Quantum Confinement in Nanoclusters: Brus Model

Appendix A provides a general description of the basic physics of ideal quantum confined structures (dots, wires and wells). One gains insight into the real physics of nano-clusters, which are in effect an approximation of a quantum dot, by recasting aspects of the discussion in Appendix A using the language of band

[96] A further defect-related issue is that of *self-trapped excitons* in the SiO_2 matrix. These are electron-hole pairs localized at a self-induced lattice distortion that typically result from strong electron-phonon interactions. These are typically found to have an energy of 2.4 eV (517 nm) in *a*-SiO_2 (J. L. Shen, et. al., J. Phys.: Condens. Matter **15**, L297 (2003)).

structure theory. The simplifying feature of dots is that there is essentially no consideration of a quasi-continuum of states along any spatial dimension.

The energy band structure of a solid is normally calculated and expressed by considering the bulk material, *infinite in extent*, without regard to boundary (surface) effects of any kind. In this way, the *E(k)* structure can be taken in a rather literal sense because each quasi-electron can be considered to be infinitely delocalized (over the entire infinite solid) and therefore reside completely in a single Bloch state (molecular orbital) of single well defined wave-vector *k* [29]. Such a Bloch state has the general form:

$$\Phi_{\vec{k},\mu}(\vec{r}) = \exp^{i\vec{k}\bullet\vec{r}}\, \chi_{\vec{k},\mu}(\vec{r}) \tag{3.4}$$

Where $\chi_{\vec{k},\mu}$ has the periodicity of the unit cell (and weak *k* dependence). The exponential pre-factor is plane-wave like and connects the wave-vector with a wavelength $\lambda=2\pi/k$. Based on this form, the spatially localized wave function in a nano-cluster could be synthesized as a Fourier transform wave packet of Bloch states.

$$\psi_i(\vec{r}) = \sum_{\mu} \int_{K} f_{i\mu}(\vec{k}) \Phi_{\vec{k},\mu}(\vec{r}) dk \tag{3.5}$$

The μ index the different bands. The energy eigenfunctions of the electron are now superpositions of bulk *k*-states ranging over some Δk (weighted by the $f_i(k)$).[97] The energy associated with the localized wave function can be estimated by writing a Taylor's series expansion for *E(k)* about the central *k* in Δk. The result is the same as described in Appendix A (keeping only the first two non-zero terms):

[97] The properties of the Fourier transform are reminiscent of the Heisenberg uncertainty principle here in the sense that as the nano-cluster decreases in size, a larger region of *k*-space is required to achieve the necessary wave function localization within the cluster.

$$\varepsilon \approx E_c + \Delta E = E_c + \left(\frac{\hbar^2}{2m_e^*}\right)\left(\frac{\pi^2}{d^2}\right) \tag{3.6}$$

The discussion to this point has considered only an electron. One can consider a confined electron-hole pair by writing a Hamiltonian containing both of their kinetic energies with effective mass along with an interaction term. The latter term accounts for correlation effects via a shielded Coulomb potential. The energy eigenvalues can be calculated as the expectation value of the Hamiltonian using wave functions determined by the method of equation 3.5. The lowest energy is denoted E^* and represents the effective theoretical quantum confined band gap of the nano-cluster:

$$E^* = E_g + \frac{\hbar^2\pi^2}{2d^2}\left[\frac{1}{m_e^*} + \frac{1}{m_h^*}\right] - \frac{1.8e^2}{\varepsilon d} + (smaller\_terms) \tag{3.7}$$

The quantity E_g is the band gap of the bulk material. Note that the Coulomb term lowers E^* as d^{-1} while the confinement energy term (containing the additive and independent confinement energies of the electron and hole) raises E^* as d^{-2}. This is one of the most important results for the present study for it indicates that the band gap will always increase with decreasing nano-cluster size.

The density of states (DOS) provides an intuitive way of considering the so-called 'band-gap opening' of nano-clusters with decreasing size. Given the bulk $\varepsilon(k)$ structure occupied by the multitude of electrons from a semi-infinite crystal, one considers gradually decreasing the crystal size all the way down to a single atom, at which point there remain only widely discrete atomic levels. The confining boundary would gradually force the localization of the wave functions which, in effect, would become a [Fourier] super-position of bulk k-states over some increasingly large range Δk. As the confinement becomes more severe, fewer wave functions can meet the boundary conditions and increasing numbers of bulk states would be required to form an acceptable wave function. Converting the many bulk states into progressively fewer localized states enhances the

density of states at some energies and reduce it elsewhere. Increasing discretization of energy (and DOS) features appears first at the band edges and then proceeds gradually to the centre of the bands. Because a semiconductor band gap is based on band edges, this is tantamount to progressively opening the band gap.

The phenomenon of band gap enlargement with decreasing cluster size and the concomitant decrease in the DOS at the band edges is particularly relevant to the current study for its effect on surface and/or trap states. In bulk material, trapping defects localize an electron or excitonic wave function in the vicinity of the defect; the degree of localization depends on the defect. When these defects are present in a nano-cluster, the energy levels of the defect will rise depending upon the degree of enhancement of the wave function localization at the defect forced by the confinement relative to the bulk case. Highly delocalized bulk defect states (usually shallow states in semiconductors) can become indistinguishable from the Fourier transform states, while tightly localized bulk defect states (usually deep states in semiconductors) may increase only slightly in energy. These latter states would become increasingly separated in energy from the Fourier transform states as illustrated in Figure 3.3. In this way, the energy gap between a mid-(band gap) defect state and an energy band edge can increase as the cluster size decreases. This is an important point because it will be seen later that defect states play an important role in Si nano-clusters.

3.2.2 Quantum Size Effects and Luminescence

The preceding discussion makes it clear that semiconductor nano-clusters should exhibit different luminescence (and absorption) properties than their bulk counterparts – even though they may have the same internal bonding geometries. In nanocluster luminescence, the important excitation under consideration is an electron-hole pair – often in an exitonic state. Electron-hole pair thermalization is

usually extremely fast in nano-clusters and localization of the electron-hole pair favours the formation of such a bound state over dissociation (which dominates in

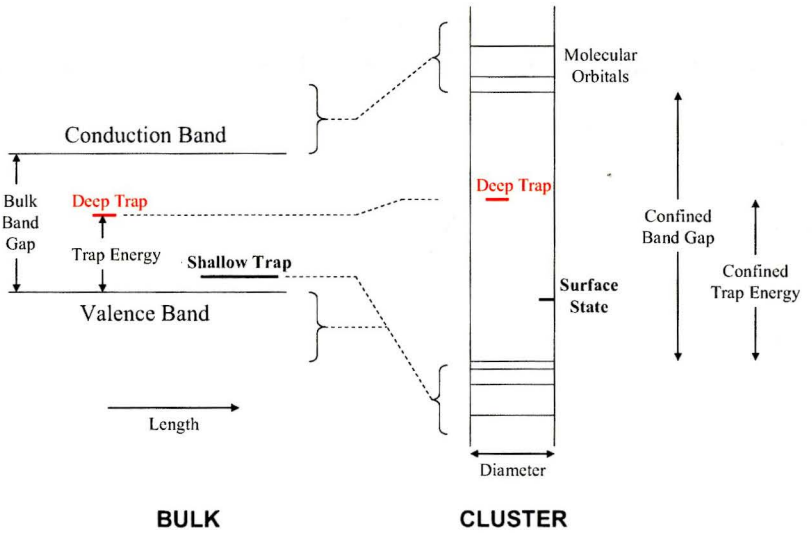

Figure 3.3: Depiction of the effect of decreasing size on the energy band edges as well as isolated states with varying degrees of localization (adapted from [29]).

bulk semiconductors above cryogenic temperatures). For this reason, a useful criterion for the onset of the quantum confinement regime in nano-clusters is the point at which the cluster diameter falls below the excitonic Bohr radius of the bulk material (approximately 5 nm in Si).

Confinement alters the transition energies and associated dynamics corresponding to electron-hole recombination luminescence[98] and electron-hole generation by photon absorption or impact ionization. The opening of the band gap and the shifting of trap energies will often blue-shift all emission/absorption edges relative to the bulk material. Furthermore, the pronounced energy level discretization and corresponding reduction in the density of states at the band edges concentrates oscillator strength into fewer transitions. This increases the probability of radiative recombination across these transitions and manifests itself

[98] Recombination luminescence includes band-to-band and excitonic recombination, trap-assisted (Shockley-Read-Hall) recombination, and Auger recombination.

as the appearance of discrete features in the optical absorption/emission spectra that are appropriately reminiscent of atomic-like spectral features (although these may be well resolved only at reduced temperature).

Quantum confinement effects are uniquely apparent in indirect band gap nano-clusters such as Si. Within a nanocluster, the three dimensional confinement severely limits the diffusion length of the carriers and forces a greater wave function overlap between an electron and hole that favours exciton formation. The confinement of the carriers into a small region of space enhances the likelihood of recombination. In addition, thermally enhanced non-radiative recombination pathways such as free carrier absorption and Auger recombination are suppressed because the band-gap enlargement reduces the intrinsic carrier population in the conduction band. In addition to all of this, the k-selection rule is relaxed by the small dimensions. This is intuitive given that the k-selection rule is a consequence of the translational symmetry of the Si lattice and the resultant phasing of the molecular orbitals pertaining to electric dipole transitions. The strong symmetry breaking in the nano-cluster relaxes this rule. Theoretically, this can be understood on the basis of the increased uncertainty in the wave vector Δk due to the spatial localization of the electron and hole wave functions. If the cluster is sufficiently small, Δk can be large enough to allow a 'quasi-direct' transition across the band gap. This increases the corresponding transition rate.

Most mathematical formalisms do not address the impact of quantum confinement on surface-sensitive luminescence. Unlike bulk material, the number of surface atoms in a nano-cluster may be a comparatively large proportion of the total number of atoms. This changes the thermodynamic properties of the cluster relative to the bulk. And, it has been calculated that even a single non-radiative trapping defect (such as a neutral dangling bond) at the interface can prevent all luminescence from a cluster [96]. Given that Si nano-clusters are often embedded in a solid matrix, the interface geometric and electronic structure depends heavily on the passivating atoms. Different atoms bond differently at the surface exert

different electric fields into the cluster interior. They modify the energy level structure in addition to introducing trap states as previously discussed. The effect of the surface in Si nano-clusters has perhaps been the greatest source of controversy in the study of their luminescence mechanisms. The problem is that the surface passivation of the clusters can be highly specific to the method of film deposition, any post-deposition heat treatment, and any contamination occurring therein. If the cluster luminescence is sensitive to single atoms at the surface then it is little wonder that there is conflict in the literature; a dirty annealing furnace could be sufficient to produce bizarre results. The combination of quantum confined defects, size and surface effects define an entire spectrum of luminescence mechanisms which must be modelled individually – hence the often debated issue about whether the Si cluster luminescence is due to quantum confinement or surface states. It is inevitably due to both and any attempt to discuss this matter in terms of extremes is futile.

3.3 Luminescence of Si Nano-clusters in SiO_x ($x \leq 2$)

3.3.1 Current Model

While the question of the luminescence mechanisms in Si-rich SiO_x is not a 'solved problem', a number of principles have become generally accepted within the last ten years; controversies have shifted to finer theoretical details. It is now accepted that a characteristic broad luminescence can originates from the Si nano-clusters themselves as opposed to other defects introduced by the excess Si. The channels of photon emission and absorption are not necessarily identical but involve a combination of 'pure' quantum confinement and surface effects; the optical properties are co-determined by the cluster size *and* the exact surface passivation. This relative balance gives rise to a whole spectrum of emission and absorption energies and processes. This balance can be conceptualized through the wave functions (or molecular orbitals) of the highest occupied and lowest

unoccupied molecular orbitals (HOMO and LUMO) associated with the entire cluster including the surface. If the cluster is small enough that the orbital is strongly delocalized over the *entire* cluster, then strong quantum confinement is dominant. If the cluster is sufficiently large that the orbital is concentrated more towards the interior, then there is only weak quantum confinement. The bond geometry inside the cluster can introduce inhomogeneity in the overall delocalization by focusing charge density more towards certain interior atoms depending on local bond strain or interior defects. The surface passivating atoms (which could include impurities) and their bond geometries can create two general alternative scenarios. First, it can concentrate the molecular orbitals uniformly on the surface atoms; this alters the HOMO-LUMO gap energy relative to the above delocalized cases. While this is indeed a *surface-based* state, it is not a well-localized surface state in the sense of a point defect. Alternately, the surface may introduce a particular localized site (or discrete set of sites) at which the orbital becomes very strongly localized similar to a point defect; this is typically what is meant in the literature by 'surface state' and causes the most drastic deviation of the HOMO-LUMO gap from the pure quantum confinement case.

Simulation and Modelling

Computer simulation provides the means to model the wave functions and their chemical-geometric responses just described. Indeed, it has proven particularly necessary in the study of Si nano-cluster luminescence because experimental investigations of electronic structure tend to sample a large population of clusters having various size and surface passivation. Unlike many other semiconductors, it is difficult to isolate single nano-clusters of Si with the appropriately controlled surface chemistry. This is because quantum confinement effects are not apparent in Si until extremely small size (approximately 5 nm) in comparison with other materials such as gallium arsenide with a de Broglie wavelength of 25 nm for electrons at 300 K [97].

Modelling consists of the specification of the material bond structure (either by energetically optimized geometric relaxation or by assumption) followed by the calculation of the energy levels. Both isolated clusters (usually with monolayer surface passivation) and embedded clusters are studied. In the case of the embedded clusters, the structural relaxation has also been simulated in order to investigate the transition region between the cluster and the far-field host matrix. Coupling between clusters does not seem to have been investigated although, intuitively, this should become important when the cluster spacing falls below the relevant de Brogie wavelength.

There are three calculation techniques which seem to have been the most successful in modeling the systems. The latter two methods have been used extensively to include various surface effects:

1) Standard bulk band structure calculation techniques relying on empirical pseudopotential methods or self-consistent tight binding (linear combination of atomic orbital) methods accounting for variously extended neighbours. In general, these methods employ the local density approximation (see below). The use of these techniques usually proceeds on the assumption that the bond geometries are close to those of the bulk material and that bond structure relaxations are prevalent only near the interface. As a result, these techniques are common in treating larger clusters – containing hundreds or even thousands of atoms. They are therefore probably more accurate in this size regime [98,99].

2) Density functional theory (DFT) with the local density approximation (LDA): DFT is a clever method for handling the many-body problem of the electrons in a solid so that electron-electron interactions and external potentials can be taken into account for large numbers of electrons. Instead of using the N-electron Schrödinger equation to calculate the N-body wave function (which has 3N spatial variables), the DFT reformulates the problem in terms of the electron

density as the basic variable (which is a scalar field of just three spatial variables). It is based on the Hohenberg-Kohn theorem which states that the expectation value of any operator is a unique functional of the ground-state electron density.[99] In this way, all excited states, excitation energies, transport properties, etc. are determined.[100] Using the LDA, the non-local aspects of the functional dependence of the exchange-correlation (XC) potential are ignored.[101] This assumes that the density of the system varies slowly.[102] It has been noted that the LDA is useful in determining the atomic geometries of semiconductor clusters but tends to severely underestimate band gaps – although it tends to accurately portray band gap trends. An arbitrary correction factor is usually required to align the absolute values with experiment. For this reason, the LDA is typically used to efficiently test a wide range of systems for trends but not to compare absolute quasi-particle band gaps with experiment. Time dependent DFT (TD-DFT), including a time dependent LDA, is the generalization to handle calculations involving time-dependent phenomena such as optical transitions. See [100].

3) Quantum Monte-Carlo (QMC) simulation: this technique has been used to address the shortcoming of the DFT-LDA in computing band gaps. In this approach, many-body effects in the wave function are included by stochastically sampling the Schrödinger equation. This being a full many-body formalism, the

---

[99] Thus, there is a one-to-one mapping between the system Hamiltonian (including external potential and exchange/correlation potentials) and the ground-state electron density. The ground state electron density uniquely determines all eigenstates of the system and the expectation value of any operator.

[100] There is reasonably simple computational scheme for the implementation of DFT provided by the Kohn-Sham formalism. A non-interacting reference system is considered (which is an easily soluble N electron Slater determinant) and one self-consistently calculates an external potential such that the non-interacting system has the same ground-state electron density as the real, interacting system.

[101] That is, the XC potential at a point is determined only by the electron density at that point.

[102] Conceptually, it represents the lowest-order term in a series expansion of the XC energy in powers of gradients (of first and higher order) of the density. The inclusion of these higher gradients can be made within the generalized gradient approximation (GGA). An improvement of the GGA has been reported with so-called hybrid functionals; see Z. Zhou, et al., *Nano Letters* ***3****, 163 (2003)* for application to Si clusters and K. Raghavachari, et. al., *J. Chem. Phys.* ***116****, 825 (2002)* for application to SiO_2 point defects.

LDA quasi-particle band-gap problem is removed. A further advantage is that required calculations scale linearly with system size, allowing larger systems to be investigated.[103] QMC has been used primarily to make the predictions of the LDA compatible with experimental comparison [101].

Optical Absorption

The mechanism of photon absorption depends on the energy of the excitation [13]. For wavelengths greater than 600 nm, the photon can be weakly absorbed by localized surface states. At shorter wavelengths, progressively stronger absorption sets in and is dominated by photo-generation of electron-hole pairs in the 'bulk' of the cluster across the quantum confined band gap (which increases approximately as the inverse square of the confinement radius). As a result, the size of the cluster will determine the absorption edge and absorption cross-section. A strong Stokes shift observed in Si nano-clusters would indicate that the absorption gap is larger than the emission gap.[104]

Matrix Effects

In principle there should not be significant absorption of visible photons (400-700 nm; 3.10-1.77 eV) in the SiO_2 host matrix because the band gap will be on the order of 8-9 eV. This does not, however, account for absorption by common oxide defects or Si-rich regions in the matrix resulting from non-precipitated Si (possibly having a much lower band gap) which should exhibit their own optical absorption characteristics.

The most important matrix effect is the structural mismatch between the Si cluster and SiO_2. DFT simulations (with GGA) of the structural relaxation of small Si nano-crystals embedded in SiO_2 (β-cristobalite) identified three regions [102].

---

[103] For comparison, under the full many-body Schrödinger equation the required calculations scale faster than exponentially with the number of electrons. This rapidly becomes prohibitive.

[104] Note that most band gap calculations determine the absorption gap (ie. optical gap) when it is the emission gap that is often more technologically relevant.

1) The interior Si nano-cluster which is strained with respect to bulk Si
2) An interfacial capping shell of distorted β-SiO_2 about 8-9 Å thickness which gradually reduces in stress from the Si cluster surface to the exterior region
3) An exterior region of unstressed β-SiO_2 around the stressed interface shell

EFTEM imaging has corroborated the presence of a stressed silica transition shell about 1 nm thick around the cluster.[105] The important implication here is that the cluster relaxation is determined by the matrix – which is not always pure SiO_2.

Optical Emission

The recombination pathway of photo-generated carriers depends upon the surface passivation:

1) Surface completely passivated with hydrogen: if the surface of the Si nano-cluster is completely passivated with hydrogen, then there are no dangling bonds at the interface and, in principle, no surface states of any kind which could constitute localized states within the band gap. In the isolated cluster, the core is essentially that of bulk Si. DFT with a nonlocal hybrid functional [103] showed that in a $Si_{35}H_{36}$ cluster (1.1 nm diameter) both the LUMO and HOMO are delocalized but with significant concentration near the surface. As the cluster increases in size, even by 1.8 nm diameter, the LUMO and HOMO increasingly shift into the cluster interior but are still highly delocalized. Consistent with this finding, the band gap opens significantly with decreasing size *in good agreement with the quantum confinement model* [104]. In fact, the band gap increases from the bulk Si value of approximately 1.1 eV up to 5 eV for a 1.1 nm diameter nano-cluster. Within the nano-cluster, an electron-hole pair will form a free exciton

[105] One therefore has a progressive transition from the Si nano-*crystal* core to amorphous Si to stressed SiO_2 to the SiO_2 embedding matrix. These transitions are probed with EFTEM and synchrotron x-ray absorption in (N. Daldosso, et. al., Phys. Rev. B **68**, 085327 (2003)).

and photon emission will occur via the recombination of this exciton. This excitation will increasingly concentrate at the surface with decreasing cluster size. Simulation suggests that for extremely small clusters (less than 2 nm) the band gap transition becomes dipole allowed with radiative rates near 10^{-7}-10^{-8} second. For larger clusters, the band gap is indirect, showing the long 10^{-3} second lifetime typical of dipole-forbidden transitions [103].

2) Oxygen-based surface passivation: the surface of a Si nano-cluster could contain one or more oxygen atoms bonded in various configurations. Some band gap enlargement occurs as a result of the quantum confinement as the cluster size decreases, however the enlargement is not as large as predicted by quantum confinement theory (as achieved in fully hydrogen passivated clusters). The degree of the reduction of this enlargement depends on the type of oxygen passivation considered. The most commonly modeled of these are:

(a) *Complete passivation with singly-bonded oxygen*: The oxygen termination always concentrates the HOMO and LUMO towards the oxygen atoms (although they are still delocalized) and always reduces the extent of the band gap enlargement with decreasing cluster size relative to complete hydrogen passivation. This is ascribed to the ability of the surface oxygen atoms to weaken the Si–Si bonding of those Si atoms bonded to surface oxygens [103]; this is likely due to the high electronegativity of oxygen. Such clusters exhibit the standard dipole-forbidden indirect band gap. Once again, photo-generated carriers will form a free exciton, with the excitation concentrated near the surface oxygens. However the wave function will still be delocalized because of the absence of localized states on the oxygens.[106]

---

[106] For example, $Si_{35}(OH)_{36}$ in which the cluster surface is composed entirely of Si–O bonds (with the oxygen atoms capped by hydrogen for ease of modeling) exhibits a HOMO-LUMO band gap that is a factor of 2 smaller than its purely hydrogen passivated counterpart (5.0 eV to 2.73 eV).

2) *Incomplete oxygen passivation*: in this case, there is partial hydrogen passivation and partial oxygen passivation, with the oxygen being either:

(i) *Singly bonded*: this induces a significant structural relaxation in the Si core relative to bulk geometry. When there are only a few of these bonds present, the change in electronic properties relative to the fully hydrogenated case is not severe but there is still a reduction of the band gap. This is the result of conduction band-edge states localized on the oxygen atoms [105].

(ii) *Doubly bonded*: the presence of the Si=O (silanone) bond results in limited structural relaxation in the Si core, this bond orients itself perpendicular to the surface Si–Si bonds. These bonds concentrate the LUMO and HOMO on the oxygen atoms and introduce corresponding [surface] states at the band edges within the band gap [105]. These can act as charge traps and it has, in fact, been suggested that the electron trap is actually a p-state localized on the Si atom, and the hole trap is a p-state localized on the oxygen atom [104]. This significantly red-shifts the energy of photons produced by electron-hole recombination with respect to the band-edge emission for the case of full hydrogen passivation. The extent of the relative red-shift increases with the number of silanone surface bonds but is significant even for a single one [105]. These states dominate the cluster optical properties *if they actually lie within the band gap*. Studying the effect of these bonds over a large range of cluster size has revealed three important size regimes (Figure 3.4) [104]. For clusters larger than 3 nm diameter, the state introduced by the silanone bond is not within the quantum confined band gap and so is not stabilized with respect to the band gap. Recombination of photo-generated electron-hole pairs proceeds via free exciton recombination as in the case of full hydrogen passivation. For clusters in the range of 1.5-3 nm diameter, the silanone bond introduces a state below the quantum confined conduction band.

The excited electron becomes trapped at this state while the hole is still free within the quantum confined valence band. There is still a blue shift of the energy of emitted photons with decreasing cluster size, but it is now less than that predicted by quantum confinement. Finally, for clusters smaller than 1.5 nm diameter, the silanone bond introduces both electron and hole states within the band gap; Recombination proceeds via a trapped exciton.[107] The formation of Si=O bonds at the Si cluster interface with and SiO_2 host matrix is plausible given that they could represent a natural bond geometry to satisfy broken Si–O bonds which result from the large stress at the Si/SiO_2 interface. Increasing the number of interfacial Si=O bonds non-linearly red-shifts the emission gap up to a point of saturation [106].

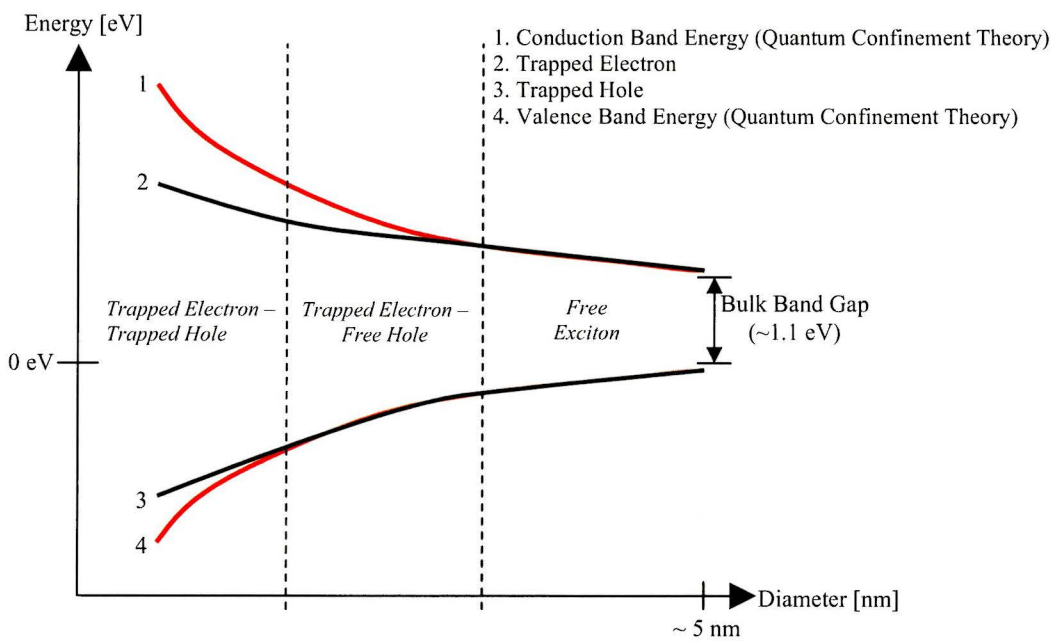

Figure 3.4: Schematic of the increase of the band edge and localized state energies with decreasing cluster size. The surface passivation determines the presence of the surface-based states. Adapted from [104].

[107] The emission energies calculated by Wolkin et. al., Phys. Rev. Lett. **82**, 197 (1999) in each of these three regimes have actually found experimental confirmation (see J. S. Biteen, et. al., Appl. Phys. Lett. **84**, 5389 (2004) and J. S. Biteen, et. al., Mat. Res. Soc. Symp. Proc. Vol. 770, 16.2.1 (2003)).

(iii)*Singly bonded oxygen and doubly bonded oxygen*: the change in the electronic properties is dominated by the double bond so that the band gap shift follows closely the discussion given in (ii) [105].

Embedded Clusters

The electronic properties of Si nano-clusters embedded in SiO_2 are highly influenced by the strained capping layer surrounding the cluster. The localization of the orbitals on oxygen atoms is an effect that penetrates from the immediate Si surface into the capping layer. This means that oxygen atoms in the SiO_2 can participate in the optical activity of the cluster because they introduce states in the band-gap of the SiO_2 which are near the relevant energies for the isolated cluster itself. Simulations indicate a resultant re-organization of energy levels near the Si cluster band edges and a correspondingly altered shape of the absorption spectra [102].

3.3.2 Implications of the Si Nano-cluster Luminescence Mechanism

The model discussed above has many important implications that need to be discussed because they affect the interaction between Si nano-clusters and Er ions.

Optical Gain

There have been some reports of optical gain in Si nano-crystal systems (produced under optical pumping) [13,14]. The model that has emerged to explain this phenomenon relies on an effective four level system based on the Si=O defect luminescence centre [107]. This is easily depicted on the configuration coordinate diagram (Figure 3.5); the x-axis represents the separation between the bonded Si and O atom.

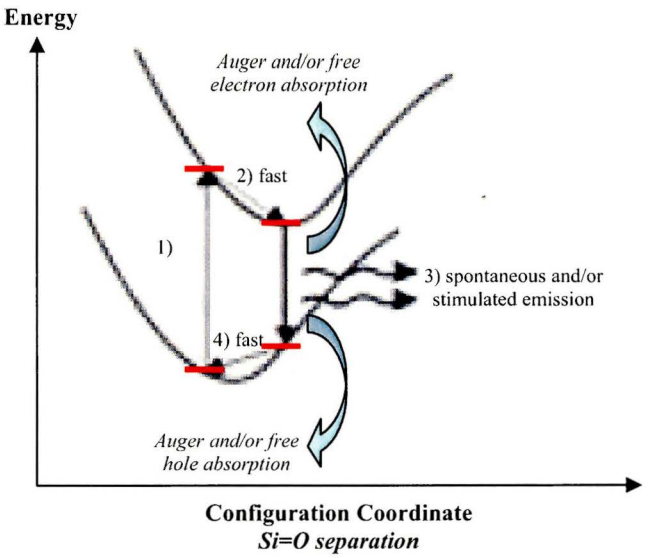

Figure 3.5: Configuration coordinate diagram describing the 4-level mechanism for population inversion in Si nano-crystals containing localized Si=O bond states. Adapted from [107].

Single Si 'Quantum Dot' Linewidth

Si-rich SiO_x films which have been annealed to induce the formation of the nano-structured Si phase always display a smooth and wide PL emission band (typically with a FWHM on the order of 200-300 nm or close to 500 meV).[108] Part of the reason for this is that the PL measurements are typically sampling a large ensemble of nano-clusters and most film preparation techniques give rise to a broad distribution of cluster sizes. The presence of a wide size distribution of Si nano-clusters, reflecting a spread of quantum confined emission energies constitutes a source of considerable inhomogeneous broadening. This is the main reason that the PL emission/absorption spectra do not permit the resolution of the discrete features one would expect from quantum dot luminescence. However,

[108] This is obviously not characteristic of quantum dots, which should display sharp atomic-like transitions in accordance with the near Dirac delta function density of states.

even studies of individually addressable single Si quantum dots[109] revealed room temperature single dot PL linewidths of 120-150 meV [108]. Such large broadening could be possible if the transitions were predominantly phonon assisted. Alternatively, this might be due to the presence of *multiple* oxygen related surface states such as Si=O bonds, giving rise to a quasi-band of luminescent states on a single dot [105,106]. However, these same dots at 35 K demonstrated PL linewidths as sharp as 2 meV (which is below k_BT and therefore indicates true quantum dot effects as discussed previously) [108]. Interestingly, *some* of these spectra also revealed slightly broader satellite peaks at either 6 or 60 meV from the main peak – which did not vary with dot size. The latter was ascribed to the participation of the Si TO phonon (at the Γ point) in the emission process. The 6 meV satellite was ascribed to torsional or spheroidal phonon modes of a Si nano-cluster. The presence of phonon assisted emission is indicative of the presence of an indirect band gap transition which indicates that the carriers (and wave functions) are delocalized throughout the dot; the zero-phonon lines suggest a direct transition such as might result from the breakdown of k-conservation at small dimensions *or* carrier recombination at a highly localized site such as a trap. Importantly, there was no apparent trend for the ratio of phonon assisted to zero-phonon PL emission peaks as a function of dot size – which one might have expected based on a pure mechanism of quantum confined free exciton recombination. This suggests that local differences in the dot environment including the dot geometry, and particularly strain and defects present at the interface, can alter the PL emission mechanism even for a range of dot sizes. The emission energy, however, was characteristic of the dot size. Interestingly, the PL quantum efficiency of a single luminescent dot was estimated to be as high as 35% at room temperature, however only a small fraction of the fabricated dots were luminescent.

---

[109] Single Si quantum dots have been produced by electron beam lithography of Si, followed by plasma etching and final size reduction by controlled oxidation (See: I. Sychugov, et. al., Phys. Rev. Lett. **94**, 087405 (2005)).

It is worth noting, on the subject of the difficulty of producing mono-disperse distributions of Si quantum dots, a recent technique that has significantly reduced the problem [109]. The technique involves the deposition, by reactive evaporation, of a superlattice consisting of alternating layers of SiO_2 (2-6 nm thick) and amorphous SiO (2-3 nm thick). High temperature annealing induces the break-up of the amorphous SiO layers into planar distributions of nano-clusters, with critical dimension being the layer thickness, which show extremely low size dispersion. Transmission electron microscopy indicates that the clusters are highly ordered (and highly spherical), which addresses the issue of the random location, spacing and geometry of the clusters that is typical with standard preparation techniques. Er implantation can be used to dope the superlattices [17]. These films have proven useful in the study of the nano-cluster and Er related luminescence mechanisms because they remove many of the variables and complimentary mechanisms at which complicate things in non-uniform films.

The larger than expected linewidth of single Si quantum dots has an extremely important consequence for Er sensitization by the Förster transfer process (discussed below). It has been argued that Si quantum dots do not meet the spectral overlap requirements (between donor and acceptor species) of efficient Förster transfer because the DOS in a nano-cluster should theoretically approach a Dirac delta function while the linewidths of Er^{3+} absorption manifolds are only on the order of 100 cm^{-1} with spacing of 2000-3000 cm^{-1} [110]. However, if the Si clusters actually have anomalously large emission linewidths owing to phonon broadening, then the spectral overlap with Er^{3+} may not be problematic.

Temperature Quenching

It has already been noted that luminescence in bulk Si is subject to severe temperature quenching. This effect is significantly reduced in Si nano-clusters. Increasing the temperature from 80 to 300 K in superlattice films with size-

controlled clusters typically decreases the PL by a factor of 3; this is a relatively small temperature quenching [17].[110]

The degree of temperature quenching of the PL emission at 1.54 μm of the Er^{3+} ion in a Si-rich SiO_x host has been found to be the same, or even less than that corresponding to the un-doped material [17,111]. This represents a significant improvement over Er in bulk Si.

Luminescence Decay Time

One of the most controversial results in the study of the luminescence mechanism of Si nano-clusters is the stretched exponential form of the PL decay time:

$$I_{PL}(t) = I_o \exp\{-(t/\tau_o)^{\beta}\} \tag{3.8}$$

in which β, known as the dispersion parameter, is less than unity (stretched exponential), τ_o is the mean lifetime and I_o is the initial PL intensity. The mean lifetime is found to decrease with increasing photon emission energy and is typically near 10-100 μs [112,113] (this lifetime is much longer than common direct band gap nano-clusters such as CdTe). This trend is indicative of the increased probability of radiative recombination in smaller Si nano-clusters. In Si-rich SiO_x the value of β does not vary significantly with mean cluster size. The stretched exponential is actually typical in systems with a high degree of disorder. Physically, it means that a distribution of decay rates is simultaneously present. It has been popularly taken as evidence of a transfer of charges [114] or energy between sites of carrier generation and recombination. It is suggested that there is a preferential [non-radiative] energy transfer/migration from smaller nano-clusters to their larger counterparts [115,116]. Another factor is thought to be the large

[110] Paradoxically, however, the PL decreases by 30 per cent in going from 8 to 80 K. This has been explained on the basis of the electron-hole exchange splitting of the exciton energy level into a singlet and triplet state with the triplet state having a lower energy and much lower radiative rate. The increasing tendency to populate *only* the triplet state at low temperatures thus reduces the PL emission (M. L. Brongersma, et. al., Appl. Phys. Lett. **76**, 351 (2000)). This effect was not observed for the Er^{3+} emission at 1.54μm in this host.

linewidth of individual Si quantum dots described above since this gives rise to a distribution of decay rates. Furthermore, a single sample may have multiple clusters with the same size but different surface passivations and therefore different decay properties. The fact that different clusters may be experiencing different strains, may be subject to different non-radiative processes, or simply have different geometrical shapes will contribute as well [112]. Finally, differences in the local optical density of states and charge trapping at defects leading to intermittent PL blinking in a single dot [113] could all be additional factors.

Charge transfer between nano-clusters is an important phenomenon in relation to Er sensitization because it would represent a competing pathway for cluster de-excitation; and larger nano-clusters may be less efficient sensitizers of the Er in any case. Such an energy transfer between clusters will clearly be enhanced as the cluster spacing decreases. This could be particularly important at low annealing temperatures (near 800 °C for example) at which there is evidence that the partially phase separated nano-structured Si network may be highly interconnected.

Crystalline versus Amorphous Nano-clusters

Much of the literature in the field claims to be researching Si nano-crystals. Evidence on the actual phase of the excess Si is generally gained from TEM imaging [117], x-ray diffraction [118], or Raman scattering spectroscopy [119,120]. The nano-crystal claim may not always be completely accurate since there is evidence that even at the common anneal temperature of 1100 °C, a significant fraction of the excess Si remains in an amorphous phase [117]. The extent of the crystalline quality of the clusters can affect their propensity to form defect states including luminescent surface states. Careful control of the crysallinity of Si nano-clusters can ensure that they luminesce by radiative recombination of excitons *within* the cluster instead of at a surface Si=O bond for

example. This has been achieved in plasma-processed films subsequently annealed in N_2 by using low Si excess concentrations but higher anneal temperatures (~1250 °C) [79]. It should be noted that almost all of the theoretical work to date on Si nano-structures has considered nano-*crystals* only.

As previously discussed for *a*-Si, one can identify extended electronic states (similar to *c*-Si) in addition to the presence of numerous defects which can be categorized as being either weakly or strongly localized in space. In the nano-cluster regime, these defects respond to quantum confinement. Theoretical work [121] on *a*-Si nano-clusters has indicated that for the unhydrogenated case, the extended states blue-shift with decreasing cluster size, albeit to a lesser extent than their crystalline equivalent. Weakly localized states also blue shift and nearly blend with the band gap defined by the extended states. The size must decrease well below 2 nm before the highly localized states begin to show significant blue shifting and become indistinguishable from the band edges. For the fully hydrogenated case, the blue shifting is, in general, more severe, and very close to that of nano-crystals. The highly localized states are almost entirely gone by 2.5 nm. Radiative recombination rates are found to be similar to that of nano-crystals for small (1 nm) clusters, but two orders of magnitude faster for the larger clusters. The larger clusters exhibit greater disorder and consequent breaking of dipole transition forbidding symmetries; the quasi-direct transition should be correspondingly faster.

One might expect that the ratio of radiative to non-radiative clusters would increase with crystallinity since amorphous clusters should have a greater probability of containing a non-radiative defect. Even if the defect states are very near the band edges, they may still constitute non-radiative recombination centers.

The crystallinity of Si nano-clusters does not seem to be an important factor in their ability to sensitize Er luminescence [122]. However, there is some experimental evidence that a crystalline nano-cluster may have the ability to

interact with Er over a larger separation distance than amorphous clusters (approximately 2.6 nm versus 0.4 nm) [123].

Cluster Size Effects

The experimental observation of the effects of cluster size on their optical emission/absorption cross-section or efficiency are sometimes misleading because the literature does not often account for changes in the absorbance of the films due to variations in the number density of clusters; the same could be said of the luminescence intensity relative to the number of emitting centres. However, in a size-controlled cluster distribution, it has been found that smaller Si nano-clusters exhibit a higher probability of radiative recombination of photogenerated carriers [17]. This is consistent with the progressive relaxation of the k selection rule as well as the increase in oscillator strength (as previously discussed) [124]. Smaller clusters are also found to exhibit faster luminescence decay time [125]. This is consistent with an increasingly direct transition (direct band gap quantum dots exhibit extremely fast lifetimes which decrease further with decreasing dot size).

In a separate study that actually applied depth-resolved PL to investigate the depth distribution of nano-clusters, it was found that the smallest nano-clusters formed in the region at the film surface or film/substrate interface while larger nano-clusters were predominant in the centre of the film. This was ascribed to two effects: 1) altered nucleation kinetics of Si clusters in the interfacial regions, and 2) dipole-dipole energy transfer from smaller to larger clusters which quenches the luminescence of small clusters in the centre of the film [126].[111]

Larger clusters also induce a faster decay of the Er^{3+} emission at 1.54 μm because they are thought to introduce a greater inhomogeneity of the dielectric

[111] A detailed theoretical (and experimental) study has explained this nano-cluster size/depth distribution on the basis of a dependence of the energy barrier to Si cluster nucleation on the distance from the film/substrate interface. The interesting consequence of this is *a dependence of the nano-cluster PL emission peak energy on the film thickness*; the PL peak was seen to red-shift as the film thickness increased. Furthermore, the experimental data found that the Si-poor region near the film surface actually had a propensity to contain luminescent oxide defects which they ascribed to oxygen vacancies. (See Fang, et. al., Nanotechnology **15**, 494 (2004))

function of the material thereby changing the Er^{3+} spontaneous emission rates [17]; this is particularly true for Er^{3+} located near an interface between materials of two different dielectric function [127] – such as a Si nano-cluster. Furthermore, the interaction between Er^{3+} and Si clusters is stronger for smaller clusters (more efficient energy transfer) at least within the resonant excitation mechanism [124,128,129,130]. This occurs because the luminescence dynamics of small nano-clusters are optimized for this energy transfer (discussed in section 3.4.2); furthermore, in small clusters there is expected to be greater penetration of the Si cluster exciton wave function into the surrounding oxide where the Er is located [131]. When the cluster size becomes too large (estimated at 5 nm in one study) the transfer mechanism is nearly absent [79]. Energy back-transfer from the Er ion to the cluster is also reduced in smaller clusters because of their larger band gap (or surface state recombination energy).

3.4 Luminescence of Nano-structured SiO_x:Er ($x \leq 2$)

3.4.1 Er^{3+} Luminescence near 1.54 μm

An important phenomenon occurs in nano-structured Si-rich SiO_x thin films which are doped with Er: the excess Si (in the nano-structured phase) enables a sensitization of the Er intra-4f shell luminescence, particularly the $^4I_{13/2}$ to $^4I_{15/2}$ transition at a wavelength of 1.54 μm. Given the technological importance of the 1.54 μm wavelength in telecommunications, this is significant from a physics perspective because it is difficult to populate the excited states of Er ions under a direct optical pumping scheme (as is relied upon in fibre applications).[112] The

[112] This difficulty is the result of at least two effects. The first is the extremely narrow absorption linewidth for the intra-4f transitions (resulting from the 5s and 5p electron screening effects). The second is the fact that the intra-4f transitions are only weakly dipole allowed and thereby exhibit correspondingly small optical absorption cross-sections. For example, the optical absorption cross section for resonant excitation of Er in SiO_2 is on the order of $10^{-19} - 10^{-21}$ cm^2. In summary, this means that the optical pumping of Er ions to generate 1.54 μm wavelength photons requires expensive, high-powered, precisely tuned lasers and/or high concentrations of optically active Er. In Si-based materials (Si or SiO_2), however, this latter possibility can be ruled out because of the

sensitized luminescence channel allowing the indirect excitation of Er in Si-rich SiO_x allows for pumping with cheap broadband flash lamps rather than expensive diode lasers because the nano-structured Si phase constitutes a broad-band optical absorber for photons with energy greater than the band gap [132]. In addition, the low direct optical absorption cross-section of Er in SiO_2 can be circumvented because the nanoclusters make up a much larger volume within the sample than does the Er, and the clusters have a much higher optical (and electrical) excitation cross-section (both are greater than 10^{-16} cm^2) [133]. However, Si-rich SiO_x retains the advantage of the wide-band gap of the SiO_2 matrix which successfully suppresses the non-radiative processes that tend to dominate the de-excitation of Er in pure Si – especially at room temperature.[113] The quantification and optimization of the sensitization mechanism is of primary importance and has been the focus of a great deal of research over the past ten years.

It is clear in comparing the Er PL (at 1.54 μm) from a SiO_2 host matrix and a Si-rich SiO_x host that the presence of the excess Si atoms does *something* to sensitize the Er viz. The effective excitation cross section for Er is found to be enhanced by at least three orders of magnitude over Er doped SiO_2 [134]. The introduction of the excess Si produces some kind of defect centres – relating to Si nano-clusters – which are capable of coupling to the Er atoms and transferring excitation either radiatively or non-radiatively. The following will discuss the most recent aspects of the model for this process as developed in the literature; the

---

loss mechanisms that become active when there are too many excited (metastable-state) Er ions in close proximity.

[113] It is instructive to review the mechanism of optical excitation of Er in *c*-Si beginning with the generation of an electron-hole pair by an incident photon with energy greater than the Si band gap of 1.1-1.2 eV. The electron and hole may form an exciton which becomes trapped at an Er related trap state introduced about 150 meV below the bulk Si conduction band edge (the electron and hole may also be trapped sequentially at this state). If the pair recombines (a process which should occur with reasonably high probability owing to the quantum confinement of the electron-hole wave functions in the same region of space in the trap) then the energy can transfer to the nearby Er^{3+} ion by an Auger process. This raises the Er^{3+} directly to the $^4I_{13/2}$ level from which it can radiatively relax to the ground state by emitting a 1.54 μm photon. Only the $^4I_{13/2}$ state can be excited because the band gap of Si (and associated trap state) are too low in energy to excite Er to any higher energy level. As a result, there is a high probability of energy back-transfer to the original Er-related trap state (in addition to free carrier absorption by a conduction band electron).

term "Er luminescence" will refer to the characteristic transition at a wavelength of 1.54 μm.

The current model holds that the Si nano-clusters themselves sensitize the Er through a sequential energy transfer process which is an extension of the intrinsic nano-cluster luminescence mechanism. The basic schematic of the process is illustrated in Figure 3.6.[114] The pump photon is absorbed by the Si nano-cluster through electron-hole pair generation. The electron and hole both undergo a rapid thermalization (typically <1 ns [135])[115] to the conduction and valence band edges respectively or to a trap state. As discussed previously, the formation and trapping of an exciton is determined by the type of surface passivation. The schematic assumes oxygen passivation and electron/hole/exciton trapping at the Si=O double bond. From here, an energy transfer occurs via the interaction of the carriers with the Er ion, whereby the energy of excitation is transferred to a nearby Er ion, annihilating the exciton in the process. This transfer occurs predominantly over a distance of a few nanometres or less to an Er ion outside of the nano-cluster. The time required for the entire process up to this point is on the order of micro-seconds [131] and ≥2 μs [136]. The Er ion is excited to some state likely above the $^4I_{13/2}$ level, which is typically followed by a rapid nonradiative relaxation by phonon cascade to the metastable $^4I_{13/2}$ level. From here, radiative relaxation to the $^4I_{15/2}$ ground state results in the emission of a photon with a wavelength of 1.54 μm. This description represents the ideal process of donor species excitation, energy transfer to an acceptor species, and radiative relaxation of the acceptor. Such processes are well studied in the field of organic luminescence with solutions containing donor and acceptor molecules.

---

[114] Note that the figure makes an assumption about the alignment of the energy levels between the cluster and the Er ion, but this is purely for ease of visualizing the transfer process at this point. Furthermore, the figure makes no attempt to depict the transition linewidths – which are narrow in the case of Er^{3+}.

[115] The thermalization of non-equilibrium carriers in semiconductor nano-clusters may occur slower than in the bulk material because of a decrease in the number of phonons with decreasing numbers of atoms (see P. K. Kashkarov, et. al., Physics of the Solid State, **46**, 104 (2004)). This may help explain why the estimated energy transfer time from Si clusters to Er ions occurs on a time scale of micro-seconds.

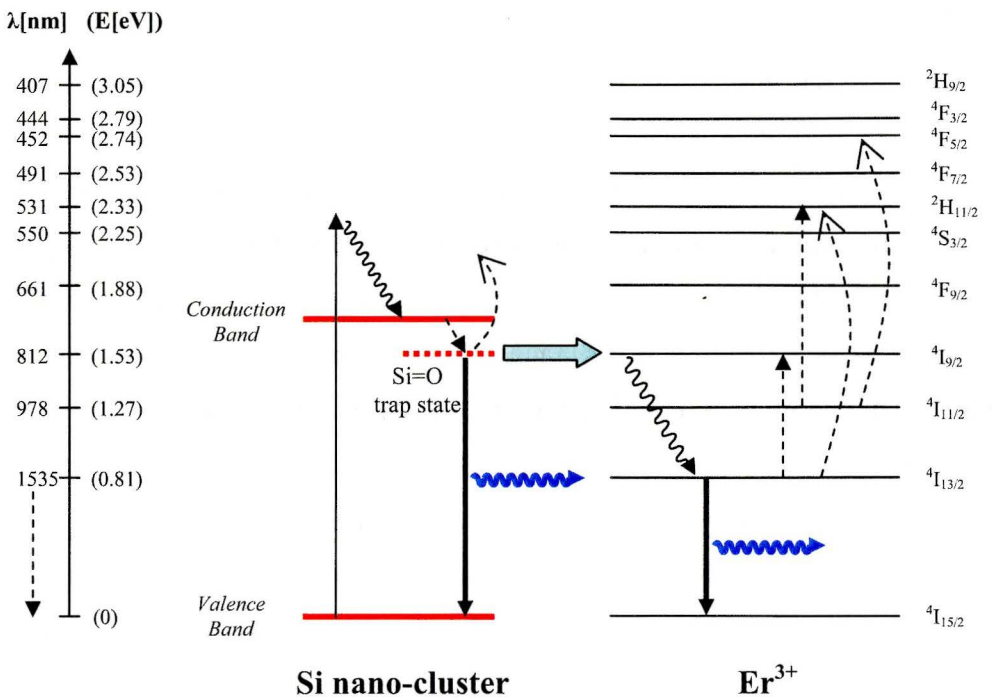

Figure 3.6: Schematic depiction of the mechanism of energy transfer for Si nano-cluster to nearby Er^{3+} ion along with dominant non-radiative processes. The blue corrugated arrows depict possible photon emission; corrugated black arrows depict phonon cascades; curved dash arrows indicate excited state absorption; straight dashed arrows depict common co-operative up-conversion transitions. Adapted from [137].

There are a number of other processes which can occur which detract from the ideal ordering of events just described. First, the Si nano-cluster may be 'darkened' by a non-radiative state which traps the exciton and promotes a relaxation within the cluster by phonon emission.[116] Alternatively, it is possible that even non-radiative defects in the nano-cluster could act as sensitizers for the Er (via an Auger effect), provided the excited state lifetime of the trap is sufficiently long, since the transfer to the Er does not necessarily involve the creation of a real photon.

[116] Evidently, a trap state is non-radiative because its electronic charge distribution is strongly coupled to the lattice, so that it can relax by the emission of phonons with a greater probability (rate) than the most probable radiative relaxation pathway.

term "Er luminescence" will refer to the characteristic transition at a wavelength of 1.54 μm.

The current model holds that the Si nano-clusters themselves sensitize the Er through a sequential energy transfer process which is an extension of the intrinsic nano-cluster luminescence mechanism. The basic schematic of the process is illustrated in Figure 3.6.[114] The pump photon is absorbed by the Si nano-cluster through electron-hole pair generation. The electron and hole both undergo a rapid thermalization (typically <1 ns [135])[115] to the conduction and valence band edges respectively or to a trap state. As discussed previously, the formation and trapping of an exciton is determined by the type of surface passivation. The schematic assumes oxygen passivation and electron/hole/exciton trapping at the Si=O double bond. From here, an energy transfer occurs via the interaction of the carriers with the Er ion, whereby the energy of excitation is transferred to a nearby Er ion, annihilating the exciton in the process. This transfer occurs predominantly over a distance of a few nanometres or less to an Er ion outside of the nano-cluster. The time required for the entire process up to this point is on the order of micro-seconds [131] and ≥2 μs [136]. The Er ion is excited to some state likely above the $^4I_{13/2}$ level, which is typically followed by a rapid nonradiative relaxation by phonon cascade to the metastable $^4I_{13/2}$ level. From here, radiative relaxation to the $^4I_{15/2}$ ground state results in the emission of a photon with a wavelength of 1.54 μm. This description represents the ideal process of donor species excitation, energy transfer to an acceptor species, and radiative relaxation of the acceptor. Such processes are well studied in the field of organic luminescence with solutions containing donor and acceptor molecules.

---

[114] Note that the figure makes an assumption about the alignment of the energy levels between the cluster and the Er ion, but this is purely for ease of visualizing the transfer process at this point. Furthermore, the figure makes no attempt to depict the transition linewidths – which are narrow in the case of Er^{3+}.

[115] The thermalization of non-equilibrium carriers in semiconductor nano-clusters may occur slower than in the bulk material because of a decrease in the number of phonons with decreasing numbers of atoms (see P. K. Kashkarov, et. al., Physics of the Solid State, **46**, 104 (2004)). This may help explain why the estimated energy transfer time from Si clusters to Er ions occurs on a time scale of micro-seconds.

Secondly, after the Er^{3+} is excited but before complete relaxation to the $^4I_{13/2}$ state, the ion may suffer a 'back-transfer' of the excitation energy, either radiatively or non-radiatively (via an Auger mechanism), to a surrounding Si nano-cluster trap state (or host matrix defect) by generation of an exciton. The back-transfer could even occur through excited state absorption of free or trapped carriers in the nano-cluster. This is very much analogous to the Auger absorption mechanism of de-excitation that plagues Er luminescence in a *c*-Si host. The probability of energy back-transfer, and indeed any of the mechanisms which give rise to temperature quenching of Er luminescence in *c*-Si, is inversely proportional to the band gap of the host matrix. This is because a host with a wider band gap forms higher energy excitons. In the initial excitation process, these are capable of exciting the Er to a higher energy level. The higher the Er energy level, the faster the subsequent non-radiative relaxation by phonon cascade occurs (as previously explained). Once the Er has relaxed to some energy level below the host excitonic band gap, there is little possibility for energy back-transfer without phonon involvement or some prior higher order up-conversion process. For example, in comparison with *c*-Si (band gap near 1.1 eV), GaN (band gap near 3.39 eV) is a superior host for increasing Er^{3+} luminescence. Even *a*-Si (optical gap near 1.4-1.6 eV) is superior to *c*-Si. The Si-rich SiO_x system is also superior to bulk Si. In this case, not only does the intervening SiO_x material have a large band gap (*a*-SiO_2 has a band gap greater than 8 eV) but the Si nano-clusters themselves exhibit an enlarged band gap – or luminescent trap state energy – owing to quantum confinement effects. One further point to be noted here is that the problem of free carrier absorption of emitted photons, which is extremely active in bulk Si, is almost non-existent in the wide-band gap Si-rich SiO_x. The result, as confirmed by experiment, is a much less severe temperature quenching than observed for Er doped crystalline Si [5].

Aside from energy back-transfer, the excited Er ion can, itself, undergo a variety of parasitic interaction processes which tend to depopulate the $^4I_{13/2}$ level.

Four such non-radiative processes along with excited state absorption and standard phonon relaxation are depicted in Figure 3.7 [68]. The energy levels are labelled to provide the simplest examples of those transitions that are particularly relevant for the 1.54 μm emission; numerous other excited states can undergo analogous transitions although these are usually of higher order.

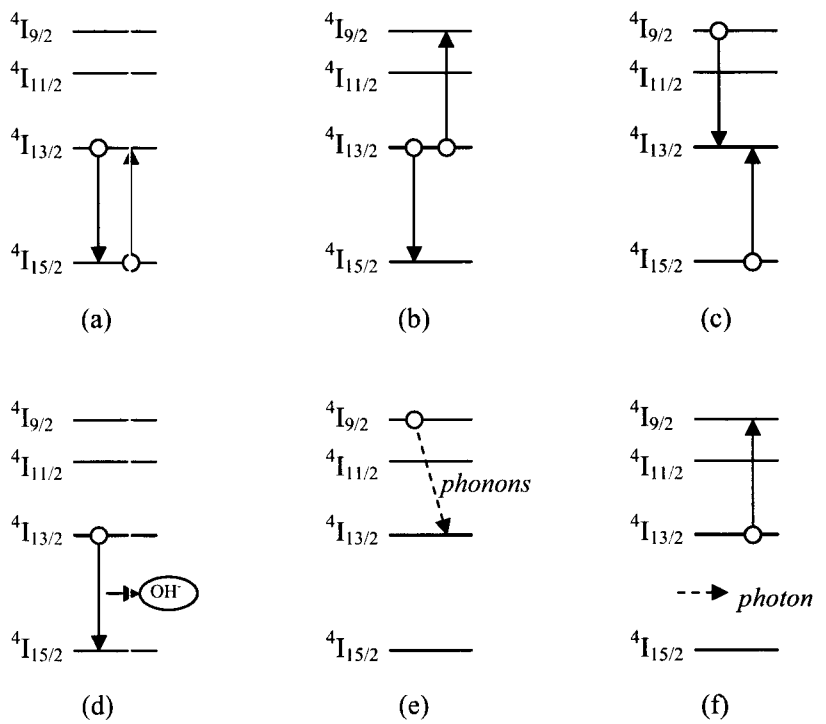

Figure 3.7: (a) energy migration, (b) co-operative up-conversion, (c) cross-relaxation, (d) quenching at impurity such as the hydroxyl ion, (e) phonon relaxation [cascade], (f) excited state absorption of a photon; the open circle represents the initial state of the Er ion(s).

Energy migration occurs when the excitation energy transfers resonantly from the excited ion to a nearby ground state ion. If the Er ions are sufficiently close to each other throughout a sample, the energy of a single excitation can migrate over thousands of Er ions. Clustered Er complexes can provide a favourable environment for significant migrations. Such migration of the energy increases the probability that the energy will be lost at an impurity site – such as the

hydroxyl ion which absorbs strongly near 1.54 μm (depicted in Figure 3.7(d)). There must be at least a small concentration of non-radiative (quenching) sites present in order to observe a shortening of the Er^{3+} luminescence decay rate in a film. *Co-operative up-conversion* occurs between two ions when both are initially in the excited state and one relaxes by promoting the other to a higher energy level; the effect appears experimentally as an increase of the Er luminescence decay rate (with increasing Er concentration). Note that if the Er-Er coupling is particularly strong (ie. beyond a certain high Er concentration), no effect on the Er excited state decay rate will be seen; in this case, the effect is termed *pair-induced quenching* [138]. Higher order up-conversion can occur through the involvement of several ions in various excited states. Processes of third and higher order can even populate levels corresponding to blue and violet transitions. *Cross-relaxation* occurs when one ion in a doubly excited state relaxes to a lower excited state and promotes another ion to the same or a lower energy state.

The processes just described occur primarily through resonant *non-radiative* ion-ion multi-polar interactions. These are the result of the interaction of the electric and magnetic fields emanating from the charge distribution on the ions. Er has a unique propensity to undergo ion-ion interactions for several reasons. First, the Er^{3+} projects a strong cationic field. Second, a review of the Er 4f energy level structure will reveal that there are many resonant energy level *spacings* between different excited states so that they can couple easily to each other. Second, being only weakly dipole allowed, the intra-4f excited states are all reasonably long. For example, the $^4I_{13/2}$ level of the Er^{3+} ion is metastable, having a lifetime on the order of milliseconds; even the higher excited states can exhibit lifetimes of several micro-seconds, which is slow in luminescence theory. Thus, it is possible to have many Er ions simultaneously in an excited energy

manifold from which interactions may occur.[117] These same factors also enhance excited state absorption (ESA) whereby an Er ion absorbs a real photon while already in an excited state. Generally speaking, these ion-ion interactions and ESA are undesirable because they waste excitation energy through phonon cascades. Furthermore, they depopulate the metastable level which is necessary for optical gain/emission at the desired 1.54 μm wavelength. Increasing the Er concentration in the material decreases the Er–Er spacing and so increases the ion-ion interactions since there is greater ion field overlap. This phenomenon of the enhancement of non-radiative losses with increasing ion concentration is typically referred to as *concentration quenching*. It places an upper limit on the quantity of useful Er that can be incorporated in an optical device. Figure 3.6 depicts only a few of the ion-ion interactions which can occur among and within Er ions. Excited state absorption is indicated by a dashed curve, while up-conversion processes are indicated by a dashed line. Phonon relaxation is indicated by a jagged line.

The extent to which the excited electronic states of Er^{3+} can relax non-radiatively by exciting vibrations within the host network is strongly dependent on the Er energy level spacing and the highest energy vibration (phonon) of the host matrix [75]. The energy level spacing, *particularly that between adjacent levels*, determines the number of phonons required to bridge the gap. The smaller the energy gap, the fewer phonons that are required, the higher will be the probability of such non-radiative decay of the excited state and the faster it will occur. The multiphonon relaxation rate has an approximately exponential dependence on the energy gap.[118] The effect of the multiphonon relaxation rate on the excited state lifetime can be easily seen. In general, the excited state lifetime τ_a is given by [139]:

---

[117] This is the same reason that population inversion is easily achieved in many erbium doped glasses.

[118] In essence, if any more than three phonons are required to bridge the gap, each additionally required phonon constitutes a higher order (lower probability) process.

$$\frac{1}{\tau_a} = \sum_b (A_{ab} + W_{ab}) = \sum_b \left(\frac{1}{\tau_{rad(a \to b)}} + \frac{1}{\tau_{non-rad(a \to b)}} \right) \tag{3.9}$$

where A_{ab} is the radiative transition probability (it is non-zero for all Er^{3+} intra-4f transitions) and W_{ab} is the non-radiative transition probability from level *a* to level *b*; the summation is over *all* terminal levels *b*. The non-radiative transition probability includes *all* non-radiative de-excitation pathways: multiphonon relaxation plus all of the ion-ion interactions and energy migration mechanisms discussed above. When the energy gap to the next-lower level is small, $W_{phonon} >> A_{ab}$ and there is little chance of observing the optical transition; the lifetime τ_a is relatively short. In principle, the luminescence decay trace is an approximately exponential function of time, based on the lifetime of the slowest step in a multi-step de-excitation. There will be an inevitable stretching of this exponential relationship when many non-equivalent Er sites are present in a sample and the host is highly disordered; in this case, the different sites will be characterized by different vibrational energies and coupling strengths.

The highest energy phonons that the host matrix will sustain (of which the most energetic defines the *cut-off energy*) are the most important in the non-radiative relaxation because they can conserve energy with lowest order process [139]. In general, if the phonon cut-off energy is greater than 25 percent of the energy gap between two levels of the Er ion, then the corresponding luminescence will be completely quenched because W_{ab} is large [68]. For cut-off energies between 10-25 percent, the quenching will induce a temperature dependence in the luminescence lifetime (recall that the higher the probability of non-radiative relaxation, the shorter the excited state lifetime; lower temperature implies fewer high energy phonons). Finally, for cut-off energies below this, relaxation by phonon cascade will be negligible. The 1.54 μm transition corresponds to an energy of 6500 cm^{-1} while the phonon cut-off energy for SiO_2 is about 1100 cm^{-1} so that the phonon quenching will be small at room temperature. This does not mean that the same reasoning applies to transitions to ground from the higher

energy levels of the Er^{3+} ion because the *adjacent energy level spacing* is the critical parameter, *not* necessarily the spacing to the ground level. An inspection of the adjacent energy level spacing in Er^{3+} will reveal that most levels are only separated by a gap of 2000-3000 cm^{-1}. This is easily bridged by two or three high energy phonons in SiO_2. Thus, if an Er^{3+} is excited to a high-lying level, it will simply undergo multiphonon cascade through the various energy levels sequentially all the way to the $^4I_{13/2}$ level. Only there will the condition $A_{ab}>>W_{ab}$ be met (in fact, W_{ab} is almost zero). Experimentally, few glassy networks exhibit any radiative transitions of Er^{3+} other than that at 1.54 μm. Some typical multiphonon decay rates for Er^{3+} transitions are given in Table 3.1:

Initial Energy Level	Final Energy Level	Energy Gap [cm^{-1}]	Multiphonon decay rate [s^{-1}]	Multiphonon Decay Time
$^4F_{9/2}$	$^4I_{9/2}$	~ 2000	~ 2 x 10^7	~ 0.1 μs
$^4S_{3/2}$	$^4F_{9/2}$	~ 3000	~ 1 x 10^6	~ 1 μs
$^4I_{11/2}$	$^4I_{13/2}$	~ 3700	~ 1 x 10^5	~ 10 μs*

* This relaxation time has also been estimated at 2.5 μs in [140].

Table 3.1: Multi-phonon decay rates for a series of transitions in the Er^{3+} ion. From [139].

Crystalline semiconductors tend to have much lower phonon cut-off energies than glasses. Optically active Er in these networks commonly exhibits visible luminescence (unless the semiconductor is Si, in which case it is dominated by other un-related non-radiative processes). For example, GaN has a phonon cut-off energy near 750 cm^{-1} and commonly emits at the Er^{3+} visible transitions [141,142].

3.4.2 Energy Transfer From Si Nano-clusters to Er^{3+} Ions

The mechanism of the energy transfer from an excited Si nano-cluster to an Er^{3+} ion has proven to be a very difficult process to isolate experimentally. The

SiO_x:Er material structure is pathological to begin with and seems to give rise to multiple simultaneous energy transfer mechanisms; and, there may be more than one type of sensitizing centre. Furthermore, the mechanism is sensitive to the film composition, method and conditions of deposition, subsequent heat treatment, and even the specifics of the optical characterization techniques used; these vary significantly between research groups and can make cross-comparison of results within the literature problematic. The de-convolution of the energy transfer mechanisms is especially prone to debate. It is in this context that the use of the Er doped SiO_x/SiO_2 superlattices is probably providing some of the most sensible information because of the much enhanced control of the film microstructure. As of the time of writing of this document, there appears to be a general consensus that much of the transfer occurs resonantly via a Förster-Dexter mechanism.

Förster-Dexter Energy Transfer

To this point, Er^{3+} ion-ion interactions have been identified only in the context of parasitic coupling between multiple Er^{3+} ions (homotransfer). In fact, these interactions can also take place between an Er^{3+} ion and another luminescence centre (or non-radiative centre) involving a different species (heterotransfer) [143].[119] This interaction has been identified as one of the mechanisms by which an excited Si nano-cluster can transfer energy to an Er^{3+} ion located outside the cluster.[120] The energy exchange mechanism is referred to as a Förster-Dexter transfer.

The Förster-Dexter formalism addresses the *quantum mechanical resonant interactions of the multi-polar electromagnetic fields* between a donor species (eg. exciton in a Si nano-cluster) and an acceptor species (eg. Er^{3+} ion) through the

[119] For example, ytterbium is often added as a co-dopant alongside the Er in alumina or silica hosts to take advantage of the energy transfer from Yb^{3+} to Er^{3+} and inhibited Er clustering.

[120] It has also been identified as a mechanism of energy transfer between semiconductor nano-clusters (See: A. J. Kenyon and F. Lucarz, Electrochem. Soc. Proc. **2004-13**, 255 (2005)).

exchange of virtual photons.[121] The Förster model addresses the electric dipole-dipole interaction, while the Dexter model is an extension which includes higher order multipole-multipole interactions as well as the exchange interaction [144].[122]

Within the Dexter exchange mechansism,[123] the donor and acceptor actually exchange electrons; the donor's excited electron enters the acceptor excited state with which it is resonant, and the the acceptor's lower energy electron enters the donor's lower energy state with which it is resonant. The transfer probability is given by [144]:

$$k^{Dexter} = KJe^{-\frac{2R_{DA}}{L}} \tag{3.10}$$

where J is the normalized overlap integral of the donor emission and acceptor absorption spectra, R_{DA} is the donor-acceptor separation, L is the effective average Bohr radius for the excited and unexcited states of the donor and acceptor, and K is a constant that includes wave function cancellation effects. As equation (3.10) reveals, the Dexter exchange interaction is only significant at short separation values R_{DA} in which the donor and acceptor wave functions actually overlap (usually implying less than 1 nm of separation). In the SiO_x:Er system, the Dexter mechanism is thought to require the Er^{3+} to be extremely close to the Si cluster because the strong quantum confinement in the cluster allows only small wave function penetration into the surrounding SiO_x; furthermore, the wave functions of the Er^{3+} 4f electrons are highly localized.

---

[121] Because the transfer involves *virtual photons*, Förster transfer is not sensitive to the local optical density of states at the transition energy of the Er^{3+} ion. This is not true of the spontaneous emission rate. See: de Dood et. al., Phys. Rev. B **71**, 115102 (2005).

[122] It is worth noting that energy transfer by ion-ion interactions has been given a more global sophisticated treatment by Inokuti-Hirayama theory (M. Inokuti and F. Hirayama, J. Chem. Phys. **43**, 1978 (1965)) however the corrections to the Förster theory appear primarily in the higher order couplings.

[123] This is not Coulombic/electrostatic in nature but arises from the requirement of an anti-symmetric wave function of the donor-acceptor system.

In the simplest conception of the Förster interaction (also known as non-radiative resonance energy transfer – RET), one begins with the generation of a transition dipole moment (oscillating electric dipole) in the donor, which may occur by the absorption of an incident photon [145]. This dipole moment induces a transition dipole moment in the nearby acceptor, thereby raising it to an excited state. The acceptor induced dipole interacts with the oscillating electric field of the donor in the same way that it would with an electromagnetic wave.[124] In the case of the Si nano-cluster/Er system, the quantum mechanical oscillation of the dipole moments gradually transfers the excitation energy completely to the acceptor species. The transfer is non-radiative in the sense that it is mediated solely by virtual photons through the Coulomb interaction.

The electric field E_1 of the exciton (electron-hole) dipole having moment μ_1 is given by:

$$\vec{E_1} = \frac{3\vec{n}(\vec{\mu_1} \bullet \vec{n}) - \vec{\mu_1}}{r^3} \tag{3.11}$$

where n is the unit vector in the direction of r, and r is the donor-acceptor separation distance. This electric field induces a dipole moment μ_2 in the Er^{3+} ion, which generates an electric field E_2 analogous to E_1. The interaction energy W between these two dipoles is given by:

$$W = -\vec{\mu_1} \bullet \vec{E_2} = \frac{\alpha}{r^6} \tag{3.12}$$

where α is a constant of proportionality. Consideration of higher order interactions of the multi-polar fields (such as dipole-induced quadrupole or quadrupole-induced quadrupole) is not usually necessary because their coupling strength decreases much more rapidly with separation distance.

---

[124] The most sensible classical analogy would be that of two coupled springs. Initially, one spring is excited such that its energy of excitation is gradually transferred completely to the other spring (and vice versa indefinitely if there are no loss mechanisms – a phenomenon tantamount to energy backtransfer).

The rate of energy transfer (which has the same dependence on the donor-acceptor separation as the interaction energy) can be expressed as follows:

$$k^{Forster} = \left(\frac{\Phi_D}{\tau_D}\right)(const.)\left(\frac{J}{n^4 r^6}\right) \tag{3.13}$$

where Φ_D and τ_D are the luminescence quantum yield and excited state lifetime of the donor in the absence of the acceptor, I is the spectral overlap between the donor emission spectrum and the acceptor absorption spectrum, n is the index of refraction.[125] Since a high value of $k^{Forster}$ implies a high probability for the energy transfer, it is clear that donor-acceptor spectral overlap is a critical parameter, along with a highly luminescent and short-lived donor,[126] as well as small donor-acceptor separation. This provides some indication of why Er^{3+} ions have a propensity to couple *to each other* in this way despite having extremely narrow linewidths. Recall from the configuration coordinate model that the Huang-Rhys parameter is less than unity for rare-earth ions. The resultant high concentration of energy states in the zero-phonon region between emission and absorption spectra is tantamount to a high spectral overlap between donor and acceptor for the homotransfer.

From equation (3.13), a critical parameter known as the 'Förster radius' is defined, which is the distance at which the transfer probability is 50 percent [146]. This defines an interaction volume around the Si nano-cluster in which the Er^{3+} ion must be located to undergo induced dipole excitation with any reasonable probability. Beyond this region, the lower probability of Förster interaction means that energy transfer becomes progressively more likely to take place only through uncorrelated events of real photon emission and re-absorption by the

---

[125] The origin of the index of refraction as a variable in this equation lies in the dielectric screening of the dipole-dipole coupling by the medium separating the donor and acceptor.

[126] The requirement of a highly luminescent and short-lived donor confirms that small nano-clusters should be more efficient sensitizers than larger ones; smaller clusters exhibit increased oscillator strength and shorter lifetimes as previously discussed (see: J. Heitmann, et. al., Mat. Sci. Eng. B **105**, 214 (2003)).

relevant species.[127] This region is aptly referred to as the radiation zone. Reabsorption is expected to be a negligible effect in Er doped SiO_x because of the extremely small absorption cross-section of Er^{3+} under resonant optical excitation.

In theory, the Förster radius can be estimated by comparing the lifetime of the Si nano-cluster luminescence both with and without Er doping [145,147]. It has been found to be between 1-1.5 nm for Er concentrations ranging from 0.02-1 atomic percent. This is a very short Förster radius and implies that only those Er^{3+} ions on or near the surface of a Si nano-cluster may be efficiently excited by this indirect mechanism. However, in this experiment, one must make the assumption that the observed nano-cluster emission in the doped system comes from clusters coupled to Er. This introduces an unresolved issue: can a Si nano-cluster *strongly* coupled to Er still emit its own characteristic luminescence, or does it become dark – inhibited from further radiative emission while in the presence of even a single Er ion? The "dark" nano-cluster hypothesis was first proposed [138,148] to explain the observed [149] lack of change in the cluster luminescence lifetime between Si-rich SiO_x with and without Er (despite the classic observation of instrinsic Si nano-cluster photoluminescence quenching);[128,129] however, this study considered only extremely small Er concentration. Subsequent studies [125,145] have found exactly the opposite

---

[127] Energy transfer by real photon emission and re-absorption can be viewed, in this context, as the limiting case of a Förster transfer under the condition of a large donor-acceptor separation distance. Consider that electromagnetic interactions between atoms refer, quantum electrodynamically, to the exchange of photons. The photon states that mediate these interactions are virtual states having a finite lifetime and therefore finite energy spread ($\Delta E \Delta t \geq \hbar$). Since the photon lifetime Δt is approximately the time-of-flight r/c between the two atoms (c is the speed of light), one has that $\Delta E \geq \hbar c/r$. In the far-field, where $r >> \hbar c/\Delta E$, one has that $\Delta E << E_o$ (E_o is the central energy in the photon wave packet), so that the energy transfer effectively describes a process of emission and re-absorption by a *real* photon. (See: de Dood, et. al., Phys. Rev. B **71**, 115102 (2005)).

[128] The first argument in favour of Si nano-cluster/Er coupling is the observation of a progressive quenching of the intrinsic Si cluster luminescence with increasing Er concentration. In principle, one should therefore observe a decrease in the Si cluster luminescence decay time because nearby Er would represent an additional, competing (possibly preferential), [non-radiative] de-excitation pathway with a transfer time much faster than the intrinsic Si cluster luminescence lifetime. When this was initially not observed, it was referred to as the "lifetime paradox".

[129] The dark nano-cluster hypothesis would suggest that any observed Si nano-cluster luminescence originates from those clusters *not* coupled to Er and so does not show lifetime changes.

result (ie. lifetime quenching was observed with increasing Er concentration), suggesting that nano-clusters that couple to Er may be optically active. This seems feasible, given that the excited state lifetime of Er^{3+} at the $^4I_{13/2}$ level is at least an order of magnitude larger than the lifetime of an excited nano-cluster, so that the cluster should be able to emit several times before the Er de-excites (assuming sufficient photon flux is used for excitation); intensity quenching of the Si nano-cluster luminescence then corresponds to the sequential excitation of increasing numbers of Er ions coupled strongly to a single cluster. But this contradicts the predicted short Förster radius. If the short Förster radius is indeed true, then it implies that only a small fraction of the Er ions can be indirectly excited by dipole-induced dipole interactions with Si nano-clusters. This would suggest that resonantly exciting the Er should produce much more luminescence at 1.54 μm than in the off resonant excitation case – however this is not observed either in a Si-rich SiO_x host (see for example [136]).[130]

There are a few alternative explanations for these results. First, the dark nano-cluster hypothesis may apply only to strongly coupled clusters. It is then an open question whether a class of weakly coupled nano-clusters, whose luminescence is observed, couple according to Förster theory. Second, there is some evidence that there is actually a dual energy transfer mechanism present in a single sample (discussed below), which would mean that using the Si nano-cluster liftetime to probe the Förster radius is erroneous; even the presence of a wide size distribution of Si nano-clusters in the samples used to mesure the Förster radius in reference [145] might invalidate the result. Third, it has been suggested that the dipole-induced dipole interaction is not the main energy transfer mechanism at all.[131] For example, studies which have actually quantified the Si nano-cluster/Er

---

[130] Interestingly, however, it is observed that resonantly pumping Er in a pure glass/SiO_2 host (particularly near 520 nm) does give much more luminescence near 1.54 μm than the same pumping in a Si-rich host (see for example: Falconieri et. al., Opt. Mater. **27**, 884 (2005); Kuritsyn et. al., Appl. Phys. Lett. **83**, 4160 (2003)). This suggests that Si clusters may not be effective in transferring excitation energy to Er ions.

[131] Indeed, throughout most of the literature on Si cluster/Er interactions, the Förster transfer mechanism has been *assumed* based on the physical context of the system. Very few studies have

interaction distance *objectively* (through the use of superlattice structures which can produce a mono-disperse size distribution of Si nano-clusters as well as control the Er location relative to the clusters) have found that the carrier-Er interaction distance is not r^{-6} (as in a Förster transfer) but rather exponential – with characteristic interaction distances of about 0.4-0.5 nm [24,123]. These measurements appear much more consistent with a Dexter transfer. In addition to this, very recent work [150] on imaging of the Er site in doped Si-rich SiO_x thin films has provided an insight into why the resonant excitation of Er in these materials does not enhance the emission at 1.54 μm relative to off-resonant pumping. It was shown that Er tends to prefentially from in clusters *located away from Si-rich regions of the host matrix* such that the approximately ≤10% of the Er ions are actually excitable by Si nano-clusters; and it was also shown that the upper limit on the interaction distance was about 0.6 nm. Therefore, resonantly exciting the Er does not necessarily enable luminescence from those Er ions not coupled to Si nano-clusters since that Er may be located in clusters (which are subject to concentration quenching).

Coupling Strength Regime: Number of Excitable Er Ions per Cluster

Indeed, experimental investigation suggests that there are both strongly and weakly coupled Er with the former characterized by a somewhat shorter luminescence lifetimes [151]. The strongly coupled Er would be that which is extremely close to the cluster (and therefore eligible for excitation by the exchange interaction), while the latter would be that which is more isolated [151] and only eligible for longer range Förster-based excitation. The strong coupling regime would give rise to preferential pairing of an Er^{3+} and Si cluster and permit only one or two Er^{3+} to be excited by the cluster (since the Er^{3+} ion would have to be so close to the cluster). Within the weak coupling regime, any Er^{3+} could be

---

actually sought to *objectively* determine the transfer mechanism. It is difficult to do this without a large degree of control of the film microstructure.

excited by any cluster (in theory) so that one would find that numerous ions (10-100) could be excited by a single Si cluster (no preferential pairing).

Multiple Coupling Mechanisms

It has been suggested that radiative decay measurements in Er doped SiO_x can give erroneous information about the Förster radius because they are sampling at least two distinct Er populations, each experiencing a different energy transfer mechanism. For example, Er^{3+} PL decay trace analysis [140] has revealed that there is a fast energy transfer mechanism (*energy transfer time* of less than 100 ns) and a slow energy transfer mechanism (*energy transfer time* of nearly 1 μs). The ratio of the two processes depends on the Si cluster size and the Er concentration [152]. The fast transfer is assigned to Er^{3+} ions within, at most, 1.5 nm from the Si cluster surface or present inside a Si nano-cluster (recall, however, that Er has a very limited solubility in pure Si leading to a maximum optically active concentration of $3x10^{17}$ cm^{-3} in *c*-Si [68]) wherein they undergo a luminescence mechanism similar to that of Er in *c*-Si (exciton trapping at an Er-related defect trap state followed by Auger excitation of the nearby Er^{3+}); this process is normally subject to severe temperature quenching in bulk Si because of energy back-transfer, but one wonders if it might be more efficient in the nano-clusters owing to the enlarged excitonic band gap. The slow transfer mechanism is assigned to Er^{3+} ions from 1.5-2.5 nm from the Si cluster surface. The dominant transfer mechanism here is assumed to be the Coulombic Förster interaction discussed above. The contribution of the fast process increases with increasing Si content in the SiO_x [152].

Resonant Energy Transfer

In principle, the resonance aspect of the Förster-type Coulombic energy transfer (and even the Dexter transfer) should be observable as spectral dips in the Si nano-cluster luminescence peak (a kind of spectral hole burning) at those energies

corresponding to the resonant absorption bands of the Er^{3+} ion (the dips could be shifted by the relevant Si phonon energy if the cluster has an indirect band gap). This is difficult to observe experimentally because fine structure in the Si nano-cluster PL spectrum tends to be 'washed out' by inhomogeneous broadening (due to the distribution of cluster sizes in a given a sample) and luminescent defect states in amorphous or incompletely crystallized Si clusters. Furthermore, the tendency to use excitation energies much higher than the emission band of the nano-clusters means that a huge proportion of the clusters (both amorphous and crystalline) are eligible to be excited. Resonant excitation of a small fraction of nano-clusters requires the wavelength of the excitation light to be in the PL spectral band [79,140].

Recent studies [79] which used higher than normal anneal temperatures to improve the quantity and quality of crystalline Si clusters (and decrease the fraction emitting via defective surface states) as well as PL excited at cryogenic temperatures have succeeded in observing dips in the PL emission spectra. For Si clusters of 5.8 nm diameter, the cluster PL peak showed a dip at an energy 57 meV below the 1.28 eV absorption transition ($^4I_{15/2}$ to $^4I_{11/2}$) of the Er^{3+} ion with no dip at the resonant energy. This indicates a Si TO phonon assisted resonant transfer to the $^4I_{11/2}$ state from the cluster band gap at 1.28 eV; this means that clusters at this band gap energy have a strongly indirect gap. Alternatively, for a smaller cluster size, there were two dips in the Si cluster PL: one exactly resonant with the 1.55 eV absorption transition from the $^4I_{15/2}$ to $^4I_{9/2}$ level of Er^{3+}, and a second dip was located 57 meV below this.[132] This is evidence of two modes of resonant energy transfer for Si clusters in this region of band gap energy. The first is a quasi-direct nonphonon assisted transfer to Er^{3+}; this is evidence of the breakdown of the *k* selection rule for band-edge optical transitions in these Si

[132] Resonant transfer to this level should not be surprising given that the Si nano-cluster PL emission is usually peaked between 800-850 nm; the $^4I_{9/2}$ Er^{3+} level would therefore correspond to the statistical modal Si cluster emission.

clusters. The second is another TO phonon assisted resonant transfer. The two processes appear to be in competition. No-phonon transfer has the highest rate.

This important study ([79]) provides rare spectroscopic evidence that there is indeed an energy transfer from Si clusters to Er ions, and that this transfer occurs resonantly at least some of the time. This resonant energy transfer may occur both by phonon-assisted and quasi-direct recombination of excitons in the Si nano-cluster. Furthermore, this transfer was found to be non-radiative.

This precisely tuned resonant energy transfer mechanism does not explain why the entire broad Si nano-cluster PL band (which includes clusters of the 'wrong size' to be resonant with Er levels) would be quenched as the Er content increases (and with little change of shape); clearly, there must be a non-resonant mechanism operating as well. Clusters which are not resonant with an Er energy level could meet the energy conservation requirement with the involvement of a combination of optical and acoustic phonons, as necessary, to bridge the gap and add to yield zero momentum [125].[133]

Sensitizers Other Than Si Nano-clusters

There is evidence that Er luminescence may also be sensitized by other defect centres [110] other than Si nano-clusters.[134] The effect has been suggested as a mechanism giving rise to visible transitions of the terbium ion (Tb^{3+}) in Si-rich SiO_x [153,154]. Some of the centres identified as defects in the SiO_2 matrix (see section 3.1.4) have been put forth as possibilities. Concerning those defects that are luminescent, one can see immediately that many have emission bands resonant with the Er^{3+} absorption bands; this meets the first criterion for a Förster transfer. The presence of such defects in the Er-doped Si-rich SiO_x system seems

[133] This observation of "hole-burning" in the measured PL from Si nano-clusters seems to be evidence that they can indeed emit intrinsic luminescence when coupled to nearby Er^{3+} ions.

[134] Various co-dopants such as Yb^{3+} ions and Ag^{+} ions are known to be useful sensitizers that can be added to SiO_x films (A. Polman and F. C. J. M. van Veggel, J. Opt. Soc. Am. B **21**, 871 (2004)). Furthermore, sensitization by host matrix defects in Er-doped GaN (and in Mg co-doped GaN:Er) has been observed (See: Thaik, et. al., Appl. Phys. Lett. **71**, 2641 (1997) and Kim, et. al., Appl. Phys. Lett. **76**, 2403 (2000)).

immediately feasible given the large degree of disorder in the amorphous SiO_x host matrix. Figure 3.8 shows how such a defect could be incorporated into the model proposed in Figure 3.6. The defect provides a relevant absorption band near 325 nm. Transfer both to Er^{3+} ions and nearby Si nano-clusters could be possible with a potential preference for one or the other.

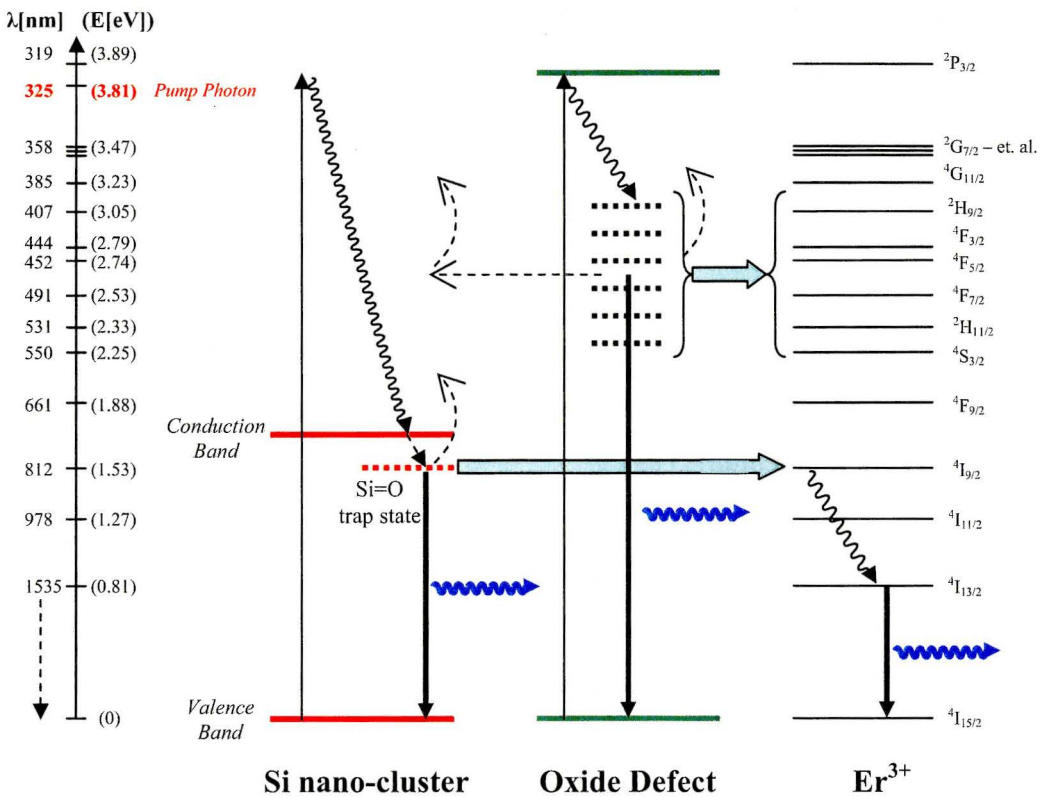

Figure 3.8: Schematic depiction of the presence of both Si nano-cluster *and* luminescent oxide defect centres acting as sensitizers for a nearby Er^{3+} ion. An attempt has been made to identify the relevant Er^{3+} energy levels involved in the transfer.

A related channel of sensitization could also relate to the formation of organic chromophores near Er luminescence centres, the functionalization of organo-lanthanide complexes (resulting from the Er doping with the metal-organic precursor) with various chromophores, or the formation of luminescent organo-

silane compounds [38]. Many organic chromophores have a well-known ability to act as sensitizers of trivalent rare-earth ions (including Er) via a Förster-Dexter transfer from singlet or triplet excitons generated in the molecule (though only the singlet excitons generate an intrinsic luminescence); this is known as the "antenna effect" [155].[135] It is not uncommon to achieve efficient rare-earth PL under pumping with a UV laser since many chromophores have broad absorption bands at UV and violet/blue energies. Organo-lanthanide complexes are often intentionally functionalized with highly absorbing chromophores to enable the antenna effect [156]. Such complexes have exhibited broad luminescence bands between 350-650 nm and sensitized Er^{3+} luminescence at 1.54 μm; low temperature PL under 325 nm excitation reveal sharp spectral dips in these visible PL bands corresponding to at least seven high-lying intra-4f Er^{3+} levels between 377-650 nm, confirming the energy transfer from the ligands [157]. Such organo-lanthanide materials have been specifically engineered for their luminescence properties and have even been applied in organic light emitting diodes [158]. Such sensitization pathways can be included in Figure 3.8 either in place of or in addition to the channel labelled "oxide defect".

[135] The following is a recent critical review article: J.-C. G. Bünzli and C. Piguet, "Taking advantage of luminescent lanthanide ions", *Chem. Soc. Rev.* **34**, 1048 (2005).

Chapter 4

Structural Description and Thermal Evolution of SiO_x:Er ($x \leq 2$) Thin Films

One of the objectives of this study was to connect optical properties to structural properties for the Si-rich SiO_x:Er system deposited by the ECR-PECVD technique. This allows one to engineer the film preparation (deposition and heat treatment) to optimize the structural properties so as to optimize the optical properties. To succeed in this regard requires two questions to be addressed:

1) What is the chemical bonding structure of the as-deposited films and what are the resulting material properties?

2) How does the chemical bonding structure of the films and the resulting material properties change as a result of annealing?

4.1 Chemical Bonding Strucutre of SiO_x ($x \leq 2$)

Consider the first question regarding the as-deposited film. As a first order approximation, disregarding the Er doping, most of the Si and O should be located in a metastable SiO_x phase. From a purely thermodynamic standpoint, most SiO_x compounds with x sufficiently different from *2* do not exist, which is

why they phase separate at high temperatures.[136] Thin film growth by PECVD is, however, intrinsically a non-equilibrium process through which such metastable phases can be formed. A real description of the bond network is complicated but can be resolved into two idealized (through extreme) structural models.

1) **Random Bonding Model (RBM)**: This proposes a uniform SiO_x phase ($x \leq 2$) built from a random distribution of $Si–Si_nO_{4-n}$ ($n=0,1,2,3,4$) tetrahedral bonding units (schematized in Figure 4.1). The statistical distribution of n depends on the quantity of excess Si, being increasingly skewed towards the n=4 value for increasing excess Si. Clearly, the limit of a Dirac-delta distribution at n=4 would correspond to pure Si, while that at n=0 would correspond to pure SiO_2 [159].[137]

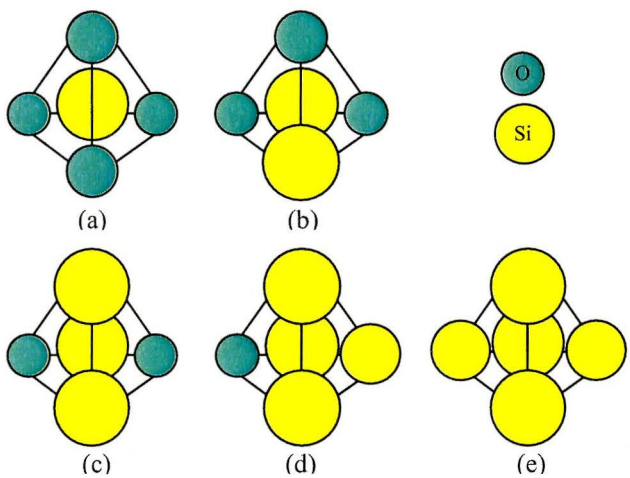

Figure 4.1: Schematic bond diagram depicting various tetrahedral bonding units involving Si and O atoms; linked together at the corners, these units should comprise any purely Si-O based network solid.[138]

---

[136] The SiO_2 network does not readily dissolve excess Si. Low temperature thin film growth can produce a supersaturated SiO_x solution, however this is thermodynamically unstable. Phase separation is kinetically slow at low temperature but speeds up quickly at higher temperature.

[137] X-ray photoelectron spectroscopy has proven to be a useful technique in measuring this statistical distribution (See: van Hapert, et. al., Phys. Rev. B **69**, 245202 (2004)).

[138] Note that no concerted effort has been made to properly schematize the actual size of the Si and O atoms. The sizes would not, in any case, be those corresponding to O^{2-} (radius of 1.4 Å) and

2) **Random Mixture Model (RMM)**: This proposes a mixture of distinct phases built from a random distribution of Si–Si_4 and Si–O_4 tetrahedral bonding units *only* (see Figure 4.1(a) and (e)). This model would accurately describe SiO_x films once they have been annealed [160].

Film Formation and the Resulting Bond Network[139]

During the ECR-PECVD process, the films are produced by quenching[140] the species produced in the oxidation and decomposition of silane on a cool substrate (near 120 °C in this study). The as-deposited film is therefore thermodynamically unfavourable at room temperature. This sort of deposition forces the film into an amorphous state which should be describable by the continuous random network model[141] of amorphous solids [161].[142] The Si sp^3 bonds will still exist between nearest neighbours, but the bonding is imperfect as a result of the restricted movement of the atoms during quenching. This may yield the familiar four-fold coordinated Si atoms over small regions throughout the film, but it may not be true tetrahedral symmetry and the various regions are not linked to give long range order. The structure may have significant bond distortion from the ideal structure, coordination numbers may be distributed, and the imperfect bonding typically results in the inclusion of small voids and numerous electronic defects (some of which can be radiative).

Si^{4+} (radius of 0.4 Å) ions since the Si–O bond is not ionic. The covalent bonding prevents the typical ion contraction/expansion effects.

[139] The intent of this section is not to discuss the macroscopic process and kinetics of the film growth itself. This topic is adequately addressed with classical nucleation theory and the theory of growth modes. Rather, this section discusses the bond structure at the atomic level along with the specific phase(s) that result from the deposition process.

[140] Quenching refers to a rapid cooling in which low-temperature processes such as phase transformations are prevented by providing only a narrow window of time in which the reaction is *both* thermodynamically favourable (meaning that the products have a lower energy on the reaction coordinate than the reactants) *and* kinetically accessible (meaning that the activation energy is sufficiently low).

[141] Under this model, crystalline connectivity is preserved but the geometrical parameters are distributed over certain numerical ranges.

[142] The often discussed 'frozen liquid' amorphous state (which can occur in alloys) is not likely a valid description in this case, because of the strong tendency of Si atoms to form sp^3 covalent bonds.

Experimental evidence has suggested that plasma processed films, such as those of this study, exhibit an RBM-like distribution of tetrahedra [160]. However, in Si-rich SiO_x, the $Si(Si_4)$ and $Si(O_4)$ components are energetically preferable to others as a result of an energy penalty associated with the intermediary Si oxidation states, particularly Si^{1+}/Si^{2+} and sometimes Si^{3+}. These unfavourable oxidation states define spinodal points for the quenched SiO_x phase [160]. A partial spinodal decomposition of the as-deposited film during deposition can produce a bond network with a statistical distribution of tetrahedra that is skewed toward a RMM.[143] This is supported by the observation of Si nanocluster-related photoluminescence (PL) in some as-deposited films from the present study (McMaster ECR-PECVD system) (see Figure 4.2).[144]

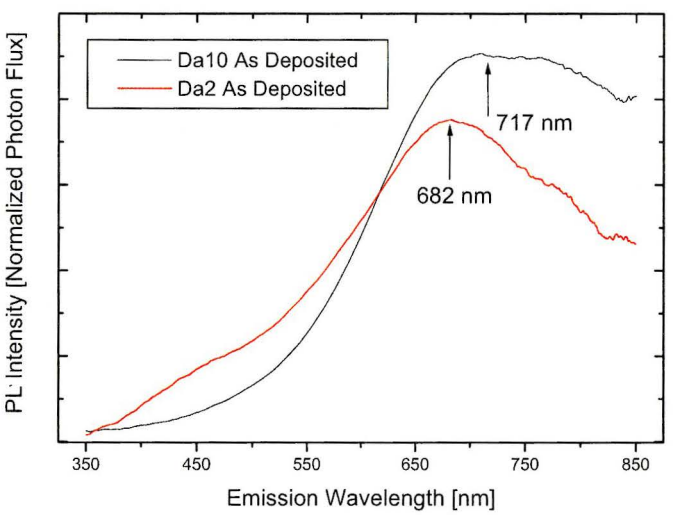

Figure 4.2: Photoluminescence spectra of two Si rich SiO_x:Er films as-deposited. Note the presence of Si nano-cluster PL prior to any annealing. Sample Da10 and Da2 contain 40 and 38.3 atomic percent Si relative to O respectively.

[143] It should be noted, however, that Si bonded to H in the as-deposited structure may not take part in the spinodal decomposition process as for Si bonded to O. Such a hydrogenated, as-deposited film may have a markedly different nanostructure relative to the non-hydrogenated equivalent. Clearly, depositions based on a silane precursor will result in a partially hydrogenated film structure (though evidently this hydrogenation is incomplete).

[144] The PL peak is too far red-shifted to be confused with a non-bridging oxygen hole centre. Furthermore, the peak red-shifts with increasing excess Si, consistent with quantum size effects.

The phase separation requires that activation energy be provided locally to break existing Si–O–Si bonds involving Si atoms in an unfavourable oxidation state and avail them for bonding. This energy can be provided during the deposition process by the energetic ions striking the films and/or from the heat released by the highly exothermic formation of Si–O bonds at the film surface [160].

As a second order approximation to the SiO_x:Er system, one could consider that there is about one Er atom per hundred Si and O atoms. This should not alter the overall network considerably but it could create competition for O atoms. For example, preferential consumption of non-bridging O atoms by either Er or Si could force the other into clusters. It is also quite likely that the Er, being a somewhat larger atom (although the Er^{3+} ion is not very large), introduces strain into the local structure; this affects the propensity of Si to precipitate because it alters the diffusion kinetics.

In the most advanced conception, one would have to consider the effect of the incorporation of $Er(tmhd)_3$ precursor fragments which could introduce significant distortion into the film (depending on the degree of precursor dissociation) which could promote the Si and O bonding towards either an RBM or RMM model and/or form entirely new complexes involving Si to carbon bonds or even Si to Er bonds. This should be a non-negligible effect given that there are 33 carbon atoms per Er on the precursor. In fact, the precursor is also a secondary source of hydrogen (along with the silane), carrying 57 hydrogen atoms per one Er, as well as oxygen, carrying six extra oxygen atoms per one Er. This does not mean, however, that the entire precursor actually incorporates into the film. Heavy ion elastic recoil detection analysis (HIERDA) was carried out on a subset of these films using a 40 MeV $^{29}Cu^{8+}$ beam at the Ecole Polytechnique in Montreal [37,162]. The intent was to quantify those elemental film constituents (particularly carbon, hydrogen, and nitrogen) which are not adequately resolved using 1.5 MeV RBS with a $^{4}He^{2+}$ beam because of Si substrate effects. Films measured, as deposited, yielded typical carbon concentrations at approximately

three to ten times that of the Er.[145] In addition, hydrogen atoms were present in amounts up to 10 atomic percent. Trace amounts of nitrogen were also evident, likely sputtered from the deposition chamber walls.[146] Finally, in addition to all of this there is argon present in the as-deposited films owing to its use as a carrier gas for the Er precursor as well as a plasma gas and diluent for the other precursors.

While this confusing picture of the composition is not the most useful to work with, the pathological reality should be retained as a conceptual backdrop to all future discussion of structural and luminescent properties. For example, it illustrates the fact that the as-deposited bond network will likely have a large propensity to contain defects, especially those related to oxygen, since its composition is highly distorted relative to stable SiO_2. These will impact the film luminescence properties. Furthermore, the way in which this complicated $SiO_vC_wEr_xH_yAr_z$ system undergoes phase transformation upon annealing could be significantly different from a simple ion implanted Si in SiO_2 system as a result of the altered diffusion kinetics.

4.2 Annealing-Induced Changes in the Bond Structure

4.2.1 Phase Separation of the SiO_x Structure

$$SiO_x \rightarrow \left(1-\frac{x}{2}\right)Si + \left(\frac{x}{2}\right)SiO_2 \qquad \text{(Ideal)}^{147}$$

a. Excess Si begins to phase separate/precipitate (initially into some amorphous nano-structured Si phase which can then be transformed into a crystalline

---

[145] Interestingly there was little correlation of this ratio with the concentration of Er.
[146] The McMaster ECR-PECVD system has historically been used for SiO_xN_y deposition.
[147] An alternative way to express the stoichiometry is to write Si_yO_{1-y} since y is then directly the atomic fraction of Si (otherwise equal to $^1/_{1+x}$ in SiO_x). The phase separation can then be written as: $Si_yO_{1-y} \rightarrow (^{3y-1}/_2)Si + (^{1-y}/_2)SiO_2$.

phase). Note that the complete phase separation of *all* of the excess Si will be a very gradual process. This is fundamentally because of the low diffusivity of Si atoms in SiO_2. There is evidence that even after annealing at temperatures up to 1250 C, a significant fraction of the excess Si cannot be precisely accounted for. It may be present in ultra-small clusters, with critical dimension below 1 nm, or it may still be contained in a SiO_x phase interspersed in an SiO_2 matrix [117].[148]

b. A more uniform host matrix (relative to the phase separated Si) begins to form around, and form an interface with, the phase separated Si and Er complexes. This matrix will be amorphous Si-rich SiO_x [117].[149] Higher temperatures will force the phase separation of more excess Si, thus driving the host matrix composition towards SiO_2. There will be an increasing ordering of the oxide and a significant reduction in defect structures (especially non-radiative defects[150]) but this will be incomplete at lower anneal temperatures (<1100 C). Although plasma-based, low temperature deposition will give rise to a high concentration of bond defects, many of them, including some dangling bonds, have low thermal stability can be repaired by annealing up to 600 °C. Built-in film stress/strain from the deposition process may be relieved in this way.[151] Defect-prone regions such as the interface between the oxide and the

---

[148] There is actually very little distinction between these possibilities since such small nano-clusters effectively contain only a few Si atoms.

[149] At low anneal temperatures (for example below at least 1100 °C) this matrix will still contain regions of Si-rich SiO_x since exceedingly high temperatures will likely be required to phase separate all of the excess Si.

[150] The dominant non-radiative recombination centre in Si-rich SiO_x is usually ascribed to the Si dangling bond, as determined by electron paramagnetic resonance (A. Hryciw, et. al., Nucl. Inst. Meth. Phys. Res. B **222**, 469 (2004)).

[151] Some SiO_x defects have excellent thermal stability. For example, cetain vacancy defects can be stable beyond 1100 °C (See: Brusa, et. al., J. Appl. Phys. **94**, 7483 (2003)). Some luminescent defect actually require such anneal to become activated (See: Lin, et. al., IEEE J. Quant. Electron. **41**, 441 (2005)).

phase separated Si or Er complexes could still be subject to the effects of incomplete bonding and strain.[152,153]

4.2.2 Formation of Er Complexes

By determining the location of the Er in the films, the Er-Er spacing, and the coordinating environment of the Er, annealing establishes the optical activity and tendency for multipolar interactions of the Er dopant. Although Er has a limited capacity to diffuse below 1000 °C, it will getter nearby anions to form a preferential coordinating complex – presumably a centre similar to ErO_6 involving NBO coordination. There are two phenomena that will detract from the formation of optically active Er:

1) Clustering: Annealing drives the formation of Er-O clusters (similar to Er_2O_3) to increase the Er^{3+} ions' mutual anionic coordination number if there are too few NBOs to fully coordinate each Er^{3+} ion individually.[154,155]

2) Precipitation: In general, the Er-O complex is thermally unstable above 900 °C, and will readily dissociate to produce metallic Er clusters (and perhaps metallic erbium silicides) [163,164,165,166].[156]

---

[152] Although SiO_2 can form a near atomically flat interface with flat single crystal Si, the interface under consideration in the films of this study consists of a topologically convoluted amorphous Si network, and the constantly evolving matrix is not pure SiO_2 but contains excess Si atoms along with the Er.

[153] Fourier transform infrared spectroscopy of Si-rich SiO_x films from the ECR-PECVD system with 42% Si indicate that the formation of SiO_2 (ie. the phase separation) is extremely small for anneals up to and including anneal temperatures of 800 °C (See. Roschuk, M.A.Sc. thesis, McMaster Univeristy, 2003). This has also been corroborated by x-ray diffraction data – discussed below.

[154] To see that the formation of an Er_2O_3 cluster reduces the NBO requirement, consider that an isolated Er^{3+} might require 3-7 NBOs, whereas Er_2O_3 only requires 3 NBOs for every 2 Er^{3+} ions.

[155] These Er^{3+} ions are optically active but their luminescence is mostly quenched by Förster-Dexter coupling interactions. This effect decreases the Er^{3+} luminescence yield and shortens the luminescence lifetime.

[156] Despite consisting of Er^{3+} ions, these precipitates are optically inactive. This effect decreases the Er^{3+} luminescence intensity without shortening the luminescence lifetime. See: de Dood, et. al., Phys. Rev. B **71**, 115102 (2005).

It has been noted that Er can exhibit a tendency to 'follow' an amorphous-crystalline Si interface (remaining in the amorphous Si phase) due to solubility differences [167]. The inevitable formation of similar interfaces in the process of the phase separation (and eventually crystallization) of the excess Si in Si-rich SiO_x films may cause similar movement of the Er atoms towards the interface of the Si clusters. This should also keep most of the Er outside of the Si clusters since their solubility in the oxide matrix is higher.

4.2.3 Release of Gaseous Impurities from the Film (Outgassing)

Exposure to high temperatures, in excess of 600 °C leads to outgassing of various impurities from the film. Certain impurities such as Ar and H are unavoidable contaminants from the deposition process; their devolution from the films upon high temperature annealing is easily studied with heavy ion elastic recoil detection [168]. Elastic recoil detection (ERD) analysis has confirmed that the H concen-tration decreases steadily in ECR-PECVD films similar to those of the present study, for anneal temperatures beyond 400 °C, falling below the detection limit of ERD by 1100 °C [39].[157] Rutherford backscattering spectroscopy (RBS) has revealed the disappearance of argon from the Er-doped films of the present study when they are annealed at temperatures beyond 800 °C (and possibly even prior to this since no RBS measurement were made on films subjected to lower anneal temperatures). This is not surprising given that there should be considerable non-bonded Ar within the films.[158]

A more ambiguous consideration in these films pertains to the outgassing of $Er(tmhd)_3$ fragments. It is not known exactly how the *tmhd* ligand incorporates

---

[157] The same reference found the H incorporation (in the form of Si-H bonds) in as-deposited Si-rich SiO_x films to be quite random, and suggested that this was the result of a memory effect occurring in the ECR-PECVD system for consecutive depositions carried out without an Ar-plasma cleaning.

[158] Because the signal to noise ratio in the RBS data prevents the detection of argon concentrations below approximately 10^{19} Ar/cm^3 (approximately 0.01 atomic percent) this data only confirm that the argon concentration drops below this value for anneal temperatures at or beyond 800 °C.

into the film, but the ligand itself has a melting temperature near 180 °C. The RBS data does not reveal any decrease in the Er content with annealing; no HIEDRA measurements were carried out on annealed films.

One of the consequences of outgassing is the densification and contraction of the film upon annealing. This changes the strain fields in the films and thereby affects diffusion kinetics and the activation of phase transformations. The release of bonded H can expose dangling bonds and other defects. Additionally, outgassing could lead to the formation of voids, particularly if the vacating species first coalesce in the film [169].[159] In particular, one of the films in the present study (label Er118) which contained nearly 4 atomic percent Er (film average) in a slightly oxygen rich SiO_x film actually formed 'blisters' on the film surface upon annealing at temperatures as low as 600 °C. These spherical-cap shaped blisters were actually 4-10 microns high and 20-80 microns in diameter, as determined by scanning electron microscopy[160] (Figure 4.3). They were always the same shape but quite randomly sized and randomly distributed on the film surface (except at the very edges of the samples, where they were absent). The most plausible reason for this anomalous formation is the incorporation of large amounts of argon (as confirmed by RBS) along with hydrogen and *tmhd* fragments, which formed clusters near the film-substrate interface. The film/substrate interface seems the likely location for the gaseous clusters because of a large spike in the Er – and therefore argon and *tmhd* – concentration that occurred in the first 50 nm of the film in which the Er concentration reached nearly 6 atomic percent, the highest doping level achieved in this study. Interestingly, however, while the bubble formation occurred for anneals carried

[159] This is, for example, a well known tendency for hydrogen (and helium) in Si. It is under investigation as a technique for forming nano-porous low-k dielectrics and as a method of forming nano-cavities for gettering transition metals in Si. It has been used to advantage in the fabrication of ion-cut Si-on-insulator and even Si based LEDs. (See: Brusa, et. al., Appl. Phys. Lett. **88**, 011920 (2006)).

[160] Images (a) and (b) were taken using a Philips SEM 515 (operated by the McMaster University Brockhouse Institute for Materials Research) with a lanthanum hexaboride filament and approximately 30 kV accelerating voltage.

out in N_2 or (Ar + 5% H_2), no blisters appeared for an anneal in O_2 ambient. Furthermore, at the end of the O_2 anneal, the film appeared to have decreased in thickness by a significant margin, consistent with the complete release of the impurity gases. It is not clear why the O_2 allowed these gases to escape while N_2, and (Ar + 5% H_2) did not; it is possible that the *tmhd* molecules (or fragments thereof) in the bubble reacted with O-based species (not necessarily O_2) produced by the in-diffusion of O_2 through the film and created new smaller species which were able to diffuse out of the film.

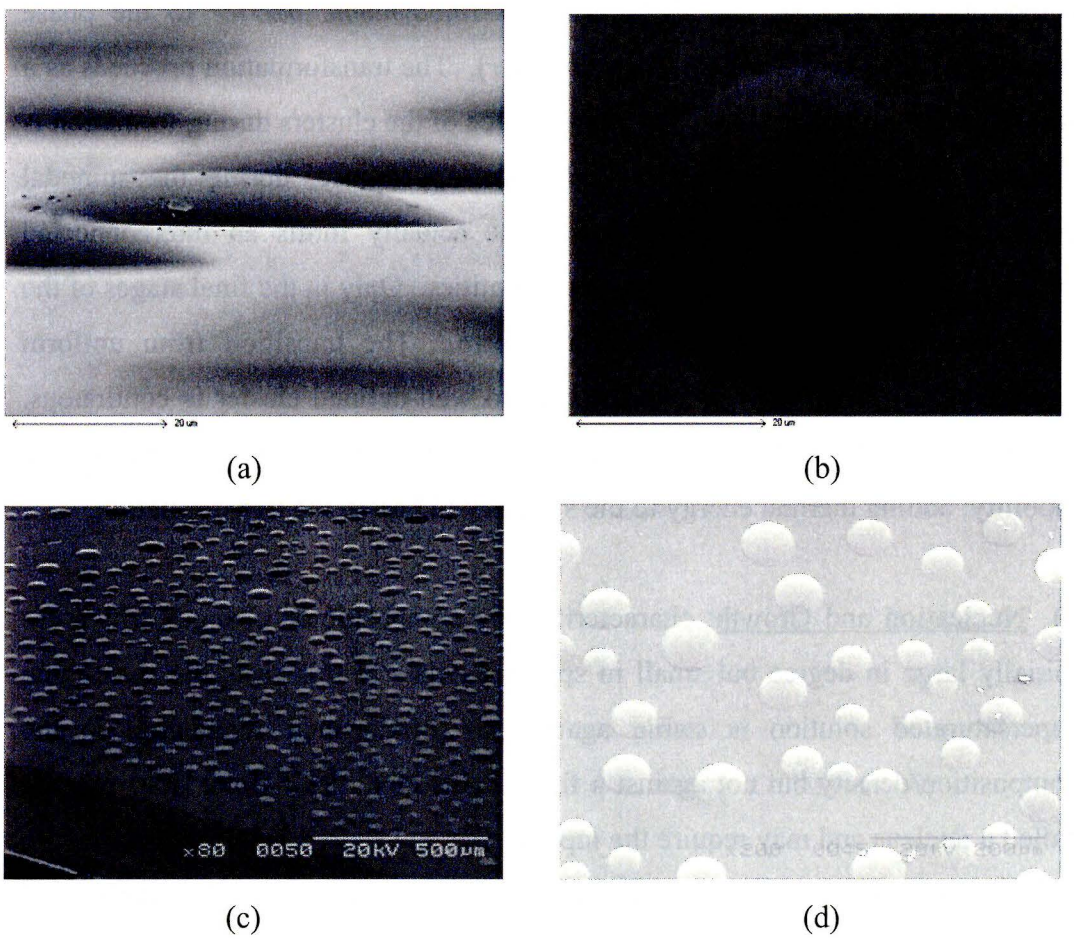

Figure 4.3: Scanning electron microscope images showing different perspectives of the annealing-induced surface micro-structure (domes) formed on sample Er118. (a) the clear dome is 7.2 μm high at 65 μm diameter; (b) dome is 35 μm across; (c) and (d) show the non-uniform distribution of the domes.

4.3 Annealing-Induced Phase Separation Mechanisms

The phase separation processes for Er-doped Si-rich SiO_x can be approximated by first disregarding the doping. There are two types of first order phase transformations [170].

1) Spinodal Decomposition: characterized by compositional changes which are initially small in degree but large in spatial extent. In this case, the metastable supersaturated solution is unstable against an infinitesimal fluctuation in the composition/density so that there is no *thermodynamic barrier* to the phase separation (there will still be a *kinetic barrier*). The transformation proceeds as a sort of compositional wave so that the interface of the clusters during formation is diffuse (see Figure 4.4). This creates the appearance, during the spinodal decomposition, that the transforming phase actually forms an interconnected network instead of discrete, well separated entities. Only in the final stages of the transformation would a sharp interface form. The transition from uniform supersaturated solution to diffuse network to well-defined cluster is continuous. The *kinetics* may be fast or slow depending upon factors such as the atomic mobility; adding thermal energy to the system will hasten the transformation.

2) Nucleation and Growth: characterized by compositional changes which are initially large in degree but small in spatial extent. In this case, the metastable supersaturated solution is stable against an infinitesimal fluctuation in the composition/density but not against a finite fluctuation. This finite fluctuation is called a nucleus and may require the input of thermal energy in order to form with any reasonable probability. In contrast to spinodal decomposition, the interface of the nucleus is always sharp (depicted in Figure 4.4). The stability of the nucleus is determined by a balance between its surface energy (which is usually associated with high energy because of the presence of unsatisfied bonds and surface tension) and its volume energy (which is usually negative since it represents the

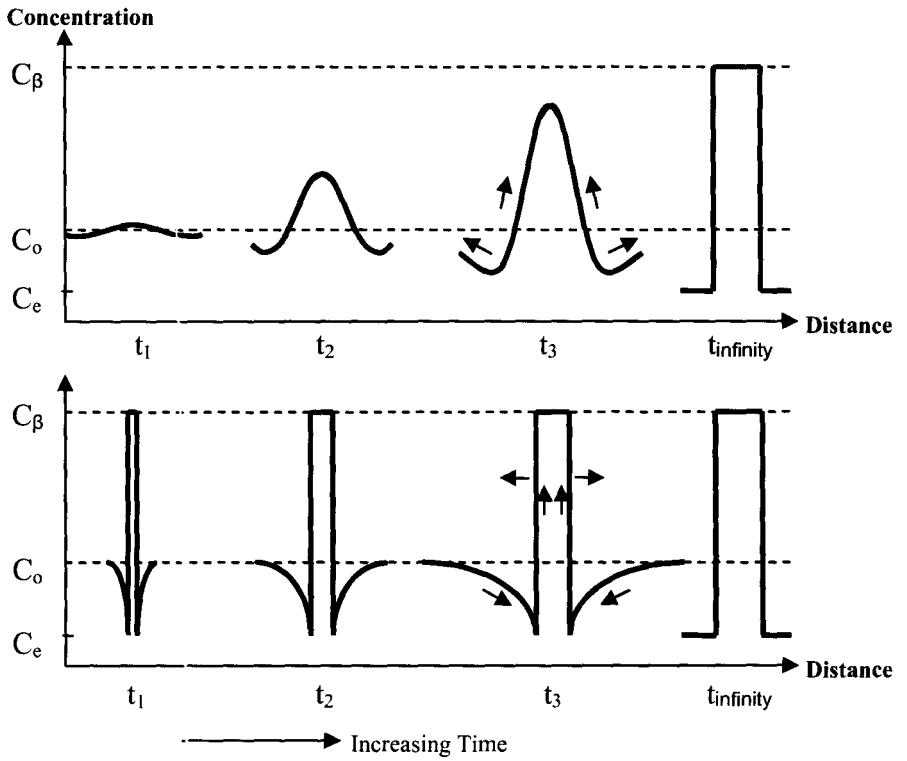

Figure 4.4: One-dimensional schematic depiction of the spinodal decomposition mechanism of phase separation (upper panel) relative to cluster nucleation and growth (lower panel). The arrows depict the path of diffusion of the solute; C_β is the cluster composition, C_o is the background matrix composition during cluster growth, C_e is the final matrix composition once the cluster reaches its equilibrium size. Adapted from [170].

more stable phase and therefore the driving force for the transformation). This balance defines a thermodynamic (free energy) barrier to the phase transformation which is a function of the cluster size. Only nuclei beyond a critical size will grow while smaller clusters are unstable and easily dissociate. For supercritical nuclei, growth initially proceeds by drawing further dissolved solute from the matrix; later, the growth proceeds by the phenomeon known as Ostwald ripening. Ostwald ripening is the 'coarsening' process of competitive growth in which larger precipitates grow at the expense of the smaller precipitates. This occurs because precipitates lower their formation energy by transporting matter from smaller to larger members. This process continues asymptotically in time until a

uniform distribution of clusters at an equilibrium size is reached. The equilibrium cluster size is approached because the diffusion fields of adjacent clusters increasingly overlap and compensate each other. Eventually, there is no longer a concentration gradient between clusters and the driving force for *net* diffusion disappears (see Figure 4.5). At this point, the metastable matrix has also reached a new equilibrium composition (C_e in Figures 4.4 and 4.5) with a lower solute concentration (though not all of the initial supersaturation may have yet precipitated). No further cluster growth will occur beyond this point until sufficient thermal energy is applied to stabilize a larger equilibrium cluster and/or precipitate more solute from the matrix (decreasing C_e). At some point, continuing to increase the temperature will begin to decrease the cluster density as

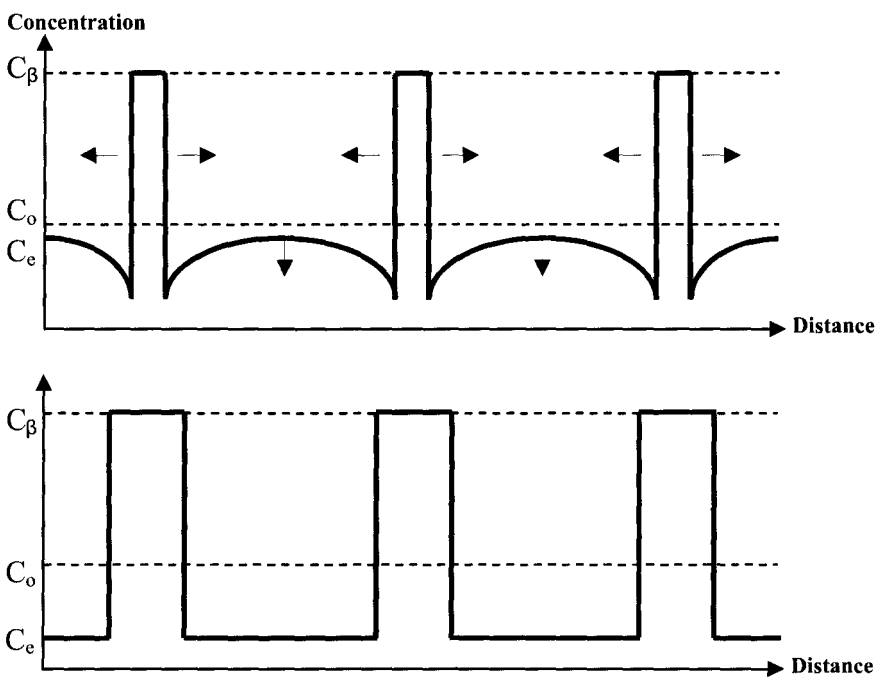

Figure 4.5: Depiction of the overlapping of diffusion fields between adjacent clusters leading to a temperature-dependent equilibrium cluster size. In reality, the equilibrium background composition would include those clusters which only consist of a few atoms (and are therefore on the verge of ambiguity about the definition of a nanocluster) and are therefore too small to be seen even by energy filtered transmission electron microscopy. Adapted from [170].

the ripening process becomes more severe – a process which may or may not be compensated by the liberation of additional solute from the matrix. The kinetics may be fast or slow but are, again, hastened by the application of thermal energy.

Application to Si-rich SiO_x

The sequential occurrance of these phase separation mechanisms in Si-rich SiO_x is depicted in Figure 4.6. Conceptually, the initial distribution of Si clusters form by either the spinodal decomposition mechanism or by the cluster nucleation mechanism:

1) *spinodal decomposition* forms an interconnected, nano-structured amorphous Si network. At sufficiently high anneal temperatures and durations this network would break into discrete fragments and undergo some diffusive growth.

2) *cluster nucleation* followed by rapid pure diffusive growth always produces a discrete distribution of Si clusters

Once the initial cluster distribution is established, the clusters undergo asymptotically slower diffusive growth and Ostwald ripening. Simulations [117,171,172,173,174,175] of the entire process are invariably carried out in the literature by disregarding spinodal decomposition and using only the cluster nucleation, growth and ripening picture.

(i) Initial nucleation and growth are modeled using classical nucleation theory assuming diffusion-limited growth (no depletion of the excess Si available for cluster growth). The model can be made more sophisticated by considering nucleation barriers and changes in the excess Si concentration available for further precipitate growth as a function of annealing time [117].

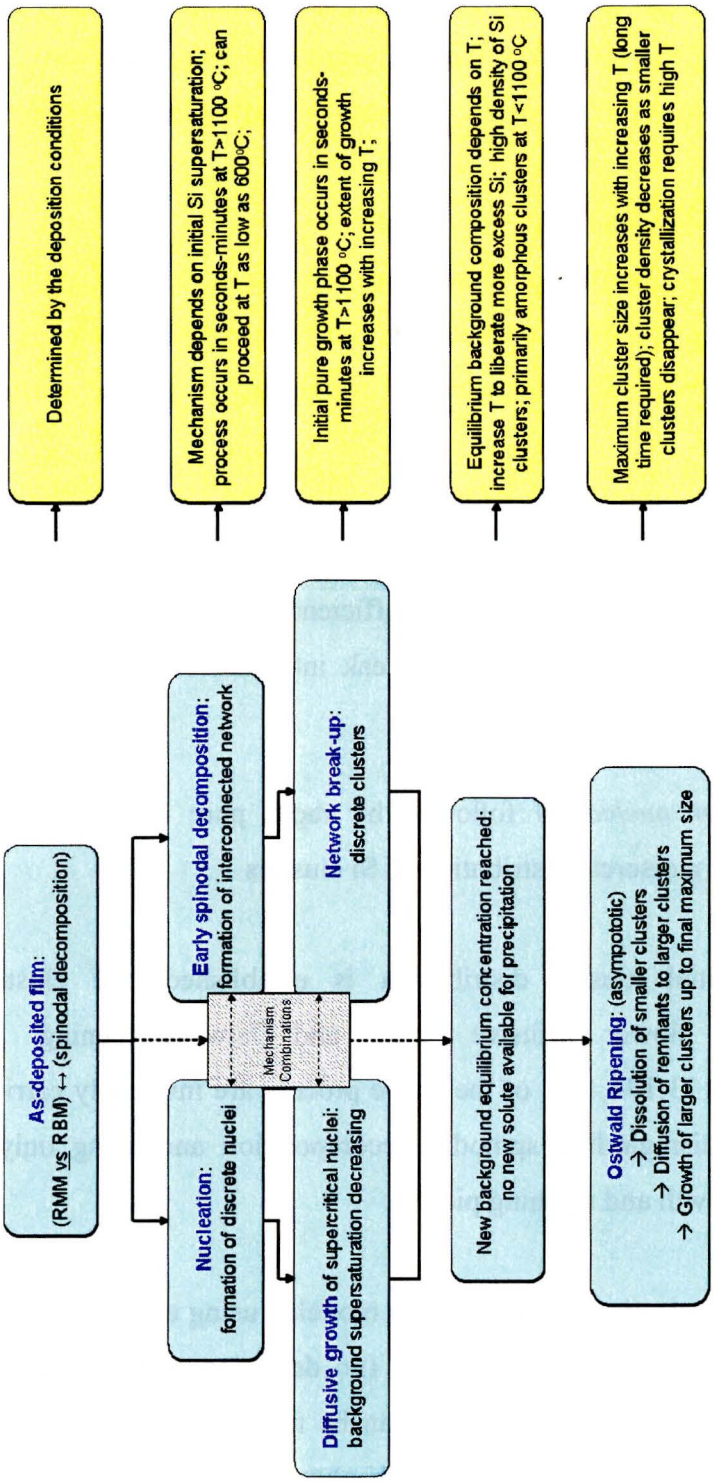

Figure 4.6: Schematic depiction of the sequence of physical mechansims involved in Si nano-cluster formation in Si-rich SiO_x thin films (left-hand panel). The right-hand panel contains the physical manifestation of the mechanisms.

(ii) Assuming that all of the excess Si is now present in clusters, the Ostwald ripening can be modeled using diffusion-limited Ostwald ripening theory. This model has the weakness of being derived only for very dilute systems so that it considers the distance between Si clusters to be much larger than the cluster size. The *mean field approximation* is made whereby the clusters do not 'see each other' but only the mean supersaturation within the matrix. This assumption takes no account of overlapping concentration gradients in the vicinity of the clusters. The model can be improved by including the interaction of the diffusion fields associated with individual clusters – this removes an important disagreement between the theory and experimental results [175]. The theory predicts that the equilibrium cluster size at a given temperature will be independent of the initial Si supersaturation (a result of the assumption of low supersaturation). However, experiment shows just the opposite dependence of mean cluster size on initial supersaturation.

One of the difficulties with these models is precisely their inability to account for spinodal decomposition. Both experiment [160] and simulation [172] suggest that the importance of Si cluster formation by spinodal decomposition increases with increasing excess Si content. Experimentally, Si plasmon loss energy filtered transmission electron microscopy (EFTEM) has been successfully used to provide an elemental map of phase separated Si (ie. Si bonded to Si) [117,176]. The plasmon[161] energy associated with elemental Si is sufficiently different from that associated with Si bonded to oxygen (as in SiO_2) that the two can be separated by energy filtering. The technique uses a conventional TEM in conjunction with an electron energy loss spectrometer. The image is formed using only electrons which have lost a specific amount of energy in interacting with the sample The utility of this technique is its ability to image not only crystalline Si clusters, but also amorphous Si aggregates. Figure 4.7 shows

[161] A plasmon is the quanta of the collective excitation of free carriers (electrons) into a longitudinal oscillation.

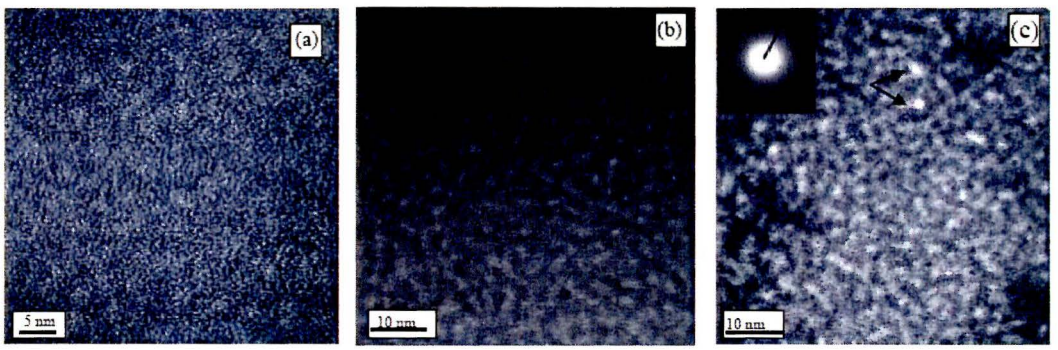

Figure 4.7: Si plasmon loss plan view EFTEM images of Si-rich SiO_x films, with 46 atomic % Si. (a) as-deposited; (b) annealed for one hour in N_2 at 900 °C; (c) annealed for one hour in N_2 at 1000 °C (inset shows selected area diffraction pattern). These images differentiate Si–O bonds from Si–Si bonds including amorphous phases. The formation of an *a*-Si inter-connected nano-structured network at all temperatures is evident. Reproduced from reference [176].

plasmon loss EFTEM of a SiO_x film (published as Figure 3.8 in reference [176]) with 45 atomic percent Si as deposited and at various stages of annealing. Light coloured regions represent Si bonded to Si. These images reveal that the as-deposited film is essentially a uniform phase with no well defined Si precipitation. For the anneal at 900 °C, there appears to be a semi-interconnected network of [phase separated] Si, all of which is completely amorphous. Some extremely small, isolated nano-clusters near 1 nm in diameter are present. This may be illustrative of a certain degree of duality in the phase separation mechanism (spinodal decomposition versus nucleation). For the anneal at 1000 °C the network becomes increasingly well defined and begins to contain *some* nano-*crystals*. Although not shown here, at anneal temperatures beyond 1100 °C, many discrete clusters with diameters of a few nm have formed. Approximately 25% of these clusters are crystalline. Similar EFTEM images have also been made on films doped with Er (ion implanted at 300 keV to a dose of $5x10^{14}$ cm^{-2}) and the same images occurred [122].

Simulation of phase separation from thin Si-rich SiO_x films on Si have indicated [172][162,163] that at low excess Si concentration, a series of very small discrete, well-separated clusters form at low temperature, which grow (decreasing the number density) at the highest anneal temperature (see Figure 4.8). However, as the initial supersaturation increases, the intermediate anneal no longer produces

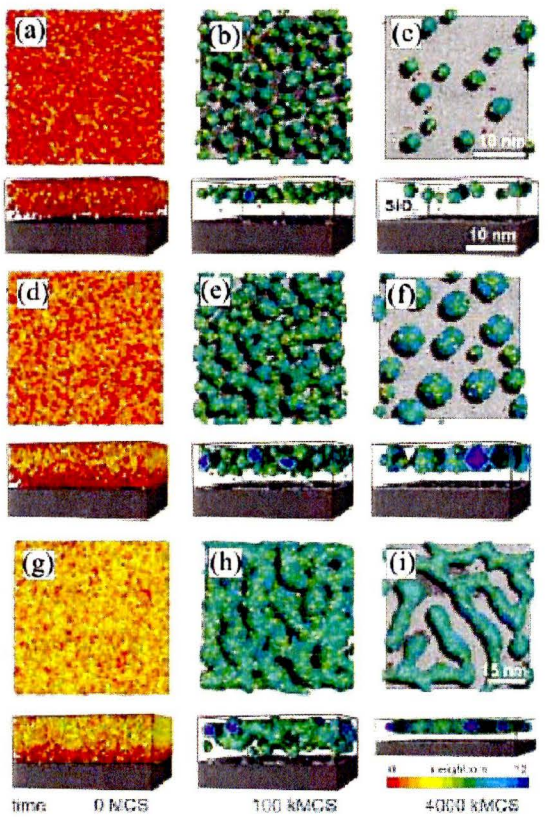

Figure 4.8: Simulations of the thermally induced phase separation Si-rich SiO_x for various concentrations of excess Si. Three regimes are identified: (a-c) *nucleation and growth*: depicts a Si excess of $2x10^{15}$ cm^{-2} at three progressive anneal times; (d-g) *spinodal decomposition*: depicts a Si excess of $5x10^{15}$ cm^{-2} at progressive anneal times; (g-i) *percolation*: depicts a Si excess of $1x10^{16}$ cm^{-2} at progressive anneal times. From [172].

---

[162] The study uses a kinetic three-dimensional lattice Monte Carlo (KMC) method. The anneal times and temperatures considered are embedded in a single internal time unit referred to as a Monte Carlo step (MCS); absolute comparison of this quantity with experimental data is difficult.

[163] These simulations also predict the existence of a zone denuded of Si nano-clusters just above the substrate. The size of this zone is a function of the excess Si content and results from the diffusion and incorporation of excess Si into the substrate.

such well-separated clusters, and only at the highest anneal temperature are well separated (and larger) clusters formed. Furthermore, relative to the case of low Si concentration, the Si nano-clusters become larger and dissolve slower. Finally, at sufficiently high initial supersaturation, a highly interconnected network forms which never forms discrete entities. This simulation, though largely qualitative, suggests that at low Si supersaturation, the nucleation model would provide a more accurate description, while at higher Si content the spinodal decomposition model would be more accurate.

4.4 Impact of the Anneal Parameters on the Film Structure

4.4.1 Input and Output Variables in Anneal Processing

Every step in the phase separation process has its own unique dependence on three independent variables: duration of annealing, anneal temperature, and the Si supersaturation (also referred to as the excess Si concentration). One might include a fourth variable as ambient gas(es) under which the annealing takes place. These can be called the process 'inputs'. The 'outputs' would be the real-time description of the phase transformation. Such a description might consist of as few as four dependent variables: the mean Si cluster size, the width of the distribution of cluster sizes, the cluster density (clusters per cubic centimeter or cluster spacing), and the cluster phase (crystalline or amorphous). In order to discuss the relationship between the inputs and ouputs, a schematic is shown in Figure 4.9, which summarizes the primary variables. The as-deposited film structure has already been discussed, as has the role of the initial Si supersaturation in the early precipitation. Beyond this, a number of general relationships hold (illustrated in Table 4.1; the 'up' and 'down' arrows in the table refer to 'increasing' and 'decreasing' respectively).

Four of the most important, experimentally observed relationships from this table are as follows:

(1) The mean cluster size increases with increasing annealing time and temperature

(2) The mean cluster size increases with increasing initial Si supersaturation

(3) The cluster density decreases with increasing time and temperature

(4) The cluster density increases with increasing initial Si supersaturation

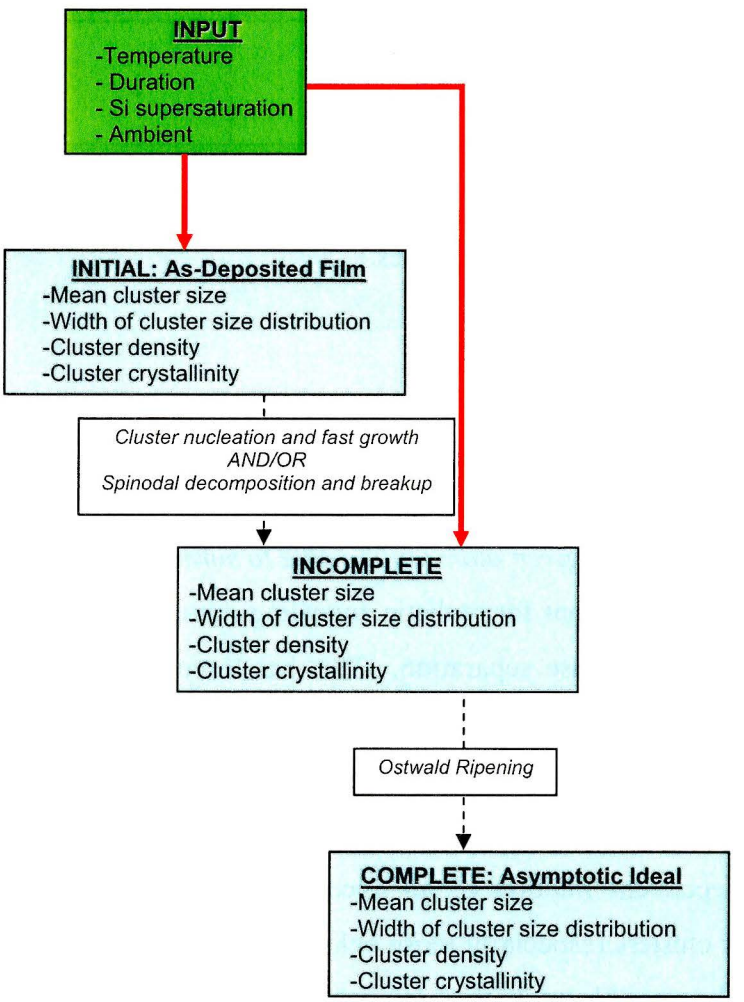

Figure 4.9: Schematic diagram illustrating the relationship between the anneal process variables (inputs) and the response of the Si-rich SiO_x thin film at various stages in the phase separation. The blue boxes list the basic cluster properties which change as a function of the input parameters. The process can be started and stopped at any time/stage but there is no way to reverse the phase changes that have taken place.

	Mean Cluster Size	Distribution of Cluster Sizes	Distance Between Clusters	Fraction of Crystalline Clusters
Initial Si Supersaturation ↑ *(fixed anneal temperature and time)*	↑	↑	↑	↑
Anneal Temperature ↑ *(fixed Si super-saturation and anneal time)*	↑	↓	↓	↑
Anneal Duration ↑ *(fixed Si super-saturation and anneal temperature)*	↑	↓	↓	↑

Table 4.1: Depiction of the experimentally observed effects of anneal parameters on the Si nano-cluster material properties.

4.4.2 Anneal Temperature

Physically, the anneal temperature determines at least three main properties:

1) *The probability that a given atom will be able to surmount its energy barrier to diffusion.* This implies that for realistic annealing durations a given temperature allows only a partial phase separation. This has three consequences. First, the intervening oxide between nano-structured Si entities can be SiO_x ($x<2$) and *not stoichioimetric* SiO_2. In terms of Figure 4.5, the composition of the background matrix C_e at steady state is a function of temperature.[164] Second, only a temperature-dependent fraction of all excess Si atoms is available to cluster. Third, smaller clusters (especially those below the 'equilibrium' cluster size) will be increasingly unstable at higher temperatures owing to the lower diffusion barrier of their surface atoms. Liberated surface atoms may then diffuse to the larger clusters, which are characterized by a lower free energy owing to their

[164] This activation energy, supplied thermally, required to overcome the diffusion barrier will not be identical for every Si atom because it depends on the binding energy associated with its current bond environment. For example, under-coordinated Si atoms could have a reduced activation energy because they require the breaking of fewer bonds to be released. Additionally, Si atoms bonded to Si atoms have a different binding energy than Si atoms bonded to O atoms.

smaller surface to volume ratio. In this way, higher temperatures promote the disappearance of smaller clusters and the growth of larger clusters. In the limit of long anneal time, this accounts for Ostwald ripening.

2) *The characteristic diffusion velocity.* In other words, it determines the characteristic 'diffusion length' or mean net distance that an atom will be able to traverse in a given amount of time. This implies that a higher anneal temperature means the Si atoms diffuse farther. The mean diffusion distance (diffusion length) $\bar{x}$ can be simply approximated as [170]:

$$\bar{x} = \sqrt{Dt} \tag{4.1}$$

(this is occasionally expressed with various pre-factors such as 2.4) where t is the time duration of the anneal, and the temperature dependent diffusion coefficient D, is given by the Arrhenius relationship:

$$D = D_o \exp^{-E_A/(kT)} \tag{4.2}$$

Where E_A is the activation energy, k is the Boltzmann constant, T is the temperature, and D_o is a material-dependent constant pre-factor (diffusivity). Increasing the diffusion length increases the probability that multiple Si atoms will be brought into contact, potentially forming a cluster. Various attempts have been made to model the diffusion of excess Si atoms in a SiO_x host and to measure values for the diffusion parameters [117,118,177,178].[165] Variability in the diffusion kinetics of material deposited by different techniques, and subjected to different degrees of heat treatment (and even ambient), leads to disagreement in the literature over the activation energy. In general however, Si atoms do not easily diffuse in SiO_2. Using a value of $D_o \approx 1.2x10^{-9}$ cm^2/s and $E_A \approx 1.9$ $eV/atom$ (from [177]), generates the diffusion length curves depicted in Figure 4.10. For

[165] These studies have been motivated not only by photonic applications but also the use of Si-rich Si oxide gates in MOSFETs and capacitors for non-volatile memory devices.

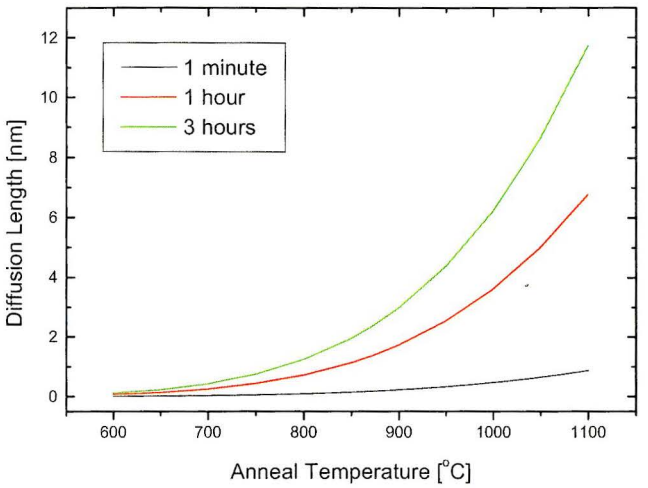

Figure 4.10: Diffusion length of a Si atom in an SiO_2 host matrix (self-diffusion) as a function of the temperature for various durations. This serves to approximate the diffusion of excess Si atoms in Si-rich SiO_x upon annealing in inert gas ambient.

anneal temperatures up to 800 °C and anneal times up to three hours, the diffusion length for an excess Si atom in SiO_2 is approximately less than 1 nm. In reality, the presence of under-coordinated Si, defects/voids (including impurities – especially carbon) and strain as a result of these complexes could enhance the rate of Si diffusion – or hinder it [179].[166]

3) *The crystallization kinetics of the a-Si clusters.* The initial phase separation process forms amorphous nanoclusters. Complete crystallization of an array of *a*-Si nano-clusters is a process which requires high temperature (at least 1100-1250 °C) and long duration (at least one hour at the highest temperature) annealing [117].[167] The crystallization kinetics are quite different from those of bulk *a*-Si [180] becuase each individual amorphous nano-cluster must form its own

[166] In fact, a study completed on some of the undoped Si-rich SiO_x films from the ECR-PECVD system suggest that, at excess Si fractions of 7-12 atomic percent, the activation energy is actually lower than that typically reported in the literature for lower Si supersaturation. (See: Comedi, et. al., J. Appl. Phys. **99**, 023518 (2005)).

[167] There is probably always a transitional region of amorphous Si between the crystalline core of a Si nano-cluster and its embedding matrix.

nucleation site for crystallization. Crystallization of bulk Si, which can proceed globally from only a few nucleation sites, can take place at half the temperature required for Si nano-clusters.[168] Important for the present study is the finding that impurity atoms such as C affect the cluster phase in Si-rich SiO_x films doped with Er.[169] At the very least, C seems to inhibit the formation of nano-*crystals* [162,181], though amorphous nano-cluster formation is still possible.[170] Experimentally, the degree of crystallinity of the nano-structured Si phase can be investigated on a site-specific basis by high resolution EFTEM [117][171] and on a non-site-specific bases by x-ray diffraction (XRD), particularly the use of x-ray rocking curves [118].[172,173] An XRD study [118] was carried out for SiO_x films deposited on the McMaster ECR-PECVD (and inductively coupled PECVD) system. Importantly for the present work, the lowest Si supersaturation considered (40 atomic percent Si relative to O) detected almost no *measurable* phase separation for a 900 °C anneal. Nano-*crystal* formation was extremely limited even up to a two hour anneal at 1100 °C. Nano-*crystal* formation at 900 °C was not observed below 45 atomic percent Si. Evidence was found for limited spinodal decomposition effects. Additionally, small Si clusters were suggested to be strained in tension due to the stretching of Si–Si bonds at the nanocluster/oxide

---

[168] The energetics of phase changes involving nanoclusters are expected to be size-dependent because the interface can contain an appreciable fraction of the total number of atoms.

[169] Impurity atoms will affect the thermo-chemical properties of the films in general. This is particularly relevant in the present study owing to the metalorganic Er precursor.

[170] Cluster formation itself *can* be inhibited if the Si is trapped in Si_xC_y or $Si_xC_yO_z$ phases. Furthermore, any retarding effect of the C on the diffusion kinetics of the excess Si is unknown.

[171] This technique has shown the ability to resolve nanoclusters which are partially crystallized and partially amorphous owing to a defect within the cluster. The high-resolution EFTEM technique has even been used to qualitatively observe strain effects in the immediate vicinity of clusters.

[172] Because the material is in the form of a thin film, this technique relies on a glancing angle x-ray beam with a slight rocking motion applied to the sample to increase the path length of the beam in the film. This technique can also provide some quantitative information about the size of the nanocrystals, strain effects in their vicinity, and even the degree of formation of the SiO_2 phase. The size determination comes from the peak width on the diffractogram; a simple diffraction effect in which decreasing the size of the coherent scattering entity broadens the Bragg peak. Information on SiO_2 can be drawn from the 'first shift peak' (broad background peak) which is indicative of increasing medium range ordering.

[173] Perhaps a more common technique in this regard is Raman scattering, based on the *c*-Si absorption at about 521 cm^{-1} and the analogous *a*-Si absorption at 480 cm^{-1}.

interface. The effect was attributed to the bond length mismatch between Si–O and Si–Si bonds and is therefore reduced in the larger nanoclusters, which exhibit a larger unperturbed core.

4.4.3 Silicon Supersaturation Relative to SiO_2

The Si supersaturation affects the probability of initial cluster nucleation and has an important effect on the inter-cluster spacing that affects the cluster size. Two extreme regimes can be considered:

> CASE 1: The Si supersaturation is low enough to yield a cluster density such that the concentration gradients in the vicinity of the clusters (which is a function of C_e and therefore the temperature) do not overlap. In this case, the 'final' mean cluster size should be effectively independent of the excess Si content. However, the density of the clusters will increase with increasing Si content.
>
> CASE 2: The Si supersaturation is sufficiently high to locate adjacent clusters near enough to each other (increase the number density of clusters) that the diffusion fields of individual clusters overlap. Now the emission and capture rates (of Si atoms) for the adjacent clusters are strongly coupled. The mean size of the clusters will depend strongly on the Si supersaturation. Increasing initial Si excess determines a larger mean cluster size.

Physically, as already discussed, the equilibrium cluster size which results at a given temperature and Si supersaturation is determined by the interaction of the diffusion fields. The diffusion of the free Si atoms continues until all of the excess Si atoms available for clustering, at that temperature, are contained in precipitates. Net diffusion then stops and, *assuming the medium is perfectly*

uniform, the clusters are all of the same 'equilibrium' size so that *no further growth occurs*. In practice, however, the intermediate condition is actually a distribution of cluster sizes. The free energy of the system then decreases primarily by Ostwald ripening, increasing the fraction of clusters at the 'equilibrium size' defined above; this narrows the cluster size distribution.

4.4.4 Anneal Duration

As equation (4.1) reveals, the main effect of the duration of the anneal step is to increase the diffusion length of the free Si atoms. This can be considered in two regimes:

1) *Time < 1 minute*: the rate of initial cluster formation (nucleation) is a function of the temperature, but can be very fast in the 1100 °C anneals commonly used to optimize the luminescence [171]. At this temperature the period of 'pure growth' lasts about one minute and yields a high number density of nano-clusters.
2) *Time >> 1 minute*: the primary effect of long annealing time is the asymptotic [Ostwald] ripening process. This decreases the number density of clusters, provided that the nucleation and pure growth regime are "over". The secondary effect is the increase in the crystalline fraction of the clusters and the reduction in non-radiative defects.

4.4.5 Anneal Ambient Gas

With respect to the effect of annealing ambient on the formation of Si nano-clusters, the most important aspect is that it be reasonably inert. The ambients most commonly used are Ar, N_2, H_2, (Ar + 5% H_2), and even vacuum. O_2 contamination of the ambient will oxidize the phase separated Si to produce SiO_2. Because the clusters present a large aggregate surface area, they can be quickly consumed. Under controlled circumstances – such as the use of a low oxygen

partial pressure – the size of the nanoclusters can actually be tailored to some extent (albeit with a concomitant reduction in the number density of clusters) [182]. As N_2 is not as inert as Ar, there has been some investigation into the nitridation effect of N_2 gas ambients on the films. While N_2 usually requires temperatures greater than 1200 °C to react with Si because of the strong N≡N bond, it has shown the ability to react at temperatures ≥760 °C in the presence of gaseous impurities such as H_2, O_2 and CO_2 to form thin SiO_xN_y films [119]. Nitridation of Si nano-clusters reduces the concentration of strained Si-O bonds (such as might give rise to Si=O surface state); it also consumes the clusters similar to oxidation. This has been shown to blue-shift the resulting luminescence [119]. In terms of material evidence for the incorporation of N at the interface, positron annihilation spectroscopy has suggested that N and O can become trapped in voids near the interface of Si nanoclusters formed at low temperature (<700 °C) [183]. At high temperature (>700 °C), the N can incorporate in the nanoclusters, resulting in a volume increase which shrinks the intrinsic open volume in the films to reduce stress in the host matrix. Furthermore, it is thought that N actually suppresses the diffusion of Si in SiO_2 so that agglomeration of the excess Si occurs more slowly [184]. The deposition of Si-rich SiO_x films by PECVD using a N_2O precursor for oxygen has been shown to produce significant nitrogen contamination [185]. It was found that the host matrix in such a system is actually a SiO_xN_y phase, though it does not contain sufficient non-radiative defects to degrade the optical qualities of the films. It is probable that the action of annealing in N_2 is not as severe as this given the fact that the plasma in PECVD is actually producing N ions.

The use of H or H-containing gas mixtures (eg. Ar + 5% H_2) has shown the ability to enhance the luminescent signal from Si-rich SiO_x films (including Er doped films). The first reason for this is the ability of the H to passivate various non-radiative defects in the films, particularly those carrying a net negative charge – such as dangling bonds like the E' and P_b centres. More sophisticated

explanations for the luminescence enhancement deal with the arrangement of atoms in and near the Si clusters; this includes H-passivation at the Si nano-cluster interface which, as discussed in Chapter 4, can change the radiative recombination pathway relative to an O-containing anneal. This will be discussed further in Chapter 6.

4.5 Description of a Silicon Nano-cluster

There has been some debate about whether the bond structure of bulk Si (crystalline or amorphous) prevails into the nano-cluster regime or whether there is a rather different bonding structure entirely. This can result from the effect of interfacial stresses or strains since the small nano-cluster size means the interior atoms "feel" the forces being exerted on the surface atoms much more than in bulk Si. In fact, the surface passivation itself can alter the bond geometry [105]. In general, reducing the cluster size disrupts translational symmetry but does not significantly alter the local tetrahedral bonding for cluster with more than 100 Si atoms [98]. Under the assumption that a cluster is bonded in the tetrahedral geometry of the bulk, a cluster of less than 1 nm in diameter likely contains tens of Si atoms (assuming the atomic density to be the same as that of bulk Si).[174] A cluster ~5 nm in diameter likely contains thousands of Si atoms (see Figure 4.11 for an estimation of the number of atoms contained in the cluster as a function of the cluster diameter). For the larger clusters, XRD and Raman spectroscopy data suggest that the structure is essentially that of bulk Si. Detailed structural information on the small cluster regime cannot be obtained with current materials characterization technology. Simulations, however, have indicated that,

[174] A semantic concern that arises when discussing those clusters well below the 1 nm diameter regime is the use of the terminology 'nanocluster' and 'defect'. The boundary between the two seems arbitrary. As an example, consider the Si cluster model for E_δ' defect centres. Such a structure might have a diameter near 0.5 nm. Alternatively, Si nanoclusters with this size are also discussed, particularly in reference to higher energy luminescence and strong quantum confinement. It is probably more appropriate to think in terms of defects at this level given that it is virtually impossible to make a distinction between a 'surface' and a 'bulk' region.

depending on the surface chemistry, there can be a significant structural relaxation that occurs in small Si nano-clusters such that the structures are actually more compact than the bulk material. High resolution EFTEM images [117] seem to suggest that, for high temperature annealing (≥1100 °C), the clusters are rather spherical in nature (this is not true at lower annealing temperatures).

One can get a quantitative sense for the number of atoms in a Si nano-cluster by making the simple assumption that the cluster is spherical. Then, it is easy to show that a cluster containing N Si atoms has a diameter $d(N_{Si})$ given by $d(N_{Si})=3.3686N_{Si}^{1/3}$ [Å] where the cluster has a mass density equal to that of bulk Si [98]. Figure 4.11 plots this function over the relevant nano-cluster size for luminescence optimization.

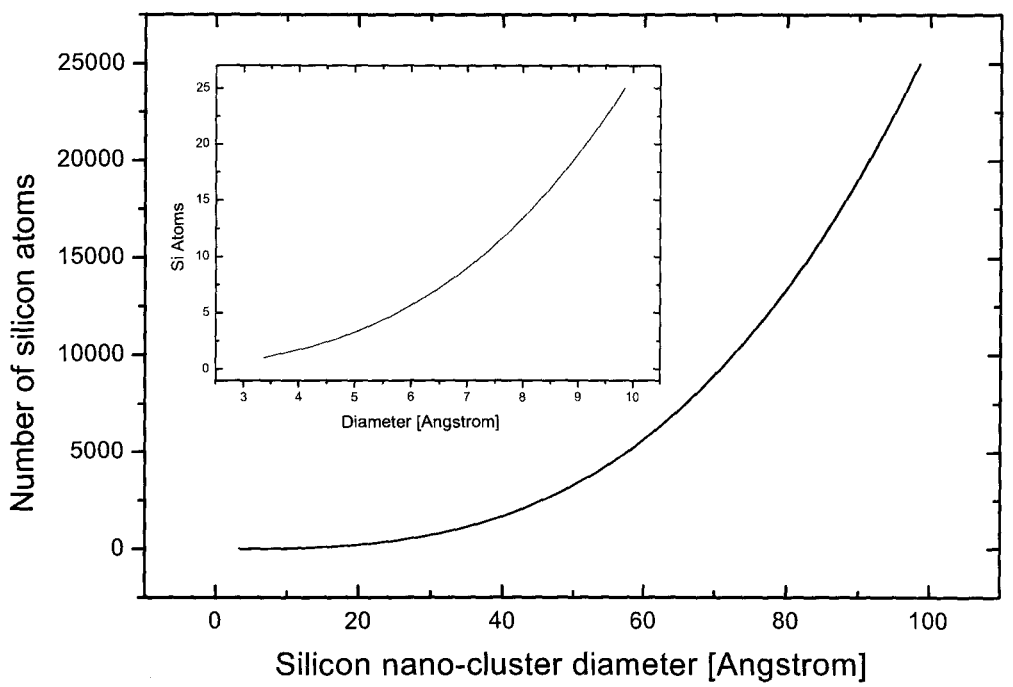

Figure 4.11: Approximation of the number of Si atoms in a spherical nano-cluster as a function of diameter. This figure assumes that the density of Si atoms in the cluster is the same as that of bulk Si. The inset shows the small diameter range.

Chapter 5

Experimental Details and Process Control Issues

The approach taken in this study has been to grow a sufficient number of films to cover a broad portion of the composition space, to then subject each film composition to a range of annealing treatments, and finally, to then characterize the resulting luminescence properties of each resultant sample by photoluminescence spectroscopy. A total of twenty-five films, each with a different composition, were grown by the ECR-PECVD technique. The simplest description of the composition space consists of two independent variables:

1) The quantity of excess Si relative to SiO_2

   This study considered films ranging from 31 to 60 atomic percent Si (calculated as the fraction [Si]/([Si]+[O]) using concentrations of areal atomic density).[175]

[175] Another way to describe the Si content is to describe the concentration of excess Si only (relative to all of the Si and O). This can be calculated from the measured areal atomic densities of Si and O as follows: divide the O concentration by a factor of 2, and then subtract this value from the total Si concentration. This gives the areal density of Si *above that of* SiO_2. Dividing this value by the sum of the total Si and O areal densities (and expressing the final value as a percentage) yields a result called the *excess Si content*. Alternately, from the perspective of the stoichiometric ratios in the phase separation equation in section 4.2.1, the excess Si content in SiO_x would be calculated as $[^{(1-x/2)}/_{(1+x)}]x100\%$. If one writes Si_yO_{1-y} (where $y = {}^{1}/_{1+x}$) then the excess Si content is given by $[^{3y-1}/_{2}]x100\%$.

2) The concentration of Er relative to Si and O

The study considered films ranging from 0 to 4 atomic percent Er (ie. the fraction [Er]/([Si]+[O]+[Er]) using values of areal atomic density).

As previously mentioned, the films additionally contain C and H, neither of which were directly quantified nor intentionally controlled as part of this study (they were treated as variables dependent on the Si and Er concentrations).[176]

5.1 ECR-PECVD Deposition Parameters

The two independent variables of the composition space must be mapped into the deposition parameter space. Previous work [33,39] carried out on Si oxide-based films both with and without Er has already isolated the particular deposition parameter subspace considered in this work. The microwave discharge power was fixed at 500 W (which meant that the Er and excess Si content of the films are coupled). De-coupling, or at least a decrease of the Er content to a point at which effective de-coupling occurs, requires the power to be on the order of 800 W [37]. While the 500 W regime is near to the optimum power (580 W) for maximum Er incorporation, working in the 800 W regime would have severely limited the amount of Er which could be incorporated. In general, the "500 W" required about 515 W of forward power with subsequent adjustment of the stub tuners to reduce the reflected power to about 15 W.

The substrate stage was heated to a temperature of 120 °C for all depositions;[177] this is considered to be a low temperature for this type of

---

[176] The H and C could have been quantified using elastic recoil detection (ERD) and/or nuclear reaction analysis (NRA). NRA would have been a useful technique to verify the O concentration as well since Rutherford backscattering measurements in the present study yield an O peak that is superimposed on that of the Si substrate.

[177] Some heating is needed to ensure that any H_2O contamination of the substrate/stage is driven from the surface; such H_2O can, for example, be generated by several of the film forming reactions taking place in the chamber during the deposition. Water incorporation in the film is a serious problem because it introduces OH^- (hydroxyl) radicals whose overtones produce infrared absorption bands; the hydroxyl ion is a well-known quenching site for Er^{3+} luminescence.

deposition. The Er dispersion ring temperature was fixed at 170 °C (in order to prevent condensation of the Er precursor in the dispersion ring). The $Er(tmhd)_3$ precursor gas was carried from the heating cell to the dispersion ring by an Ar carrier gas flow of 18 sccm (standard cubic centimeters per minute where "standard" refers to STP conditions: 1 atmosphere and 0 °C).

The reaction chamber was maintained at a vacuum of approximately 10^{-7} Torr prior to deposition, and the pressure during depositions was nearly constant at approximately 3 milliTorr regardless of gas flow rates. The substrate was always rotated at 20 RPM to enhance growth uniformity. The deposition time was varied in order to generate the desired film thickness, which was monitored throughout the deposition by an in-situ ellipsometer (single wavelength); films were always grown approximately 100 Å beyond the desired thickness in order to account for the contraction of the film upon cooling to room temperature. Depositions are started and stopped precisely by a manual shutter which isolates the plasma from the reaction chamber. The electromagnets which tune the geometry of the magnetic field in the plasma chamber were set to carry the same electrical currents each time. This is an important practice for deposition repeatability because the magnetic field determines the location of densest plasma (highest ion density) relative to the substrate and so influences the energetics of the interaction of the plasma with the film/substrate. The upper electromagnet carried a current of approximately 21.7 Amperes at 180 volts, while the lower electromagnet was set at 13.7 Amperes and 115 volts.

The following precursor and plasma gases were used:

1) Si precursor: 30% SiH_4 by weight in Ar diluent
2) O precursor/plasma gas: 10 % O_2 by weight in Ar diluent
3) Ar plasma gas: pure Ar
4) Er precursor: $Er(tmhd)_3$ sublimation in pure Ar carrier gas

The excess Si concentration in the films is controlled by varying the relative flow rates of the Si and O precursors. The relative Er concentration is controlled by varying the temperature of the cell containing the $Er(tmhd)_3$. Increasing the temperature produces more precursor vapour. Table 5.1 provides the gas flow rates for this study. Note that the sample labelling scheme, as introduced in this Table (and used throughout this entire thesis), reflects the official label assigned to this film as part of the master indexing scheme for all depositions carried out on the ECR-PECVD system. This indexing scheme assigns the prefix "Er" to all Er-doped SiO_x samples to distinguish them from the intentional deposition of un-doped films. The subsequent three-digit number reflects the sequential order of the depositions. For example, "Er116" refers to the 116^{th} deposition of Er-doped SiO_x. The labels beginning with "Da" reflect a departure from the master indexing scheme only in the sense that the film was to be distinguished from the database of samples for GroupIV Semiconductor; the number still indicates the sequential ordering. Note that "run sheets", labelled according to the above indexing scheme, are filled out at the time of each deposition. They describe all of the deposition parameters and are stored together as a dated, permanent, accessible archive of all depositions that have ever been carried out.

Wafer	SiH_4/Ar flow rate [sccm]	O_2/Ar flow rate [sccm]	$Er(tmhd)_3$ cell temperature [°C]	Notes
Er116	11	64	100	1,2
Er117	11	64	120	1,2
Er118	11	64	130	1,2
Er119	20	64	80	1,2
Er120	20	64	90	1,2
Er121	20	40	80	1,2
Er122	20	40	90	1,2
Er147	20	56	140	2,3
Er149	20	64	120	2,3
Da1a	20	64	140	4,5,9
Da1	20	64	140	4,5,9
Da2	20	56	140	4,5,9
Da3	20	52	110	4,5,9
Da4	20	40	140	4,5,9
Da5	11	64	130	4,5,9
Da6	11	64	150	4,5,9
Da7	11	78	0	6,7,8,9,10
Da8	20	64	140	6,7,9
Da9	20	56	140	6,7,9
Da10	20	52	110	6,7,9
Da11	20	40	140	6,7,9
Da12	11	64	130	6,7,9
Da13	11	64	150	6,7,9
Da14	11	64	100	6,7,8,9
Da15	20	40	90	6,7,8,9

[1] (100) Cz-Si doped with boron to a resitivity of 0.02-0.03 Ω·cm; single-side polished; supplied by Si Materials Inc.

[2] these depositions were not monitored with the in-situ ellipsometer

[3] (100) FZ-Si doped with boron to a resistivity of 0.007-0.01 Ω·cm; single-side polished

[4] (111) Cz-Si doped with boron to a resistivity of <<1 Ω·cm; single-side polished; supplied by Virginia Semiconductor

[5] these depositions were unknowingly carried out with pre-melted precursor in the Er heating cell; the Er concentrations are therefore anomalously low and do not reflect the Er cell setpoint temperature relative to depositions Er116-Er149

[6] (100) Cz-Si doped with boron to a resistivity of <<1 Ω·cm; single-side polished; supplied by Virginia Semiconductor

[7] these depositions represent the second attempt at deposition with a high Er cell temperature; the problem described in note (5) was evidently not resolved because these depositions produced films with no more Er than the previous attempt

[8] quartz substrate of 3 mm thickness

[9] these depositions were monitored with the in-situ ellipsometer

[10] this deposition employed zero Ar gas flow associated with the Er carrier line since the intended film was un-doped SiO_2

Table 5.1: Summary of the ECR-PECVD deposition parameters that were controlled as part of this thesis and their corresponding values for all depositions.

Deposition Parameter Coupling and Associated Process Control Issues

Considering all of the gases that intentionally enter the chamber during a deposition it is clear that there are present, in varying amounts, significant quantities of at least six elemental constituents: hydrogen, carbon, oxygen, silicon, argon, and erbium. Collisions with the energetic ions and electrons in the plasma generate almost innumerable molecular and radical species made of permutations of these elements along with their fragmented precursors all exhibiting a variety of charge and excited states. As previously alluded to (section 2.3), this diverse assortment of species gives rise to a complex array of incorporation and desorption processes at the substrate. It is clear that the various couplings and reactions occurring between the constituent species both in the plasma and at the substrate will affect the film growth mode, final film composition and structure. Such factors as the ratios of the different ions striking the film and their impingement energy, along with the total flux of each individual species can influence the film bond structure dramatically.[178] For example a higher incident ion flux can increase the film growth rate which can change the film growth mode by limiting the atomic diffusion at the surface.

Small fluctuations in processing parameters such as microwave power, chamber pressure, and gas flow rates can alter all of the quantities mentioned above. In this way, the concept of *process control* can present a serious engineering challenge. Even when as many of the deposition parameters as possible have been fixed, there is still no simple relationship between the precursor gas flows (along with the Er cell temperature), as varied in the present study, and the final film composition. In fact, the absolute composition represents only half of the issue. Slightly shifting the plasma properties can completely alter the film bond structure for films with the *same absolute composition* (see [186]). This is easy to visualize in SiO_2 films because of the almost free rotation around the Si-O-Si "bridge" bond and the resultant distribution in the bond angles as a

[178] Even changes in the relative populations of different charge states of a single ion species in the plasma can alter the film structure.

function of the growth method [50,51,52]; the experimentally observed dependence of the refractive index and infrared absorption bands on the deposition technique also illustrates this effect.

Although this study intended to produce a *uniform* map of the film composition space, this was simply not possible. The result was a rather ill-balanced representation of possible film compositions. In addition, deposition repeatability *was never achieved once.* The immediate source of error seems to be the Er doping cell, wherein apparently slight imprecisions in the control of the sublimation process had a magnified image in the resulting composition space. It is also speculated that small fluctuations in plasma properties and heating effects at the substrate were able to cause changes in the film composition and possibly larger – and more difficult to detect – changes in the film bond structure.[179] Such structural variations were evidenced by dramatic changes in the luminescence properties of films which [attempted] to identically repeat previous deposition conditions (parameter set points).

Two sets of depositions, comprising a total of fifteen films, revealed (and confirmed) a flaw in the Er precursor delivery system. In both instances, several high Er cell temperatures up to and beyond 140 °C were used, in conjunction with a range of SiH_4 flow-rates. Composition measurements, however, revealed Er concentrations nearly two orders of magnitude lower than expected based on previous work. The problem was initially attributed to insufficient (and uneven) heating of the Er cell resulting from an ill-placed thermocouple along with inadequate baking tape, which is used to heat the Er cell. In conjunction with this it was supposed that there was insufficient heating of the stainless steel lines through which the Ar gas carries the Er precursor to the deposition chamber; insufficient heating of the dopant dispersion ring was also suspected. Heating of all carrier lines is a necessity because the $Er(tmhd)_3$ vapour has a strong

[179] To remedy the confusion, a full study must be made using optical emission spectroscopy (OES) of the plasma, which attempts to connect the plasma properties (such as relative ion populations as determined with OES) to the film structure (as characterized by *bond-structure sensitive* techniques such as XPS and TEM) and deposition parameter set-points.

propensity to condense in lines which are cooler than the heating cell – a process which can rapidly constrict and even obstruct the line.[180] However, having remedied this problem, a second set of identical depositions yielded the same anomalously low Er content.

The most likely alternative possibility is that a reduced $Er(tmhd)_3$ vapour pressure was generated from the dopant cell owing to a loss of surface area available for sublimation [187]. The $Er(tmhd)_3$ precursor is purchased and placed in the dopant cell in the form of a fine crystalline powder. Such a powder presents an enormous surface area for sublimation. However, the constant heating of the cell over numerous film depositions, especially to temperatures as high as 140 °C (not far from the melting point of 180 °C), has the effect of sintering the grains together and even melting the precursor in the bottom quarter of the cell; the localized melting occurs because of non-uniform heating of the cell. This drastically reduces the surface area of the precursor available for sublimation and results in an overall reduced vapour pressure. Note that this would imply that, for the depositions carried out in this study, the dopant cell was exhibiting a memory effect – which could explain why composition repeatability was never achieved. One possible solution to this problem would involve designing multiple large flat dopant cell chambers, and completely melting the $Er(tmhd)_3$ powder in each of these *prior* to any depositions. In this way, each cell would present a uniform surface area of precursor at all times regardless of subsequent heating. As such a scheme could not be implemented as part of this project, that sub-section of the parameter space involving high Er cell temperatures has remained un-investigated.

One of the origins of the imprecision in the Er sublimation was the use of baking tape as the only source of heat applied to control the Er cell temperature. The baking tape does not fit the Er cell geometry exactly, so that it inevitably creates a non-uniform temperature profile along the vertical axis of the cell.

[180] To preven this condensation, the carrier line is wrapped with baking tape and the dispersion ring is heated.

Furthermore, only one thermocouple was placed to measure the cell temperature. The regular required manual un-wrapping and re-wrapping of the baking tape almost certainly led to un-repeatable differences in the thermal profile within the Er cell. One thermocouple cannot provide information on these thermal profile differences. This problem is magnified, especially at temperatures beyond 100 ^{o}C, because the $Er(tmhd)_3$ vapour pressure is highly sensitive to temperature changes in this range – as indicated by the vapour pressure curve [70]. Depositions carried out for two different re-wraps of the baking tape resulted in very different Er precursor sublimation for the same cell temperature setpoint. This was very clearly evidenced in a few of the depositions in this study (eg. Er147 versus Er054) in which the same deposition parameters gave rise to radically different film compositions. Given the sensitive inter-dependencies outlined above for the deposition parameters, it is realistic to expect that changes in the Er precursor supply can dramatically alter the entire film.

Two additional points must be mentioned about process control. The first pertains to the control of the substrate temperature. The substrate heater element lies a few centimeters below the substrate stage and provides radiative heating only (through vacuum). The thermocouple is not in contact with the wafer[181] and there is a 230 ^{o}C difference between the heater stage and the substrate when the former is at 350 ^{o}C (this is based on a previous measurement). The sensitivity of the film growth processes to substrate temperature in this regime is difficult to gauge. From one perspective it could be that at such low substrate temperatures, the only practical purpose of the heating control is to maintain the substrate at constant temperature throughout the deposition. The heater is used, in effect, to counter the variable heating of the substrate during deposition due to particle bombardment and film growth. The second process control issue relates to substrate biasing during deposition. While none of the depositions carried out in this study used intentional substrate biasing (as a method to control the

[181] There is no such contact because the wafer must rotate at 20 RPM during the deposition in order to ensure film uniformity.

impingement energy of the incident species), substrate *self-biasing* inevitably occurs because it is being allowed to electrically float, uncontrolled, relative to the plasma potential; the plasma potential is a function of the mass of the ions in the plasma, since their mobility is determined by their mass, and so might be expected to vary with plasma gas flow rates. This means that the substrate is subject to charging effects during deposition because it is not grounded. This may well have affected the deposition kinetics in the films for this study; it is, for example, thought to be responsible for the occurrence of unwieldy strains detected in to other films grown with this system [188].

In summary, an inability to achieve deposition repeatability in this study appears to be the result of a lack of sufficient control over the $Er(tmhd)_3$ sublimation process. The effects of variations in the real substrate temperature and substrate self-biasing are open to speculation. Attempting to untangle the coupling of multiple luminescence mechanisms within this kind of a processing framework proved to be a serious challenge. In order to begin to remedy this problem the Er cell (as well as the accompanying carrier lines) requires custom built heating sleeves of high quality along with multiple thermocouples in order to gauge changes in the thermal profile. Secondly, some depositions should be carried out with no substrate rotation, to allow for a contact thermocouple, which can gauge the variation of the real substrate temperature as a function of the other deposition parameters. Finally, an attempt should be made to measure the effect of substrate biasing on the film optical properties, for example, in order to ascertain whether or not it is necessary to introduce manual control.

5.2 Post-Deposition Thermal Processing

5.2.1 Conventional Furnace Annealing

Upon deposition, all samples were diced or cleaved into individual sub-samples for annealing. Dicing was carried out using a Loadpoint MicroAce dicing saw.

No individual sample produced in this way was thermally treated more than once. The parameter space for the annealing consists of three major independent variables:

1) annealing soak time
2) annealing soak temperature
3) the specific type of ambient gas in which the annealing is carried out

This study considered soak times of one and three hours. The soak temperatures were 600, 700, 800, 900, 1000, and 1100 °C. All samples were annealed under flowing ulta-high purity N_2 gas in order to displace O_2 from the ambient. However, a subset of samples was also annealed at 800 °C for one hour under flowing (Ar + 5% H_2) gas. Another subset of samples was annealed at 800 °C for one hour under flowing oxygen gas (~95% purity). To the three variables listed above, one can add the ramp rate to and from a soak/peak temperature, as well as ambient gas flow rate with resultant anneal chamber pressure. These variables were analyzed only for a subset of the total sample space.

Three different annealing furnaces were used in this study. Two of these were standard tube furnaces with quartz tubes and a quartz boat and push rod for sample loading and unloading. The tubes were purged with the relevant process gas at high flow rate (as measured by either a ball flow metre or an oil bubbler) for a period of minutes up to an hour prior to sample loading. Following a high temperature soak, the samples were allowed to cool under the flowing gas atmosphere. Samples were loaded and unloaded with a one to two minute push-in/pull-out to and from the centre of the tube. In these furnaces, the temperature is controlled by a PID (proportional-integral-derivative) controller regulating the power supplied to a resistive heating element, which heats a thick layer of ceramic material in intimate contact with the quartz tube along its entire length. The temperature in the tube reaches a steady state when thermal equilibrium has been established between the ceramic layer and the tube so that they are at the same

temperature. For the temperature range used in this furnace ($\leq$1100 °C) thermal conduction is the dominant heating mechanism because there is comparatively negligible radiative heating below temperatures of approximately 1200 °C. The large thermal inertia of the system coupled with the inherent slowness of thermal conduction (due to the heat capacity of the heating materials) mean that long ramp times are required in order to reach soak temperatures as well as limit setpoint overshoot and large oscillations.

5.2.2 JetFirst 100 RTA Annealing and Calibration

The third furnace used was a JetFirst 100 bench top rapid thermal annealer (RTA) built by Jipelec (a division of Qualiflow Therm, which is, itself, now a division of Semco Engineering Group). The setup of this furnace was part of the work undertaken for this project with the aim of establishing a dedicated, high precision furnace for Si processing. In fact, to this end, RTA equipment is highly engineered and rapid thermal processing theory well refined owing to its popularity in the manufacture of Si ULSI microelectronics (see [189] for a discussion of temperature profile flattening and Chapter 4 of [190] for general principles). It therefore offers several advantages over conventional furnaces from a process control aspect. The main difference from the tube furnaces described above is that the dominant heating mechanism is radiative, with a minimum of conductive heating.

The furnace of the RTA supplies heat in the form of electromagnetic radiation (mostly infrared) produced by a set of twelve powerful, tungsten filament, multizone, halogen lamps. A power source supplies up to 30 kW to the lamps. The lamp filaments themselves can reach temperatures of a few thousand degrees Celsius within a fraction of a second. At these temperatures there is a significant amount of [infrared] radiation produced. The lamp surfaces themselves (made of quartz) are cooled by a 300 litre per second forced air flow (at approximately one atmosphere pressure). This forced air flow prevents the lamp

surface from melting but more importantly eliminates conductive heating. The temperature in the chamber can be controlled solely by the changing electromagnetic irradiance directly from the lamp filament, which can have an extremely fast response time.

A simplified diagram of the JetFirst 100 RTA is shown in Figure 5.1. The process chamber – which surrounds the sample – is a polished aluminum cylindrical wall which seals against a similarly constructed platen with a Viton O-ring. The chamber seal is sufficient to hold a vacuum of 10^{-2} mbar (~7.5 milliTorr) using an optional vacuum pump. Radiation from the lamps passes into the chamber from above through a quartz infrared window. A mirror polished aluminum reflector above the lamps directs errant radiation back into the chamber. Beveled quartz pins resting in the platen support wafers up to four inches in diameter. The process chamber, along with the reflector and platen are water-cooled at all times so that the reaction chamber is termed "cold-wall". This is designed to improve the response time of the chamber to temperature changes. The machine has a readable temperature range from 0 °C to 1300 °C.

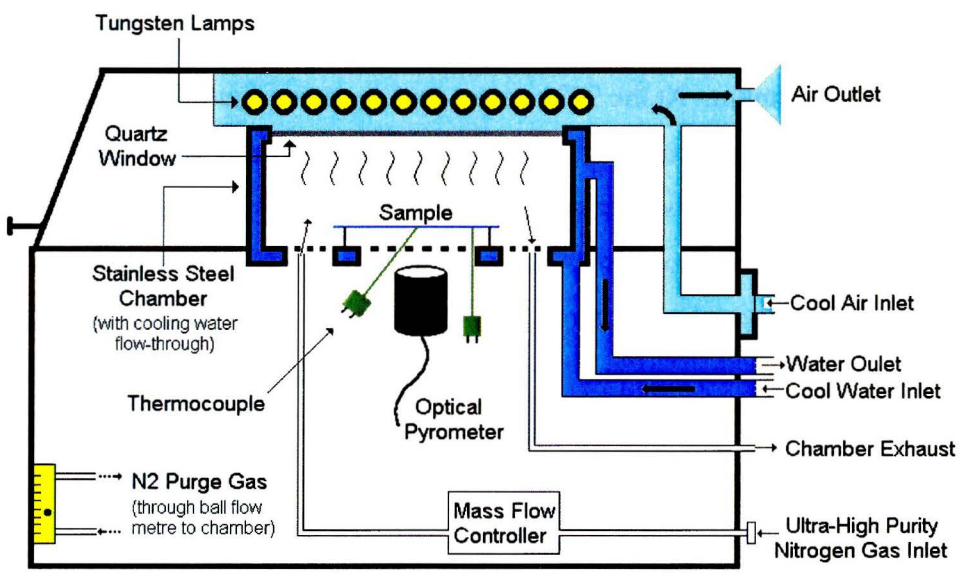

Figure 5.1: Simplified side-view diagram of the Jipelec JetFirst 100 RTA.

Two closed loop temperature control modes are available (employing either a thermocouple or an optical pyrometer as a sensor) as well as one open loop "power control" mode. The first closed loop control employs sheathed K-type (chromel-alumel) thermocouples. Two thermocouples are in contact with the backside of the sample in the chamber: one at the sample edge is used purely for reading the temperature; the second, which is centrally placed, both reads and controls the temperature via a fast response control board employing a feedback loop with a proportional only controller (ie. there is no integral or derivative control). Temperatures up to 1000 °C can be measured in this mode, however K type thermocouples are most accurate somewhat below this maximum value. The second closed loop control mode uses an optical pyrometer which "sees" the bottom of the sample only (not the lamps). The pyrometer detects infrared radiation in the range (4.8-5.2 μm wavelength). It is specifically suited to high-temperature measurement – up to 1300 °C – and cannot be used below 450 °C. A third control option, the "power mode", allows the user to set the actual power supplied to the lamps. Because this mode employs open loop control it does not provide active temperature control – it merely keeps the supplied power fixed. In this case it is, in fact, possible to reach temperatures far exceeding the 1300 °C readable maximum. At the 95% power setting, it was found that a Si wafer would melt completely within a few seconds – and even partially vapourize.

The machine is equipped to supply up to two process gases (N_2 and O_2), each having an electronic mass flow controller (MFC) allowing flow rates up to 1500 sccm (standard cubic centimeters per minute where "standard" refers to STP conditions: 1 atmosphere and 0 °C). A separate purge line is manually controlled using a ball flow metre on the RTA front panel. The external stainless steel line which supplies UHP nitrogen from the gas cylinder to the N_2 MFC has been divided so as to supply the purge gas line as well.

All processing is controlled through the Jipelec Process Image Management System (PIMS), which is a Microsoft compatible Visual Basic

software package operating on a dedicated PC running Windows NT. Annealing recipes allow for precise specification of temperature control mode and numerous setpoints, including gas flow rates, ramp rate (demonstrated from arbitrarily slow to over 200 °C per second with time base of 1 or 0.1 second) as well soak temperature (+/- 2 °C). The software provides significant flexibility in setting the anneal conditions – well beyond that available with the tube furnaces used. The time evolution of the complete set of actual processing parameters during a cycle are tracked, recorded and graphically displayed alongside the corresponding recipe setpoints to allow for real-time visual monitoring during annealing as well as for future reference.

In practice, the system executes with excellent precision, however, some difficulty was encountered in the temperature "calibration" process which later led to inaccurate temperature measurements. The problem occurs because the software has a built-in (pre-defined) linear calibration curve for the thermocouple, which does not actually reflect the true response of the thermocouple and cannot be changed within the software. This was initially a rather curious discovery, given the fact that the user actually runs a so-called "calibration" routine defined in the operating manual. An effort has been made to quantify this error and it should be understood in relation to this "calibration" process.

Temperature Control Theory and Calibration

Temperature control with a micro-controller is a problem analyzed with modern control theory. In a thermal control process there are fundamentally three important "temperature quantities". These are as follows:

1) true temperature → the "real" or actual [output] temperature at the point of contact between the sample and the thermocouple junction
2) displayed temperature → the temperature which the sensor detects and the software then "reads out"; it is based on the potential difference

created in the thermocouple leads. In order that the displayed temperature and the true temperature coincide, it is necessary that the thermocouple calibration curve (mapping the true temperature into the thermocouple electrical output) is known, and that the intervening electronics does not alter this mapping without later correcting for it.

3) setpoint temperature → the input (ie. desired output) temperature which the user specifies in the process recipe.[182]

A schematic of the feedback loop for temperature control in the RTA is shown in Figure 5.2. The thermocouple produces a millivolt signal in its leads as a result of the *true temperature* established at the wafer-thermocouple junction point of contact. This millivolt output is a non-linear function of the *true temperature* over the operating range of the thermocouple. This millivolt signal then passes through an amplifier on the electronics board. The resulting output voltage from

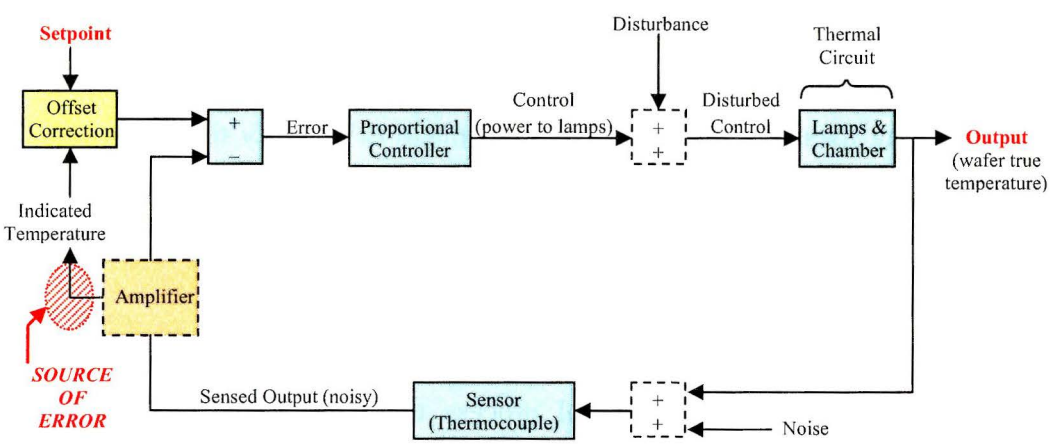

Figure 5.2: Schematic diagram of the temperature control feeback loop based on the thermocouple. The point at which the source of error is introduced is indicated with the red cross-hatch pattern.

[182] Making the true temperature equal to the setpoint is the subject of control theory. A feedback loop must be established with a controller which can adjust the heat supply so that the sensed temperature coincides with the setpoint temperature. This in turn requires that the controller is working with a properly calibrated sensed temperature.

this amplifier is a linear image of the input voltage. The amplifier output lies in an interval from zero to ten volts. The software is programmed to convert this amplifier output voltage into the *displayed temperature* according to a fixed linear relationship VOLTS = (10 x INDICATED TEMPERATURE [°C]) / 1300. An uncorrectable source of error occurs here because this equation assumes that the thermocouple produces a voltage which is a linear function of the *true temperature*, which, as stated above, is not the case. The actual non-linear calibration curve is unknown and the software makes no provision for directly implementing one. The result is an offset between the *true* and *displayed temperature* as exemplified in Figure 5.3.

The "calibration" process consists of executing a recipe which scans the *setpoint temperature* from 50 °C to 1000 °C in thirty second soak increments of 50 °C. The software records the *displayed temperature* based on the thermo-couple. Next, the user compares the *displayed temperature* to the corresponding

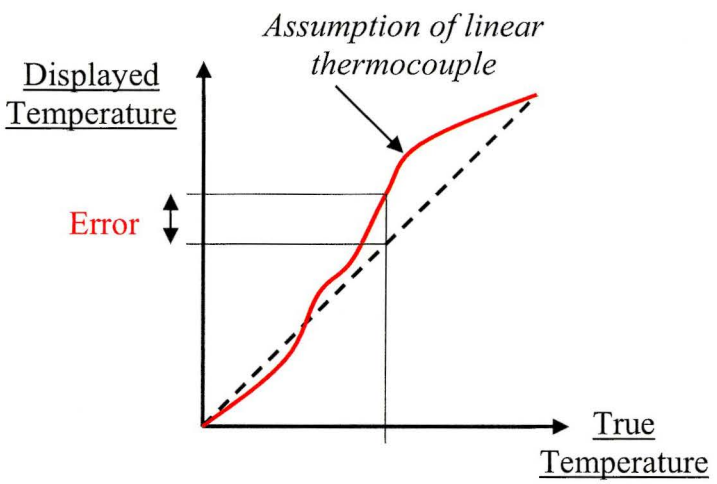

Figure 5.3: Thermcouple calibration error in the JetFirst 100 RTA. In an ideal system, the displayed temperature is exactly equal to the true temperature – this scenario is depicted by the dashed line. With an incorrectly implemented or unknown calibration curve, the displayed temperature (despite having already been corrected for the micro-controller electronics) deviates from the true temperature by an unknown margin or error.

soak *setpoint temperature* so as to calculate a correction factor according to:

$$CORRECTION\ FACTOR = 100 \times (Setpoint\ T - Displayed\ T) / Setpoint\ T.$$

These correction factors are then manually entered into a column in a "calibration" table in the software, each at its corresponding setpoint. If done correctly, this correction factor will eliminate the offset between the *displayed temperature* and the *setpoint temperature.* The reason that this offset occurs can be seen from the feedback schematic (Figure 5.2). Because the micro-controller employs only proportional control without integral or derivative action, there will always be a steady state error between the input and output – provided that the thermal circuit, in this case, is over-damped.[183] The schematic depicts the application of the correction factor to eliminate this error. In this way, the thermocouple calibration process corrects for the error between the *setpoint* and *displayed temperature* without addressing the error between the *true* and *indicated temperature.* In order to ensure process repeatability, within the bounds of the inherent error discussed, the entire thermocouple calibration process should be repeated regularly. The cyclic heating of the thermocouple – especially to temperatures at the high end of its operating range (>600 °C) – anneals and crystallizes the material at the junction which can change its thermo-electric response.

An accurate thermocouple calibration is essential because the optical pyrometer is calibrated based on the thermocouple readout; and a table of offset correction factors is determined analogously to those of the thermocouple. For temperatures beyond 1000 °C, at which the thermocouple cannot be used, the optical pyrometer response is estimated by a linear extrapolation. It is known that

[183] A proportional controller applies a control which is equal to the difference between the setpoint and sensed output, multiplied by a constant gain factor. Increasing the gain decreases the steady state error. However, increasing the gain too far can result in under-damping of the thermal circuit and instability of control leading to oscillation of the *true temperature.* The steady state error occurs because a proportional controller (considering the RTA) only brings the system to a temperature which can be maintained by constant non-zero output from the controller; this temperature must be *below* the setpoint because otherwise the controller output would go to zero.

for a temperature of 1300 °C, the offset between the *displayed* and *true temperature* goes to zero. Optical pyrometers often rely on a precise knowledge of the [temperature dependent] sample emissivity (ratio of the radiation actually emitted from a material to that of a perfect blackbody at the same temperature) in order to convert the radiant spectrum into a temperature. This is not the case for this system because a thermocouple is used to calibrate the radiant emission of the sample, seen by the pyrometer, as a function of its *true temperature*. However, thermal cycling of the sample, especially in the event that it causes oxide films to form, can affect the emissivity. Changes in the emissivity, while not needing to be quantified, will necessitate re-calibration with the thermocouple. For this reason pyrometer calibration must be carried out regularly. Evidently, an error in the calibration of the thermocouple itself will render an error in the pyrometer calibration and the two may not even agree with each other during actual processing.

An attempt to quantify the error resulting from the *displayed/true temperature* offset, within the most important temperature range for this project, was made by growing SiO_2 on single crystal Si substrates by the process of dry thermal oxidation under flowing oxygen gas. Highly accurate, though somewhat empirical, models of SiO_2 growth kinetics on Si are available owing to the historical prevalence of this system in CMOS processing – including the deep sub-micron regime. For this present study, single wavelength ellipsometry (Ellipsometer model PZ2000 manufactured by Philips) at 632.8 nm was used to determine the thickness of the SiO_2 film. Two separate rounds of calibration were carried out approximately six months apart. The first calibration consisted of two sets of growths:

1) Czochralski Si (100) doped with boron to a resistivity of ~1 Ω·cm. Oxidations were carried out at setpoint temperatures of 800, 850, and 900 °C, each for a soak time of 60 minutes, under a 500 sccm flow of high purity oxygen gas.

2) Float zone Si (100) with a resisitivity of ~4000-8000 Ω·cm. Oxidations were carried out at setpoint temperatures of 800, 850, and 900 °C, each for a soak time of 180 minutes, under a 500 sccm flow of high purity oxygen gas.

The second calibration consisted of one set of growths over a greater selection of setpoint temperatures. Substrate doping levels were low enough such that they should not significantly enhance the oxidation rate. Samples were cleaned and etched with hydrofluoric (HF) acid prior to oxidation. All anneals were carried out in the thermocouple control mode. Figure 5.4 shows the measured thickness of the resulting SiO_2 film along with the thicknesses predicted by both the Han and Helms SiO_2 growth model [191] as well as the Massoud growth model which is implemented in the Silvaco semiconductor device simulation software [192,193].

The conditions used for these oxidations put the growth within the so-called thin oxide regime (< 500 Å), characterized by an anomalously high growth rate. The simple Deal-Grove model [194] does not accurately account for the initial rapid oxidation kinetics. More sophisticated models are required, two of which are compared in Figure 5.4. No attempt will be made to discuss the physical basis of these models here, however all are known to be in excellent agreement with data for the thin oxide regime. It is evident from the figure that the error between the true and displayed temperature was approximately 45-55 °C in the first calibration and 65-75 °C in the second calibration, with the true temperature being greater than the setpoint. Since the same thermocouple was used for both sets of calibrations, the increase in the thermocouple error over time confirms the detrimental effect of the cyclic heating on the metal junction. This is important because RTA systems (specifically the halogen heating bulbs) are typically not designed for the long duration anneals that the present system is being used for (i.e. processing of Si-rich SiO_x films); they are designed for anneals on the order of seconds to a few minutes. Beyond this, the halogen bulb lifetime could be severely shortened (it is probable that their lifetime is only ~500

by a few tens of degrees Celsius over a period of one hour, after which there is again a phase of stability. If this RTA system is to be used for this type of demanding processing (high temperatures and long durations), frequent re-calibration of the thermocouple will be required to keep the error below a certain threshold. Initial work on the effect of rapid thermal annealing on the films of the present study (using soak durations of 10-60 seconds) suggests that short anneals could be a viable processing option, provided that one is willing to sacrifice perhaps 20% of a film's potential luminescence yield near 1.54 μm.

5.3 Photoluminescence Characterization

The technique of *photoluminescence spectroscopy* (also known as *fluorometry*, especially among chemists) is a common materials characterization technique whose utility lies in making the connection between the electronic structure and optical properties of materials. In this technique, a material is illuminated with light and, absorbing some of the electromagnetic waves, may re-emit them at a different frequency. The measurement of this characteristic emission can allow the identification of various luminescent centres (especially radiative defects). Identifying the centres and tracking changes in their emission line-shape and relative intensities as a function of numerous variables[184] can give valuable insight into the changing bond complexes and defects present in the material.

Single wavelength laser-excited photoluminescence (PL) spectroscopy was used to characterize the luminescent emission from the Er-doped Si-rich SiO_x samples of this study. The excitation source is a continuous wave, 17 mW, He-Cd laser (manufactured by Kimmon Electric Co. model IK3151R-E) operating at a wavelength of 325 nm[185] (single mode – TM) with a spectral bandwidth of 3

[184] Examples of these variables include film preparation conditions, heat treatment, ambient temperature, excitation conditions, etc.

[185] The selection of the laser wavelength in a single wavelength PL system that is being used to measure sensitized luminescence must be carefully chosen so as not to cause erroneous results because of undesired resonant pumping of the acceptor species (eg. erbium).

GHz (corresponding to a wavelength spread of about 0.00106 nm). The system is set up to allow the beam to follow one of two different paths. The system schematic is shown in Figure 5.5 and should be referred to throughout the following two sections.

5.3.1 Infared Photoluminescence Measurement

For measurement of near-IR PL in the wavelength range from 900 to 1700 nm, the laser beam is passed through a mechanical chopper operating at a frequency of approximately 325 Hz.[186] The modulated beam is incident on the sample with an effective power density of approximately 0.26 W/cm^2 (approximate photon flux of 4.3x10^{17} photons/cm^2). The effective power density is the total incident power density minus the power density reflected from the sample surface[187]; these measurements are made with an optical power meter (model P3000 manufactured by Kimmon Electric Co.). A portion of the resulting PL emission cone – which is modulated at the chopper frequency because of the modulated excitation – is gathered with a collimating lens and directed into a grating monochromator (model SpectraPro-500i manufactured by Acton Research Corporation) using a focusing lens (both lenses are un-coated). A long pass filter is placed just in front of the entrance slit of the monochromator to remove any harmonics of the laser beam itself generated from the sample surface. The entrance and exit slit of the monochromator were both set to 3 mm.[188] Light selected by the grating within the monochromator is directed onto an InGaAs photodetector (model ID441 manufactured by Acton Research Corporation). Custom written LabView® soft-

[186] Lock-in detection usually avoids chopper frequencies that are multiples of 60. Note also that towards the end of this study, it was found that decreasing the chopper frequency below 20 Hz and raising the low pass filter RC time constant to 1 second significantly improved the signal-to-noise ratio of the measured PL.

[187] Note that the effective power density exciting the sample should, in principle, be measured explicitly for every sample. The values are based on measurements from a previous study.

[188] This is well above the diffraction limit for the PL wavelengths being measured, however the PL peak FWHM is still a function of the slit width in this size regime. Note that the grating in the monochromator is large enough to receive the image of the 3 mm slit.

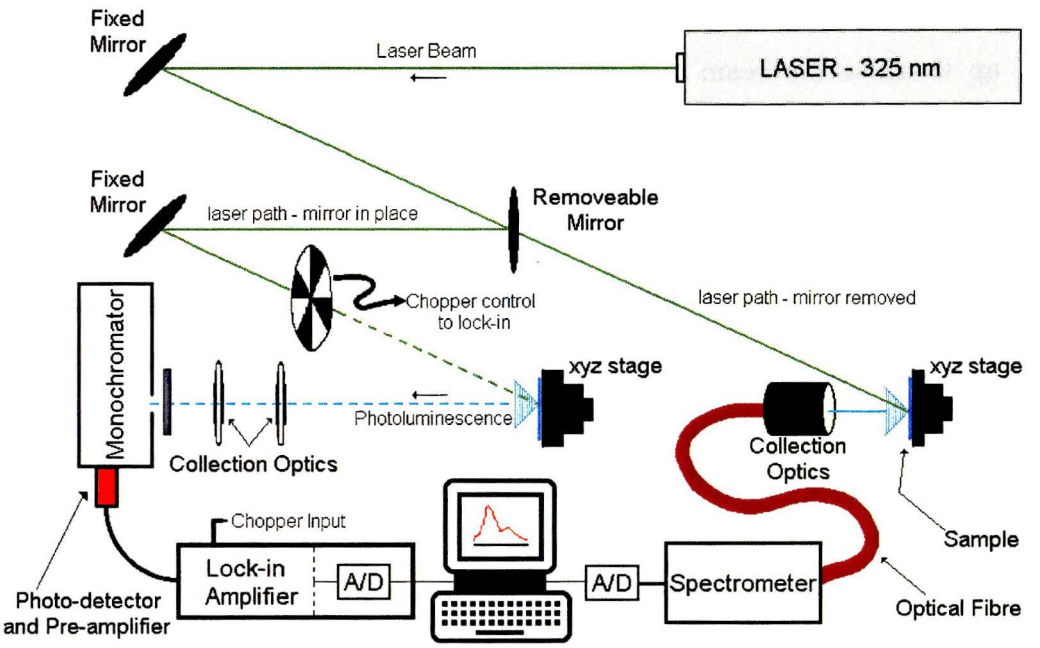

Figure 5.5: Schematic diagram of the single wavelength photoluminescence spectroscopy apparatus as used throughout this research project. Although both laser beam paths are shown simultaneously, the removeable mirror allows only one path to be followed at a time.

ware drives a stepper motor used to rotate the grating so that only light of a narrow wavelength band impinges on the photodetector at any given time, allowing a range of wavelength space to be scanned in sequence. The electrical output from the photodetector is pre-amplified at source and then connected to a lock-in amplifier (model SR510 manufactured by Stanford Research Systems Inc.). The chopper controller (model SR540 manufactured by Stanford Research Systems Inc.) is also connected to the lock-in amplifier.[189] The lock-in amplifier

[189] Using the square wave input from the chopper as the reference frequency, the lock-in amplifier amplifies only the signal from the photodetector having frequency components within an extremely narrow band of this reference. Signals at other frequencies (which should include most of the obscuring noise) are rejected, along with signals at the reference frequency but which are not phase coherent with it. The lock-in amplifier achieves this by using a linear phase detector which mixes the input and reference signals and then passes the output – a DC signal dependent only on their relative phase – through a narrow low pass filter. The user sets the RC time constant of the low pass filter to specify the filter bandwidth (often approximately 0.1-1 Hz) which

contains an internal A/D converter, the output from which is read and displayed on a computer using the LabView® software. The spectral response of the system has been measured to be flat from 1350-1650 nm, so that no correction of the PL spectra measured in this study is necessary. As a result, the units of PL intensity in this wavelength range are not absolute. The spectral resolution is a function both of the groove density of the grating and the diameter of the entrance slit to the monochromator. For this study, the spectral resolution was limited by the wavelength step size, which was 1 nm in all cases. Note that the measurement repeats with about a 0.01 nm error.

5.3.2 Visible Photoluminescence Measurement

For measurement of PL in the wavelength range from 350-950 nm, the laser beam is directed, un-modulated, by an alternate route relative to the above (IR) scheme, onto the sample with an effective power density of 0.64 W/cm^2 (approximate photon flux of 1x10^{18} photons/cm^2)[190]. A portion of the PL from the sample is then collected and coupled into an optical fibre using a collimating and focusing lens fastened in a lens tube and mounted on a xyz translation stage. The optical fibre is butt-coupled to the entrance slit (50 μm width) of a grating spectrometer (model S2000 manufactured by Ocean Optics). Inside the spectrometer, the light is dispersed by a fixed grating and the entire signal is simultaneously incident on a linear CCD (charge coupled device) array of some 2048 (readable) detectors such that each cell measures a different wavelength component. Spectral calibration, relating the pixel position to the measured wavelength is carried out with a mercury (argon) lamp (Oriel Hg (Ar)-6035). A polynomial fit has been made for the pixel number as a function of wavelength. This fit introduces an error into the wavelength calibration, which is a function of the wavelength itself but is always

---

determines the signal to noise ratio. This is a common technique which enables weak signals to be extracted from noise which may be orders of magnitude larger than the signal.

[190] Note that the effective power density exciting the sample should, in principle, be measured explicitly for every sample. The values are based on measurements from a previous study.

≤0.4 nm. To determine the spectral resolution, a Gaussian fit has been made of the broadening of a spectral line of approximately zero width (generated by a Na vapour lamp) after having passed through the system optics (including the entrance slit). This Gaussian had a FWHM of about 2 nm.

The spectrometer output connects to an A/D converter so that the measured data is displayed on a computer using software (OOI color/OOII rad) from Ocean Optics. The signal to noise ratio of the data is improved by integrating the signal from the CCD for a fixed period of time (usually 2500 ms), averaging a number of scans (usually 10) and applying a boxcar smoothing algorithm (usually over 2 spectral points). Because the fibre optic does not sufficiently attenuate residual artefacts from the laser line such as the second harmonic, it is necessary for the lenses to have a filter coating which attenuates low and high wavelengths.

Although all measurements were taken on this system with the room darkened, the software was used to perform a dark current scan (with the laser beam shuttered), which is then automatically subtracted from the subsequently measured spectra. The spectral response curve for this system (including the transmission optics and spectrometer) is highly non-linear over the wavelength range of interest for this study and so a calibration is required (see [195] for a complete discussion of these PL measurements and the system calibration).[191]

In order to facilitate a correlation of the observed spectral content with the electronic transitions of matter, it is necessary to convert the measured spectral irradiance into a photon flux (photons per second per square centimeter per one nanometer bandwidth). This permits the identification of the photonic wavelength of an electronic transition. The necessary conversion can be carried

[191] This is performed with an LS-1-Cal optical source (Ocean Optics) whose spectral irradiance is absolutely calibrated by the National Institute of Standards and Technology (NIST) – which is an agency of the U.S. Commerce Deparment's Technology Administration. Correcting the measured data with this lamp spectrum takes account of the spectral response of the entire system (including the collection optics) and allows the intensity to be given in units of spectral irradiance (microwatts per square centimeter per one nanometer bandwidth).

out knowing that the spectral irradiance I is the total optical energy per unit area A per unit time t per unit bandwidth $\Delta\lambda$ (i.e. total optical power per unit area per unit bandwidth); the total optical energy is equal to the number of photons n incident at a given energy $E = hf = hc/\lambda$:

$$I = \left(\frac{nhc}{\lambda}\right) \Big/ (At\Delta\lambda) \tag{5.1}$$

So that the photon flux density per unit bandwidth, defined by

$$\Phi_{photon} = \frac{n}{At\Delta\lambda} \tag{5.2}$$

is given in terms of the spectral irradiance I by:

$$\Phi_{photon} = \frac{I\lambda}{hc} \tag{5.3}$$

The correction that this unit conversion produces is not large. It is most significant at the longer wavelengths of the nano-cluster PL emission and is illustrated in Figure 5.6.

Since the collection optics is only receiving a portion of the cone of light emission from the sample (which was not precisely measured in this study), the absolute photon flux density is not necessarily a meaningful value in terms of calculating quantum efficiencies. In order to avoid the huge numbers that would be associated with an absolute photon flux density, it is sensible to normalize this quantity in such a way that the normalized quantity can easily be calculated from the measured spectral irradiance. This is achieved by multiplying the photon flux density (which has units of $photons/cm^2/s/nm$) by the normalizing factor $\{10^{15}hc\}$ (where h is in units of J's and c is in units of m/s) to give a normalized photon flux density (which has units of $\mu W photons/cm^2$, i.e. arbitrary units) which is simply

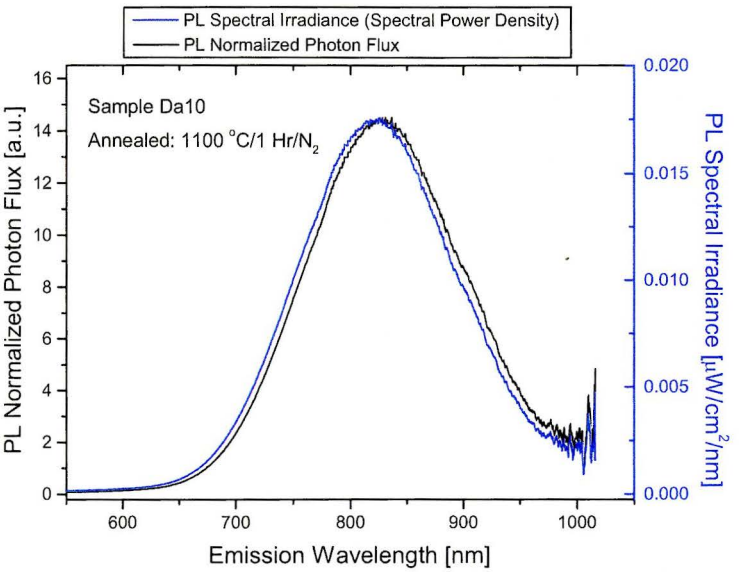

Figure 5.6: Effect of the conversion, from spectral power density (irradiance) to normalized photon flux, on the wavelength axis. The PL emission in this figure corresponds to Si nano-cluster emission.

calculated by multiplying each measured value of irradiance (in units of $\mu W/(photons)/cm^2/nm$) by its corresponding wavelength (in nm). This normalized photon flux quantity is presented for all PL data presented in the 350-950 nm wavelength range for this thesis (unless otherwise indicated).

Unfortunately, it was not possible to make comparisons between the PL data gathered in the two main spectral ranges on the system described here for this study. That is, infrared spectra could not be compared to visible spectra. The use of different detectors, different electronics, different collection optics, and different values of the incident laser power preclude such a comparison at this time.[192] In order to facilitate such comparisons in the future, one standard Er-doped Si-rich SiO_x sample annealed at 1100 °C which emits luminescence both

[192] In order to facilitate comparison between PL measurements taken at different times throughout the duration of the project, stable reference samples were assigned for both the IR and visible systems. These were scanned and the system optics adjusted as necessary in order to equalize the reference spectrum with that from previous measurements.

near 800 nm and at 1535 nm has been sent to England where its luminescence over all wavelengths was measured absolutely (allowing direct comparison over all wavelengths). The respective luminescence decay times were also measured absolutely. This sample will be used as a calibration standard to facilitate such comparisons and PL lifetime measurements on all samples measured on the present system.

5.3.3 Optical-Geometrical Effects in Photoluminescence Spectroscopy

The apparent simplicity of the PL spectroscopy technique makes it one of the most abused optical characterization methods in applied physics literature. At the very least, the data *must* be carefully corrected for the system response (described in the previous section) to have any meaning whatsoever. It is completely erroneous to discuss luminescent transitions, splitting or peak shifts without such a correction. The dramatic effect of the data correction for this study is illustrated in Figure 5.7. However, the problem is made even more complicated by spectral modulation due to the various geometrical effects (independent of any instrumentation-based data modulation); reference [196] provides an excellent re-

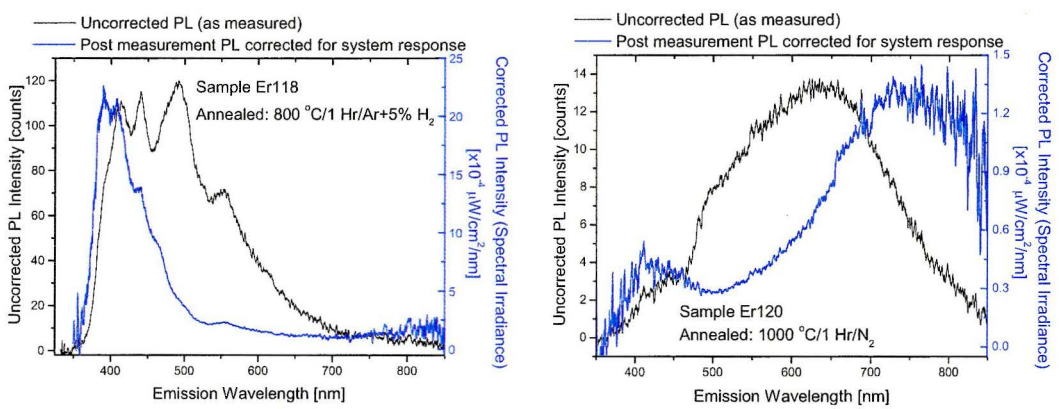

Figure 5.7: Depiction of the effect of the system correction to the PL data in the visible wavelength range. Note that the emission lines in the uncorrected spectrum of part (a) could easily be interpreted as Er^{3+} visible transitions.

view of these effects.[193] The air/film/substrate system is quite analogous to a Fabry-Perot etalon and therefore exhibits [micro]cavity-type interference[194] effects, which can modulate both the incident laser intensity profile within the film (as a function of depth) *and* the PL emitted from the film. The effect becomes more severe as the reflectivity of the film/air and film/substrate interfaces increases. This is because beams of light, whether they originate from luminescent centres within the film or from the incident laser beam, will undergo multiple reflections inside the film, with some transmission occurring at each interface. These transmitted beams will interfere with each other giving rise to either constructive or destructive interference, which is a function of the angle of transmission from the sample. Thus, the interference re-distributes the optical energy density into the regions of constructive interference.

The interference condition is a function of wavelength because, in a given direction, the film thickness will only force interference at those wavelengths satisfying what amount to standing wave boundary conditions. Therefore, the optical energy re-distribution only pertains to certain narrow bands of wavelength which are dependent on the direction of emission. In this way, the angle of detection of the PL becomes a factor in the spectral shape (as does the angle of incidence of the laser excitation since it determines the location of the nodes and antinodes in the film). The measured PL spectra are a convolution of the true (undistorted) emission and a geometry-dependent modulating function based on interference. This can give rise to *apparent* peak shifts and splittings in the PL which are spurious geometric artifacts not indicative of the actual electronic transitions in the sample.[195]

---

[193] It is common in the literature to deposit thick Si-rich SiO_x samples for PL measurements because of the often weak signal. However such micron-thick films give rise to numerous interference effects.

[194] This is the effect used in lasers to provide the optical feedback that allows amplification of the emission in certain narrow frequency bands (ie. the cavity lasing modes).

[195] On an even more sophisticated level, the convolution of the spectra also involves the depth distribution profile of luminescent centres; this is not even constant among samples of the same thickness when the composition changes.

One can get a *qualitative* sense of the effect of the various film geometrical parameters by considering the interference to arise from multiple reflections within a single highly reflective dielectric layer that is identically clad above and below by another medium. The spacing between adjacent maxima $\lambda_2 - \lambda_1$ is then given by:

$$2n_o d\cos\theta = \left(\frac{1}{\lambda_2} - \frac{1}{\lambda_1}\right)^{-1} \tag{5.4}$$

where n_o is the film index of refraction, d is the film thickness, and θ is the angle of incidence inside the film. The film thickness at which interference effects may become important occurs when the fringe spacing is of the same order of magnitude as the undistorted PL spectral bandwidth. From equation 5.4, this depends on the emission wavelength λ under consideration and the refractive index of the film. For example, in the present study, the PL is detected normal to the film surface so that the critical d and λ can be *estimated* by the simple boundary condition that a standing wave can exist for d equal to an integer number m of half-wavelengths: $\lambda=2n_od/m$. Thus, for $\lambda=400$ *nm* emission, and $n_o=1.5$ (which is a common condition for defect luminescent films in the present study) a film as thin as 133 nm could show a cavity effect. For nano-cluster luminescence near 850 nm in a film of index 1.6, the minimum thickness for these effects would be about 265 nm. The danger here is that because of wide PL emission bands, regardless of the film thickness (beyond the minimum value at m=1), there could always be wavelength ranges that are enhanced due to cavity effects – giving rise to erroneous fine structure – with relative intensities that are further dependent on the detector angle.

Additionally, a normally incident 325 nm laser beam can form a standing wave in a 108 nm thick film of index 1.5 (for film index 1.6, critical thicknesses are at 102, 203, 305 nm...). The critical thickness spacings become even tighter for higher n. One can conclude that confinement of the luminescent centres into a thin layer ($d<\lambda/2n_o$) makes their excitation particularly sensitive to the

nodes/antinodes of the incident laser intensity [167] (which become more numerous as the laser wavelength decreases) and film/cladding refractive indices (which depends on the composition).[196]

In the present study, one film in particular has potential to exhibit interference effects. This is sample Er118, which formed the surface micro-structure upon annealing as shown in the SEM images in Chapter 4. The SEM images show that the spherical-cap domes are, on average 4-10 microns in height at the centre and 20-80 microns in diameter. Figure 5.8 shows a schematic diagram for the presumed geometry of the dome micro-structure.

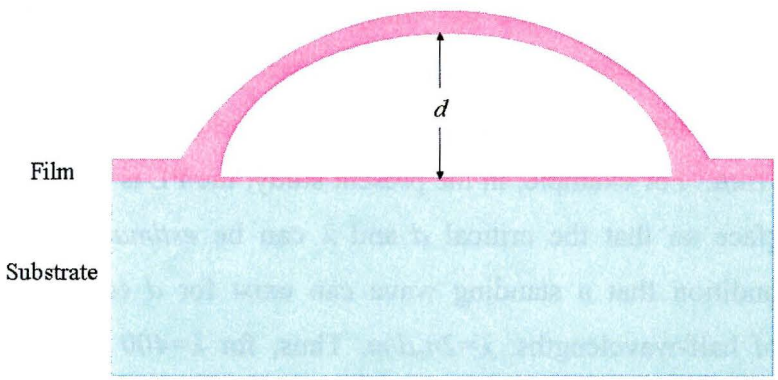

Figure 5.8: Schematic of the dome micro-structure which forms after annealing of sample Er118. Althoug the dome is not drawn to scale, the relative proportions of the film thickness on the substrate and in the bubble should be fairly accurate as determined by etching of the annealed films in hydrofluoric acid.

It should be a reasonable assumption that the un-modulated spectrum is similar to that of Er116, so that by using the various peaks identified in Figure 5.9, equation 5.4 can be used to estimate the layer thickness d. One can assume that n_o is nearly equal to unity since the domes are presumably filled with air (or the out-gas from the deposition); θ is approximately 37°. Table 5.2 presents the calculated values for d.

[196] That is, for thicker films, the effect of the laser intensity modulation tends to average out more.

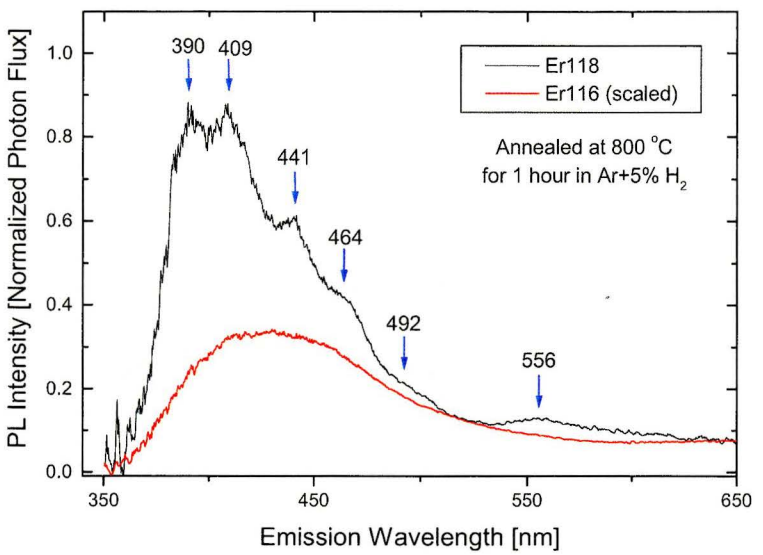

Figure 5.9: Sample Er118 PL spectrum showing the fine structure spectral features. The scaled PL spectrum of sample Er116 is shown since it is assumed to form the basis for the un-modulated spectrum of Er118.

λ_2 [nm]	λ_1 [nm]	d [μm]
390	409	4.20
409	441	2.82
441	464	4.45
464	492	4.08
492	556*	2.14

* This is probably an Er upconversion peak since it appears in other spectra

Table 5.2: Calculated values for the dome thickness of sample Er118 based on the measured peaks in the PL spectra and the interference equation (5.4). The $\lambda_{1,2}$ values are the peak wavelengths isolated in Figure 5.9.

It is apparent that the calculated layer thickness is in good agreement with that measured by SEM, suggesting that interference effects cannot be ruled out as part of the explanation for the peaks.[197] There is likely a softening of the features in

[197] While the interference calculation generally supports the peak structure, another explanation for the peaks is the superposition of Er up-conversion luminescence with some smoother oxide defect luminescence peaks. While up-conversion to these high energy levels is a very high order process,

the experimental spectrum to some extent because of the simultaneous sampling of domes of different thickness.

5.4 Ion Irradiation Study

5.4.1 Pre-irradiation Sample Preparation

For this study, sample Er149 was selected specifically because it appeared to exhibit significant oxide-defect sensitized Er luminescence with little to no formation of Si nano-clusters. Several small pieces of sample Er149 were cleaved from the as-deposited film. These pieces were all subject to an anneal step designed to maximize their PL emission at 1.54 μm: 800 °C for 3 hours duration in flowing N_2 gas. Once the samples were annealed, their PL spectra were measured both in the infrared and visible wavelength bands; these spectra are designated 'pre-irradiation' PL. Following this, the samples were subjected to a *damaging* irradiation, with beam parameters carefully chosen to avoid doping of the films through premature stopping of the projectile ions.

5.4.2 Ion Irradiation at the University of Western Ontario

Ion irradiation was carried out using the 1.7 MV Tandetron accelerator at the University of Western Ontario. Si^+ ions were implanted with an energy of 1 MeV. In all cases, the sample was tilted 7° from the normal. The most important experimental parameters are shown in Table 5.3. Immediately following irradiation, the samples were divided into two groups: one group to undergo positron annihilation spectroscopy and the second to undergo stepwise annealing and PL measurements.

---

the Er118 sample does have a very high Er content. All but the 464 nm feature could be Er^{3+} energy levels and the sharpness of the peaks supports this notion (this possibility will be explored in detail in Chapter 6). However, Er147 (which displayed an even higher Er content) does not show such fine structure.

Ion Fluence [x10^{12} Si^{+}/cm^{2}]	Irradiated Area [cm^{2}]	Ion Dose [particle μC]	Irradiation Duration [min:sec]	Beam Current [nA]	Chamber Temperature [°C]	Chamber Pressure* [x10^{-7} Torr]
1	8.970	1.4370	?	?	~23	~0.3-0.4
5	3.63	2.9076	1:34.79	30.67	~23	~1
10	3.63	5.8153	3:13.15	30.11	~23	~1
20	3.63	11.6305	6:01.51	32.17	~23	~1
40	3.63	23.2610	10:7.12	38.31	~23	~1
50	8.970	71.8497	8:16.46	144.7	~23	~0.3-0.4
1000	3.63	581.526	?	?	~27.3	~1

* During irradiation

Table 5.3: Experimental parameters for the irradiation of film Er149 with 1 MeV Si^{+}. Note that the sample heating caused by the ion beam was negligible in all cases.[198]

5.4.3 Beam-based Variable Energy Positron Annihilation Spectroscopy

Positron annihilation spectroscopy (PAS) was carried out using the slow positron beam facility at the University of Western Ontario.[199] A full description of the apparatus has been given elsewhere [197]. The system generates a nearly mono-energetic positron beam, from a ^{22}Na source with a thin transmission moderator (to slow down the high energy positrons), with energy tunable between 0 and 80 keV. Low energy positrons, such as those below 5 keV permit investigation of thin film samples and surfaces. The present study used a beam with variable energy between 0.5-33 keV corresponding to mean implant depths in SiO_2 ranging from 5 nm to 4 μm. An intrinsic Ge detector is used to measure the gamma ray energy distributions resulting from the positron annihilation events. The S and W-parameters are measured for the range of incident positron energies. All measurements are carried out under ultra high vacuum (10^{-9} – 10^{-8} Torr). In-situ annealing of samples (under vacuum) can be carried out while measurements

[198] Interestingly, after the irradiation, only the sample irradiated at the highest fluence showed a change in the colour of the film relative to the un-irradiated material (this was gauged by the shadow from the sample clip holder). This is usually related to a change in the refractive index related to irradiation damage, especially amorphization in crystalline materials.

[199] See Appendix C for a review of PAS theory.

are being made. This allows the investigation of changes in the S-W values at a particular positron energy (sample depth) as the material undergoes thermally induced structural changes. For the present study, the temperature was continuously ramped from room temperature to 600 °C over a period of about 5 hours. The R-parameter, providing an indicator of the formation of positronium, was also measured during the annealing studies.

Four samples were selected, immediately following irradiation, to undergo PAS measurements: un-irradiated, $1x10^{13}$ cm^{-2}, $4x10^{13}$ cm^{-2}, and $1x10^{15}$ cm^{-2}. Each post-irradiated sample was measured at room temperature. Following this, the two samples corresponding to irradiation fluences $1x10^{13}$ cm^{-2} and $1x10^{15}$ cm^{-2} were selected to undergo the in-situ annealing measurement to 600 °C. These two films were subsequently annealed to 800 °C under flowing N_2 gas in the RTA previously described (Section 5.2.2). Their room temperature positron annihilation spectra were then re-measured at variable energies.

In order to provide a measurement standard, spectra were taken for a sample of virtually defect-free single crystal Si. The S and W-parameters from this sample at energies greater than 20 keV (corresponding to the bulk material) were used to normalize those parameters as measured in the irradiated films.

5.4.4 Post-irradiation Annealing and Photoluminescence Spectroscopy

Samples returned to McMaster University immediately underwent a measurement of their PL spectra in both the visible and infrared wavelength ranges prior to any heat treatment. Following this, all samples were subjected to stepwise isochronal annealings of ten minute duration. The temperature sequence was as follows: 150, 250, 300, 350, 400, 450, 500, 550, 600, 650, 700, 750, 800, 900, 1000 °C. Although all of the samples were annealed at every temperature, a set of PL measurements was made only for a subset of anneal temperatures.

Chapter 6

Parameter Space Map and Luminescence Optimization

Having discussed a theoretical model for the sensitization of the Er-related photoluminescence (PL) at 1.54 μm in a Si-rich SiO_x matrix (Section 3.4), those film properties which are most important in optimizing the transfer can be identified and fine-tuned by appropriate processing steps. This should maximize the efficiencies of the initial photon absorption by a sensitizing centre, the subsequent energy transfer to the Er centre, and the radiative Er emission itself. In practice, this optimization process involves two interdependent variables:

1) Composition of the film: this includes optimizing the relative concentration of Er and excess Si in relation to any impurities in the film which may enhance the sensitization mechanism (for example carbon or hydrogen).
2) Bond structure of the film: this includes optimizing the concentration of *optically active Er*, optimizing the ratio and relative location of optically active Er to sensitizing centres so as to maximize the coupling, and minimizing non-radiative mechanisms and complexes with a propensity to quench the luminescence process at any one of its stages.

These variables are strongly coupled and depend intimately upon all of the deposition parameters as well as the post-deposition anneal temperature, time, and ambient. The optimization process and flow of variables is depicted in Figure 6.1.

As Figure 6.1 illustrates, the term "optimum composition" is only meaningful with respect to a particular annealing treatment. For this reason, and to avoid confusion since there are a large number of results, this chapter will begin by looking at a graphical representation of the integrated PL intensity at 1.54 μm as a function of both the annealing conditions and the film composition. The PL data at 1.54 μm will be considered first since this emission is the original focus of the project. That will motivate an analysis of luminescence mechanisms which will lead to the presentation of PL emission spectra at other wavelengths.

To date, most studies carried out on this material system have focused on employing a variety of characterizaton techniques over a small selection of film

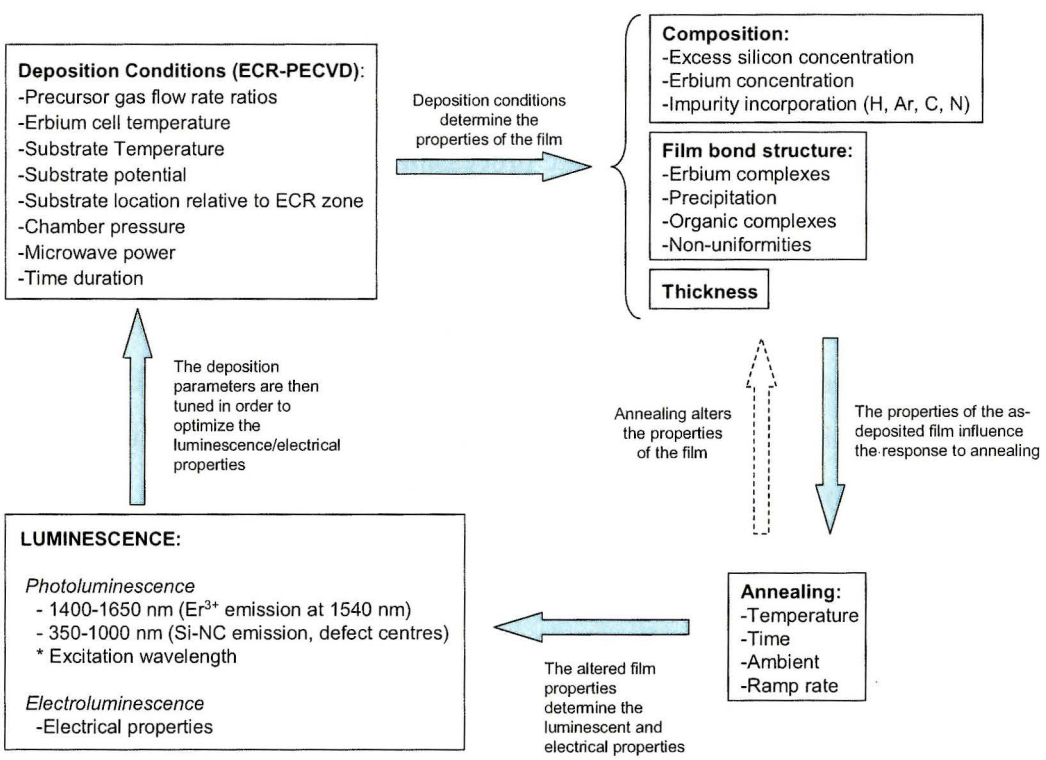

Figure 6.1: The engineering cycle for optimizing the luminescence properties of SiO_x:Er thin films deposited by ECR-PECVD. The dominant coupling relationships between the variables are illustrated.

compositions and heat treatments. They attempt to measure specific quantities that isolate precise aspects of luminescence and structural models. In *this* study, however, the approach has been to apply a small number of characterization techniques over a wide range of film compositions and heat treatments (a process most effectively handled with the aid of statistical modelling techniques such as 'design of experiment'). Many of the well-defined results in the literature are necessarily narrow in scope, so this study seeks to assess the trends in these results over a wider portion of the ECR-PECVD sample processing space. In this way, the broader applicability of specifically modelled aspects can be established.

6.1 Er^{3+} Luminescence Line-Shape of the $^4I_{1/32} \rightarrow {}^4I_{15/2}$ Transition

Three representative PL spectra have been selected to illustrate the structural features of the emission at various film compositions (Figure 6.2(a)) for similar anneals at 800 °C; one composition is shown at various anneal temperatures (Figure 6.2(b)).

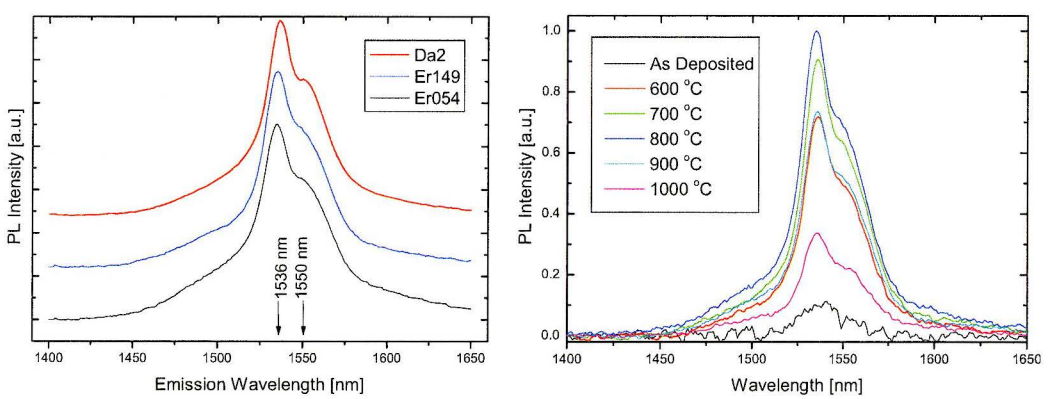

(a) (b)

Figure 6.2: Examples of Er-related PL from Si-rich SiO_x:Er thin films; (a) different compositions annealed at 800 °C; (b) single composition (Er120) annealed for one hour at several different temperatures in flowing N_2 gas.

The spectra are characterized by a primary peak at 1536 nm (0.8072 eV; 6510 cm^{-1}) and a secondary peak (shoulder) at 1550 nm (0.7999 eV; 6452 cm^{-1}), with the latter having a peak intensity approximately 70% that of the primary peak. This luminescence lineshape is very characteristic of the Er^{3+} ion and is easy to identify as the transition from the $^4I_{13/2}$ to $^4I_{15/2}$ manifold [60]. The fine structure is the result of the Stark splitting of the energy levels within each manifold. The resulting lineshape function (as shown above) is a superposition of overlapping Stark split levels which are not well resolved at room temperature. This is not surprising given that there could be up to 56 distinct transitions (Section 3.1.2). There is also expected to be considerable inhomogeneous broadening originating from two sources:

1) *The host matrix is a highly amorphous material* (resembling a multi-component glass). Therefore, the coordination of the Er atoms will exhibit some randomness, aperiodicity, and asymmetry resulting in several types of sites. The variation in the phonon spectrum at different sites can randomize the phonon broadening (see pages 225-226 of [60]).

2) *The host matrix contains multiple phases.* Therefore, the perturbation of the local fields near the Er^{3+} ions resulting from composition dependent fluctuations (eg. Si nano-clusters) of the dielectric function can randomize both the Stark splitting and the spontaneous emission rates for the various Er^{3+} transitions (see section 3.3.2 - "cluster size effects" subsection).[200,201]

Because PL spectra are based on a highly macroscopic measurement relative to individual Er sites, they represent a superposition (or average) over all of the

---

[200] Spectral broadening of Er^{3+} luminescence resulting from inhomogeneities of the dielectric function (which become more severe with increasing excess Si) occurs because "interfaces" in the refractive index (dielectric function) modify spontaneous emission rates.

[201] Apparent inhomogeneities of the dielectric function have even been suspected in Er implanted Si-rich SiO_x superlattices with size-controlled Si cluster size distribution since larger clusters resulted in a wider Stark splitting. (See: V. Yu. Timoshenko, et. al., J. Appl. Phys. **96**, 2254 (2004)).

different sites. Changes in the spectral lineshape would therefore be suggestive of overall variations in the structure of the matrix – *especially* in the coordinating shell of the Er – and corresponding changes in the relative populations of different Er sites.

In this study we did not observe significant changes in the *lineshape* of this transition ($^4I_{13/2} \rightarrow {}^4I_{15/2}$) despite the broad range of film compositions and annealing treatments considered. This is exemplified in Figure 6.2. Variation of the full width at half maximum (FWHM) of the peak was invariably within (38±5) nm over the entire study. As a function of annealing, many samples showed a gradual increase (3-4 nm) of the FWHM with increasing temperature from 600 to 900 °C followed by a decrease of ~3 nm at 1000 or 1100 °C. This suggests that low anneal temperatures are dominated by the formation of a diverse array of optically active Er complexes, whereas the high temperatures (>1000 °C) are dominated by the precipitation of pure Si and Er, with the latter reducing the optically active Er population. The position of the main and secondary peaks was never observed to change, nor were their relative peak intensities. The main difference seemed to be the relative pronouncement of the region from 1460-1510 nm (as seen in Figure 6.2(a)), which increased with increasing Er concentration. A second difference was the degree of resolution of the secondary (shoulder) peak to that of the primary peak. Both effects were small. This suggests that the distribution of Er siting does not vary radically with composition. On the other hand, given the screening effect of the *5s* and *5p* electrons on the *4f* electrons in the Er^{3+} ion, small changes in the PL spectrum may in fact be indicative of rather larger changes in the crystal field near the Er.[202]

[202] The observed spectral changes are not nearly as drastic, however, as is observed in the literature for entirely different hosts (eg. phosphate glasses).

6.2 Summary of SiO_x:Er Film Composition and Thickness Characterization

Table 6.1 shows the thickness and composition of all of the films that were grown as part of this study. The practice will be adopted throughout this thesis of labelling figures such as PL spectra according to the sample label as shown in the following table (and Table 5.1); the reader will refer to this table for the compositions. Admittedly, this is an inconvenience to the reader, however, the large number of samples studied in this work, and the necessity to specify both a Si and Er concentration to describe a sample (along with an anneal temperature, duration and ambient), make it awkward to contain the information in figures and sentences. As an aid, portions of Table 6.1 will be reproduced throughout the text at critical junctions where a particular group of samples is being considered.

As previously mentioned, all composition measurements were made using the method of Rutherford backscattering spectrometry; no compositions were assumed based on deposition parameters. The optical thickness of the films, as measured with single wavelength ellipsometry, should be taken as the most accurate measurement of the film thickness.[203] This measurement involves no assumption about the film density, which in the case of the RBS thickness determination was always assumed to be that of standard thermally grown SiO_2 (2.26 g/cm^3). In fact, a comparison of the RBS and optical thickness values allows an estimation of the actual density of the film because the RBS spectrum yields an absolute areal atomic density.[204] In cases where the optical thickness is less than the RBS thickness, the density of the film is greater than 2.26 g/cm^3. This is only seen to be the case when there is greater than 1 atomic

[203] It will be noted that most of the Si-rich films were grown at nearly the same thickness of 200 nm; it is hoped that this removes some of the confusing PL peak shifting phenomena that depend on film thickness (See: Y. C. Fang, et. al., Nanotechnology **15**, 494 (2004)).
[204] The thin film areal density is defined as the product of the film thickness and volume density.

Sample	Absolute Atomic Areal Density[1] [x 10^{17} atoms/cm^2]				Thickness [Å]		Index of Refraction[4]	Er [at. %] Relative[5] to Si and O	Si [at. %][6] (in parentheses) *and* (excess Si [at. %][7]
	Si	O	Er	Ar	Optical[2]	RBS[3]			
Er116	3.56	7.55	0.125	0.236	1550	1680	1.486	1.11	(32.0)-1.94
Er117	3.60	7.78	0.259	0.164	1645	1935	1.499	2.23	(31.6)-2.55
Er118	3.99	8.84	0.446	0.156	1780	2220	1.502	3.36	(31.1)-3.35
Er119	3.00	4.70	0.0347	0.0489	1245	1220	1.593	0.45	(39.0)8.44
Er120	3.02	4.79	0.0425	---	1240	1200	1.600	0.54	(38.7)8.00
Er121	3.27	2.16	0.0266	---	1050	960	1.982	0.49	(60.2)40.3
Er122	3.22	2.26	0.0351	0.0596	1105	1020	1.978	0.64	(58.8)38.1
Er147[9]	4.84	8.93	0.622	~0	2750	3050	---	4.32	(35.1)2.72
Er149	4.38	8.74	0.176	0.19	1980	2100	1.498	1.32	(33.4)0.0762
Da1a	2.67	5.07	0.0127	0.135	1118	1710	1.514	0.16	(34.5)1.74
Da1[10]	4.39	8.69	0.0131	---	1994	1970	1.467	0.10	(33.6)0.344
Da2	4.86	7.84	0.0112	---	2065	1980	1.541	0.088	(38.3)7.40
Da3	5.13	7.46	0.0069	---	2278	1970	1.559	0.055	(40.7)11.1
Da4	5.21	5.41	0.0100	---	---	1785	---	0.094	(49.1)23.6
Da5	4.80	9.65	0.0122	---	2200	2140	1.456	0.084	(33.2)-0.173
Da6	4.76	9.65	0.0198	---	2176	2100	1.456	0.14	(33.0))-0.451
Da7	---	---	---	---	---	---	---	---	---
Da8[11]	4.65	8.45	0.0127	0.0789	2190	2065	1.484	0.097	(35.5)3.24
Da9	4.90	7.80	0.0144	0.0235	2120	2085	1.544	0.113	(38.6)7.87
Da10	5.00	7.48	0.0064	0.0281	2044	1985	1.6523	0.051	(40.1)10.1
Da11	5.22	4.32	0.0182	0.0201	2026[8]	1770	---	0.19	(54.7)32.1
Da12	4.90	10.1	0.0207	0.0313	2150	2145	1.452	0.14	(32.7)-1.00
Da13	4.70	9.40	0.0187	0.0242	2143	2125	1.45	0.13	(0)0
Da14	---	---	---	---	---	---	---	---	---
Da15	---	---	---	---	---	---	---	---	---

[1] The error in the areal atomic densities is approximately 2-3 %.
[2] Measured by ellipsometry on as-deposited film (ie. no annealing)
[3] Based on the assumption that the film density is that of SiO_2 (2.26 g/cm^3)
[4] Based as deposited films; real part only (ie. no extinction coefficient)
[5] This refers to the atomic fraction [Er]/([Si]+[O]+[Er]) expressed as a percentage
[6] This refers to the atomic fraction [Si]/([Si]+[O]) expressed as a percentage
[7] This is defined at the start of Chapter 5: ([Si]-½[O])/([Si]+[O]) expressed as a percentage
[8] This value is based on the ECR-PECVD system in-situ ellipsometer
[9] The C concentration has been estimated using RBS: ~10^{17} C/cm^2
[10] This film actually seemed to contain two distinctive layers. The bottom layer was slightly O-rich; the top layer was between 52 nm thick and consisted of the following concentrations: 1.14x10^{17} Si/cm^2; 2.1x10^{17} O/cm^2; 2.74x10^{14} Er/cm^2; ~10^{16} C/cm^2. This gives an excess Si concentration relative to O of 1.85% and an Er concentration relative to the Si and O of 0.084%. Si nano-cluster PL from this film therefore likely originates from the top layer while oxide defect PL originates from the bottom layer.
[11] The C concentration has been estimated using RBS: ~10^{16} C/cm^2

Table 6.1: This table gives the compositions, as determined by Rutherford backscattering spectrometry, for all of the films investigated in this thesis. The optical thickness is based on single wavelength ellipsometry at 632.8 nm. This table is colour-coded to organize the depositions into composition regimes: *orange* ($[Si_{excess}] \leq 0$ at. %); *yellow* ($0 < [Si_{excess}] < 12$ at. % and [Er]<<1 at. %); *purple* ($0 < [Si_{excess}] < 3$ at. % and [Er]>1 at. %) *green* ($[Si_{excess}] > 23$ at. %); *grey* (depositions on quartz substrates, unknown composition).

percent (at. %) Er present. In all other cases, regardless of the excess Si content, the film density is invariably less than that of thermal SiO_2.[205]

The films do appear to densify upon annealing. Although the ellipsometric data are not shown here in their entirety, the densification is demonstrated in Figure 6.3. The sample shown therein was selected because it has low excess Si content and the ellipsometric measurement is not complicated by the rise of a significant extinction/absorption coefficient k (imaginary component of the complex refractive index, $n+ik$) which occurs in films with higher excess Si (discussed below).

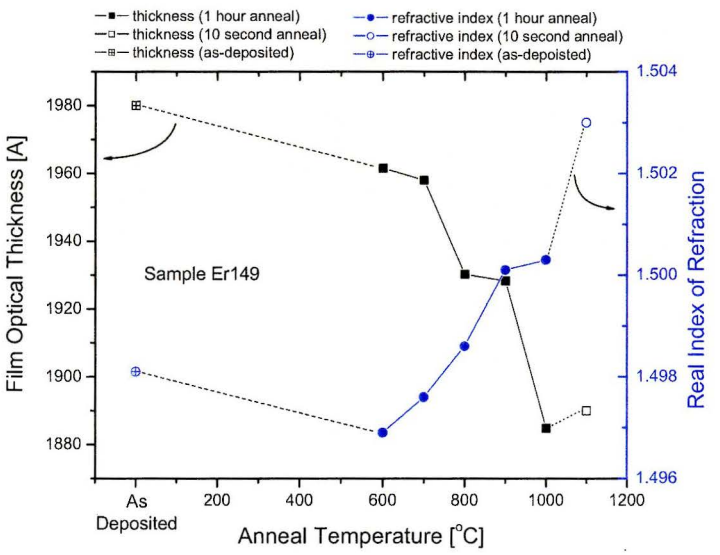

Figure 6.3: Ellipsometric measurements of sample Er149 under a range of annealing conditions; the film densification is clearly illustrated.

The film thickness was always observed to decrease upon annealing except in the case of those films with no excess Si. Densification increased monotonically with increasing Si excess and increasing anneal temperature.

---

[205] This is not uncommon in Si-oxides processed by CVD, especially those grown at low temperature such as those of this study. CVD oxides usually contain a greater volume of void space along with potentially high quantities of hydrogen. A high temperature anneal (>800 C) will usually densify such films by releasing gaseous impurities (residual from the deposition precursors) such as hydrogen and/or argon so as to repair and close the defective SiO_2 bond structure.

There is a potentially important consideration to be drawn here for electroluminescent (EL) devices based on these films. Low density oxides which are laden with void space, electronic defects, and especially non-bonded hydrogen can exhibit severely degraded electrical properties including low dielectric breakdown strength and significant random charge trapping. Given that most EL devices based on this materials system to date have been hot electron devices relying on Fowler-Nordheim tunnelling through the oxide layer, high dielectric strength is paramount to enhancing device reliability. Regardless of what kind of bond structure enhances PL yield from these films, it must ultimately be remembered that the intended application requires stable EL and that the electrical properties of the film will ultimately be as important as the luminescence properties. Adressing this design trade-off is expected to be an important aspect in future work.

The index of refraction, as determined by the same ellipsometric measurement, has been included in the table alongside the optical thickness because it provides an indication of the relative amount of excess Si [37].[206] Increasing the excess Si content increases the refractive index relative to SiO_2 since the bond structure contains increasing numbers of Si–Si bonds. It should be noted that the refractive index values for Si-rich films made in this study should not be taken as exact, although the trends should be accurate. Ellipsometric determination of absolute optical constants in such films is complicated (owing to phenomena such as the simultaneous presence of *c*-Si and *a*-Si phases) and requires careful analysis with spectroscopic ellipsometry [97,198].[207] For the purposes of this study, accurate optical constants were not required but were

---

[206] This is to be expected because the index of pure SiO_2 (approximately 1.46 – depending on the growth conditions) is significantly different from crystalline or amorphous Si (approximately 3.52).

[207] The Er dopant should not affect the ellipsometry measurement significantly because it is present only as a small volume fraction of the total film and has no obvious absorption band near the laser wavelength used (632.8 nm). However, the presence of the C may have an effect and this is likely evidenced with Er116-118, which shows a slight increase in the index with increasing Er (and presumably C) content.

merely used as a check for thermally induced structural changes. Evidently, no attempt was made to measure the absorption coefficient for any of the films. Previous measurements [39] (using spectroscopic ellipsometry) on Si-rich SiO_x films from the ECR-PECVD system have indicated that k is less than 0.05 (at a wavelength of 600 nm) for films containing less than 53 at. % Si, or annealed at temperatures below 1100 °C; this is because of insufficient excess Si phase separation.

As Table 6.1 indicates, the composition space for this study spanned a Si content from 31 to 60 at. % (relative to O) along with an Er content from 0.05 to 4 at. % (relative to Si and O). The portion of the parameter space with both high Er and high excess Si is not well represented because of the problems previously discussed (Section 5.1) with the Er delivery system on the ECR-PECVD.

6.3 Evolution of Er^{3+} Infrared PL with Nitrogen Annealing

The graphs of Figure 6.4 depict the integrated PL intensity in the 1400-1650 nm band (containing the 1540 nm Er emission from the $^4I_{13/2} \rightarrow {}^4I_{15/2}$ transition) for various films as a function of the annealing temperature.[208] The anneal duration in all cases was one hour and the ambient was always flowing ultra-high-purity N_2 gas. Each coloured curve corresponds to a different film composition; the lines have been drawn to guide the eye. In all cases, the integrated PL intensity has been normalized to a thickness of 200 nm since not all of the films were grown to identical thickness.[209]

---

[208] Integrated PL intensity was defined here as: $I_{Er} = \int_{400nm}^{650nm} I(\lambda) d\lambda$

[209] It is important to note that this assumption of a linear relationship between PL intensity and film thickness commits an error with respect to many of these films because the RBS data has revealed that the composition profile was not always uniform. The assumption is therefore being made that the potential PL emission is a uniform function of depth through the film. This has been argued to the contrary in the literature based on a tendency for non-uniform Si nano-cluster formation dynamics as a function of distance from the substrate (ie. film thickness). One can separately argue, on the basis of expected Er clustering in regions of high Er concentration (as shown in the RBS spectra), that certain film depths are emitting more PL than others. In addition to these effects, the instantaneous laser intensity is not a linear function of the depth of penetration

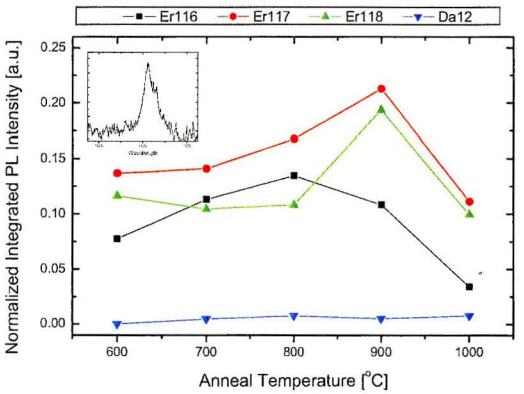

(a)

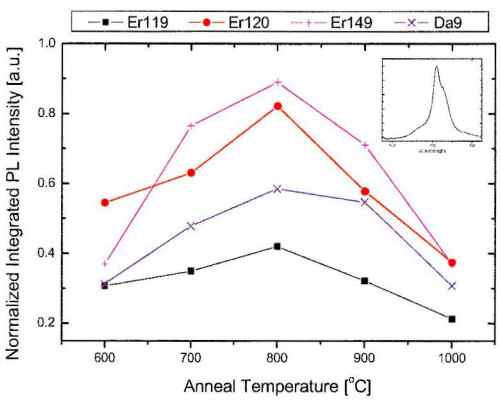

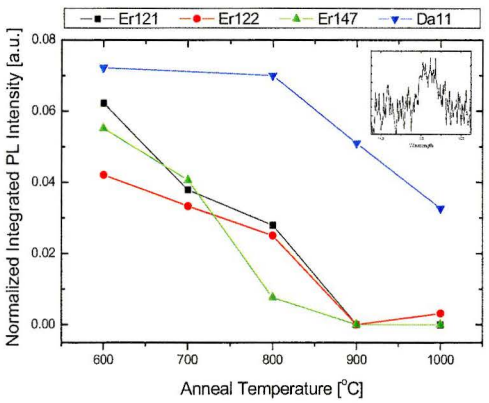

(b) (c)

Figure 6.4: Anneal-PL curves showing the integrated Er-related PL intensity (in the 1400-1650 nm band for one hour annealing in flowing N_2) as a function of temperature. (a) Anneal-PL curves for films containing no excess Si; (b) anneal-PL curves for Si-rich films; (c) expanded anneal-PL curves for the most extreme compositions.[210] The y-axes of the anneal-PL curves are synchronous. The insets show a sample raw spectrum to illustrate the signal to noise ratio.

---

into the sample and nor is the absorption of the radiation. This means that the true PL emission is a convolution of a number of effects, none of which has been explicitly measured in this study.

[210] While not shown in the figure, only Si-rich films showed 1.54 μm PL in the as-deposited films. The intensity of the as-deposited PL was weak relative to that after annealing, however it was directly dependent on the excess Si content *regardless of the Er content* (over an Er concentration range of 0.05-2 at. %). The as-deposited PL increases with Si excess even up to 23 at. %. It seems to be the result of some kind of cluster sensitization since films containing no excess Si did not show as-deposited PL at 1.54 μm despite showing as-deposited defect PL.

The annealing information in Figure 6.4 has been subdivided into three graphs, each depicting a different range of the composition space; the y-axes can be read synchronously (i.e. they are normalized to each other). The y-scale has been normalized to a value of unity defined by the most intense PL measured from the samples depicted.

6.3.1 Oxygen-Rich Films

It is clear that for films with no excess Si (Figure 6.4(a)), the 1.54 μm PL increases with increasing anneal temperature up to a maximum between 800-900 °C and then decreases for higher anneal temperatures. Figure 6.5 depicts the PL data at 800 and 900 °C as a function of the Er concentration for three different anneal durations. For one hour anneals, the intensity increases strongly with increasing Er concentration up to a point near 2.5 at. % before decreasing at the highest Er concentration near 4.0 at. % (Figure 6.5 left panel); for three hour anneals at 800 °C the behaviour is the same, however for three hours at 900 °C the PL increases monotonically with Er content. An Er concentration of 1 at. % corresponds to an Er-Er spacing (assuming perfect uniformity) of ~1 nm – well within the range of efficient Förster transfer. The observation of PL at and *above* this concentration suggests that much of the Er must reside in large optically inactive clusters, with the optically active Er isolated and better separated. The PL data for short (five minute) anneals clarifies this point by the following argument. In certain cases in Figure 6.5, it will be noticed that the PL increased quickly in the first five minutes, then decreased at one hour, and then increased again to a maximum at three hours. This means that the PL was dominated in the first five minutes by an initial rapid reduction in non-radiative defects and the formation of optically active Er complexes (recall that there is no PL in this band in these films as-deposited). By one hour, Er clustering and/or precipitation have become dominant over the disappearance of defects, which has slowed after the intial fast reduction, and the PL reflects a net decrease in the optically active Er

concentration. After three hours, however, the clustering and precipitation have slowed considerably (possibly having entered a slow Ostwald ripening regime) as the matrix has stabilized an equilibrium concentration of [solvated] optically active Er centres; now, the long term (slow) reduction of non-radiative defects has taken over and compensated the previous PL reduction, leading to an overall PL enhancement. Note that the formation of Er precipitates cannot be reversed by further annealing. In summary, the decrease in the PL between five minutes and one hour is evidence of the aggressive formation of Er aggregates.

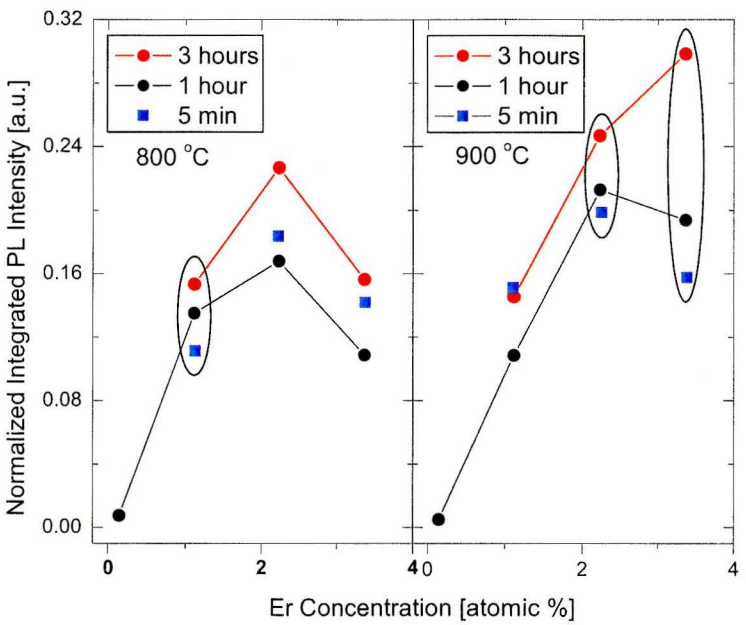

Figure 6.5: Integrated PL intensity in the 1400-1650 nm band as a function of the Er concentration in films containing no excess Si; three anneal durations are shown. The left panel shows this data for an anneal temperature of 800 °C while the right shows it for 900 °C.

While the anneal-PL curves (Figure 6.4(a)) peak near 800 °C for the lower range of Er concentration (Er116 and Da12), the curves exhibit a different shape and, instead, peak at 900 °C for the highest Er concentration (Er117-118). There is a correlation here with the ellipses drawn in Figure 6.5, which show the Er concentrations, at each temperature, that exhibit a monotonic increase of the PL

intensity with anneal duration. Note that these ellipses occur at exactly the temperature at which each particular film obtains its maximum PL. This suggests that the anneal temperature that maximizes the PL does so because it results in the least sever Er clustering/precipitation. For Er116, this occurs at 800 °C, with the onset of Er clustering losses at 900 °C. For Er117-118, this occurs at 900 °C, meaning that the Er clustering losses are greater at 800 °C. This latter case is a curious result since 900 °C corresponds approximately to the temperature at which Er–O luminescence centers would be expected to dissociate, leading to the formation of optically inactive Er precipitates.[211] This points to the conclusion that the host matrix is substantially altered by Er concentrations greater than 2 at. %. For example, perhaps there is indeed enhanced Er precipitation at 900 °C in Er117-118, but the large metallic Er inclusions give rise to new sensitizing defects at their interface with the embedding matrix; or perhaps the inclusions create a plasmon enhanced energy transfer. Regardless of this, Figure 6.4(a) shows that Er precipitation has clearly become dominant by 1000 °C.[212]

Although Figure 6.5 is ultimately consistent with concentration quenching effects, the quenching regime occurs at a much higher Er concentration than observed for SiO_2:Er fabricated at high temperature (ie. the maximum optically active Er concentration in melt glasses is ~0.1 at. % [68]), indicating that the ECR-PECVD technique forms films with less tendency for Er-coupling and/or clustering. While this is likely the result of a characteristic reduction in the diffusion of Er ions within the host matrix typically observed for low temperature CVD deposition[213] (see p. 261 of [68]), other complementary effects are expected. The C in the films may be supplementing the non-bridging oxygens (NBOs) in the Er coordinating shell.[214] In conjunction, the inclusion of excess O in the SiO_x

[211] This would be expected particularly at the high Er concentrations of Er116-118.
[212] In addition, while not shown in Figure 6.4, annealing at 1100 °C further quenches the PL.
[213] This may be evidence of a general retardation of typical diffusion kinetics in these films. That this may be the result of carbon impurities would concur with the observation (to be discussed later) that the presence of carbon seemed to retard the formation of Si nano-clusters.
[214] This would not necessarily reduce the optical activation of the Er since C is highly electronegative.

matrix should increase the formation of NBOs; the RBS data suggest that Er116-118 and Da12 are O-rich. Both of these effects ease the usual constraint on the availability of NBOs for Er-coordination and they thereby reduce the driving force for Er clustering and ion-ion coupling.[215]

Given that the [maximum] PL intensity observed in those films *with no excess Si* is approximately 10-20% of the typical 1.54 μm PL observed for Si-rich [Si nano-cluster-containing] films (anneal-PL curves depicted in Figure 6.4(b)), the question arises as to what is sensitizing the Er in the former. These films should not contain Si nano-clusters, and the pump laser line at 325 nm is not directly resonant with an Er^{3+} energy level.[216] This means that some other defects are capable of absorbing a 325 nm photon and transferring excitation to nearby Er. The only potential co-dopant in these particular films stems from the $Er(tmhd)_3$ molecule, and the PL seems to increase with higher Er concentrations. This suggests that the Er incorporation itself (or some fragment of the *tmhd* molecule) introduces the sensitizing defects.

6.3.2 Silicon-Rich Films

Considering films which are *Si-rich* (Figure 6.4(b,c)), there are two prototypical anneal-PL curves: 1) the first show a maximum near 800 °C and are characteristic of the strongest emitters,[217] which happen to be those with ~36-40 at. % Si and <2 at. % Er; 2) the latter decrease monotonically as the anneal temperature is raised above 600 °C (the lowest temperature used) and correspond to "extreme" film compositions, that is, those with very high Si content (~49-60 at. %), and those

---

[215] This explanation should not be exaggerated. The unequivocal quenching of the PL in these samples at anneals ≥1000 °C is almost certainly caused by clustering and ion-ion interaction.

[216] One might question whether the laser line could be absorbed in the phonon wings of the $^2P_{3/2}$ level of the Er^{3+} ion; while PL excitation spectra in the literature suggest otherwise, UV absorption measurements should be carried out on the present films to rule out such resonant absorption.

[217] A very similar anneal optimization has also been seen for EL emission (see. G.-Z. Ran, et. al., J. Appl. Phys. **90**, 5835 (2001)).

[with moderate Si concentration] having a very high Er content (~4 at. %). These two cases will be discussed separately.

Moderate Excess Silicon Concentrations

The strongest emitters have a prototypical anneal-PL curve with negative curvature and a maximum near 800-875 °C.[218] Naively, such an optimum anneal temperature can be explained by three processes: 1) the formation of optically active Er complexes, 2) the initial formation of a small and dense array of Si nano-clusters, and 3) the disappearance of non-radiative bonding defects. A progressive decrease in the non-radiative defect population should persist over the entire range of anneal temperatures, even though the thermally-induced phase transformation processes occurring in the film probably create more such defects. While defect repair is certainly an important effect up to 800 °C, it does not dominate the PL trend above 900 °C. The increase from 600 °C to 800 °C is probably dominated by the formation of optically active Er complexes – presumably the ErO_x ($x>3$) centers discussed in Chapter 4 with the addition of some C in the coordinating shell. C-assisted coordination in Si-rich films is supported by Fourier transform infrared spectroscopy of C and Er co-implanted Si-rich SiO_x films, which indicated that Si–C bond formation is negligible for the full range of anneal temperatures [199]. This implies that the C is bonded to Er, O or possibly other C.[219] It must be that either these optically active Er complexes can form with little thermodynamic/kinetic barrier or they form during film deposition (see section 2.5), because they are already present after rapid thermal anneals at low temperature.[220] At least up to 800 °C, annealing should increase the population of optically active Er. It is tempting to ascribe the drop in

[218] The maximum has actually been more precisely isolated to be in the 850-875 °C range.
[219] To fully confirm the results, the absence of the Si–C bonding should be verified with x-ray photoelectron spectroscopy (XPS; C–C bonding should be verified with Raman spectroscopy and $Si_xO_yC_z$ complexes should be detected with electron energy loss spectroscopy (EELS).
[220] Rapid thermal annealing of Er120 and Er149 at 600 °C (the lowest temperature investigated in this study) with a soak time of only 1 minute resulted in a PL increase to 25-50% of the maximum observed from that sample. A 10 second anneal at 900 °C put the PL at 65% of the maximum.

PL at 900 °C to Er precipitation. Such an explanation does not seem complete, however, since some of the most severe decreases in PL beyond 900 °C appeared in the most lightly doped films (0.1 at. % Er). While this drop in PL is contrary to the O-rich SiO_x films Er117/118, it is universal both among the Si-rich films and the O-rich films with Er content below 1 at. %.

If the PL quenching beyond 900 °C is not due [solely] to Er precipitation, then it might relate to Ostwald ripening of the Si clusters. This would explain why the roll-off is more severe in films with higher excess Si. It also concurs with literature results based on EFTEM imaging stating that an anneal temperature of 800 °C determines the largest number of sensitizing Si centres [122]; these centers are very small amorphous clusters. Evidently, their small size should make them the most efficient Er sensitizers.[221] Not only would such a dense array of small nano-clusters increase the extent to which the incident laser beam is absorbed, but it will also decrease the number of Er ions strongly coupled *per nano-cluster*, thereby reducing the tendency toward Er-Er interactions. It can be argued that by increasing the anneal temperature to 900 °C and beyond, the number of Si nano-clusters decreases (and their size increases) because of the Ostwald ripening. This results in a higher ratio of Er ions to nano-clusters, meaning that more Er ions are located at a cluster surface and in range for mutual coupling. In addition, at this anneal temperature, the Förster transfer is less efficient because the nano-clusters are larger. PL quenching is thus expected. The present data therefore support the notion that very small, amorphous Si nano-clusters are indeed efficient sensitizers.[222] The only difficulty with this explanation is that the phase separation of excess Si at anneal temperatures as low as

---

[221] It is interesting that the complete lack of Si nano-*crystals* is not detrimental to the PL.

[222] The limiting factor in this assertion seems to be that one could ascribe the enhanced PL, in the case of a dense array of nano-clusters, not to a more efficient sensitizing centre but simply to *more of them* and enhanced absorption of the pump light. Hence, the 800 °C anneal would be analogous to increasing the pump laser power. The only way to resolve this issue is to measure the absorption/transmission of the incident laser photons in each film. The literature has not addressed this possibility very well. However, detailed ellipsometric modelling on similar films from the ECR-PECVD system (see Tyler Roschuk, M.A.Sc. thesis, 2004) has suggested that a significant extinction coefficient does not arise until the Si concentration approaches 50-60 at. %.

600-800 °C is likely very limited, especially at the low excess Si contents depicted in Figure 6.4(b). A Si atom may not even be able to diffuse 1 nm under these conditions (see section 4.4.2 and Figure 4.10). This is not a serious problem, however, if it is true that the *as-deposited* film already contains many small Si clusters (as in the RMM resulting from spinodal decomposition) or at least excess Si that is atomically close [81]. The formation of Si_5 clusters (similar to the cluster model of the E_δ' defect) may be all that is required to sensitize the Er once the non-radiative defect population is reduced.

Erbium Sensitization by Oxide and Carbon-based Defects

The explanation of the preceeding section is not very satisfactory in the case of films such as Er116 and Er149, which exhibit the negative curvature anneal-PL curve with maximum 1.54 μm PL at 800-900 °C but contain a negligible amount of excess Si; these films should contain no Si nano-clusters. Although these data do not falsify the previous explanation, they do suggest that neither is it singularly complete. As previously stated, the only apparent explanation for the 1.54 μm PL in the O-rich SiO_x:Er films is an Er sensitization by oxide-related defects.[223] One could explain the anneal-PL curve of Er116 (and Da12) in Figure 6.4(a) on the basis that a subset of oxide defects reach their maximum of activation and/or coupling to Er at an anneal temperature near 800 °C. The reduction of the defect population due to 'thermal repair' at and above 900 °C could explain part of the concomitant PL quenching. Combining this notion with the Er concentration trends of Figure 6.5 supports the previous assertion about the origin of these defects: they may be introduced by the incorporation of the Er itself. This would explain why the PL initially increases with increasing Er content (as in

[223] A rather more esoteric explanation could be that the consumption of NBOs in Er/O complexes leaves Si atoms available to bond to each other. However, the observation in the RBS data that the Er doping seems to leave an O surplus in these films (which does not release upon annealing) weakens this argument. It could also be argued that in SiO_2 films, Si-Si bonding has a greater propensity to appear as oxygen-deficient defect centres such as a neutral oxygen vacancy rather than full Si nano-clusters.

Da12→Er116→Er117). The decrease at the highest Er content (Er118) could indicate a transition in which concentration quenching exceeds the defect sensitization capacity. As noted previously, the different shape of the anneal-PL curves for Er116 versus Er117/118 could simply be the result of a different defect coupling balance at the high Er content as a result of the introduction of new defects around Er-based precipitates.[224] Given the pathological structure of these films (as discussed in Chapter 4), it is fully expected that defects could be introduced in the vicinity of the Er that are capable of a Förster-Dexter transfer just as with a Si cluster. The bond-type mismatch occurring at the surface of the Er coordinating shell between the highly ionic Er–O bonds and the covalent Si–O bonds could indeed give rise to defects there.[225] Enhancing the formation of such defects may be another role of C impurities; in fact, it is possible that the Er appears to increase the defect population only because of the C that it introduces (this possibility will be discussed later). Not only might the C introduce oxide defects, but it may form luminescent C nano-clusters; such clusters are thought to emit in the energy range from 2.0-2.95 eV [200]. Similarly, $Si_xO_yC_z$ complexes have been assigned to PL emission near 2.7-2.8 eV. Note that all of these defects are spectrally compatible with a Förster transfer to Er^{3+} [201].[226,227] Interestingly,

---

[224] Indeed, the Er clustering seems to introduce new defects since the annealing of Er116 (and other films) at 1100 °C actually causes a resurgence of the *defect related PL*, while continuing to decrease the 1.54 μm PL.

[225] In fact, the introduction of defects, such as the dangling bond D centre, in the vicinity of the Er (as a result of Er) is the basis for the defect-related auger excitation (DRAE) model for 1.54 μm PL in *a*-Si:Er. In this model, a free electron captured by a neutral D centre (D^0) transfers its energy to a nearby Er^{3+} ion by an Auger process. The introduction of such traps has also been suggested in SiO_2:Er even when the Er is introduced by a soft doping method (J. H. Shin, et. al., Appl. Phys. Lett. **76**, 3567 (2000)). One wonders to what extent DRAE might be sensitizing Er in the Si-rich SiO_x films of the present study, since D centers become increasingly common as the excess Si content increases. See: R. S. Brusa, et. al., J. Appl. Phys. **94**, 7483 (2003). On the other hand, it has been suggested that there are too many inconsistencies in the application of the DRAE model to Si-rich SiO_x and the data are, for the most part, better explained by a Förster transfer. See: A. Janotta, et. al., Phys. Rev. B **68**, 165207 (2003).

[226] Amorphous silicon oxycarbide films doped with Er have been presented as a promising material for enhanced the 1.54 μm Er-related PL (see: S. Gallis, et. al., Mat. Res. Soc. Symp. Proc. Vol. 866, p. 183 (2005)).

[227] Although there does not seem to be significant Si–C bonding in the present films, co-doping should be investigated as a possible method of enhancing the 1.54 μm luminescence. Not only

the fact that the 1.54 μm PL emission from the heavily doped O-rich SiO_x:Er films is only an order of magnitude lower than that for the Si-rich films (which apparently rely on Si nano-cluster sensitization) suggests that in certain instances the defect-mediated sensitization could be a very important alternative excitation pathway which has so far been relatively unexplored in the literature. The McMaster ECR-PECVD system, with its unique dopant delivery method, might have the novel capability of producing films with a large population of these sensitizing centres.

This model can be extended to account, at least in part, for the enhancement of the Er-related PL for an 800 °C anneal in the Si-rich films.[228] The presence of these defects, along with the numerous and small Si clusters, at these lower annealing temperatures effectively increases the number of sensitizing centres available for coupling to Er^{3+} ions. One wonders whether the incorporation of the excess Si itself is also capable of introducing other oxide defect sensitizing centres.

Extreme Silicon-Rich Compositions

The anneal-PL curves for the most Si-rich films (greater than 50 at. % Si; Er121-122, Da11) tend to be simpler to interpret (shown in Figure 6.4(c)). They always display much lower PL intensity than their counterparts just discussed. This is likely due to the formation of Si clusters that are much too large to display effective quantum size effects or act as sensitizers for the Er^{3+} ions. Furthermore, the large Si aggregates may be effective in re-absorbing the excitation (either radiatively or by coupling) from the few luminescent clusters eligible to act as

---

may SiC nano-clusters in SiO_x effect an energy transfer capable of reaching higher Er^{3+} energy levels (due to the large band gap > 3eV) but *a*-$Si_{1-x}C_x$:H alloys with small C content and doped with Er have been found to effect an efficient Förster transfer to Er^{3+} (instead of a DRAE transfer) from resonant electron-hole pairs thermalizing in tail states. The C co-doping forces the band-tail states into a shallower region which can be tuned resonant with the Er^{3+} 1.54 μm transition. Such films may exhibit improved electrical conductivity relative to SiO_x:Er but without the charge trapping problems of Er-doped *a*-Si:H. (See: G. Weiser, et. al., Phys. Stat. Sol. (c) **1**, 1275 (2004)).

[228] This applies especially to those films with very little excess Si. In particular, sample Er149, which was among the strongest emitters at 1.54 μm, contains almost no excess Si.

sensitizers. There will also be an increased probability for the Er to be located *inside* the Si aggregates, which should subject those centres to the same luminescence quenching mechanisms of Er in bulk Si. In agreement with this, the maximum PL occurs for the lowest annealing temperature – corresponding to the smallest possible clusters. The excessive growth of the nano-clusters with increasing anneal temperature eliminates their luminescence potential. At these high Si concentrations, even low temperatures induce aggressive phase separation, particularly through spinodal decomposition (according to section 4.3) and cluster crystallization. Furthermore, the PL decreases with increasing Si content, regardless of the Er content; this is also consistent with the formation of progressively larger clusters from an increasing Si supersaturation.

With respect to Er147, which represents a moderately low Si excess but the highest Er doping of the study, the PL quickly decreases monotonically from the lowest anneal temperature down to zero emission. In this case, the Er concentration is extreme (>4 at. %) and Er clustering almost certainly takes place immediately upon annealing. Non-radiative Er-Er interactions dominate this range of composition. It is also possible that the high Er concentration results in a significant amount of optically inactive Er–Si complexing (due to the potentially insufficient NBO population – assuming it is not compensated by C).

6.3.3 Effect of Long Duration Annealing on PL at 1.54 μm

Sample	Absolute Atomic Areal Density[1] [x 10^{17} atoms/cm^2]				Thickness [Å]		Index of Refraction[4]	Er [at. %] Relative[5] to Si and O	Si [at. %] [6] (in parentheses) *and* (excess Si [at. %][7]
	Si	O	Er	Ar	Optical[2]	RBS[3]			
Er116	3.56	7.55	0.125	0.236	1550	1680	1.486	1.11	(32.0)-1.94
Er117	3.60	7.78	0.259	0.164	1645	1935	1.499	2.23	(31.6)-2.55
Er120	3.02	4.79	0.0425	---	1240	1200	1.600	0.54	(38.7)8.00
Er121	3.27	2.16	0.0266	---	1050	960	1.982	0.49	(60.2)40.3
Er149	4.38	8.74	0.176	0.19	1980	2100	1.498	1.32	(33.4)0.0762

Sub-section of Table 6.1

Increasing the anneal duration from one hour to three hours does not significantly alter the shape of anneal-PL curves, however it does shift the relative intensities slightly as shown for five representative spectra, representing five regions of the composition space, in Figure 6.6.

It is clear that that for O-rich films (Figure 6.6(a,e)), an enhancement of the emission is observed beyond 700 °C. This is probably due to a decrease in non-radiative defects at the longer anneal time; there may, however, be *further* activation of radiative defects. The more severe quenching beyond 900 °C, relative to the one hour anneal, signals the more advanced Er precipitation. Indeed, in support of this view, Er149 (Figure 6.6(d)), having an even higher Er content than Er116 (Figure 6.6(a)) shows a correspondingly more severe quenching in this temperature range, and Er117 (Figure 6.6(e)) is still more severe. The preservation of 800 °C and 900 °C as the anneal temperatures for maximum PL in Er116 and Er117 respectively, emphasize the fundamental difference in the host matrix arising from the different doping regimes as discussed in section 6.3.1.

For moderately Si-rich films, the enhancement with anneal duration is most pronounced from 700-800 °C and then actually decreases below the one hour PL emission at temperatures near to and greater than 900 °C. While this decrease below the one hour PL emission could be the result of Er precipitation, it also reflects the progressive decrease in the number density of Si nano-cluster sensitizers due to the Ostwald ripening.[229]

Finally, for those films with the highest excess Si content (greater than 20 at. %), the three hour anneal values are well below those for one hour of annealing, and go to zero for temperatures beyond 900 °C. This is almost certainly the result of a combination of exacerbated growth of Si nano-clusters, which are too large to act as sensitizers, and the disappearance of any persisting small clusters (which could act as sensitizers) due to Ostwald ripening.

---

[229] As the one hour anneal-PL curves suggest, the Er-related PL seems to have an important dependence on the actual number of sensitizers.

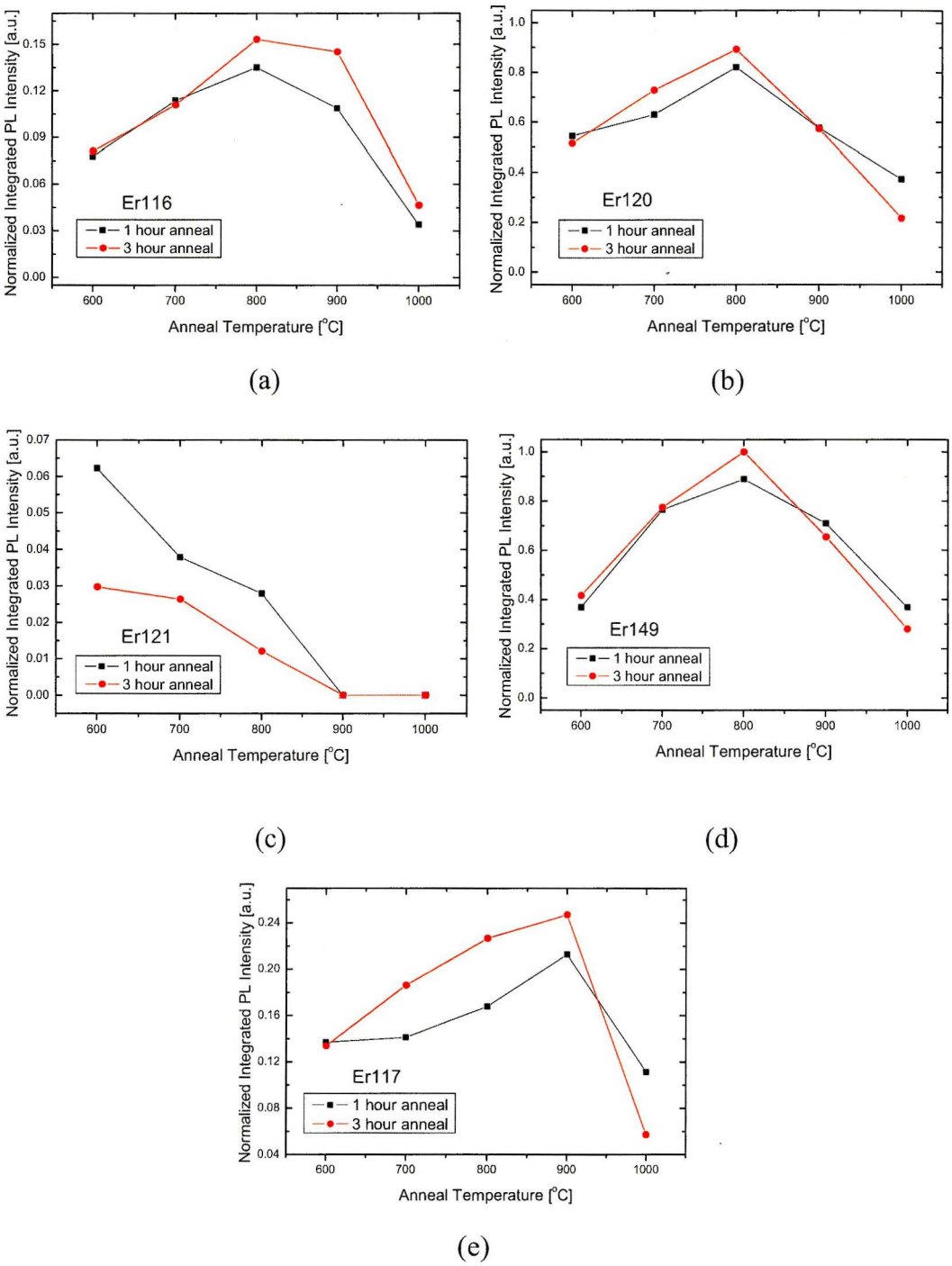

Figure 6.6: The anneal-PL curves for one hour versus three hour annealing duration, in flowing N_2 gas, are superimposed for comparison in a selection of representative films covering the composition space. (a) Er116; (b) Er120; (c) Er121; (d) Er149; (e) Er117

6.3.4 Isolation of the Optimum Composition for PL at 1.54 μm

The anneal-PL curves are not displayed for all of the film compositions studied. In order to more clearly isolate the optimum composition for PL at 1.54 μm, a three dimensional plot is shown (Figure 6.7) which depicts the integrated PL intensity, normalized to the highest PL observed in this study, over the space of Er and excess Si concentrations. The anneal temperature, in all cases, is 800 °C, for one hour duration with a flowing N_2 gas ambient.

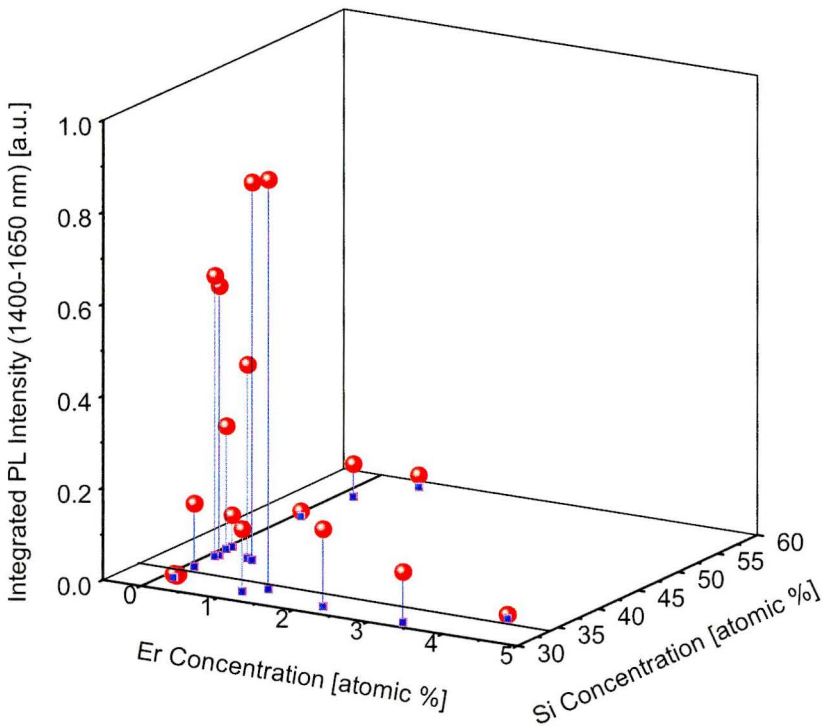

Figure 6.7: Plot of the integrated PL intensity at 1.54 μm (1400-1650 nm emission band) as a function of the entire composition space. In all cases, the general optimum anneal condition, as isolated from the anneal-PL curves, is shown: 800 °C, 1 hour, flowing N_2 ambient.

The figure shows that the optimum composition has a Si concentration greater than zero but less than 39 at. % (more specifically in the range 33.3-36.3 at. %) and an Er concentration between 1.0-2.0 at. % (more specifically closer to 2.0 at. %). This is an interesting fact because it suggests that only a relatively small

amount of excess Si is required to optimize the 1.54 μm emission, while a large amount of Er can be usefully incorporated. Within the literature, the optimum film composition usually varies depending on the deposition system and typically involves higher excess Si content than that here.[230]

6.3.5 Sensitizing Defects at the Optimum Anneal Temperature

The most important piece of information derived from the anneal-PL curves is that the optimum anneal temperature for those compositions with the highest *potential* PL is between 800-900 °C. This finding concurs with various other studies conducted on this material system including those using other preparation techniques [122,165,202,203]. In an effort to identify the oxide/carbon-based defects which are capable of acting as sensitizes for the Er, it is worth drawing attention to a study conducted on Si-rich SiO_x:Er at the University of Catania (Italy) by Pacifici et. al. [204].[231] They were studying the effect of anneal temperature on Si-rich SiO_x films annealed to form Si nano-clusters just prior to Er-implantation. Specifically, they found that a pre-anneal of 800 °C (for one hour duration in N_2 ambient) led to an optimization of the Er-PL at 1.54 μm relative to a pre-anneal at 1250 °C at which well defined Si nano-*crystals* would be generated; this is depicted in Figure 6.8. This is significant because EFTEM imaging shows that the 800 °C anneal generates only weakly defined amorphous Si nano-clusters. The 1.54 μm PL emission was then analyzed by photoluminescence excitation (PLE) spectroscopy at the various pre-anneal temperatures (Figure 6.9(a)). The PLE intensity for each anneal temperature was then normalized relative to the sample pre-annealed at 1250 °C (Figure 6.9(b)).

---

[230] Interestingly, a group in Korea (J. H. Shin et. al.) using an ECR-PECVD system similar to that at McMaster along with in-situ doping by sputtering of a metallic Er target finds the similar optimization at low excess Si concentration to this study.

[231] The films are prepared by RF-PECVD of Si-rich SiO_x (42 at. % Si) followed by (pre)-annealing under N_2 gas (to precipitate some of the excess Si), ion implantation of the Er dopant at 300 keV to a dose of $5x10^{14}$ Er/cm^2 and a final 1 hour anneal at 900 °C under N_2 (to repair the implant damage and activate the Er).

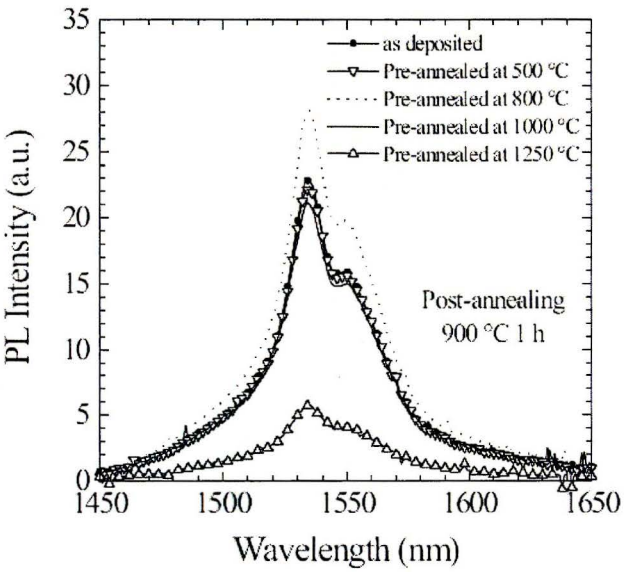

Figure 6.8: Room temperature PL spectra based on various pre-implant anneal temperatures; these different anneals determine different types of Si nano-cluster distributions. Excitation was carried out with a 10 mW Ar laser at 488 nm. The sample contains 42 at. % Si. Reproduced with permission from [204].

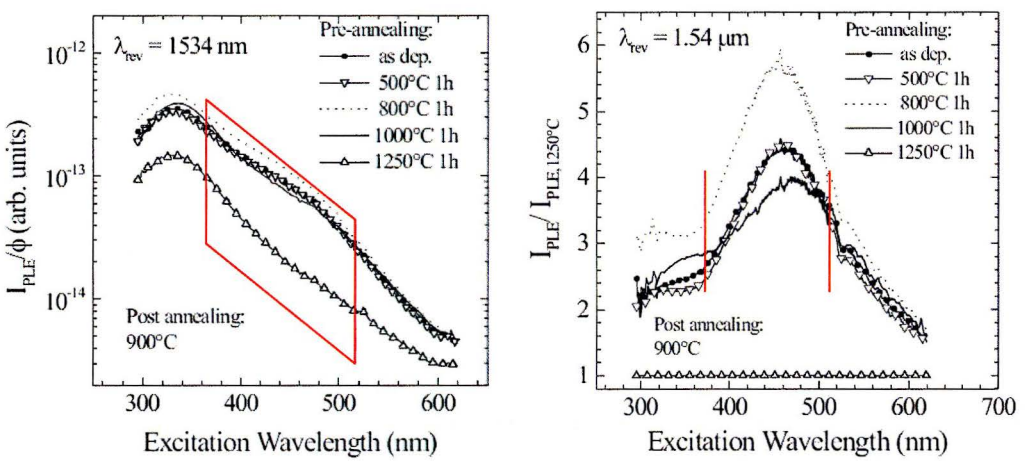

Figure 6.9: (a) Semi-logarithmic plot of the PLE intensity measured at 1.54 μm for various pre-implant of Er anneals, normalized for the incoming photon fluxes; the feature at 340 nm, characterizing all of the PLE spectra is an interference effect caused by refractive index mismatch between the film and Si substrate. The red lines denote the band from 380-540 nm. (b) Ratio of the 1.54 μm PLE intensity for various pre-implant anneals to that for the 1250 °C pre-anneal. Reproduced with permission from [204].

Interestingly, Figure 6.9(b) reveals the presence of centres which are strongly absorbing between 300-600 nm (peaking near 460 nm). Furthermore, the presence of these centres is highly dependent on the pre-anneal temperature, showing a maximum at 800 °C – exactly the temperature at which the 1.54 μm PL is optimized. Based on the apparent absorption band of the sensitizing defects, one might make a preliminary connection with the common luminescent oxide defects whose dominant radiative transitions were identified in Chapter 2. Indeed, many of the defect transitions are strongly resonant with several of the higher-lying Er^{3+} energy levels, thus making them good candidates for resonant energy transfer.

This provides strong evidence that oxide-based defects exist in the samples, which can act as sensitizers for the Er luminescence. It explains, in part, the tendency for optimization at the 800 °C anneal in the present films. Annealing at higher temperatures seems to reduce the presence of these defects, with a concomitant decrease in the 1.54 μm PL intensity.

6.4 Thermal Evolution of the Intrinsic Luminescence Emission of Erbium Sensitizers

In order to identify the sensitizing luminescent centres in the films of this study, including both Si nano-clusters and oxide-based defects, the corresponding PL emission in the 350-1000 nm band was measured. As might be expected, the PL in this band reflects multiple luminescent centres with overlapping emission bands and so is significantly more complicated than the PL between 1400-1650 nm. Figure 6.10 shows some of the representative PL spectra observed in this band with the intent of illustrating some representative relative magnitudes. The red curve, from a sample containing ~7.4 at. % excess Si, is highly characteristic of the emission ascribed to Si nano-clusters, with a peak near 800 nm. The green and black curves are suggestive of a superposition of luminescent defect peaks and possess a variably broadened tail extending out into the infrared; the black

curve corresponds to a sample with no excess Si, while that of the green curve contains a small Si excess of ~3 at. % (and an apparently large amount of C).[232] It will be noticed immediately that the defect luminescence is primarily concentrated in the 400-550 nm band (similar to the feature of Figure 6.9(b)).

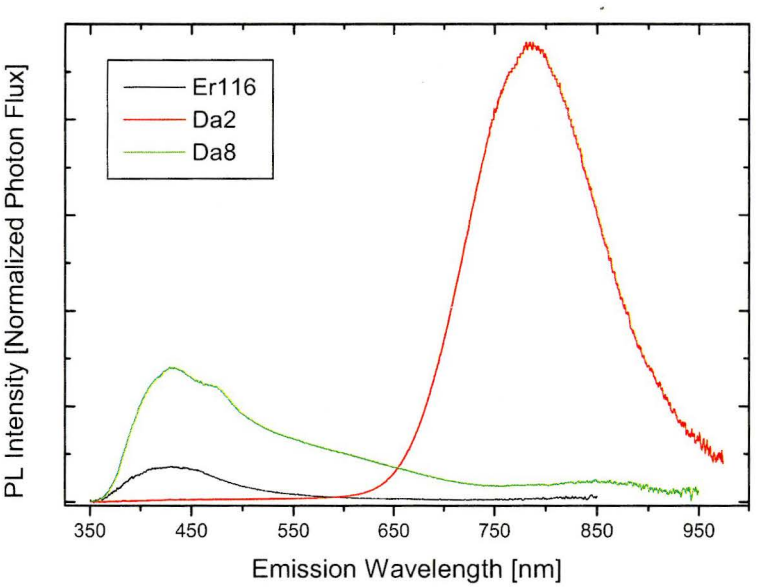

Figure 6.10: Representative PL spectra observed in the 350-1000 nm band. Both Si nano-cluster (red curve) and oxide defect PL (black curve) is shown, with a combination of these two apparently giving rise to the green curve.

The anneal-PL curves for this wavelength range manifest the differences in the active luminescent centres. Without distinguishing between the characteristic forms of luminescence on the individual spectra,[233] the curves are divided between three figures corresponding to three different composition ranges. The anneal conditions are the same as those for Figure 6.4: one hour anneal duration in a flowing N_2 gas ambient.

---

[232] This is evidenced by the lack of Si nano-cluster PL and anomalously large defect PL (despite the relatively low Er content).

[233] This should not commit a serious error because most of the spectra were completely dominated by either one form of luminescence or the other (i.e. either oxide defects or nano-clusters).

6.4.1 Oxygen-Rich and Near Zero Excess Silicon Films

Sample	Absolute Atomic Areal Density[1] [x 10^{17} atoms/cm^2]				Thickness [Å]		Index of Refraction[4]	Er [at. %] Relative[5] to Si and O	Si [at. %][6] (in parentheses) *and* (excess Si [at. %][7]
	Si	O	Er	Ar	Optical[2]	RBS[3]			
Er116	3.56	7.55	0.125	0.236	1550	1680	1.486	1.11	(32.0)-1.94
Er117	3.60	7.78	0.259	0.164	1645	1935	1.499	2.23	(31.6)-2.55
Er118	3.99	8.84	0.446	0.156	1780	2220	1.502	3.36	(31.1)-3.35
Er149	4.38	8.74	0.176	0.19	1980	2100	1.498	1.32	(33.4)0.0762
Da12	4.90	10.1	0.0207	0.0313	2150	2145	1.452	0.14	(32.7)-1.00
Da13	4.70	9.40	0.0187	0.0242	2143	2125	1.45	0.13	(0)0

Sub-section of Table 6.1

Figure 6.11 corresponds to those films with little (0.05 at. %) to no excess Si. These spectra showed no nano-cluster PL and only the defect PL concentrated between 400-550 nm.

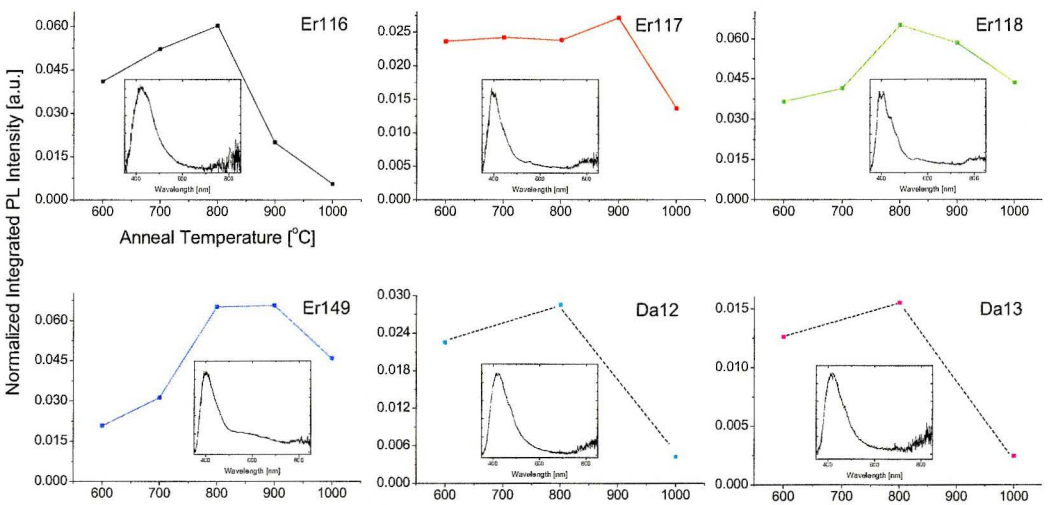

Figure 6.11: Anneal-PL curves for the 350-1000 nm band for those films with zero to negative excess Si; 1 hour annealing in N_2 is shown throughout. Only the axes in the first graph are explicitly labelled. The insets show a sample raw spectrum to illustrate the peak content.

It is apparent that, in strikingly similar fashion to the corresponding anneal-PL curves for the 1400-1650 nm range (Figure 6.4), the PL tends to increase with

annealing temperature, reaching a maximum between 800-900 °C and then decreasing beyond 900 °C. The initial increase in the PL is probably the result of a decrease in the population of non-radiative centres in the film in possible conjunction with the thermal activation of some of the radiative defects. This makes sense if it is true that the defects occur (as previously hypothesized) as a result of the Er incorporation. The formation of optically active Er complexes (at the interface of which the defects may form) progresses continuously as the anneal temperature is increased to 800 °C.[234]

The PL intensity at the 800 °C anneal increases with increasing Er concentration, reaching a maximum near 1 at. %, before decreasing at the highest Er concentrations (depicted in the left panel of Figure 6.12).[235] The PL decrease in the film with an Er content of ~2.2 at. % corresponds to an increase in the corresponding PL at 1.54 μm. When the visible PL increases again at the highest Er content, there is a corresponding decrease in the PL at 1.54 μm. This suggests a coupling of the defect luminescence to the Er wherein the defect PL experiences quenching as the coupling strength increases and reaches a maximum near an Er content of ~2.2 at. %. The ellipse outlines in Figure 6.12 correspond to the same ellipse outlines drawn in Figure 6.5. From these it will be noticed that the trend in the [maximum] PL intensity for each sample as a function of the anneal duration is exactly opposite between the visible and infrared emission bands. This is further evidence of a coupling between the defects and the E^{3+} ions wherein an energy transfer from the excited state of the defect to a nearby Er^{3+} represents a competing de-excitation pathway to radiative recombination at the defect.

---

[234] Once again, rapid thermal annealing (sample Er149) showed that the defect PL rises rapidly, reaching 25% of the maximum within 60 seconds at 600 °C – the same ratio of increase as the corresponding 1.54 μm PL.

[235] It is not completely clear that the PL intensity values from film Er118 warrant a fair comparison with the other films (although the trend is probably correct). This is because the surface micro-structure that formed on these films after annealing is almost certainly producing a micro-cavity effect in the spectrum, causing an artificial enhancement of the PL intensity.

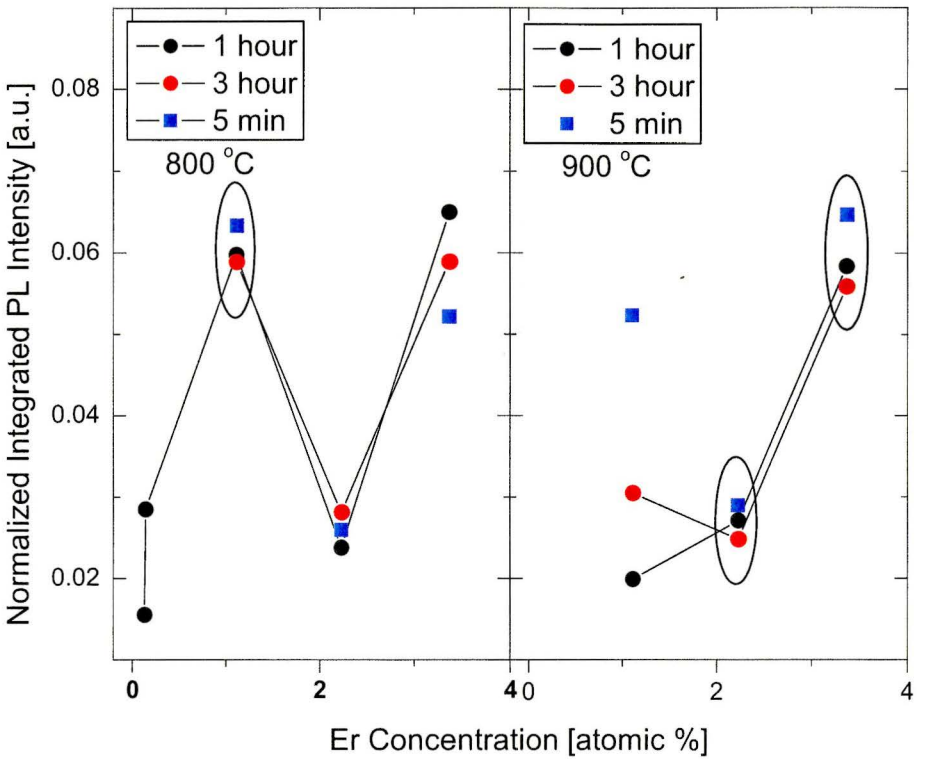

Figure 6.12: Defect-related PL near the 400-550 nm band for O-rich SiO_x:Er films as a function of the Er concentration. The Er118 data point is shown separately because its surface micro-structure may disqualify it as a valid comparison.

The monotonic decrease in the defect PL observed universally in Figure 6.11 beyond anneal temperatures of 800-900 °C is probably due to the thermal instability of these luminescent defects at the higher temperatures. They may be repaired through a rearrangement of the SiO_x network as the Er begins to precipitate more aggressively at the high temperatures. The corresponding reduction in the need for NBOs should result in the annihilation of defects, such as neutral oxygen vacancies, which were previously stabilised by the consumption of NBOs at Er^{3+} sites. Based on the defect-Er coupling hypothesis, this PL quenching should correspond to a decrease of the PL near 1.54 μm; this is indeed observed (see Figure 6.4). In fact, the overall similarity of the shape of the

anneal-PL curves for the defect and 1.54 μm luminescence suggests that they are in fact different manifestations of the same phenomenon: the energy transfer from defects coupled to nearby Er ions. Such sensitization is reminiscent of the energy transfer to an Er^{3+} ion from a localized Si=O bond (effectively a point defect) at the interface of a Si nano-cluster. The oxide point defects, however, can occur in films with no excess Si. The question then arises as to whether the particular population of defects, whose PL is probed in the measured spectra, correspond to those which are coupled or un-coupled to Er. Does a point defect coupled to nearby Er have the ability to emit intrinsic luminescence? Given that the intrinsic PL from the defects identified in Chapter 3 is often very fast (~ns), the argument could be made that, unless the defect is strongly coupled to several Er ions, it could emit while the nearby Er exist in their long-lived $^4I_{13/2}$ states (provided the pump photon flux was sufficiently high). Regardless of whether the PL originates from coupled or uncoupled defects, the trend in the anneal-PL curves of Figure 6.11 is still indicative of the relative defect concentration; even Er that is optically inactive may still be able to receive excitation transfer from a defect (though the Er ion may quickly de-excite non-radiatively).

6.4.2 Silicon-Rich Films

Moderate Excess Silicon Concentrations

Sample	Absolute Atomic Areal Density[1] [x 10^{17} atoms/cm^2]				Thickness [Å]		Index of Refraction[4]	Er [at. %] Relative[5] to Si and O	Si [at. %] [6] (in parentheses) *and* (excess Si [at. %][7]
	Si	O	Er	Ar	Optical[2]	RBS[3]			
Er119	3.00	4.70	0.0347	0.0489	1245	1220	1.593	0.45	(39.0)8.44
Er120	3.02	4.79	0.0425	---	1240	1200	1.600	0.54	(38.7)8.00
Da9	4.90	7.80	0.0144	0.0235	2120	2085	1.544	0.113	(38.6)7.87
Da10	5.00	7.48	0.0064	0.0281	2044	1985	1.6523	0.051	(40.1)10.1

Sub-section of Table 6.1

Figure 6.13 depicts typical anneal-PL curves for films with Si concentration ranging from 38-40 at. %.

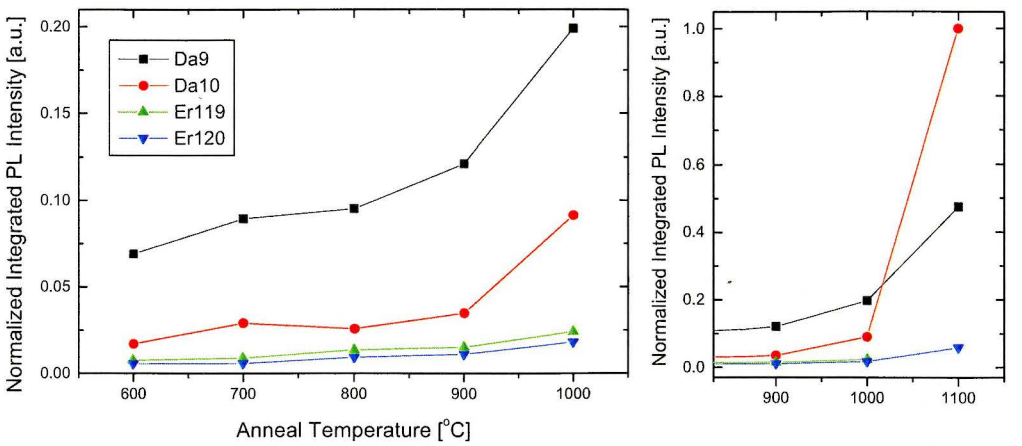

Figure 6.13: Anneal-PL curves for films containing 38-40 at. % Si with Er concentrations below 1 at. %; anneal duration was 1 hour in N_2. The PL in this range is dominated by the Si nano-cluster emission. The figure is divided in two to show the high temperature anneals without losing y-axis resolution.

There is a clear monotonic increase of PL intensity with increasing anneal temperature, with the most significant increase occurring for an anneal temperature of 1100 °C; this is characteristic of Si nano-cluster luminescence. The extent of the increase in PL intensity between an anneal temperature of 1000 and 1100 °C grows strongly as the Er concentration is decreased. Indeed, the PL over the entire range of anneal temperatures quenches progressively as the Er concentrations increases (eg. Er120 and Da9 have the same Si concentration but different Er concentrations) – consistent with Si nano-cluster/Er^{3+} coupling ; it has been found that beyond an Er content of 1 at. % the nano-cluster PL is almost completely quenched. The growth of the PL intensity for adjacent anneal temperatures up to 900 °C is faster for lower Er concentration. The generally small visible PL yield at these low annealing temperatures probably reflects the maximization of the concentration of optically active Er which can couple to the Si nano-clusters. Furthermore, the low temperatures form a dense array of amorphous Si nano-clusters which are not expected to radiative efficiently; they are plagued both by the persistence of defects inside the clusters and at their

interface which require abnormally high anneal temperatures to repair, as well as the incomplete phase separation which gives rise to ill-defined cluster interfaces and a corresponding degree of Si-rich SiO_x interconnection between the clusters through which energy migration occurs. In actuality, the phase separation is extremely limited at these low excess Si concentrations and annealing temperatures.[236] By contrast, the *significantly enhanced* phase separation at 1100 °C along with the much-increased formation of Si nano-*crystals* is probably responsible for the large PL increase there. There was no significant oxide defect PL contribution in these spectra.

Extreme Compositions of Silicon-Rich Films

Sample	Absolute Atomic Areal Density[1] [x 10^{17} atoms/cm^2]				Thickness [Å]		Index of Refraction[4]	Er [at. %] Relative[5] to Si and O	Si [at. %] [6] (in parentheses) *and* (excess Si [at. %][7]
	Si	O	Er	Ar	Optical[2]	RBS[3]			
Er121	3.27	2.16	0.0266	---	1050	960	1.982	0.49	(60.2)40.3
Er122	3.22	2.26	0.0351	0.0596	1105	1020	1.978	0.64	(58.8)38.1
Er147[9]	4.84	8.93	0.622	~0	2750	3050	---	4.32	(35.1)2.72
Da4	5.21	5.41	0.0100	---	---	1785	---	0.094	(49.1)23.6

Sub-section of Table 6.1

Finally, Figure 6.14 depicts the anneal-PL curves for those Si-rich films with the most excess Si (Si concentration of 49-60 at. %; Er121-122, Da4) or the most Er (~4 at. % in Er147). For the highest Si content, the PL increases monotonically with increasing anneal temperature (beginning with zero emission at 600 °C). This trend is exactly the opposite for the corresponding PL in the 1400-1650 nm band. However, the increase in the PL, while weak, actually contained some defect luminescence in the case of Er121/122 which exhibited the largest Si concentration (>58 at. %). These defects may be forming at the interface between very large Si nano-clusters and oxide regions. The nano-cluster luminescence (which is likely due mostly to nano-crystals) is weak because the clusters are too

[236] This is supported by FTIR data (see: T. Roschuk, M.A.Sc. thesis, 2004).

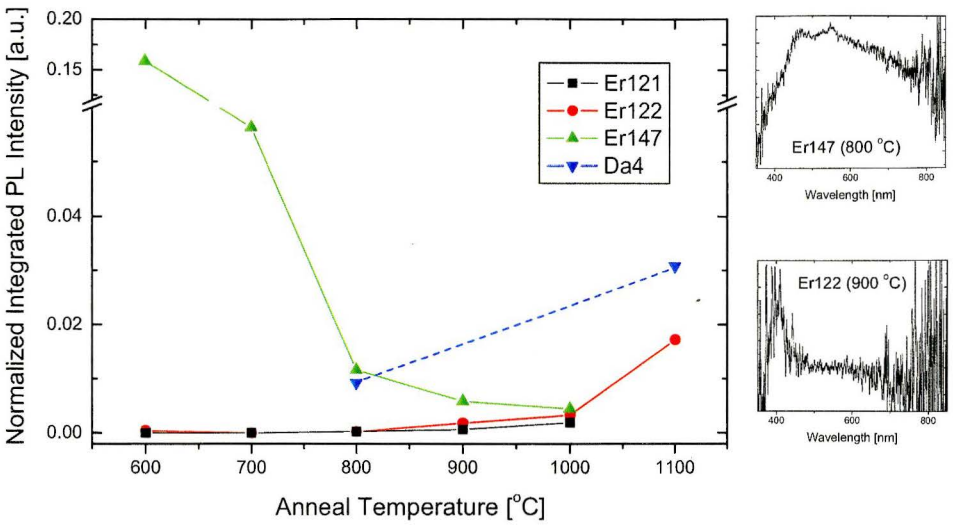

Figure 6.14: Anneal-PL curves for Si-rich films containing extreme amounts of excess Si or Er; anneal duration of 1 hour in N_2 ambient. The insets show a sample raw spectrum to illustrate the peak content.

large to exhibit quantum confinement; indeed, they may be more like micro-crystals and exhibit the properties of bulk Si. These are inherently weak emitters for the same reasons as they are poor Er sensitizers. The observed PL is likely coming from the smallest Si clusters in the film.

Figure 6.14 also depicts the anneal-PL curve for the most Er-rich film containing excess Si (Er147). The trend parallels that of the corresponding 1400-1650 nm band (Figure 6.4(c)) and decreases monotonically with increasing anneal temperature. The PL emission at these low temperatures was very intense, being one of the two strongest emitters of defect luminescence.[237] This fully supports the argument that the defects result from the Er incorporation. Interestingly, in this case the more minimal the anneal (eg. 600 °C for 5 minutes), the more intense was the luminescence. The monotonic decrease of the PL intensity with further annealing could be the result of Er-clustering (reducing the concentration of Er-centres and therefore the number of defects), the relaxation of built-in strain

[237] The PL appears bright white to the naked eye with the room lights on.

(which may have been significant given the large Er concentration), or simply the thermal dissociation and repair of the defects. The formation of nano-clusters in this film is dubious, given the enormous defect PL; they do not seem to play a dominant role in the optical emission. It should be noted that the RBS data suggested that this film contained an appreciable amount of C (near 9.75×10^{21} C/cm^2).[238] This film could therefore contain any of the C clustering effects or $Si_xO_yC_z$ phases giving rise to defects as previously discussed; such defects are indeed luminescent in the spectral band observed for this sample. The PL may also result from organic chromophores or luminescent metal-organic Er complexes in the matrix. The decrease of PL with annealing may be associated with the decomposition or outgassing of these ligands.

6.4.3 Effect of Annealing Duration on PL in the 350-1000 nm Band

Sample	Absolute Atomic Areal Density[1] [x 10^{17} atoms/cm^2]				Thickness [Å]		Index of Refraction[4]	Er [at. %] Relative[5] to Si and O	Si [at. %] [6] (in parentheses) *and* (excess Si [at. %][7]
	Si	O	Er	Ar	Optical[2]	RBS[3]			
Er116	3.56	7.55	0.125	0.236	1550	1680	1.486	1.11	(32.0)-1.94
Er120	3.02	4.79	0.0425	---	1240	1200	1.600	0.54	(38.7)8.00
Er121	3.27	2.16	0.0266	---	1050	960	1.982	0.49	(60.2)40.3
Er149	4.38	8.74	0.176	0.19	1980	2100	1.498	1.32	(33.4)0.0762
Da9	4.90	7.80	0.0144	0.0235	2120	2085	1.544	0.113	(38.6)7.87

Sub-section of Table 6.1

As with the PL in the 1400-1650 nm band, increasing the anneal duration from one hour to three hours did not significantly alter the *shape* of the anneal-PL curves; the relative changes in *intensity* depended on whether the PL was primarily due to defects or Si nano-clusters. Five compositions representing the parameter space are shown in Figure 6.15.

---

[238] In fact, this film apparently contained more C than any other film deposited in this study. This is concurrent with the enormous Er content, but the extent of C incorporation was also affected by the plasma properties. For example, Er118 contained a comparable Er concentration but significantly less C, presumably as a result of different species in the plasma caused by the different gas flow rates.

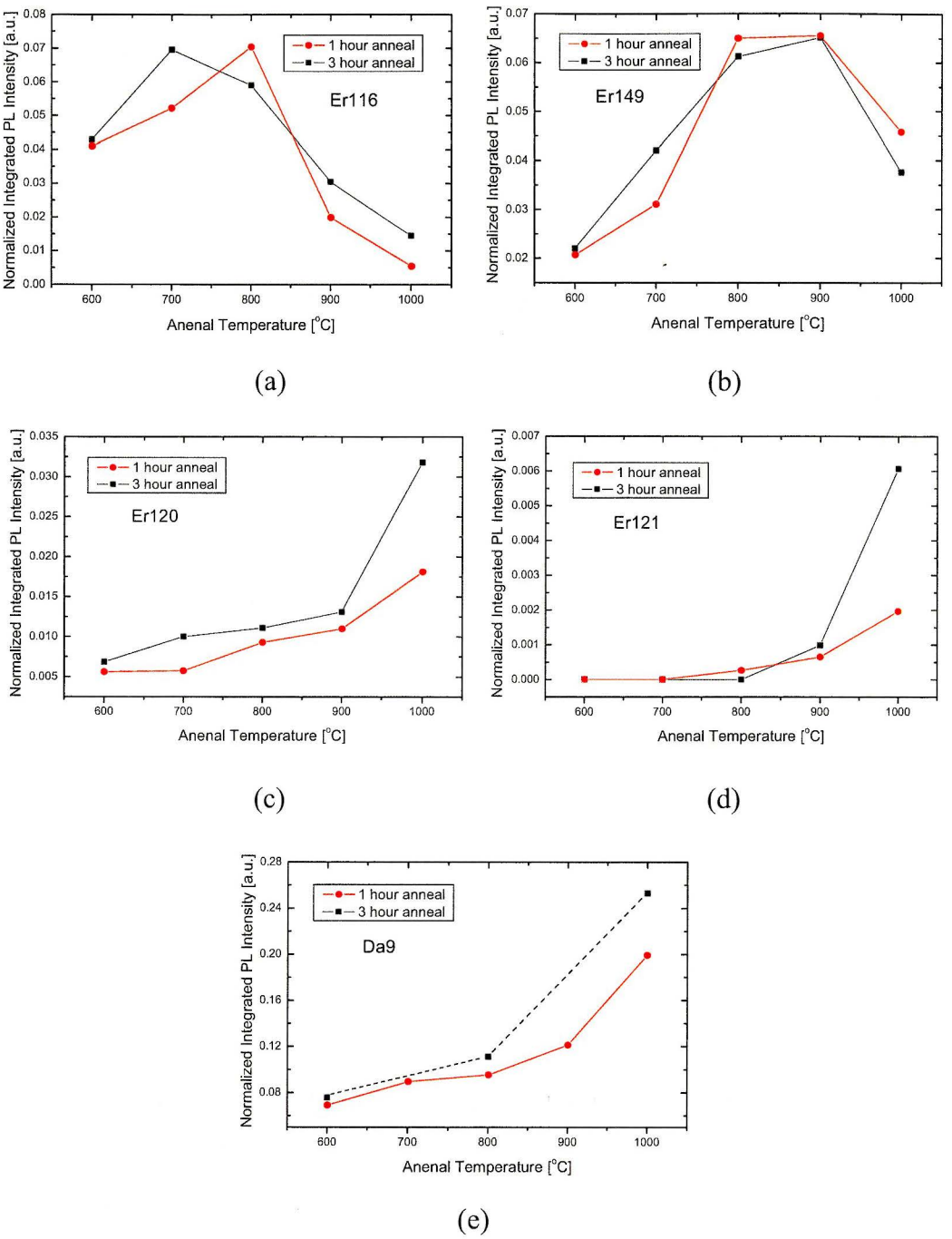

Figure 6.15: The anneal-PL curves for one hour versus three hour annealing duration, in flowing N_2 gas, are superimposed for comparison in a selection of representative films covering the composition space. (a) Er116; (b) Er149; (c) Er120; (d) Er121; (e) Da9.

Those films with little or no excess Si (Er116/149 in Figure 6.15(a,b)), which had one hour anneal-PL characteristics peaking between 800-900 °C (dominated by defect emission), did not show significant changes to the intensity except for a consistent decrease at 1000 °C for the longer anneal. This is similar to the corresponding 1.54 μm PL, which decreased severely at 1000 °C for 3 hour annealing. Evidently, there is not a significant change in the defect population below this temperature for longer annealing.[239]

For the moderately Si-rich films, however, there was invariably an enhancement at all anneal temperatures up to 1000 °C (no three hour anneals were carried out at 1100 °C). This enhancement is, at low temperatures (<900 °C) primarily the result of the decreasing non-radiative defect population in the cluster vicinity – particularly interfacial dangling bonds. The continued formation of the nano-clusters is not likely the dominant effect since the long anneal time is well beyond the initial pure growth regime at these low temperatures. The particularly dramatic increase in PL at 1000 °C is probably due to the partial onset of crystallization in the nano-clusters at the long anneal duration. This would correct many of the structural defects *inside* the amorphous clusters that were causing PL quenching. The extent of the enhancement at 1000 °C between one and three hour anneals is larger for those films containing more Er, probably because there is a greater tendency in the low Er films to maintain optically active Er even at high temperatures (due to the larger Er spacing), which still couples off much of the cluster luminescence. In principle, the most Si-rich film (Er121) showed an enhancement similar to the moderately Si-rich films, however the PL yield was extremely low (the highest signal was barely detectable). Given that these compositions are prone to form excessively large Si clusters, it is possible that the

---

[239] Alternatively, if there is a decrease in the radiative defect population (due to thermal repair), then this decrease seems to be balanced by a corresponding decrease in the non-radiative defect population. While some reports in the literature have claimed that oxide defects in PECVD SiO_x are stable up to 1100 °C at 3hours, it would be dubious to claim the same in this study because the stability will be highly sensitive to the film structure as determined by the specific deposition technique and system.

lowest temperature alone might be able to form actual *luminescent clusters*, however these are not directly observed (their existence is merely "suggested" from the weak Er-PL near 1.54 μm). For this reason, the enhancement at 1000 °C, between one and three hour anneals, observed in Figure 6.15(d) is rather odd but may be related to crystallization in the smallest clusters. Evidently the Er-PL is quenched at this high temperature since the Er is probably engaged in various optically inactive metallic Er and erbium silicide inclusions.

Rapid Thermal Annealing and the Silicon Nano-cluster Pure Growth Regime

It is interesting to study the initial increase of the visible PL within the pure growth regime of Si nano-clusters (approximately the first minute of the anneal at 1100 °C). While not studied for all compositions and temperatures, Figure 6.16 depicts the effect for Er120 (0.54 at. % Er; 38.7 at. % Si) by rapid thermal annealing at 1100 °C. This sample had the highest Er concentration for which simultan-

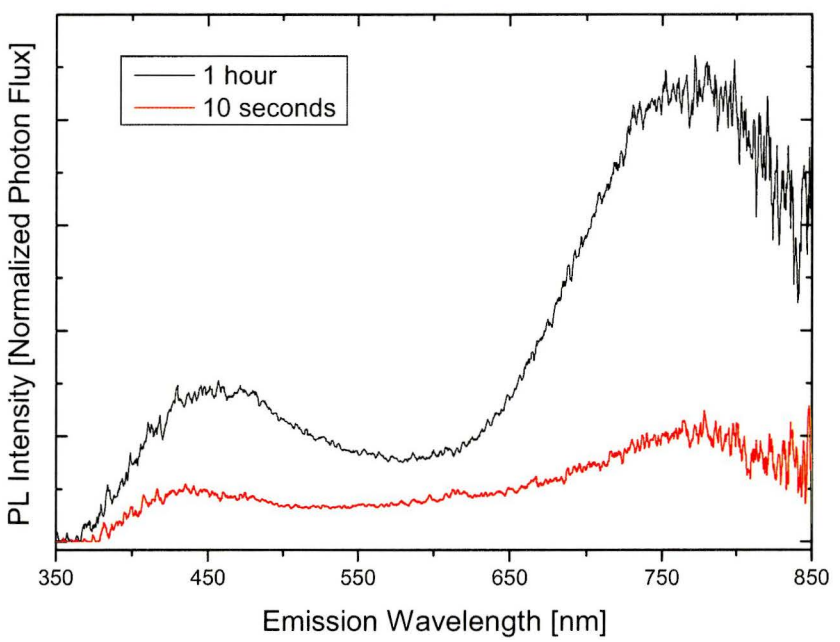

Figure 6.16: Simultaneous rise of PL emission from defects and Si nano-clusters for anneal durations of 10 seconds versus 1 hour at 1100 °C in flowing N_2 gas in sample Er120.

-eous, definitely identifiable Si nano-cluster PL was observed.

The simultaneous increase of the defect and Si nano-cluster PL peaks occurs within the first ten seconds.[240] The lack of a significant red-shift of the cluster PL between 10 seconds and one hour suggests that the emitting clusters have the same average size in both films; evidently the cluster growth is extremely fast to begin with (in agreement with the literature [171]).

At this Er content, the Si cluster PL is very weak and shows a slightly broader Si nano-cluster PL band, with enhanced contribution at the high-energy side of the peak only, in comparison with a film of similar excess Si content but containing less Er (Er120 and Da9 allow such a comparison and show that the Si nano-cluster emission in Er120 is ~24 nm broader on the high energy side of the peak [205]). This broadening suggests that the Si nano-cluster size distribution is wider in the sample containing more Er, and contains many smaller clusters but none larger. The presence of Er therefore appears to determine an overall smaller nano-cluster size distribution.[241] This would concur with the inhibition of the Si cluster formation with increasing Er (and C) content as previously mentioned; this may be a fortuitous coincidence if it is true that smaller clusters sensitize the Er more efficiently and may explain why C-codoping can enhance the 1.54 μm emission in SiO_x:Er films. In this context, one might speculate that the presence of the Er or C somehow introduces nucleation sites which allow for the formation of a greater number of clusters which are correspondingly smaller.

---

[240] This was similarly observed in SiO_x films prepared by ion implantation (no Er doping), however the defect PL was centered at 550 nm and decreased with annealing durations beyond 10 seconds.

[241] Alternatively, it might not suggest this at all. Rather, the larger the Si cluster, the more Er ions it can have right at its surface. Since the closest Er ions couple most strongly to the cluster, it might be that the larger clusters simply lose all of their excitation to Er. The smaller clusters, however, being strongly coupled to fewer Er ions (since there can be fewer Er closer to the surface) can still emit an intrinsic photon periodically.

6.5 Silicon Nano-cluster/crystal PL and Sensitizing Functions in the Presence of Low Er concentrations

Sample	Absolute Atomic Areal Density[1] [x 10^{17} atoms/cm^2]				Thickness [Å]		Index of Refraction[4]	Er [at. %] Relative[5] to Si and O	Si [at. %][6] (in parentheses) *and* (excess Si [at. %][7]
	Si	O	Er	Ar	Optical[2]	RBS[3]			
Da1a	2.67	5.07	0.0127	0.135	1118	1710	1.514	0.16	(34.5)1.74
Da1[(10)]	4.39	8.69	0.0131	---	1994	1970	1.467	0.10	(33.6)0.344
Da2	4.86	7.84	0.0112	---	2065	1980	1.541	0.088	(38.3)7.40
Da3	5.13	7.46	0.0069	---	2278	1970	1.559	0.055	(40.7)11.1
Da4	5.21	5.41	0.0100	---	---	1785	---	0.094	(49.1)23.6
Da8[(11)]	4.65	8.45	0.0127	0.0789	2190	2065	1.484	0.097	(35.5)3.24
Da9	4.90	7.80	0.0144	0.0235	2120	2085	1.544	0.113	(38.6)7.87
Da10	5.00	7.48	0.0064	0.0281	2044	1985	1.6523	0.051	(40.1)10.1
Da11	5.22	4.32	0.0182	0.0201	2026[(8)]	1770	---	0.19	(54.7)32.1

Sub-section of Table 6.1

The Si nano-cluster PL intensity depends on *both* the [excess] Si and Er concentrations. In agreement with a Si nano-cluster/Er coupling model, the PL from Si nano-clusters is progressively quenched as the Er concentration increases. Three regimes in the Er concentration can be identified:

1) The Er concentration exceeds a value of ~1 at. %: The PL from Si nano-clusters is effectively quenched[242] regardless of the annealing temperature or excess Si concentration. In such films, the PL at 1.54 μm ranges widely – from extremely strong to absent – depending on the exact composition (see Figure 6.7), though ~33-36 at. % Si is optimal.

2) The Er concentration is ~0.5 at. %: The PL from Si nano-clusters is generally very weak, (it becomes obvious only at anneal temperatures ≥1000 °C). The PL at 1.54 μm is also present, it is sensitive to small changes in the Er concentration, and is optimal near ~38 at. % Si.

[242] The term "effectively quenched" means that any PL that is observed in the usual Si nano-cluster emission band (i.e. 650-950 nm) is weak, does not have a well-defined peak, and is ambiguously combined with the PL of oxide defects. The data from the present study are not sufficient to say that the PL is "completely absent" when the Er concentration increases above a certain value, however a progressive PL quenching is unequivocal.

3) The Er content is ≤0.1 at. %: The PL from Si nano-clusters is weak at anneal temperatures ≤900 °C but can be very strong beyond 1000 °C. The PL at 1.54 μm can be within a factor of 5 of the PL in case 1 (above); a Si concentration of ~40 at. % is optimal.

It is not clear whether the Si cluster PL that is observed simultaneously with the 1.54 μm PL originates from those nano-clusters which are strongly coupled to Er (see discussion in section 3.4.2). Nonetheless, such samples that clearly show the PL in both spectral ranges are very useful in studying the Si nano-cluster/Er coupling because they reveal the response of the nano-cluster formation both to the presence of Er and to the formation of optically active Er complexes.

An example of the response of the Si nano-cluster PL spectrum to anneal temperature, for a sample with very low Er content (Da9), is shown in Figure 6.17 alongside the corresponding 1.54 μm PL. This figure makes the connection between the characteristic anneal-PL curves for PL in the 1400-1650 nm band (Figure 6.4) and those in the 350-1000 nm band dominated by *nano-cluster* emission (Figure 6.13). It is immediately clear, and in good agreement with previous assertions, that while the cluster nucleation (and some growth) may take place at low temperature [206], the cluster nuclei do not undergo significant growth for anneal temperatures below 1000 °C. At temperatures <1000 °C there is not enough excess Si liberated from the matrix; this is evidenced by the lack of a red-shift of the cluster peak with anneal temperature, which should occur based on a quantum confined luminescence mechanism.[243] The biggest increase of cluster PL occurs for the 1100 °C anneal; the lack of peak shifting between 1000-1100 °C indicates that the *emitting clusters* have already reached the critical size,

[243] As will be seen later, increasing the amount of Si available for cluster formation significantly red-shifts the PL peak.

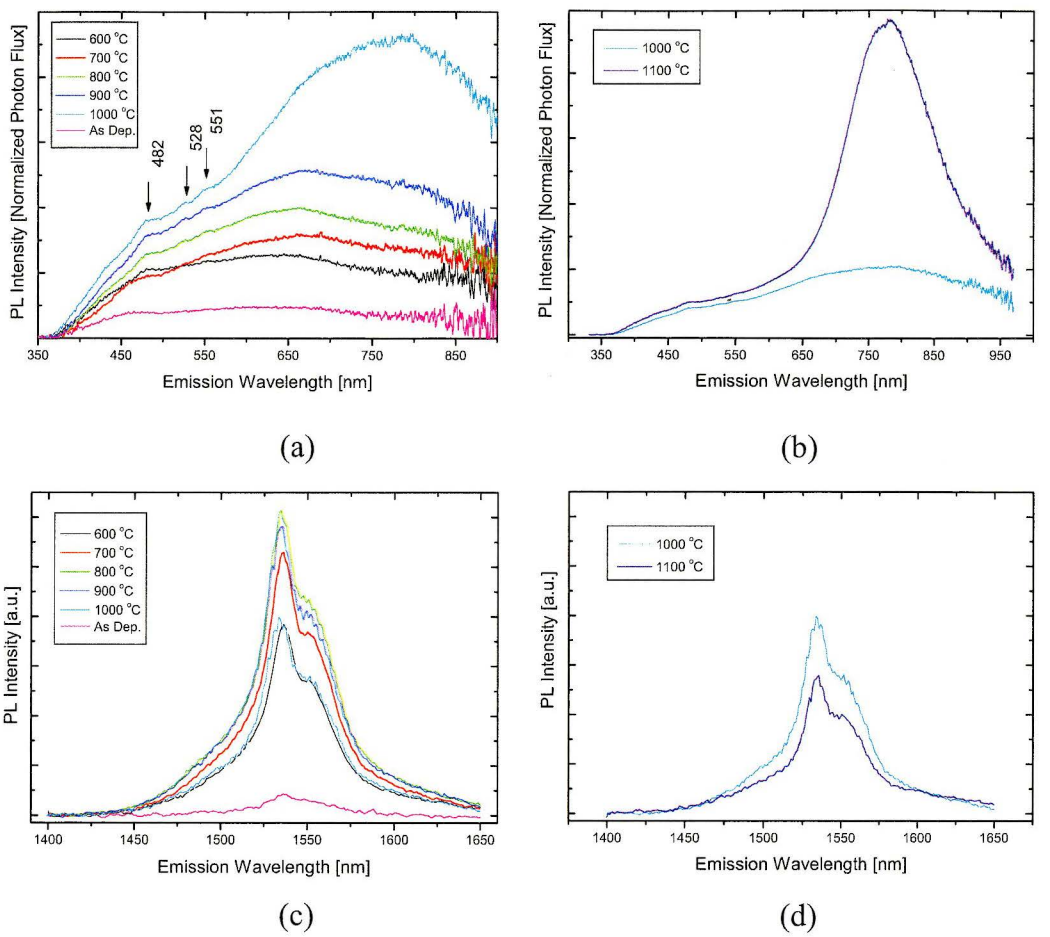

Figure 6.17: Comparison of the 350-1000 nm band PL (showing the rise of Si nano-cluster emission), figures (a,b), and the corresponding 1400-1650 nm band Er PL, figures (c,d), in sample Da9 over a range of anneal temperatures of one hour duration in flowing N_2 gas. The y-axes of (c,d) are synchronous.

by 1000 °C, for the given Si supersaturation. Energy transfer from the smaller to larger clusters may also be producing a preferential emission from the larger members, in which case, the PL yield enhancement at 1100 °C is primarily the result of Ostwald ripeneing and the reduction of defective clusters.

It might be argued that the broad PL observed at low anneal temperatures in Figure 6.16(a) is due to the NBOHC defect since it seems to be peaked near

650-660 nm.[244] While this defect may be contributing in *part* to the signal, it does not seem to be the dominant contributor. There are four reasons for this [207]:

1) Such a defect, based on an O dangling bond, is inherently unlikely in a film containing both excess Si and Er, since both of these species should aggressively consume non-bridging oxygen atoms.

2) NBOHC defects are known to anneal out of Si-rich Si_yO_{1-y} thin films below 600 °C, which is not consistent with the progressive increase in PL observed with anneal temperatures beyond 600 °C observed in Figure 6.17 [208,209].

3) Third, hydrogenation at 800 °C in an ambient of 5% H_2 in Ar gas results in an increase in this PL relative to that at 800 °C in N_2 as shown in Figure 6.18 (as well as an enhancement of the long wavelength contribution characteristic of Si nano-clusters [210]).[245] The PL from a NBOHC would be expected to quench during such an anneal due to passivation of the O dangling bond [211,212].

4) Films which are deposited with a similar Er concentration but progressively more Si show a gradual red-shifting of this exact PL band – consistent with an increase of the average Si-nc size.

---

[244] One could even argue that small peak shifting of the NBOHC PL could occur at low anneal temperatures as a result of the evolution of H from the film, possibly changing the relative populations of the two types of NBOHCs (which emit at different energies) identified in chapter x. One could go further and argue that because the NBOHC is resonant with the Er $^4F_{9/2}$ level, it too could sensitize the Er and would therefore be consistent with the strong Er emission at 1.54 μm.

[245] In addition, such a hydrogenation at (800 °C) exposes an unmistakable Si nano-cluster PL peak (see Figure 6.32(b)), suggesting that it is merely not *entirely* apparent in the spectra in Figure 6.17(a) due to non-radiative defects. The apparent Si nano-cluster PL in the present sample probably represents only the smallest cluster nuclei since they have less chance of containing non-radiative defects than their larger counterparts which become luminescent only upon H-passivation.

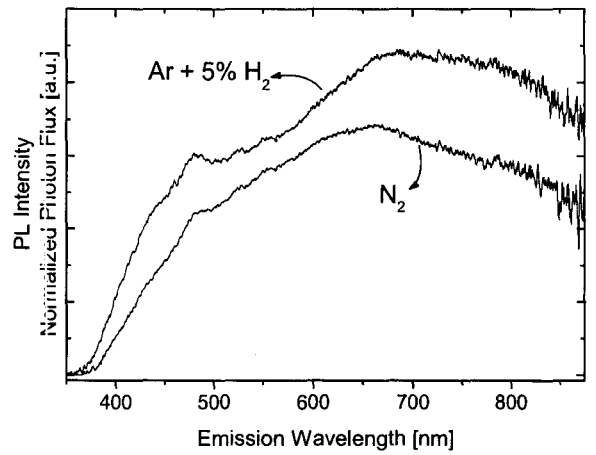

Figure 6.18: Enhancement of the PL from film Da9 following an anneal at 800 °C for one hour in a H-containing ambient of (Ar + 5% H_2) gas compared to N_2 gas.

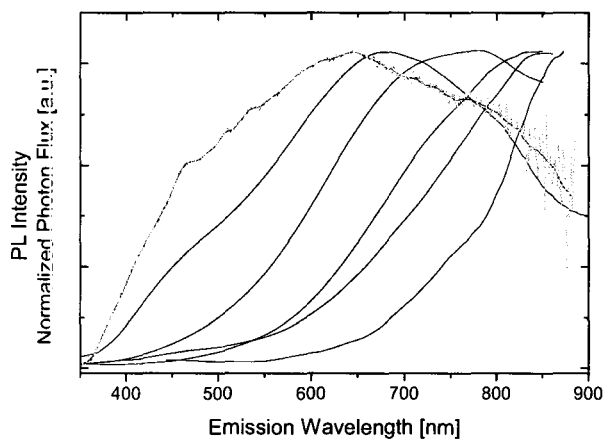

Figure 6.19: PL spectra of films Da2-4,9-11 following annealing at 800 °C for one hour in N_2; the red-shift of the peak of the characteristic emission band is evident.

Figure 6.17 reveals the presence of defect PL at the high energy side of the Si nano-cluster peak. Three small features superimposed at 482, 528, and 551 nm likely correspond to Er up-conversion luminescence from the $^4F_{7/2}$, $^2H_{11/2}$, and $^4S_{3/2}$ manifolds respectively. Although these peaks are weak, it is interesting that up-conversion PL could be present in a film with such low Er content (near 0.1 at. %).

Studying the Si nano-cluster luminescence at an anneal temperature of 1100 °C provides numerous insights into their structural and optical properties in the presence of [low concentrations of] Er. The red-shifting of the PL peak with increasing mean cluster size seems to be well-observed in the films of this study. Increasing the Si supersaturation increases the equilibrium cluster size and should therefore red-shift the peak emission energy. This is depicted in Figure 6.20.

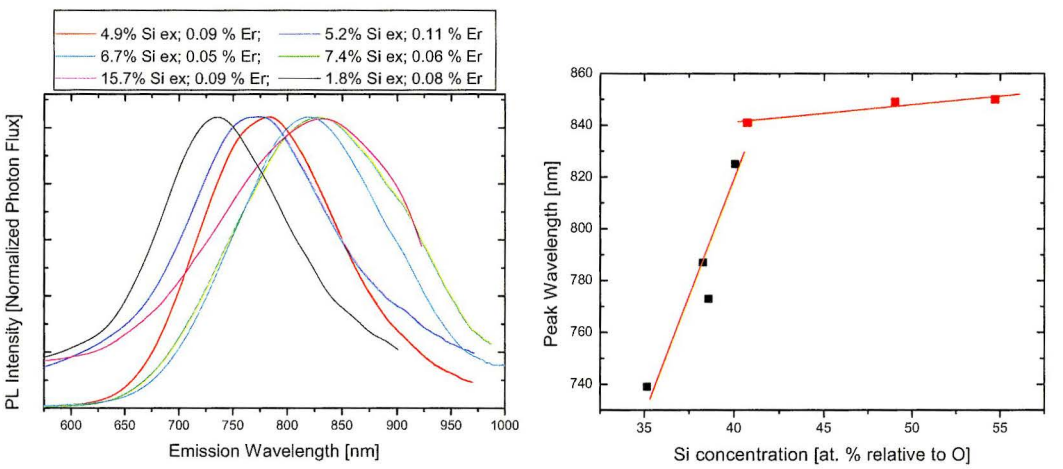

(a) (b)

Figure 6.20: (a) Si nano-cluster PL normalized to constant amplitude to observe the red-shift and increase of the FWHM of the peak with increasing excess Si content; (b) Peak wavelength as a function of Si excess with linear fits to illustrate the two regimes of red-shifting.

Figure 6.20(a) shows the Si nano-cluster peak PL normalized to the same intensity to allow the visualization of the red-shift. The extent of the peak shifting seems to be defined by two different regimes depending on the excess Si content; each is depicted with a linear fit in figure 6.20(b). The saturation of the peak emission energy near 850 nm suggests that the quantum size effects begin to break down for clusters larger than those emitting near this energy; that is, bulk-Si-like nonradiative recombination pathways re-appear. These larger clusters become 'dark'. This could also be taken as evidence of the dipole-dipole energy

transfer from smaller to larger clusters. This effectively darkens the smaller clusters as the excess Si is increased and produces an exaggerated red-shift of the overall luminescence peak relative to the actual cluster size distribution.

It is also clear in Figure 6.20(a) that there is an increase of the full width at half maximum of the Si cluster PL peak with increasing Si supersaturation. This supports the proposition that a larger cluster size distribution will form when there is more excess Si present; this is effectively a statistical effect. Interestingly, the Si cluster PL peak is well described by a single Gaussian lineshape. This is depicted in Figure 6.21 for sample Da2.

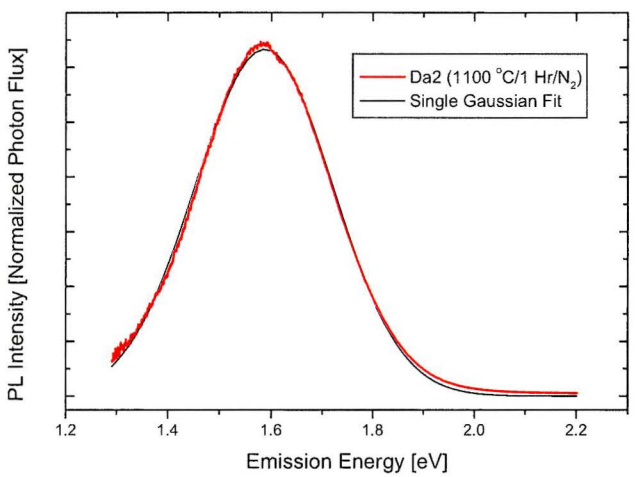

Figure 6.21: Single Gaussian fit of the Si nano-cluster PL emission in sample Da2 (annealed at 1100 °C for one hour in flowing N_2 gas).

The FWHM appears to be a linear function of the Si excess (depicted in Figure 6.22).[246]

It is revealing to compare the trend in the 1.54 μm luminescence (as a function of Si content) alongside that for the nano-cluster luminescence for annealing at 1100 °C. At this anneal temperature, one is effectively isolating the

[246] While the large cluster size distribution has been identified as an undesirable randomizing effect in these films, it has been suggested that the broad PL emission might actually be beneficial in the context of wavelength division multi-plexing applications.

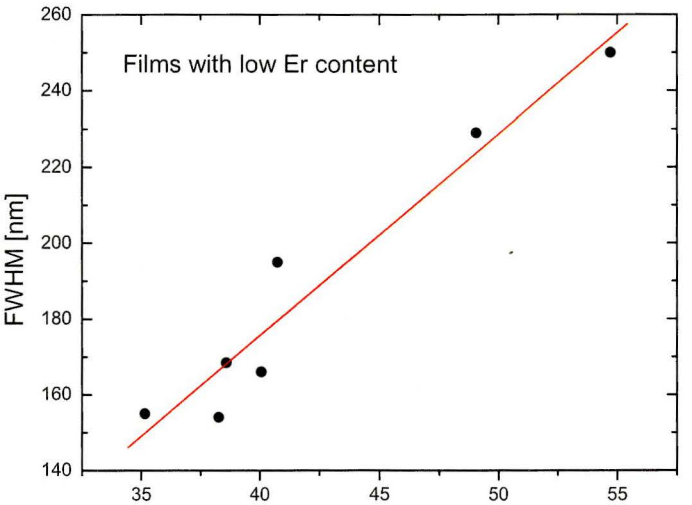

Figure 6.22: Full-width-at-half-maximum of the Si nano-cluster PL distribution as a function of excess Si content; all samples were annealed at 1100 °C for one hour in flowing N_2 gas and the Er content in all samples was near 0.1 atomic percent.

Si nano-cluster (and nano-crystal) sensitization without the complication of significant defect sensitization. This is depicted in Figure 6.23(a); note that all of the films depicted in the figure have similarly low Er concentrations. The figure does not permit comparison of the absolute luminescence intensity between the visible and infrared spectral ranges, but only the trend is important here; to isolate this trend, lines have been drawn to guide the eye. As an additional detail, the data is reasonably well described by a Lorentzian lineshape. Figure 6.23(b-d) depicts this Lorentzian fit for each set of data, as well as the overlap of the two Lorentzians.

To begin with, it is clear from Figure 6.23 that an excess Si content of about 6 at. % relative to SiO_2 is optimum for the Si cluster luminescence. This optimizes the cluster size and separation. More interesting, however, is the striking similarity of the trend in the curves in each spectral range. The Er and Si cluster luminescence is optimized nearly identically. This suggests that the sensitization of the Er by the Si nano-clusters is the main energy transfer mechanism under these anneal conditions; this is a plausible argument regardless

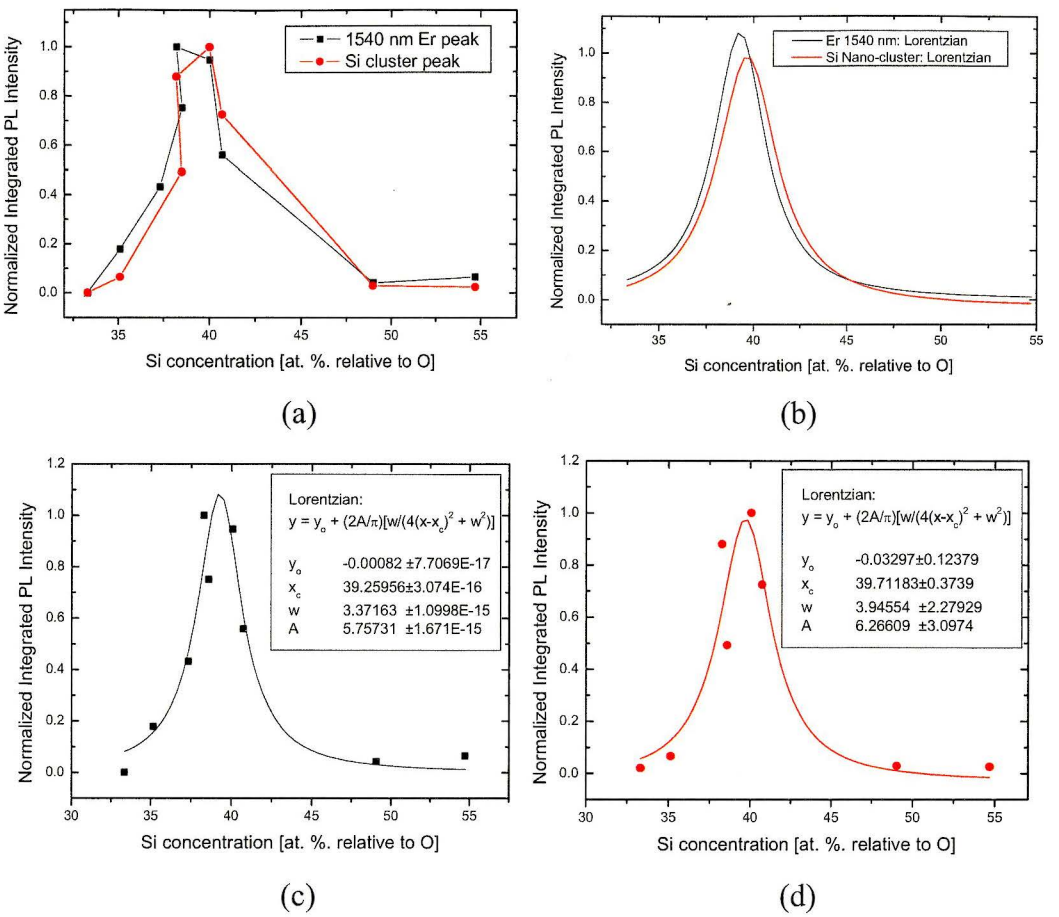

Figure 6.23: Film composition dependence of the PL emission from both Er (1.54 μm) and Si nano-clusters; all films have low Er content (≤0.1 at. %). These films are annealed at 1100 °C for one hour in flowing N_2 gas in an attempt to isolate the Si nano-clusters as the sole sensitizers.

of whether one considers the observed cluster PL to originate from Er-coupled *or* uncoupled clusters.

This information has a subtle importance with regard to EL devices based on films from the ECR-PECVD system employing the in-situ doping. While an 800 °C anneal might be absolutely optimum for the 1.54 μm PL as a result of the presence of defects and the pathological SiO_x matrix, this might be completely un-optimum in terms of favourable electrical injection properties. One might expect more predictable and reliable current injection in the more uniform and ordered films which inevitably result from the 1100 °C anneal. It is important to

realize that an effective nano-cluster-based sensitization mechanism is possible at these temperatures but that it requires a low Er concentration. This is perhaps a subtle point because most other research groups form SiO_x films containing nano-crystals *before* they introduce the Er (typically by ion implantation). They can therefore use a low temperature post-implant anneal to activate the Er without clustering – without sacrificing the nano-crystal formation which requires high temperatures. With the in-situ doping, one must rely on a single anneal step, which seems to rule out the required high temperature anneal for fear of clustering the Er. However, apparently as a result of the reduced clustering tendency in the present films, it is possible to take advantage of the Si nano-cluster/crystal sensitization with a single anneal step.

6.6 Defect PL and Other Er-Sensitizing Centres

6.6.1 Characteristic Spectral Forms

Sample	Absolute Atomic Areal Density[1] [x 10^{17} atoms/cm^2]				Thickness [Å]		Index of Refraction[4]	Er [at. %] Relative[5] to Si and O	Si [at. %] [6] (in parentheses) *and* (excess Si [at. %][7]
	Si	O	Er	Ar	Optical[2]	RBS[3]			
Er119	3.00	4.70	0.0347	0.0489	1245	1220	1.593	0.45	(39.0)8.44
Er120	3.02	4.79	0.0425	---	1240	1200	1.600	0.54	(38.7)8.00
Da1a	2.67	5.07	0.0127	0.135	1118	1710	1.514	0.16	(34.5)1.74
Da1[10]	4.39	8.69	0.0131	---	1994	1970	1.467	0.10	(33.6)0.344
Da2	4.86	7.84	0.0112	---	2065	1980	1.541	0.088	(38.3)7.40
Da3	5.13	7.46	0.0069	---	2278	1970	1.559	0.055	(40.7)11.1
Da8[11]	4.65	8.45	0.0127	0.0789	2190	2065	1.484	0.097	(35.5)3.24
Da9	4.90	7.80	0.0144	0.0235	2120	2085	1.544	0.113	(38.6)7.87
Da10	5.00	7.48	0.0064	0.0281	2044	1985	1.6523	0.051	(40.1)10.1
Er116	3.56	7.55	0.125	0.236	1550	1680	1.486	1.11	(32.0)-1.94
Er117	3.60	7.78	0.259	0.164	1645	1935	1.499	2.23	(31.6)-2.55
Er118	3.99	8.84	0.446	0.156	1780	2220	1.502	3.36	(31.1)-3.35
Da5	4.80	9.65	0.0122	---	2200	2140	1.456	0.084	(33.2)-0.173
Da6	4.76	9.65	0.0198	---	2176	2100	1.456	0.14	(33.0))-0.451
Da12	4.90	10.1	0.0207	0.0313	2150	2145	1.452	0.14	(32.7)-1.00
Da13	4.70	9.40	0.0187	0.0242	2143	2125	1.45	0.13	(0)0
Er147[9]	4.84	8.93	0.622	~0	2750	3050	---	4.32	(35.1)2.72
Er149	4.38	8.74	0.176	0.19	1980	2100	1.498	1.32	(33.4)0.0762

Sub-section of Table 6.1. The table rows have been arranged by their colour codes.

Shifting attention to the oxide-based defects that are giving rise to the blue-violet PL, one considers anneal temperatures below 1000 °C. It is useful to define three *composition regimes* in order to differentiate the defect PL from that of the Si-clusters. The first regime is that containing moderate amounts of excess Si and a low quantity of Er (yellow highlighting in Table 6.1). These films are unambiguously dominated by the nano-cluster PL at high anneal temperature (1100 °C) and were discussed in the previous section. At lower temperatures, however, the defect PL *and* low temperature cluster PL are combined and exhibit intensities of similar magnitude (see Figure 6.24(b-d) below and Figure 6.17(a) and Figure 6.19 for example). The cluster PL appears as the broad region of *positive curvature* that extends into the red/infrared. The second composition regime corresponds to films containing no excess Si (orange highlighting in Table 6.1); these films are dominated by blue-violet PL *only*, regardless of the Er content, and show an exponentially decreasing tail of *negative curvature* which extends into the yellow-red portion of the spectrum (see Figure 6.24(a)). The third regime consists of films containing moderate amounts of excess Si and large amounts of Er (purple highlighting in Table 6.1); these films may be dominated by the defect PL but show an additional segment of *positive curvature* extending out into the yellow-red-infrared wavelengths which becomes more significant with increasing excess Si (see Figure 6.24(e-i)). All of the spectra in Figure 6.24 correspond to films either as-deposited or annealed at temperatures between 600 and 900 °C.

The defect PL is easily identified in all the spectra of Figure 6.24 and is clearly seen to be highly sensitive to the composition. It is primarily concentrated between 400-500 nm and is generally quite smooth with only occasional minor structural resolution. Annealing does not seem to significantly change the environment of the defects as the corresponding luminescence lineshape does not change, nor is there any apparent shift of the peak wavelength. This is exemplified in Figure 6.25 for sample Er149.

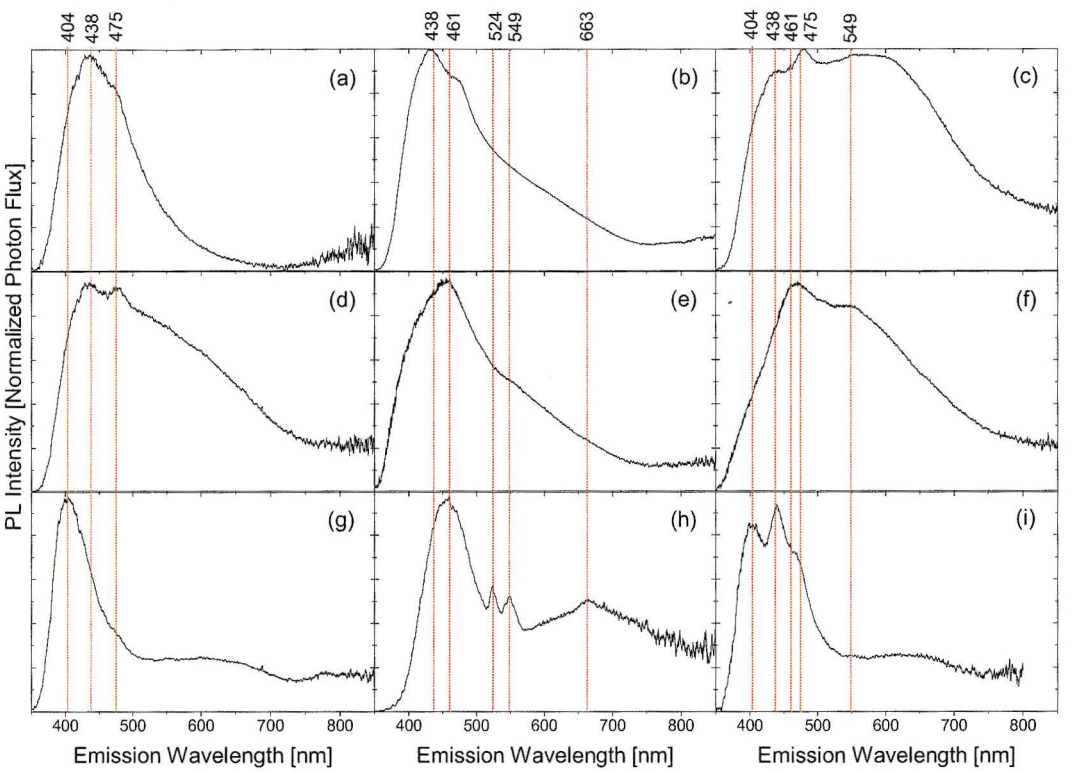

Figure 6.24: Representative visible PL spectra showing defect (and some Si nano-cluster) PL at low temperature annealing; intensity axes are not comparable; (a) Er116/800°C/1h; (b) Da8/600°C/1h; (c) Da8/900°C/1h; (d) Da1/as-deposited; (e) Er147/as-deposited; (f) Er147/600°C/1h; (g) Er149/800°C/3h; (h) Er054/800°C/5h; (i) Er149/800°C/3h/Si irradiation $2x10^{13}$ cm^{-2}/150°C/10 min.

It is intuitively expected that these defects should correspond to some of the common radiative oxide defects identified in Chapter 3. Some of the dominant peaks have been identified by the red lines in Figure 6.24. The peaks near 461 and 475 nm, for example, could be correlated with a neutral oxygen vacancy (NOV).[247] This defect seems to increase strongly with increasing Er content.

[247] It should be kept in mind that the measured emission wavelengths might not correspond exactly with those wavelengths quoted in Chapter 3 because those were based on pure SiO_2 whereas the present host matrix contains numerous compositional perturbations. One would expect the same defects in the present sample to emit in bands *similar* to those found in SiO_2. Positive identification of the defects requires PLE spectroscopy extending into the UV to isolate the characteristic absorption bands; this data should then be correlated to EPR measurements.

One could speculate that this fact is consistent with a NOV since film stoichiometry

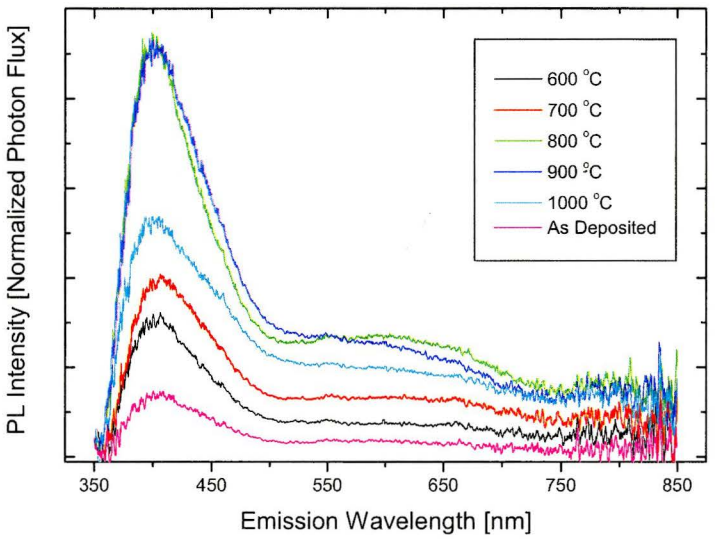

Figure 6.25: Sample Er149 PL emission shown for a range of annealing temperatures; in all cases the anneal duration was 1 hour and the ambient was flowing N_2 gas. It is clear that there is essentially no peak wavelength shifting.

considerations require the formation of oxygen deficient centres to compensate the consumption of NBOs by the Er ions. Peaks near 404 nm could potentially correspond to either divalent Si or a perturbed weak oxygen bond. The 404 nm peak appears too broad to correspond to up-conversion luminescence from the $^2H_{9/2}$ to ground transition of Er^{3+}. The peak near 438 nm might also result from divalent Si. The NBOHC does not seem to be well resolved in these spectra but it may be contributing to the broad emission between 600-700 nm in those spectra in Figure 6.24(g-i).

There are generally no dominant features at wavelengths longer than 500 nm unless the film contains excess Si (Figure 6.24(b-i)). In this case, there seems to be either a marked feature near 550 nm or a broader peak centred closer to 600 nm. The feature near 550 nm may be related to the presence of an E_δ' centre or a small peroxy radical. The E_δ' centre would make sense given that the films are Si-rich, particularly since the above spectra correspond to low anneal

temperatures at which there would be limited Si phase separation. The intensity of the broad emission near 600 nm increases with excess Si but decreases with increasing Er. This might correspond to small Si nano-clusters with the appropriate quantum confined emission energy. Once again, the presence of small clusters would be consistent with the low anneal temperatures. If this emission is indeed the result of Si clusters, one would expect that an anneal at 1100 °C should red-shift and enhance the peak intensity as was observed in the films with low Er content (Figure 6.20). In actuality this was *not* seen to occur for the films with high Er content but may be the result of the altered Si cluster formation kinetics in the presence of high impurity concentrations.[248]

6.6.2 Visible Er Luminescence

The distinction between defect luminescence and that due to Er visible transitions is not difficult to make because the latter exhibits an extremely sharp lineshape. This is exemplified by the two sharp peaks of Er054 (Figure 6.24(h) amd 6.26) corresponding to the $^2H_{11/2}$ and $^4S_{3/2}$ transitions to the ground state of Er^{3+}.[249,250] In fact, this double peak emission is the most commonly observed visible Er^{3+} luminescence in these films but is usually extremely weak (at least one or two orders of magnitude lower than the defect PL). The emission is probably caused

---

[248] Interesting from a processing perspective was the odd red-shift in sample Da8 (Figure 6.24(b,c)), which coincidentally seems to have incorporated a significant amount of C. In this case, the broad PL emission maximized for a 900 °C anneal and decreased beyond this; the maximum emission was also the most red-shifted, apart from which the emission was blue-shifted. Given that the signal was peaked at an energy greater than 2 eV, this seems to be evidence that the clusters were not pure Si but perhaps closer to SiC. Given that this was actually a repeat deposition of sample Da1 (which exhibited standard behaviour), this anomalous behaviour is strong evidence of the impact of small variations in the plasma during deposition. The film was obviously bond-structured differently from Da1 and accordingly responded differently to annealing.

[249] For example, the $^4S_{3/2}$ level can be reached by co-operative up-conversion of an Er^{3+} ion in the $^4I_{13/2}$ level through relaxation of a nearby ion in the $^4I_{9/2}$ level. Two ions in the $^4I_{13/2}$ level can similarly couple to yield one ion in the $^4I_{9/2}$ level. In addition, the $^4I_{9/2}$ level seems to be directly excited by the Förster transfer from Si nano-clusters.

[250] The sharp peak near 663 nm is probably the $^4F_{9/2}$ transition of Er^{3+}. It is apparently superimposed on a broad background which may be a NBOHC or weak PL from small Si clusters.

by either cooperative up-conversion between Er ions or by resonant excitation of the level by small Si nano-clusters or oxide defects emitting in the blue-violet.

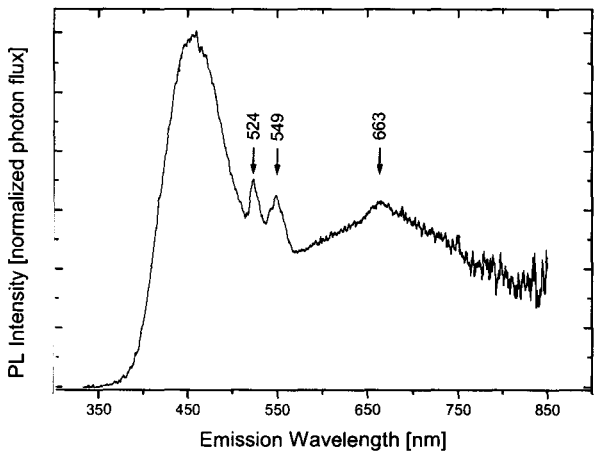

Figure 6.26: Spectra of Er054 showing Er up-conversion luminescence at 524 and 549 nm (and possibly some at 663 nm). The sample was annealed for several hours at 800 °C in flowing Ar ambient.

When there is no (or very little) excess Si, this Er luminescence does not occur until the Er concentration is approaching 1.5 at. %. When there is 2-7 at. % Si excess, it appears weakly even for the lowest Er content and increases with increasing Er but is not present for Er contents beyond 3 at. %. The connection with the excess Si is obvious because there is enhanced excitation of the Er to the $^4I_{13/2}$ level. In theory, up-conversion luminescence becomes a progressively higher order process for higher lying levels and therefore should occur with lower probability. In agreement with this, the only other likely up-conversion luminescence might be the feature (presumably super-imposed) at 438 nm, which may correspond to both the $^4F_{3/2}$ and $^4F_{5/2}$ transitions to ground.

6.6.3 Spectral Decomposition and Identification of Radiative Defects

The obvious method for assessing the above assignment of luminescent centres is to de-convolute the PL spectra into individual transition lineshapes. This has been attempted on a number of the spectra and several excellent fits were

achieved assuming Gaussian lineshape function.[251,252] Caution must be exercised when considering the results, however, because there is no guarantee that all of the components have been identified (in this sense, the fitting has an inherent ambiguity). Figure 6.27 depicts the Gaussian fits for samples Er116 and Er149, both annealed at 800 °C.

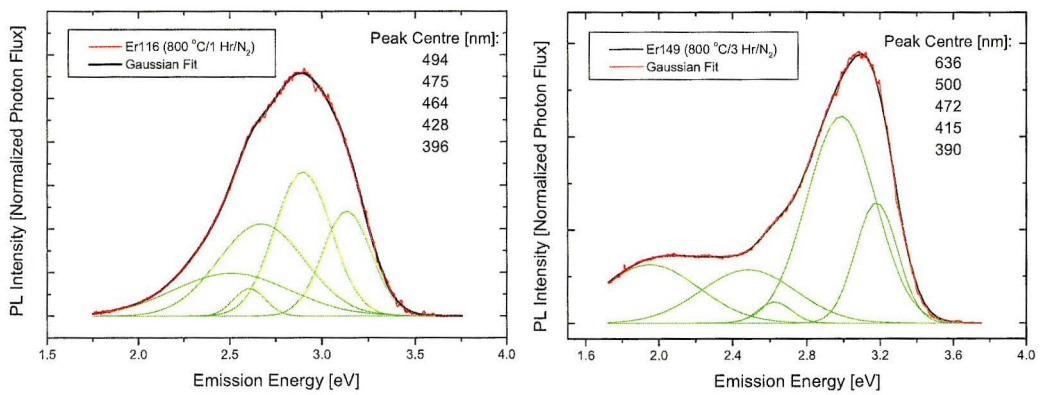

(a) (b)

Figure 6.27: Gaussian de-convolution of representative PL spectra; (a) Er116; (b) Er149

The two spectra show some similar components. The 415 nm component may confirm the presence of the WOB, while the 460-475 nm components may correspond to the NOV. In the case of Er149, the broad 636 nm component may be the NBOHC or small Si nano-clusters. If it is a NBOHC then it is interesting that this component does not appear in the spectrum of Er116. The wide range of speculation on the divalent Si centre means that the 390 nm and 496/500 nm components might actually be ascribed to it.

---

[251] The use of a Gaussian as the sole lineshape function commits a small error. An actual transition lineshape is described by a Voigt function, which is a convolution of Lorentzian and Gaussian functions. There are, in effect, multiple sources of linewidth broadening. For example, Doppler broadening is described by a Gaussian function, whereas lifetime and collision broadening are described by Lorentzian functions. In all case, these linshape functions employ the photon *energy* (ie. frequency) as the independent variable and *not the wavelength*.

[252] Because of the noise in the experimental spectra, the raw data were typically subjected to a 35 point Fast Fourier Transform smoothing prior to peak fitting.

These spectra can be compared with a PL spectrum of dry thermal SiO_2 grown on (111) Si at 1000 °C for one hour. The signal is over an order of magnitude weaker than that observed in the Er-doped ECR-PECVD films and is depicted in Figure 6.25. The overall inhomogeneous linewidth and location of the emission band is very similar to the Er-doped films containing no excess Si. A weak component appears at 476 nm in very similar fashion to the Er-doped films. Similar to Er116, there are also components near 400 and 430 nm. Finally, the component near 500 nm appears in all three spectra. The only irregular component is that at 445 nm, however it is unclear whether this actually represents more than one peak since any fine structure between 2.7-3.0 eV is obscured by noise due to the weak signal.

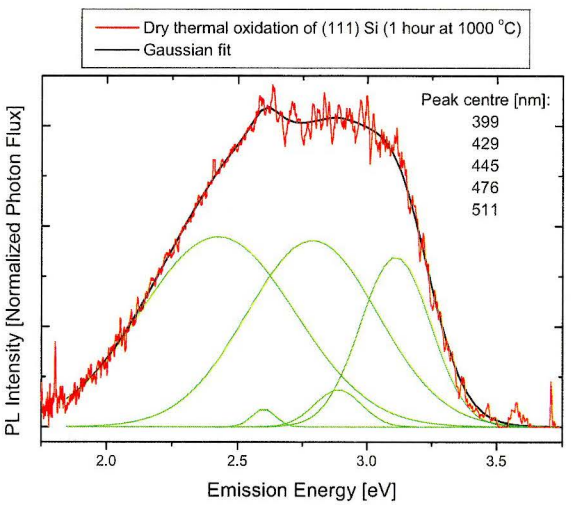

Figure 6.28: Gaussian deconvolution of the PL spectrum of dry thermal SiO_2 grown at 1000 °C for one hour on (111) Si. The emission band is similar to the oxide defect PL in Er-doped films.

It is interesting to consider a Gaussian de-convolution of the spectrum of Er118, for which the spectral fine structure was previously discussed in the context of micro-cavity effects (resulting from an annealing induced surface micro-structure). Ironically, nearly all of the fitted components can be assigned to high-lying Er^{3+} transitions as depicted in Figure 6.29.

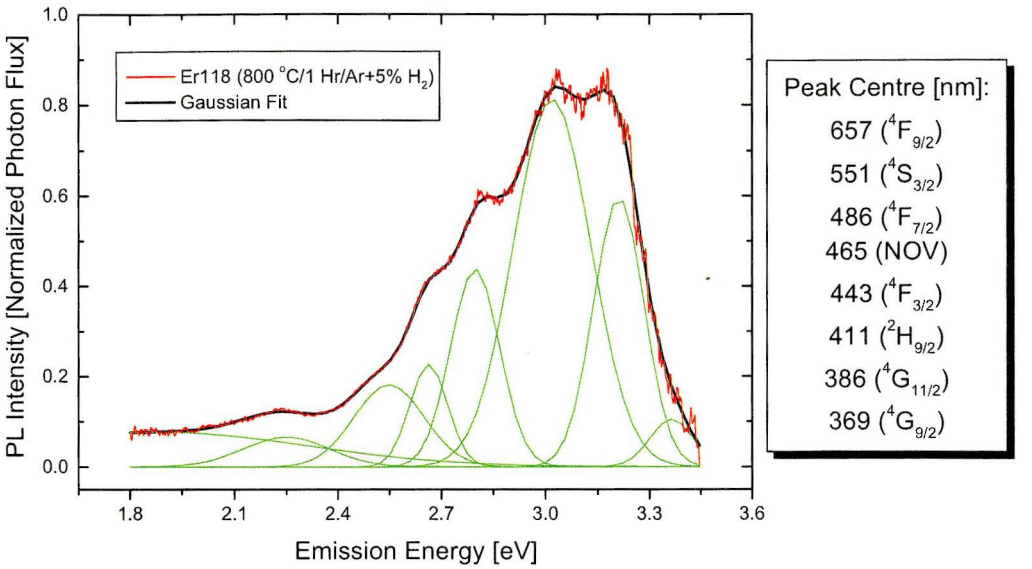

Figure 6.29: Gaussian de-convolution of the PL spectrum of sample Er118 annealed for one hour at 800 °C in flowing forming gas (5% H_2 in Ar) to form the surface micro-structure. The transitions seem to be those of high lying Er states.

It is tempting to ascribe this to up-conversion, but the fact that the peaks become more intense with increasing energy level seems to be at odds with the fact that up-conversion to successively higher levels is a successively lower probability event. It is difficult to ascertain whether or not this is even feasible at an Er concentration near 4 at. %. The intensity ordering of the peaks *could* potentially be explained if the Er^{3+} ion is actually cascading down through these levels from even higher-lying levels. Unless the Er can absorb the pump photons directly, however, or an extremely high energy level transfer takes place from a defect, this does not seem feasible. There is an obscure proposal in the literature, however, that certain Er-Er based clusters (in *a*-Si) could introduce states in the host matrix that could resonantly absorb a 325 nm photon. It was suggested that PL similar to Er118 could result from the relaxation of these states by a phonon-assisted process [213,214]. This would imply that, for Er118 film, the observed 1.54 μm PL could simply be due to phonon cascade from the original resonantly excited state. The trouble with this explanation is that the fine structure in the Er118 PL

does not correspond to a constant energy step (corresponding to the dominant phonon). Although it is difficult to properly assess the feasibility of such an explanation, it would explain why this particular spectrum only occurs at the highest doping levels (it is not apparent in Er147 but this might be the result of the presence of excess Si).[253] In any case, it would be rather mysterious that such high-lying Er levels would not relax non-radiatively by phonon-cascade, given that the photon flux being used to excite the system (~10^{18} *photons/cm^2/s*) is only sufficient to provide 1 photon per second for every thousand Er ions (assuming a direct optical absorption cross section per Er ion of 10^{-21} cm^2).

Some of the lower energy transitions appear far too broad to be assigned to Er, however there may be some broad low energy components missing from the fit (such as a NBOHC). The component near 465 nm does not correspond well to any of the Er^{3+} visible transitions but could be assigned to the NOV. One may be able to confirm the origin of this luminescence by plotting the intensity of one of the spectrum peaks as a function of the corresponding1.54 μm PL for various incident laser powers. The exponent in the functional relationship between these two quantities (2, 3, etc.) is indicative of how many steps would be involved in an up-conversion process.[254]

---

[253] Either of the up-conversion or resonant absorption mechanism gains some credence over the purely interference mechanism when comparing the present PL spectra with sample Er117. This latter film has slightly lower Er content, but a completely flat film surface (confirmed by SEM) and shows a very similar PL spectral content (albeit of lower intensity) to Er118 though with less peak resolution. This similarity of Er117/118 concurs with the similarity of their anneal-PL curves for the 1.54 μm luminescence. The visible PL spectrum of Er116 is different from these, in agreement with its different anneal-PL curve at 1.54 μm.

[254] For example, if two Er ions in the $^4I_{13/2}$ level are required to produce one Er ion in the $^4I_{11/2}$ level (and therefore one 980 nm photon), then the PL intensity at 980 nm should be the square of the PL at 1.54μm. Similarly, the double peak luminescence at $^2H_{11/2}$ and $^4S_{3/2}$ levels is a second order up-conversion process between two Er^{3+} in the $^4I_{11/2}$ state (populated by the $^4I_{9/2}$ state). The $^4F_{9/2}$ transition is due to relaxation from higher level states.

6.7 Isolation of the Optimum Compositions for PL from Silicon Nano-clusters and Defect Centres

Figure 6.30 shows a three dimensional plot which summarizes the PL emission in the 350-1000 nm band (due to both Si-clusters and oxide defect) as a function of both the Si and Er concentration *for a one hour anneal at 800 °C in flowing N_2 gas*. The anomalous Da8 sample has not been depicted in the figure. The PL intensity axis has been normalized to the highest PL observed in the study (Si nano-cluster PL at 1100 °C annealing for sample Da10).

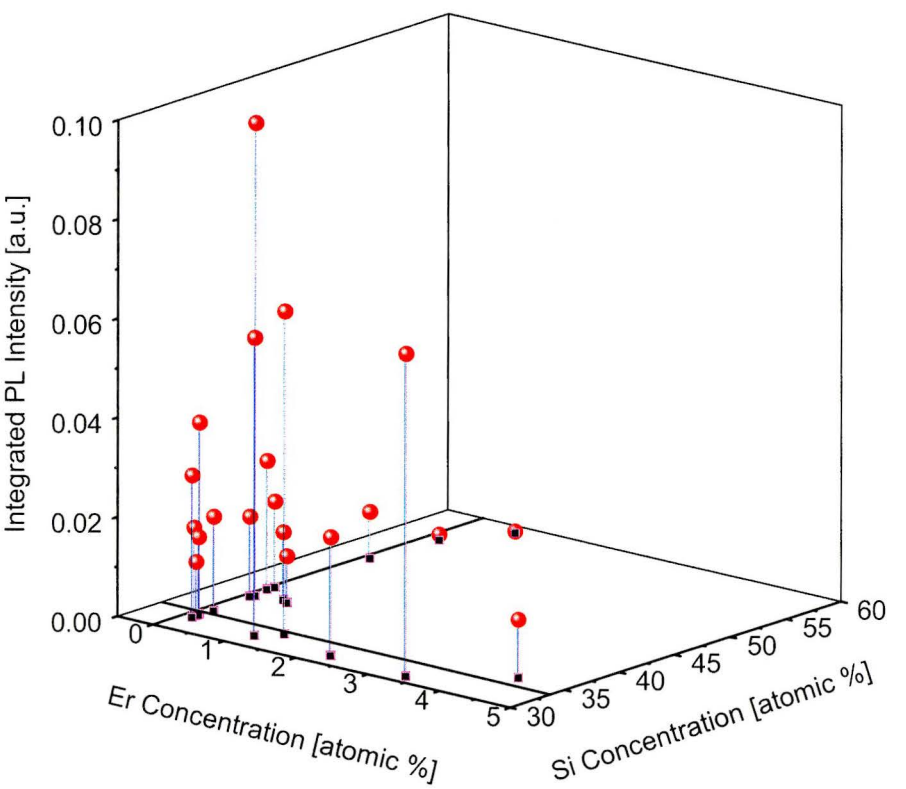

Figure 6.30: Plot of the integrated PL intensity in the 350-1000 nm band as a function of the entire composition space. In all cases, the anneal condition is the same as that in Figure 6.6: 800 °C, 1 hour, flowing N_2 ambient. The intensities have been normalized to highest PL observed in the entire study.

Careful comparison of this figure with the corresponding 3D plot for the 1.54 μm PL (under the same annealing conditions) reveals that the visible PL is generally strongest where the 1.54 μm PL is weakest and vice versa. This provides further evidence for the coupling between the emitting species of Figure 6.11 (defects) and the emitting species of Figure 6.4(a,b) (Er ions) under these anneal conditions. In order to maximize the visible defect PL, one has two choices: deposit a film with no excess Si but greater than 1 at. % Er (or as much as possible) and anneal at 800-900 °C, or deposit a film with about 1-2 at. % Si excess and as much Er as possible (greater than 4 at. %) and conduct a limited anneal (eg. 1-5 minutes at 600 °C).

6.8 Coupling of Radiative Defects to Silicon Nano-clusters

Sample	Absolute Atomic Areal Density[1] [x 10^{17} atoms/cm^2]				Thickness [Å]		Index of Refraction[4]	Er [at. %] Relative[5] to Si and O	Si [at. %][6] (in parentheses) *and* (excess Si [at. %][7]
	Si	O	Er	Ar	Optical[2]	RBS[3]			
Da1a	2.67	5.07	0.0127	0.135	1118	1710	1.514	0.16	(34.5)1.74
Da1[10]	4.39	8.69	0.0131	---	1994	1970	1.467	0.10	(33.6)0.344
Da2	4.86	7.84	0.0112	---	2065	1980	1.541	0.088	(38.3)7.40
Da3	5.13	7.46	0.0069	---	2278	1970	1.559	0.055	(40.7)11.1
Da4	5.21	5.41	0.0100	---	---	1785	---	0.094	(49.1)23.6
Da5	4.80	9.65	0.0122	---	2200	2140	1.456	0.084	(33.2)-0.173

Sub-section of Table 6.1

It is evident from this discussion that for fixed Er concentration the defect PL tends to decrease as the amount of excess Si increases. This is clearly illustrated in Figure 6.31, in which the PL spectra of films with low Er content, annealed for one hour at 800 °C, are depicted for progressively increasing amounts of excess Si. As the Si increases, the defect PL progressively decreases and the dominant portion of the PL band shifts to the red. It will be suggested in section 6.10 (annealing under oxygen) that introducing the excess Si does *not* cause the defects to disappear. Thus, the quenching of the defect PL must be due to the coupling of the defects to non-radiative states introduced in the vicinity of the Si clusters.

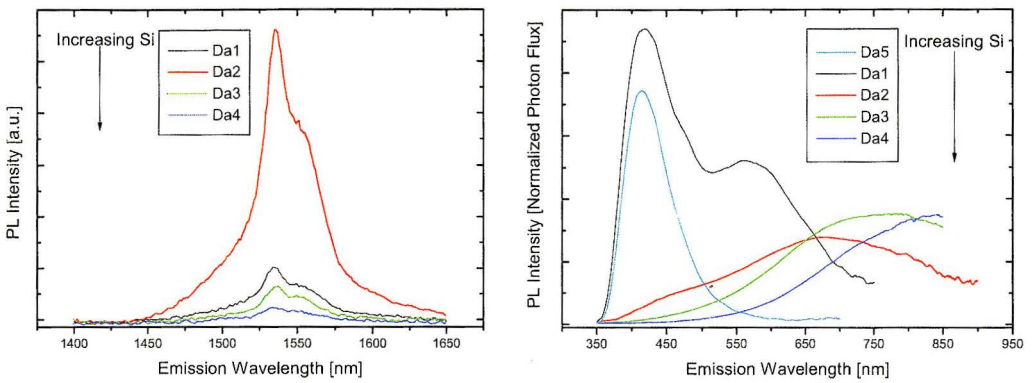

(a) (b)

Figure 6.31: The disappearance of the defect PL with increasing excess Si and the concomitant rise of the Si nano-cluster PL at low temperature annealing (800 °C for 1 hour in flowing N_2); note the effect on the Er PL near 1.54 μm; (a) Er PL near 1.54 μm; (b) defect and cluster PL

This suggests that the defects lie very near to the surface of the Si clusters [215]. Given that the Er must also lie near the Si cluster surface, this supports the idea that the defects are due in large part to the incorporation of the Er.

Figure 6.31 also depicts the corresponding 1.54 μm PL for each of the films whose visible spectra are shown. It appears that the defects are not efficient sensitizers of the Er PL. However, there are two points that must be remembered. First, the Er PL should naturally be much higher as the excess Si increases because the *number* of cluster sensitizers increases significantly. Second, these films contain low Er content, which would imply few defects, if they are indeed introduced by the Er itself. If one compares the IR spectrum of Er149 (a sample with significant Er concentration and defect sensitization) to those of Figure 6.31, it is clear that the defect sensitization mechanism can be very important – otherwise it is not possible to explain the large 1.54 μm PL for that sample.

6.9 Hydrogenation Annealing

Sample	Absolute Atomic Areal Density[1] [x 10^{17} atoms/cm^2]				Thickness [Å]		Index of Refraction[4]	Er [at. %] Relative[5] to Si and O	Si [at. %] [6] (in parentheses) *and* (excess Si [at. %][7]
	Si	O	Er	Ar	Optical[2]	RBS[3]			
Er117	3.60	7.78	0.259	0.164	1645	1935	1.499	2.23	(31.6)-2.55
Er118	3.99	8.84	0.446	0.156	1780	2220	1.502	3.36	(31.1)-3.35
Er147[9]	4.84	8.93	0.622	~0	2750	3050	---	4.32	(35.1)2.72
Er149	4.38	8.74	0.176	0.19	1980	2100	1.498	1.32	(33.4)0.0762
Da1[10]	4.39	8.69	0.0131	---	1994	1970	1.467	0.10	(33.6)0.344
Da2	4.86	7.84	0.0112	---	2065	1980	1.541	0.088	(38.3)7.40
Da4	5.21	5.41	0.0100	---	---	1785	---	0.094	(49.1)23.6
Da8[11]	4.65	8.45	0.0127	0.0789	2190	2065	1.484	0.097	(35.5)3.24

Sub-section of Table 6.1

Up to this point, the compositions with the greatest potential PL emission in the wavelength ranges of interest, along with the optimum anneal temperature and duration, have been identified in the context of the quasi-inert N_2 gas ambient only. Annealing of the films in reactive gases such as O_2 and H_2 can lend many insights into the luminescence mechanism.

The passivating properties of hydrogen and the associated enhancement of Si nano-cluster PL intensity with thermal hydrogenation have been studied in the literature [119,210,216,217,218,219]. Less work has been devoted to the effect on Er-related luminescence [220]. The present study investigated the effect of annealing as-deposited films in a gas of (Ar + 5% H_2) for an anneal at 800 °C for one hour duration. In all cases, an enhancement was observed for both the 1.54 μm and visible (defect or Si cluster) PL, however the extent of the enhancement relative to a N_2-anneal varied widely from only a few percent to over 50 percent. There was no strong correlation between the composition and the degree of luminescence enhancement in response to the hydrogenating anneal. This is indicative of the wide variability in the bond structure of as-deposited films and the extent to which they contain non-radiative defects and bonded H from the precursors. The visible and infrared PL spectra are depicted in Figure 6.32 for two representative compositions (both Er-doped but only one containing excess

Si). Da2 clearly shows a significant enhancement of the 1.54 μm PL coupled with a significant enhancement of the Si nano-cluster PL. Despite the low anneal temperature, the Si nano-cluster luminescence is unmistakable relative to the somewhat ambiguous PL in the N_2 anneal. This reveals that at the low anneal temperature, most of the Si clusters are still prevented from emitting light because of non-radiative defects presumably dominated by dangling bonds at the cluster surface (possibly in the form of P_b centres). In the case of Er118 (having no excess Si), the PL in both wavelength ranges is enhanced similarly, though to a lesser extent than in Da2. The enhancement of the oxide defect PL (Er118) with

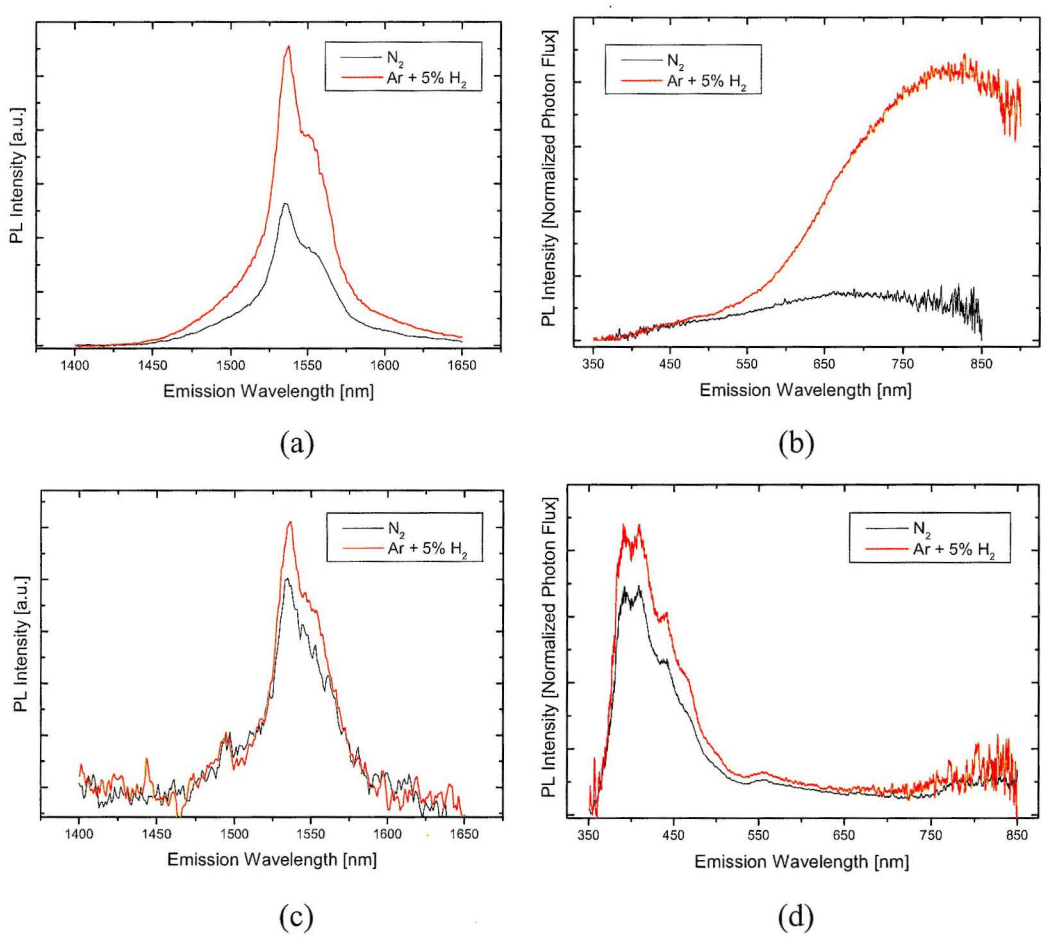

Figure 6.32: PL in the infrared and visible bands compared for annealing under N_2 ambient and (Ar + 5% H_2) gas; (a,b) Da2; (c,d) Er118.

hydrogenation is particularly important, for it supports the proposition made above that the defects are located very near the Si cluster surface when the sample contains excess Si. The passivation of dangling bonds at the cluster/oxide interface (as evidenced in Figure 6.32(b) for Da2) would therefore be expected to decrease the non-radiative coupling of the radiative oxide defects to the clusters and increase the intrinsic oxide defect PL. If the defects are coupled to Er, then the 1.54 μm PL should also increase – as observed in Figure 6.32(c) for Er118; note that the relative enhancement is about the same in each spectral range for film Er118, which has no Si nano-cluster sensitizing centres.

In reality, the effect of the H-anneal is more than simply defect passivation, for it affects the Si cluster formation dynamics (see section 4.1 and 4.4.5), electron-hole recombination pathway (see section 3.3.1 and [210]) and probably the Er complexing. For example, it has been suggested [220] that hydrogenation can actually cause the diffusion of Er towards the Si clusters. In the case of small Si clusters, this results in an enhanced Er concentration in the cluster vicinity leading to increased parasitic Er-Er interactions. The enhancement of the red contribution to the Si nano-cluster PL observed in Figure 6.32(b) is similar to an effect seen in pure Si-rich SiO_x films annealed at 1100 °C [210] and has been ascribed to the passivation of of dangling bonds at the Si nano-cluster surface. Such a passivation would allow electron-hole recombination through disorder-induced shallow states in [dis-ordered] nano-clusters – especially larger nano-clusters; this recombination path would have been much more unlikely when there was preferential trapping at surface defects. While such a shift appears to be contrary to the expectation of a blue-shift following hydrogenation as a result of the H-replacement of Si=O surface bonds [104], the prediction of a blue-shift was based on the assumption of perfectly crystalline Si clusters (such as are achievable in porous Si), which should not have disorder-induced shallow states. The nano-clusters formed at 800 °C (and even largely at 1100 °C) are amorphous. In addition, it has already been discussed in

section 4.4.5 (as well as in [168]) that the incorporation of N into the film during annealing can retard the Si nano-cluster formation dynamics by various means including the occurrence of competing reactions between Si and N. This should give rise to an overall smaller Si nano-cluster mean size when the annealing is carried out under N_2.

6.10 Oxidation Annealing

Annealing under O_2 induces significant changes in this material because of the propensity of Si (and Er) to react with O. Indeed, the oxidation of Si-rich SiO_x films already annealed to form Si nano-clusters has been used to tune to the peak PL emission wavelength of the clusters [182,221]. This occurs because the O penetrates the film and effectively shrinks the clusters by progressively consuming the surface Si atoms by a chemical reaction that presumably forms SiO_2; this can blue-shift the PL.[255] This occurs rapidly because of the large aggregate surface area that the clusters present.[256] It can also occur, in the present films, at seemingly low temperatures such as 800 °C, probably due to the reduced density of PECVD films (deposited at low temperature) which contain much more open volume space than their thermal oxide counterparts, through which O_2 in-diffusion is highly inhibited at such a temperature. In the case of the small, *a*-Si clusters that form under low (<1000 °C) anneal temperature in Er-doped SiO_x, this oxidation has been studied [222]. Energies of formation and oxidation of Si clusters have been estimated to be 1.4 and 1.06 eV respectively. For anneal durations shorter than 20 minutes (and temperatures between 800-950 °C) the cluster formation dominates over oxidation since there is insufficient thermal energy for the O_2 to penetrate through the film in this time; the 1.54 μm Er^{3+} PL

[255] The effect is more complicated because the O can introduce surface states on the Si clusters which could red-shift the emission if, for example, the cluster was previously H-passivated.
[256] For example, consider a SiO_x film containing $9x10^{17}$ Si clusters/cm^3 with an average spherical cluster diameter of 2 nm. This corresponds to over 11 square metres of Si cluster surface area per cubic centimetre of film. In a square centimetre specimen of 200 nm thickness, that is 226 cm^2 of Si cluster surface area, or roughly the surface area of 11 standard two inch diameter Si wafers.

increases. Beyond this time, cluster consumption dominates and the Er-PL decreases. This is probably exacerbated by the fast disappearance of the smallest clusters, which should be the most numerous and most efficient sensitizers. The shrinking of the nano-clusters should also increase the separation between Er^{3+} ions and the Si nano-clusters with a resultant decrease in the resonant energy transfer rate. While the Er content of the films in [222] was too high to observe significant nano-cluster PL, in the present study we were able to infer the oxidation of the clusters through the quenching of the nano-cluster PL with an anneal in O_2. All oxidation anneals were carried out at 800 °C for one hour duration. Figure 6.33 compares the Si cluster PL for the same anneal carried out under O_2 and N_2 in sample Da4. This film was selected because it contains a high excess Si concentration and therefore contains negligible defect PL and shows clear Si cluster PL at the low (800 °C) anneal tempeature. It is clear that the Si cluster PL is partly quenched during the oxidation. The residual PL is heavily blue-shifted, peaking near 510 nm (showing slight enhancement at this wavelength relative to the N_2 anneal) with some residual signal in the red. This is

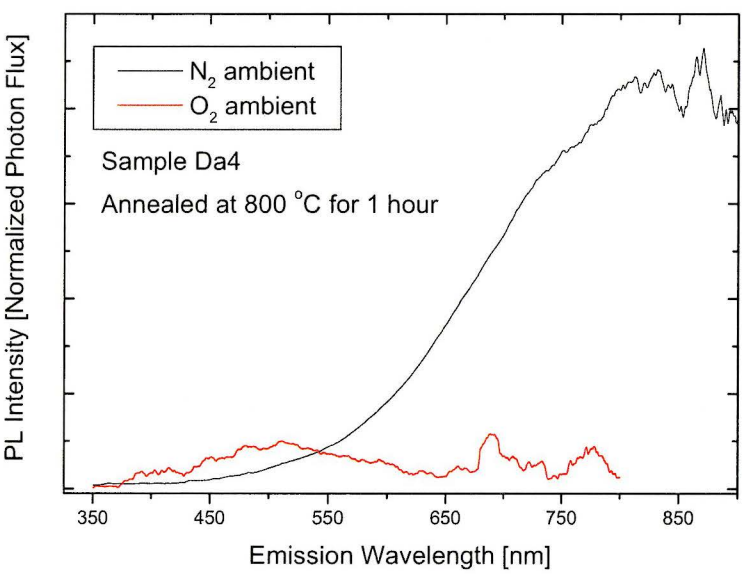

Figure 6.33: Sample Da4 annealed under flowing O_2 for one hour at 800 °C. The nano-cluster PL is significantly reduced in intensity and seemingly blue-shifted.

consistent with an overall decrease in luminescent Si nano-cluster size[257] along with a reduction in the total number of Si clusters.

This suggests that the oxidation anneal could be a useful tool for separating defect and nano-cluster PL in samples where the two peaks overlap. Furthermore, it could assist in the identification of defects since the O_2 could alter ODCs. The comparison of visible PL under O_2 and N_2 anneals for samples with moderate and no excess Si is depicted in Figure 6.34.

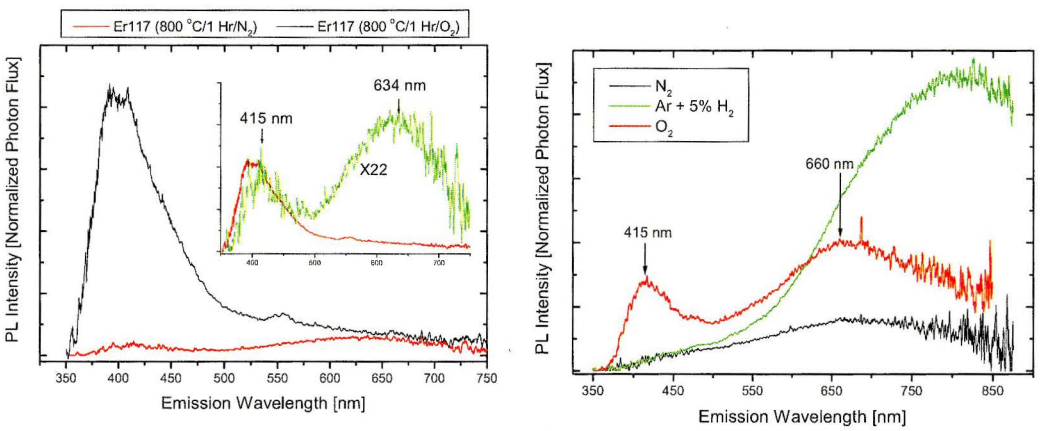

(a) (b)

Figure 6.34: Oxidation annealing is shown to induce a significant change in the PL spectrum by altering the luminescent centres; (a) Er117 – the inset shows the spectrum of the oxidized sample scaled and overlayed on the N_2 spectum; (b) Da2

In the case of the O-rich film (Figure 6.34(a)), the blue-violet defect PL along with the Er visible PL at 550 nm is severely quenched while the broad band extending into the red is relatively unchanged (although not shown, the 1.54 μm PL decreased by slightly less than an order of magnitude). A closer look at Figure 6.34(a) reveals that the broad peak is centered at 634 nm and is likely a NBOHC; this is therefore probably true of the corresponding PL tail in the spectrum under N_2 annealing in which it is difficult to resolve. The violet peak is slightly red-

[257] Down to clusters of about 1.1 nm diameter containing 35 Si atoms under the assumption that the oxidation produces clusters with a single interfacial S=O bond. (A. Puzder, et.al., *J. Am. Chem. Soc.* **125**, 2786 (2003).

shifted and peaks at 415 nm. This is consistent with the WOB defect; intuitively, one might expect such a defect to occur during a thermal oxidation. The most likely explanation for the decrease of the WOB in this sample during oxidation is the inherent thermodynamic instability of a large O-excess in the SiO_x matrix. Film Er17 is O-rich to begin with, which is consistent with the formation of a WOB. However, dissociated O_2 in-diffusing through the matrix during oxidation probably reacts with WOBs to form molecular O_2 which subsequently out-gas.[258]

The oxidation spectrum of Da2 (Figure 6.34(b)) seems to show the rise of both NBOHC and WOB PL peaks superimposed with a blue-shifted Si cluster emission. All three features indicate a decrease in the excess Si content. In fact, the similarity of the spectra under O_2 and N_2 annealing suggest that the broad emission in the N_2 spectrum may contain a NBOHC contribution as well. This would explain the lack of a red-shift in the PL spectra of Da9 (Figure 6.17(a)) with annealing below 1000 °C. It seems therefore that at low anneal temperatures and low excess Si content, most of the clusters are either coupled to Er or to non-radiative defects (the hydrogenation uncouples the clusters from non-radiative defects as evidenced in the Figure). Note in Figure 6.34(b) that the concurrent increase of the defect PL with the disappearance of Si clusters supports the previous assertion that it is the clusters themselves which quench the defect PL. In addition, the consumption of excess Si into a SiO_2 network during oxidation should stabilize a higher concentration of WOBs, which would otherwise react with excess Si and dissociate.

Considering now the various PL spectra in which de-convolution of the cluster and defect PL was ambiguous, the oxidation clearlyseems to separate the two (because it affects the defect centres and Si nano-clusters in an opposing

[258] The decrease in intensity of the violet peak could have other origins. It may be related to the reaction of the Er with the O atoms diffusing through the film; reducing the need to compete for NBOs in the matrix might have the effect of reducing the tendency for defect formation in the vicinity of the Er. There was a concomitant decrease in the PL at 1.54 μm which suggests a reduction in the number of sensitizing defects. Alternatively, if the sensitizing defects are related to C, the reaction of C and O during annealing might have produced gaseous species such as CO_2 which released from the film.

manner) and give positive identification to cluster PL by eliminating it. Figure 6.35 depicts a range of Er and excess Si contents within the most luminescent films. The extent of the Si nano-cluster PL quenching increases with decreasing excess Si content. Once again, the increase of the oxide defect PL might be the result of the disappearance of the Si clusters to which they were non-radiatively coupled. Although it is not shown in the figure, there was always a concurrent decrease of the PL at 1.54 μm following the oxiadations. The decrease was typically one order of magnitude.

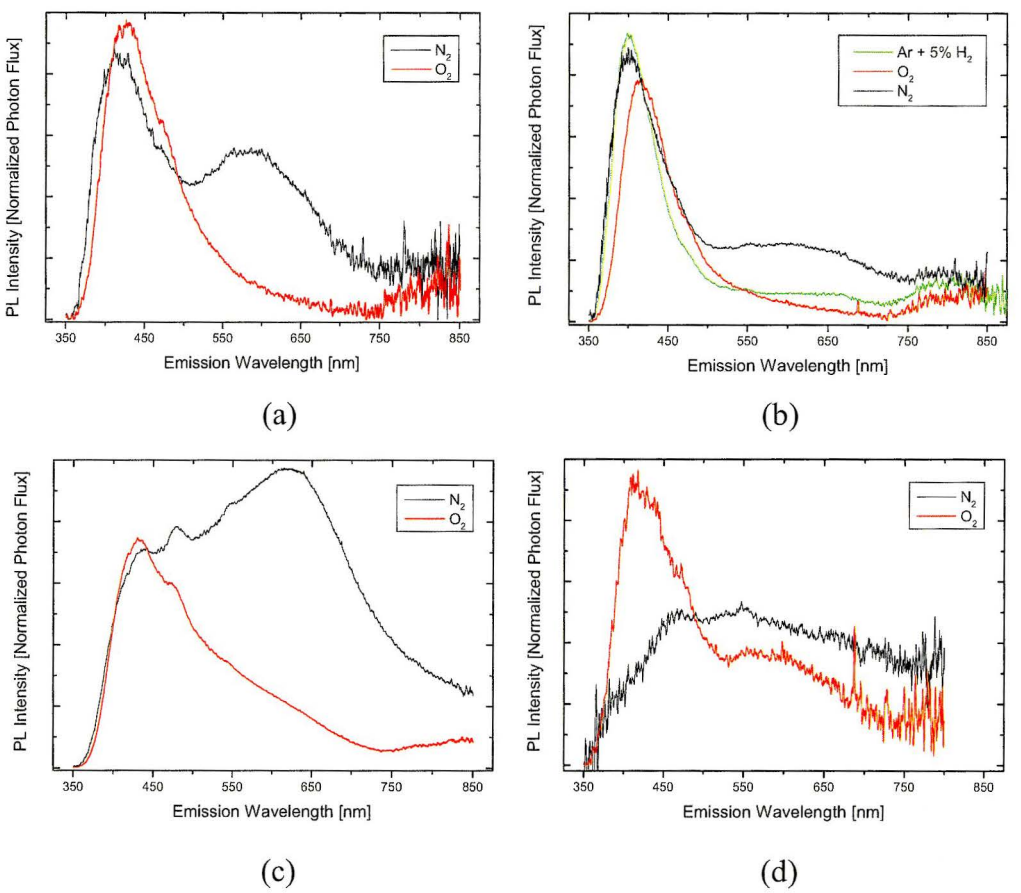

Figure 6.35: The effect of oxidation annealing on representative film compositions for which there appears to be a combination of oxide defect and Si nano-cluster PL (anneals were carried out for one hour under flowing N_2 gas); (a) Da1; (b) Er149; (d) Da8; (d) Er147; (f) Da4; (g) Da2

The decrease in defect PL under oxidation in sample Er149 (Figure 6.35(b)) is probably an illusory effect created by the disappearance of the broad PL band upon which the defect PL is superimposed in the N_2 or (Ar + 5% H_2) anneals.

Chapter 7

Response of the Luminescence and Structural Properties to High Energy Ion Beam Irradiation

It is, in general, necessary to understand the effects of ionizing radiation on the performance of micro-electronic and photonic devices. This includes the ionizing radiation to which a device is subjected during fabrication. The most important example of this is ion implantation, which is commonly used to introduce dopants into Si. Ion implantation is also regularly used to add Er dopant to pure Si-rich SiO_x thin films (grown by PECVD) which have been pre-annealed to form Si nano-clusters/crystals. In this case, it has been necessary to investigate the impact of the implant on the luminescence properties of the [pre-formed] Si nano-clusters and how post-implant annealing can repair implant-induced bond damage [180,204].[259] From a different perspective, Er-doped SiO_2 has been investigated as a radiation damage detector. The change in the luminescence lifetime at 1.54 μm as a function of anneal temperature, following exposure to ionizing radiation, produces a trace that is highly characteristic of both the ionizing species and fluence.

[259] This is particularly important since post-implant annealing typically cannot exceed 900 °C because of the risk of Er precipitation. Such an anneal temperature is not, however, sufficient to (re)-form Si nano-crystals that may have been completely or partially amorphized during the implant.

In the context of the present study, the bond (electronic) damage introduced into the films by exposure to a high energy ion beam provides a method for investigating the luminescence mechanisms, particularly with respect to sensitivities to specific non-radiative defects. Sample Er149 (0.05 atomic % Si relative to O; 1.32 atomic % Er relative to Si and O) was selected for this study because it appears to rely heavily (if not entirely) on *defect* sensitization for PL emission at 1.54 μm. Specifically, the progressive change in the photo-luminescence (PL) spectra with step-wise annealing provides information about the Er incorporation as well as the relevant non-radiative defect populations in the films. The repair of the various irradiation-induced defects in SiO_2 tends to occur at very specific anneal temperatures [209]. In this thesis, such an investigation has been carried out in conjunction with thin film variable energy positron annihilation spectroscopy, which allows the profiling of certain types of non-radiative defects in the film.

7.1 The Interaction of Ion Beams with Solid Matter

When an energetic ion is incident on a solid target, the ion interacts, via its electronic charge distribution and screened nucleus, with the atoms in the target via their electronic charge distribution and screened nuclei. Several types of interactions can occur depending on the energy of the incident ion and its distance of closest approach to the target atom (see [223], [224] and [225]). The net effect of these interactions is to progressively reduce the kinetic energy of the incident ion until it comes to rest in the material (provided the target is sufficiently thick that the ion does not pass all the way through). These stepwise losses are the result of *energy transfers* to the target nuclei and to the target electrons.[260] The

[260] These include: 1) elastic scattering between incident and target nuclei, *resonant* nuclear scattering (caused by interference of elastic scattering and weak nuclear force interaction amplitudes); 2) direct kinetic energy transfer to target electrons through inelastic electron-electron collisions, fast electron production, the generation of inner shell electron vacancies by the excitation *or* ionization of strongly bound/localized target electrons (causing emission of Auger

atomistic nature of the transfer mechanisms means that they are both highly dependent on the projectile ion species and target material.

Elastic Coulomb scattering between the nucleus of a projectile ion and that of a target atom occurs when the projectile penetrates the radius of the K electron shell of a target atom.[261] The incident ion scatters (changing its trajectory in the process) by transferring some of its energy to the target nucleus, causing the target atom to recoil. The recoiling target atom will vacate its 'lattice' site if it receives energy exceeding its 'displacement energy' – a quantity that is always strongly dependent on the target material and possibly the individual site in an amorphous material. If the recoiling atom receives less than its displacement energy, it relaxes by vibration (phonon emission). If the distance of penetration of the projectile ion into the target ion's electron distribution is such that scattering occurs between *screened* nuclei (ie. the scattering involves a *screened* Coulomb potential), then the change in the projectile's trajectory will be minimal. Such glancing angle encounters constitute a mechanism of energy loss by the penetrating ion referred to as 'nuclear stopping' or 'elastic energy loss'. If the projectile penetrates the target atom far enough to result in *unscreened scattering* between nuclei, then there will be a significant deflection of the projectile's trajectory. This is referred to as pure Coulomb (or Rutherford) scattering. Such near head-on (hard) nuclear encounters are the source of incident ion

---

electrons or x-rays), excitation of weakly bound or delocalized conduction band electrons in the target; 3) nuclear reactions (causing charged particle, gamma ray and/or neutron emission); 4) channelling. The excitation, ionization, or electron exchange in the *incident* ion is also an important electron-electron interaction.

[261] The scattering is approximately elastic because the heavy target nucleus can be considered to be unconnected to the lattice during the passing of the ion. This is valid because ion implantation uses an incident ion energy in the keV-MeV range while the energy of chemical bonds is in the eV range. Furthermore, the fact that the incident ion must penetrate the K-shell of the target atom, means that the incident ion bypasses almost all of the target atom's electrons before the scattering occurs, meaning that the electrons can be essentially ignored in the calculation. At keV-MeV energies, the scattering can be considered classically (without a k-space wave mechanical analysis) because there is no diffraction of the incident ion wave function by the target's array of [nuclear] scattering centres. A 1.5 MeV alpha particle has a de Broglie wavelength of about 10 fm, which is four orders of magnitude smaller than typical interatomic spacings (on the order of Angstroms).

backscattering.[262] Elastic nuclear scattering introduces numerous vacancy/interstitial pairs (some of which can be eliminated in replacement collisions) and phonons. Furthermore, a collision cascade effect can occur when an atom is *displaced* with enough energy that it can itself undergo further collisions capable of producing secondary displaced ions. Sufficiently high incident ion fluences (total number of ions incident per unit area) can produce overlapping damage cascades in a material. As an example, for a ^{28}Si ion beam at 2 MeV, this critical fluence is about $3.6x10^{11}$ ions/cm^2.

Besides elastic nuclear scattering, there may be inelastic Coulomb scattering events between the incident ion and the free or bound electrons in the target solid. These give rise to numerous types of electronic excitations and/or ionizations of target atoms. The aggregate of such collisions is tantamount to a 'frictional/drag force' on the penetrating incident ion. This mechanism of energy loss by an incident ion is referred to as 'electronic stopping' or 'inelastic energy loss'. The negligibly small mass of an electron relative to that of the projectile ion means that these scattering events do not notably change the trajectory of the ion. In terms of damage, these interactions can break chemical bonds. Such electronic stopping can *indirectly* give rise to the displacement of atoms from their bond sites because the breaking of their inter-atomic bonds reduces their diffusion barrier. Radiation enhanced diffusion can promote the movement of these atoms from their weakened bond sites by providing the activation energy and some heating.

For typical light-ion beams at MeV energies, the energy loss is dominated by electronic stopping; nuclear stopping is dominant only at low particle energies (~keV).[263] At MeV energies, nuclear scattering has a low cross-section (proba-

---

[262] In the films of the present study, a 1 MeV Si^+ ion backscatters within the first 200 nm in about 0.01% of cases.

[263] The references to keV/MeV orders of magnitude are less valid when the incident beam or target involves heavy ions since nuclear stopping increases with ion mass. For example, a 2 MeV beam of Au ions might have electronic/nuclear stopping powers nearly equal in Si-rich SiO_x.

bility of a scattering event between two particles).[264] Most ions will initially follow a fairly linear path through the target material[265] until they have lost sufficient energy through electronic stopping for nuclear stopping to occur with significant probability. Beyond this point[266], the probability of a single incident ion undergoing multiple nuclear scattering events becomes significant and the ions lose energy quickly and generate large amounts of damage through many displaced ions. However, on average, hundreds of vacancies per incident ion can still be created in the film itself because of collision cascades; secondary ions can have the lower energies necessary to undergo multiple nuclear collisions.

It is clear that the irradiation of a solid with a MeV ion beam alters the structure of the solid by breaking bonds (forming Frenkel pairs of electronic defects) and forming atomic vacancy/interstitial pairs. The specific type and quantity of defect complexes that form, as a result, depend strongly on the target material. In this regard, there is an important difference between Si semiconductor and insulating SiO_x targets. Electronic (i.e. chemical bond) damage is mostly unstable in Si because of the comparatively large concentration of free carriers at room temperature, which immediately fill electronic defect states. In this case, most of the quasi-stable damage is in the form of vacancy complexes[267] which coalesce to form voids if the irradiation fluence is sufficiently high. In large band gap (insulating) material such as SiO_2, however, the lack of free carriers stabilizes electronic defects [226], and these have been widely characterized in the literature (the basic defects are those identified in section 3.1.4) – which of these defects are able to trap positrons is not a fully resolved

---

[264] This can be seen from the equations for the nuclear scattering cross section in both the screened and unscreened (Rutherford) cases.

[265] For example, a 1 MeV Si projectile ion penetrating a Si-rich SiO_x:Er film on Si might experience only a dozen glancing angle nuclear collisions in the first 100-200 nm of film. The mean free path for unscreened collisions would be near about 100 nm.

[266] This occurs near a depth of 1 μm for 1 MeV Si^+ ions in 200 nm Si-rich SiO_x:Er films on Si.

[267] Among the possible vacancy complexes, the Si mono-vacancy is unstable at room temperature and will rapidly form di-vacancy defects.

issue [227].[268] For example, in SiO_2, the electronic stopping can be associated with: the breaking of Si–O bonds with the subsequent movement of the O away from the Si sufficiently far to prevent bond reforming; the breaking of a strained Si–Si bond around a pre-existing oxygen vacancy; the radiolysis of a hydroxyl group (OH^-) [209]. Of the oxide point defects identified in Section 3.1.4, the E' centre, non-bridging oxygen hole centre (NBOHC), and the perioxy radical, are the most common broken-bond defects created by irradiation [209]. Ion irradiation with a Si^+ beam is also commonly used to introduce the radiative point defects in SiO_2 [228,229,230,231,232]. In crystalline targets, it is possible to amorphize the structure. The critical ion beam parameters governing the amount and type of damage caused by irradiation include the mass of the incident ion species, the beam energy, and the total fluence.

7.2 Simulation of Ion Irradiation Damage

The irradiation of film Er149 with 1 MeV Si^+ ions was simulated using the Transport of Ions in Matter (TRIM) software contained in the 2003 version of the Stopping and Ranges of Ions in Matter (SRIM) simulation package [223]. This program employs a Monte Carlo algorithm to calculate the full damage cascades caused by the passage of each projectile ion through a well specified target. As with any ion beam simulation software, the main limitation is the accuracy of the stopping powers used; additionally, the creation of compound targets requires the assumption that Bragg's rule (the additivity of stopping powers) is valid. The Ziegler values *for the stopping of Si in SiO_2* [223] are widely used in ion beam analysis and seem to be in good agreement with experimental data in the literature [224] (with the possible exception of some of the more exotic ion beams such as Er). In the present study, film Er149 was simulated as the target material

[268] Irradiation-induced electronic defects can gain or alter their paramagnetic character through a *charge-transfer* process, in which the electrons in the original bond all go to one or the other of the resultant defects. See: M. Fujinami, Appl. Phys. Lett. **62**, 1131 (1993).

according to the RBS composition, which was taken to include an estimate of the C concentration.

Of primary importance in the present study was the requirement to prevent the incident Si ions from embedding *in* the target film since this would change the composition; this study meant to harness *only* the damage produced by the penetrating ions. To achieve this, a sufficiently high beam energy (1 MeV) was selected to drive the ions all the way through the film so that they come to rest deep in the substrate. The TRIM simulation confirmed that the experimental beam parameters yielded an ion range of 1.12 μm, which is much greater than the approximately 200 nm thick film. Figure 7.1 shows the ion trajectories of the damage cascades for 100000 incident Si^+ ions. These trajectories show that most of the [nuclear] damage occurs in the substrate towards the end of the ion range. There is very little divergence of the beam as it pases through the film. Indeed, it is likely that the energy of the incident ions is nearly constant with depth, at least through the first 100 nm of the film. It is also apparent that some of the O atoms in the film are driven into the substrate through knock-on collisions. Part (b) shows the ion range (stopping) profile.

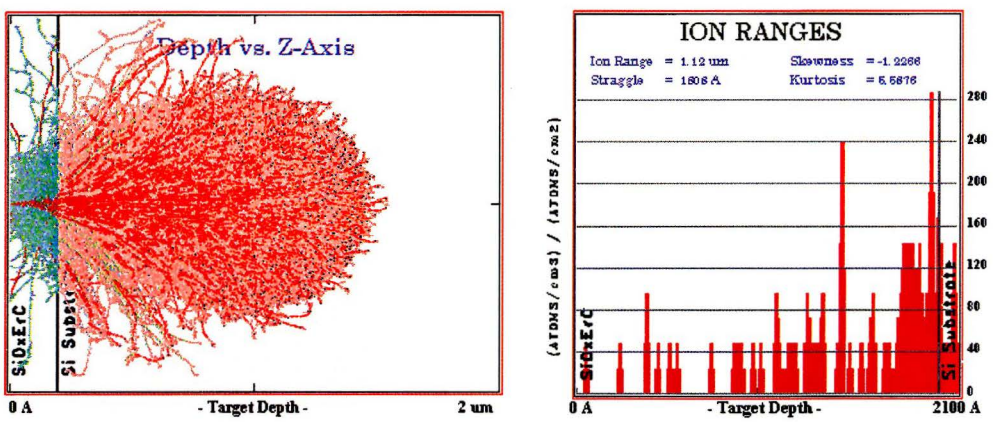

Figure 7.1: (a) TRIM simulation of ion irradiation damage cascades – the red paths correspond to substrate Si atoms, the blue and green paths correspond to film Si and O atoms respectively; (b) ion ranges for 1 MeV Si^+ irradiation into a sample similar to Er149.

This study involved irradiation fluences of $1x10^{12}$, $5x10^{12}$, $1x10^{13}$, $2x10^{13}$, $4x10^{13}$, $5x10^{13}$ and $1x10^{15}$ Si^{+} ions/cm^{2}. At the highest fluence, Figure 7.1(b) implies that the film becomes doped with fewer than $4x10^{16}$ Si/cm^{3} or less than 0.0001 at. %.

An important aspect of the irradiation damage, from a luminescence perspective, is the number of vacancies generated in the film, since these should correlate with the destruction of luminescence centres. In addition, positrons have a propensity to become trapped at vacancy-type defects. Figure 7.2 shows the vacancies for Er, O, and Si in the target film as well as the total target vacancies.

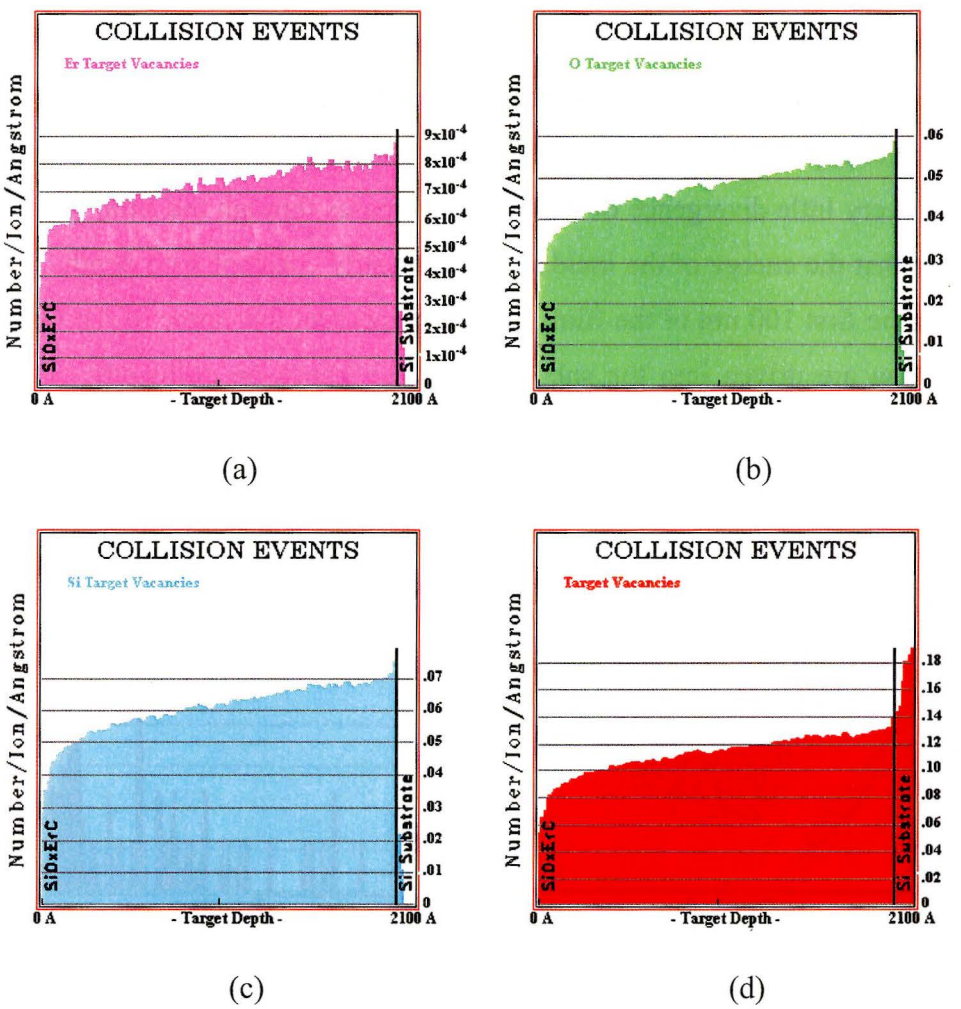

Figure 7.2: Target vacancies resulting from nuclear stopping within the film of Er149 based on TRIM simulation of the ion irradiation of 1 MeV Si^{+}.

It is clear that the vacancy concentration increases deeper in the film since the beam has lost some energy by that point and so experiences increased nuclear stopping. Considering the centre depth of the film to contain an average vacancy concentration in the defect profile, one can estimate the number of displaced atoms of each species for each irradiation fluence (this is depicted in Table 7.1).

Fluence [x10^{12} cm^{-2}]	**Si vacancies [cm^{-3}]**	**O vacancies [cm^{-3}]**	**Er vacancies [cm^{-3}]**	**Total vacancies [cm^{-3}]**
1	6.0 x 10^{18}	5.0 x10^{18}	7.0 x10^{16}	1.1 x 10^{19}
5	3.0 x 10^{19}	2.5 x10^{19}	3.5 x10^{17}	5.5 x 10^{19}
10	6.0 x 10^{19}	5.0 x10^{19}	7.0 x10^{17}	1.1 x 10^{20}
20	1.2 x 10^{20}	1.0 x10^{20}	1.4 x10^{18}	2.2 x 10^{20}
40	2.4 x 10^{20}	2.0 x10^{20}	2.8 x10^{18}	4.4 x 10^{20}
50	3.0 x 10^{20}	2.5 x10^{20}	3.5 x10^{18}	5.5 x 10^{20}
1000	6.0 x 10^{21}	5.0 x10^{21}	7.0 x10^{19}	1.1 x 10^{22}

	Si atoms [cm^{-3}]	**O atoms [cm^{-3}]**	**Er atoms [cm^{-3}]**	**Total atoms [cm^{-3}]**
Concentration in Film Er149	*2.2x10^{22}*	*4.4x10^{22}*	*8.9x10^{20}*	*6.7 x 10^{22}*

Table 7.1: The upper portion of the table gives the vacancy concentration for the main target constituents for each ion fluence in the present study; these results are based on the TRIM simulations shown in Figure 7.2. The lower portion of the table shows the actual concentration of each elemental constituent in the film Er149 used in this study (based on the RBS data from Table 6.1); these help one to conceptualize the vacancy fraction.

It is evident that the target vacancies are an extremely small fraction of the total number of atoms for all irradiation fluences except the highest. At the highest irradiation fluence, greater than one in every ten atoms is displaced without replacement. On average, each projectile ion results in about 278 vacancies *within the film.* This is interesting, for it means that if one considers the ErO_x based optically active complex, even the highest ion fluence should displace the Er from only a few of these groups; and such a displaced Er might quickly getter

displaced O atoms so that it remains optically active. This means that the main effect of the irradiation should *not* be to render a large fraction of the Er centres *intrinsically* optically inactive (though they may be optically inactive in an extrinsic sense due to surrounding non-radiative decay channels).

In terms of projectile ion energy loss *within the film*, 91.64% occurs through ionization of fixed (ie. non-recoil) target nuclei, with only 4.29% occurring through ionization of the recoiling nuclei. Another 3.57% is lost to phonons generated by recoiling nuclei. Only 0.03% is lost in the production of vacancies by collisions with fixed target ions.[269]

7.3 Characterization of both the Irradiation Damage and Subsequent Thermal Repair by Photoluminescence and Positron Annihilation Spectroscopies

7.3.1 Sample Er149 As-irradiated

It is apparent from Table 7.1 that, for most of the irradiations carried out in this study, the electronic damage will dominate the post-irradiation luminescence properties. This means that bond defects should be prevalent – particularly those involving dangling bonds such as the E' centre, peroxy radical and NBOHC. As some of these defects are always non-radiative, they will constitute pathways for luminescence quenching. The Er^{3+} ions will couple strongly to defects in the Er-coordinating shell; the strong coupling gives rise to fast energy transfers from the Er^{3+} to acceptor states of the defects. Figure 7.3 depicts the integrated PL intensity in the films as irradiated (prior to any post-irradiation annealing).

[269] It is an interesting statistic that only 0.016% of the incident ions were actually backscattered.

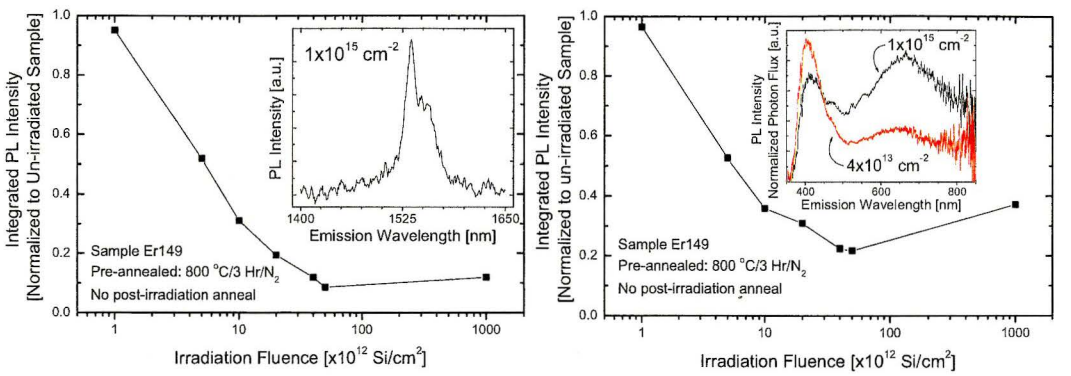

Figure 7.3: Logarithmic plot of the integrated PL intensity in film Er149 as-irradiated for (a) infrared wavelength band (1400-1650 nm); (b) visible band (350-850 nm). The inset in (a) shows the raw PL spectrum for the highest irradiation fluence (as-irradiated); the inset in (b) shows the raw PL spectrum for the two highest ion fluences (as-irradiated).

Figure 7.3 shows that the PL in both the infrared (1400-1650 nm) and visible (350-850 nm) bands responds with a similar trend to the irradiation fluence. At the lowest fluence ($1x10^{12}$ cm^{-2}) there is almost no quenching of the PL, which is at least consistent with the negligibly small vacancy concentration predicted by the TRIM simulations. For a five-fold increase in the fluence, the PL drops by 50% in both wavelength ranges. For progressively higher fluence, there is a relative decrease in all PL but it is less severe. In fact, the quenching actually saturates for an irradiation fluence of between $4x10^{13}$ and $5x10^{13}$ cm^{-2}. The PL yield will not decrease below about 10% of the pre-irradiated (maximum) value. Even if the irradiation fluence is increased 20-fold over the initial saturation dose, the PL does not quench further. In fact, in the visible band, there is a slight increase in the integrated intensity. The saturation effect may be related to the introduction of radiative defects into the films during irradiation. For fluences below the saturation value, the introduction of non-radiative defects dominates so that the PL decreases. Beyond the saturation fluence, radiative defects appear in sufficient numbers to compensate the non-radiative centres, preventing further

reduction of the the PL. These radiative and non-radiative defects should be those introduced in section 3.1.4.

In order to investigate the defect population in the as-irradiated films, four samples were selected for positron annihilation spectroscopy. This included one un-irradiated sample as well as ones irradiated at fluences of $1x10^{13}$, $4x10^{13}$, and $1x10^{15}$ cm^{-2}, respectively. Both the S and W-parameters were measured for each sample (and normalized to the spectrum of the bulk region of defect-free single crystal Si). In order to get a sense for the effect of the irradiation, Figure 7.4 shows the S and W values for both un-irradiated and most heavily irradiated samples from film Er149.[270] While this is not the most useful rendering of the data for analyzing the film itself, since the film is not even 200 nm thick, the irradiation clearly changes the S and W-parameters in both the film and substrate relative to the un-irradiated sample. Following irradiation, the S-parameter throughout the film is decreased below unity. As the mean positron implant depth penetrates the substrate, the S-parameter rises sharply and reaches a maximum

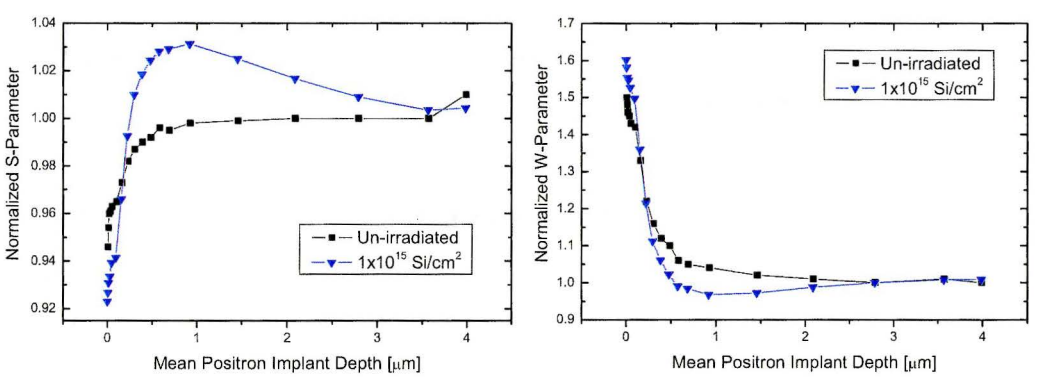

(a) (b)

Figure 7.4: (a) S-parameter and (b) W-parameter for positron annihilation in film Er149 (pre-annealed) for both un-irradiated and heavily irradiated samples.

[270] Recall that prior to the irradiation both samples were annealed at 800 °C for 3 hours in flowing N_2.

value greater than unity near a depth of 1 μm. Beyond this, the S-parameter reduces gradually to the bulk Si value (unity).

The suppression of the S-parameter at the surface occurs because the surface is an efficient positron trap and positrons implanted here have a short diffusion length.[271] They sample an electronic charge distribution that is fundamentally different (i.e. it has a wider distribution of momentum states or has a higher average momentum) than in the bulk; this is perhaps because the electrons right at the surface are more tightly bound than in the bulk (they see a larger potential barrier) and so have higher energies and velocities. Alternately, the surface could be considered to contain a much larger concentration of point defects than the bulk (as well as positron trapping species such as OH^- adsorbed at the surface); the positrons preferentially trap at such defects – which inhibit positronium (Ps) formation. Because point defects have a much higher concentration of electronic charge density than the bulk [233], the positron is automatically bound (trapped) closer to the high energy core electrons and thereby samples an electron distribution of average momenta that is higher than in the bulk. From a slightly different perspective, it could be said that the simple fact that Ps formation is severely inhibited at the surface is sufficient to explain the suppressed S-parameter there. This has been suggested as the origin of the decrease in the S-parameter at the SiO_2/Si interface [234].[272]

The decrease in the S-parameter within the film upon irradiation is likely the result of the suppressed formation of positronium (Ps) relative to the un-irradiated sample. This is attributed to the preferential trapping of positrons at irradiation-induced negatively charged electronic [point] defects, which redues

---

[271] Positrons in *a*-SiO_2 have a short diffusion length (~20 nm) to begin with because of the low mobility of the rapidly formed Ps. See: A. Rivera, Mater. Sci. Forum **363-365**, 64 (2001).

[272] Such a decrease is not clearly apparent in this study because the interface has not been isolated in such a way as to compensate for the "washing out" of features in the S-parameter spectrum over distances of tens of nanometres that results from the statistically broad [Markhovian] positron implant profile.

the probability of Ps formation.[273] To form Ps, the positron must be free to move within the bulk of the film, where it can experience larger open spaces and a lower electron density. In general, the annihilation characteristics of positrons in amorphous SiO_2 films are dominated by Ps formation because almost all implanted positrons annihilate from Ps states [233]; the Ps formation fraction in thermal SiO_2 has also been estimated at 30 %. This means that irradiation-induced changes in the S-parameter *within* the film can usually be explained in terms of Ps formation; in fact, ion irradiation is said to be able to reduce Ps formation to zero [235].[274,275]

The subsequent increase in S values (beyond unity) within the substrate is the result of positron trapping at vacancy-like defects produced by near the end of the ion range [236]. This is consistent with the TRIM stopping profile, suggesting an ion range of 1.2 μm. Most of the damage occurs within a few hundred nanometres surrounding this depth since the ions are of low enough energy to undergo significant nuclear stopping. This gives rise to numerous open volume type defects.[276] The missing ion core(s) at a vacancy constitutes a potential well for a diffusing positron because of Coulomb repulsion from the surrounding ion cores. The reduced electron density within the well gives the positron a longer liftetime than in the bulk. This reduced electron density effectively shields the positron from high energy core electron states so that the

---

[273] Note that if one were to increase the implant fluence substantially (perhaps to $1x10^{17}$ Si^+/cm^2), one would begin to form voids in the insulating film. These could give rise to significant Ps formation, which would more than compensate for the introduction of electronic defects, producing a corresponding increase in the S-parameter.

[274] One should bear in mind that the high probability of Ps formation means that the Ps annihilation events can actually be representative of the open volume defect characteristics. For example, Ps can annihilate with a broadened momentum distribution because of the momentum uncertainty resulting from the localization of Ps in a space of finite dimension. See: A. Uedono, et. al., J. Appl. Phys. **75**, 3822 (1994).

[275] Volume compaction of SiO_2 resulting from ion irradiation (due to the local release of thermal energy by the ion bombardment) has been known to suppress Ps formation because it closes open volumes. This should be less of a factor in the present films because the pre-irradiation anneal already densifies the film considerably. It is also because of the pre-anneal that irradiation-induced loss of H from the films is not expected to be a major factor in this study.

[276] At the irradiation doses used in this study, one is probably speaking more in terms of vacancy clusters than "voids".

positron typically annihilates with lower energy delocalized valence electrons, giving rise to a higher S-parameter than in the bulk. Thus, open volume defects have a high positron trapping cross-section. The possible formation of Ps in such defects in semiconductors is not fully agreed upon in the literature. In general, the free electron density is too high in defect-free Si to permit Ps formation. In the presence of defects, however, there are several complicating factors. Positron trapping and Ps formation at open volumes is always dependent on factors such as the dimensions of the "void", decoration (for example with O or H), charge state of localized electron levels, and local electric fields [237].

Both the S and W-parameters have been plotted in Figure 7.5 for a range of irradiation fluences, with the mean positron implant axis scaled to view the depth of the film only. It seems that the S and W parameters have saturated even for the sample with the lowest fluence, since there is no further decrease of the S-parameter beyond this fluence. This means that all of the positrons entering the film become trapped before they annihilate [235]; the addition of further trapping defects with higher irradiation fluence can have no observable impact on the S value. This makes the PAS data somewhat difficult to compare with the as-irrad-

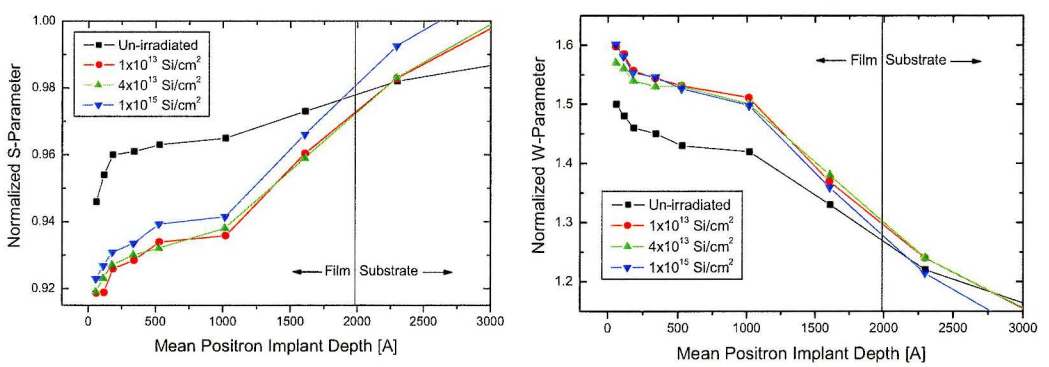

(a) (b)

Figure 7.5: (a) S-parameter and (b) W-parameter for positron annihilation in film Er149 subject to various ion fluences.

iated PL data since the positron saturation occurs at a lower fluence than the PL saturation. On the other hand, if the very small increase in the S-parameter at the two highest fluences is a "real" effect, then it may be indicative of the formation of vacancy defects which have begun to re-introduce Ps formation.

A close examination of Figure 7.5 reveals that the S-parameter (and the W-parameter to some extent) within each film seems to show two different regimes. The first is a knee-shaped region from 0-100 nm, while the second is a steeper linear section that extends into the substrate. This is different from the defect-free *c*-Si reference sample, which is smooth and featureless. The apparent bulge in the S-parameter in the first 100 nm of the film may be due to the formation of some Ps in the film.[277] It seems contradictory that the Ps would still form even though the defect concentration is high enough to cause saturation. To look for Ps formation, difference spectra have been obtained by substracting the raw gamma photopeak spectrum of the *c*-Si standard (at a positron energy of ~40 keV) from the spectra of film Er149 as various depths. These difference spectra are shown in Figure 7.6. Each spectrum contains $5x10^4$ counts. The narrow central peak present in the difference spectrum can be attributed to the 2-γ annihilation of parapositronium [238]. It is clear that the un-irradiated film shows much more Ps formation than the irradiated material (which still has a noticeable Ps signal – some of which must be coming from the substrate since it doesn't change with film depth). Unfortunately, the films are too thin relative to the broad Markhovian implant profile of the positrons to reliably profile the Ps formation with depth.

An alternative explanation for the two apparent regimes of the S-parameter in as-irradiated films is the presence of Er-related positron trapping defects. It has been suggested [239] that Er^{3+} suppresses Ps formation by trapping

[277] Note that there is no dip in the S-parameter at the film/substrate interface (which normally results from the diffusion of positrons to interface-based traps) because of the heavy damage in the substrate caused by the long range implant.

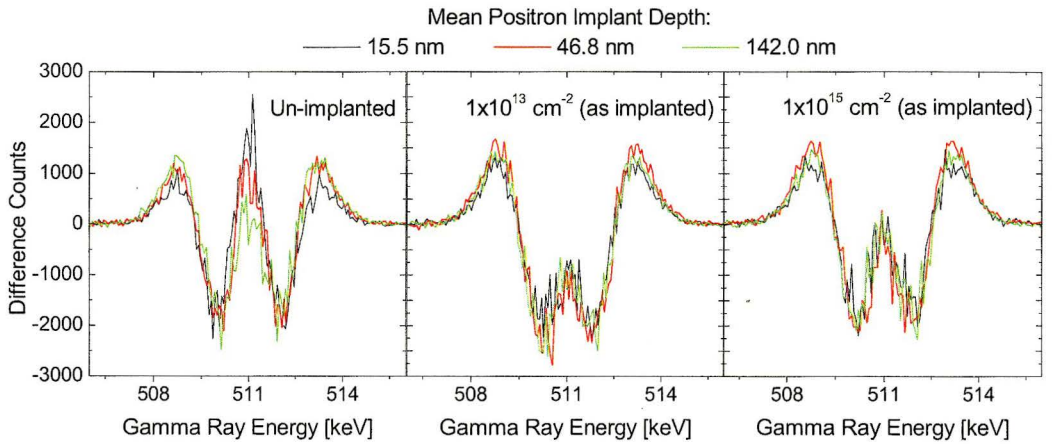

Figure 7.6: Difference spectra obtained by subtracting the raw gamma photopeak spectrum of the *c*-Si standard ($E_{positron} \approx 40$ keV) from the spectra of film Er149 as various designated depths. Each spectrum contains $5x10^4$ counts.

Ps precursors and/or occupying spaces where Ps might be formed. Film Er149 has a non-uniform Er concentration profile, as revealed by the Rutherford backscattering data. In fact, the Er concentration uniformly decreases from a value of 1.7 atomic % near the film surface to 0.9 at. % near the substrate, meaning that the region with the most Er is also the exact region showing an anomaly in the S-parameter. This could suggest that there is a unique aspect – or defect – associated with the Er incorporation in these films. This has already been alluded to in the previous chapter in which it was suggested that the ECR-PECVD system introduces the Er such that there are specific radiative defects near the Er site. Trapping near the Er site would be expected to show a unique signature in the S-parameter because the electronic charge distribution will be much different in the ionically bonded Er cage than in the intervening (covalently bonded) SiO_2-like network. This will be especially true following irradiation since the electronic defects created near the Er should be much different than those created in the network.

7.3.2 Annealing-induced Changes in Irradiated Films

In order to assess some of the assertions made above, all samples have been subjected to a stepwise isochronal (10 minute) annealing according to the scheme discussed in Chapter 5 (section 5.4.4). Changes in both the integrated PL intensity and the spectral content have been analyzed. Figure 7.7 depicts the recovery of the PL in both spectral bands for two representative samples (corresponding to fluences of $2x10^{13}$ and $1x10^{15}$ cm^{-2}). Parts (a) and (c) show the

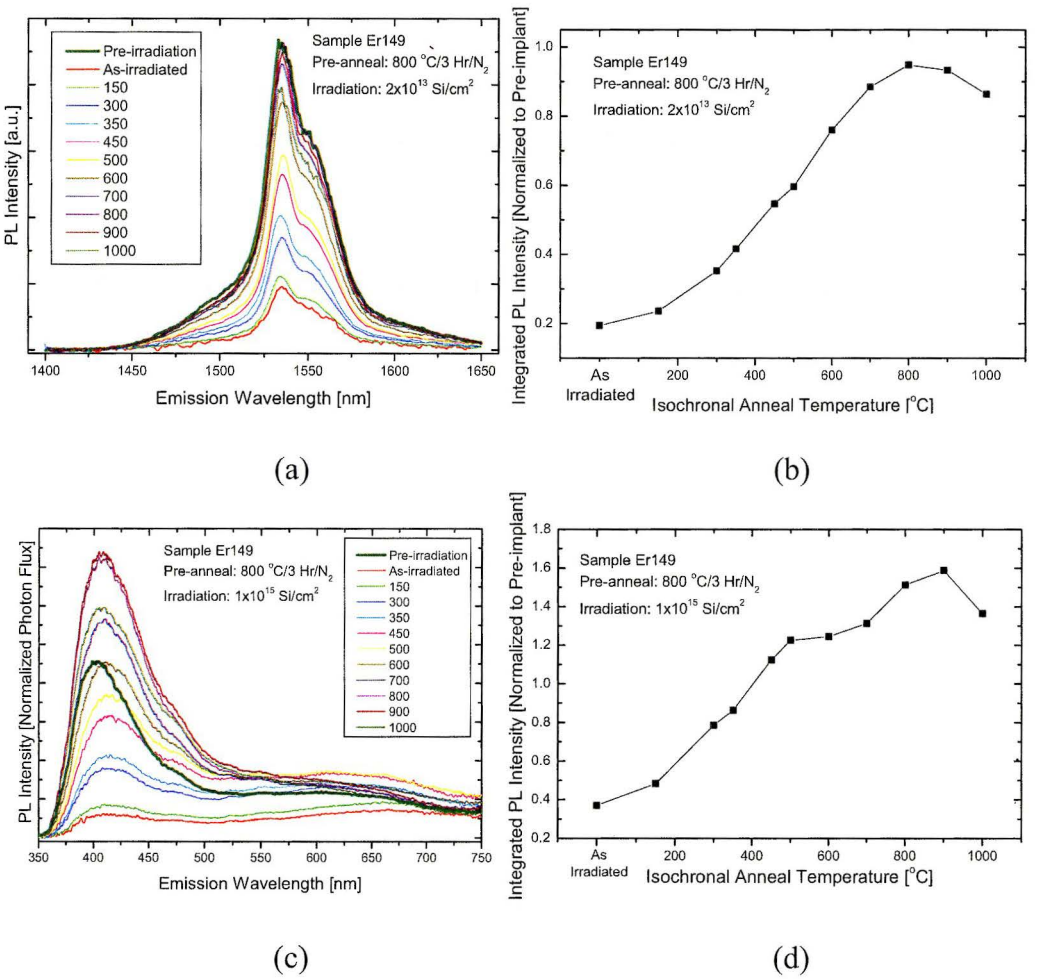

Figure 7.7: (a) Infrared PL spectra shown at each anneal temperature for film Er149 irradiated at $2x10^{13}$ cm^{-2}; (b) integrated PL intensities corresponding to (a); (c) visible PL spectra shown at each anneal temperature for sample Er149 irradiated at $1x10^{15}$ cm^{-2}; (d) integrated PL intensities corresponding to (c).

actual spectra at the various anneal temperatures along with the pre-irradiation PL. The pre-irradiation spectrum is shown with a thicker line so that it stands out against the other spectra. Parts (b) and (d) plot the integrated intensity as a function of the anneal temperature. The integrated intensities have been normalized to that of the pre-irradiation PL.

The PL signal in the infarared band shows a monotonic increase of intensity with anneal temperature up to a maximum at 800 °C, beyond which there is a gradual decrease. The shape of the curve beyond 600 °C is very much similar to the anneal-PL curves for Er149 shown in Chapter 6 (Figure 6.4(b) and 6.11). The spectral content shows almost no variation with annealing. Interestingly, the PL intensity never recovers completely to its pre-irradiation value. Although not shown in this figure, repeating the pre-irradiation anneal at 800 °C for 3 hours improves the PL only slightly over the 10 minute anneal. The recovery of the PL follows a smooth trend throughout; it does not show any sharp increases associated with the sudden disappearance of a particular defect at a certain temperature (such as an E' centre at 300 °C or a NBOHC at 600 °C). This was, in fact, true for all of the irradiation fluences. The fixing of the anneal temperature T at each particular step should repair those defects with activation energy lower than the value E_a given by:

$$E_a = kT \ln(\upsilon t) \tag{7.1}$$

where k is Boltzmann's constant, T is the Kelvin temperature, t is the time required for all of the specific defects to repair themselves once subject to the temperature (this value is typically on the order of seconds), and υ is frequency at which the defect atoms attempt to relocate. The irradiated film should contain various defects exhibiting a continuous range of critical activation energies [204]. Each step in the annealing should thus remove specific groups of defects *only*.

It has generally been found that the most common irradiation-induced defects in SiO_2 and Er-doped SiO_2 are thermally repaired by 600 °C; these include the E' centre, peroxy radical, and NBOHC (i.e. the defects that are detectable by electron paramagnetic resonance). The fact that the PL signal is only 76% recovered by 600 °C suggests that there are other defect centres in the present films which are more difficult to 'anneal out'. The destruction of Er-luminescence complexes by the displacement of Er and O should not be the main effect since these vacancies only accout for about 0.5% of the total Er and O populations. Another consideration is the damage of sensitizing Si nano-clusters. Studies of ion irradiated Si nano-clusters/crystals suggest that they can fully recover their luminescence emission at an anneal temperature as low as 800 °C [180]. Sample Er149, however, should contain no Si clusters because there is less than 0.1 atomic % Si excess.

The recovery of the visible PL (at a fluence of $1x10^{15}$ cm^{-2}) with annealing follows a much different trend. Once again, the PL increases steadily above the as-irradiated value, however in this case, the PL actually recovers 59% *beyond* the pre-irradiation PL after annealing at 900 °C. There are two notable changes in the spectral content. The first is the slight red-shift of the defect PL peak (tentatively ascribed to the weak oxygen bond) from 403 nm to 410-415 nm following the irradiation, which remains throughout the annealing. This may be due to changes in the dielectric function of the film (as evidenced by the slight change in colour of the film following irradiation) as a result of the near complete destruction of the Si-O network.[278] The second is the variation in the ratio of the intensity between the peak centered at 410 nm and the broad feature centered out near 600-650 nm. While this ratio is nearly constant at a factor of 3-4 at the other irradiation fluences (throughout annealing), in this sample it begins at a factor of 0.86 (indicating that the broad PL is more intense than the blue-violet PL) in the

[278] Alternatively, such a high fluence irradiation might result in a slight change in the film thickness (ie. compaction). This could change the film interference properties to yield small shifts in the PL emission.

as-irradiated film and increases to 6 at 800 °C, following a trend similar to the anneal recovery curve. This ratio is plotted in Figure 7.8 as a function of anneal temperature for irradiation fluences of $1x10^{13}$ and $1x10^{15}$ cm^{-2}.

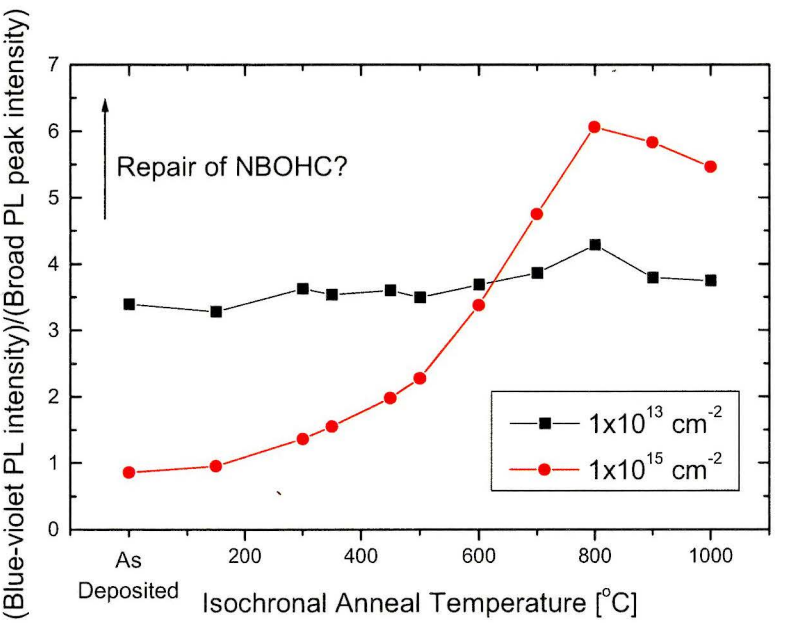

Figure 7.8: Ratio of the blue-violet PL peak intensity to that of the broad PL peak centred near 650 nm as a function of post-irradiation anneal temperature for sample Er149 irradiated with a fluence of $1x10^{15}$ cm^{-2}.

The broad PL near 650 nm does not recover nearly as fast as the violet peak, and it decreases strongly beyond 500 °C. This suggests that the defect is related to the NBOHC (possibly with some contribution from the small peroxy radical) and is largely repaired at the higher anneal temperatures.

The recovery of the integrated PL intensity for the other irradiation fluences is shown in Figure 7.9. In all cases (and in contrast to Figure 7.7), the intensities have been normalized, for each temperature, to the un-irradiated control sample which was annealed along with the irradiated samples. In order to better grasp the trends present in the data, the figure is divided into two different panels. In the first panel, parts (a-c) compare the PL recovery between samples

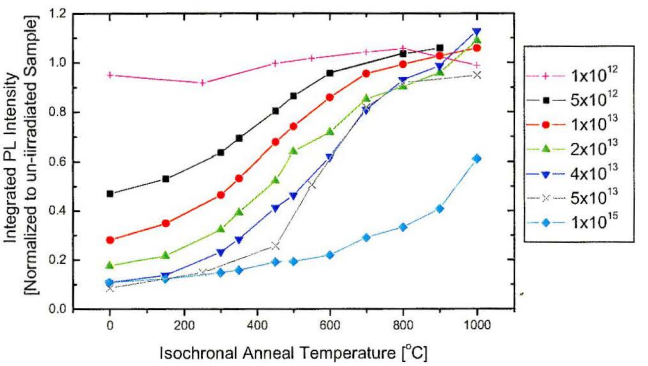

(a)

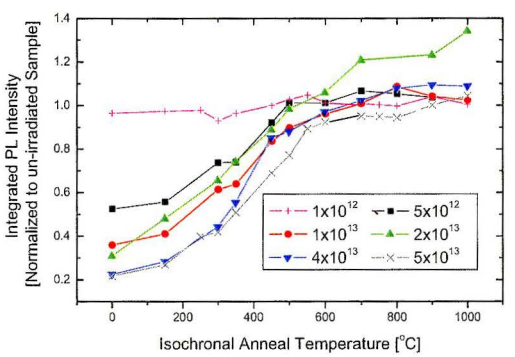

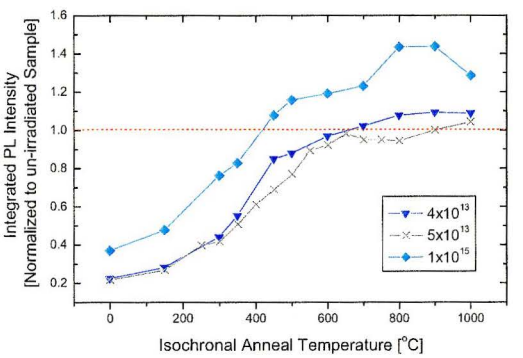

(b) (c)

Figure 7.9 PART 1: Integrated PL intensity recovery in sample Er149 as a function of isochronal anneal temperature for each irradiation fluence, (a) infrared range, (b) visible range.

within their own emission band (infrared or visible); the second panel compares the PL recovery in the infrared and visible bands *individually* for each fluence. It is clear from panel 1 part (a) that the infrared PL recovery is dependent upon the irradiation fluence. For example, the very slight reduction in the PL intensity in the sample irradiated with $1x10^{12}$ cm^{-2} has recovered by 400 °C. The intermediate fluences up to $5x10^{13}$ cm^{-2} follow similar smooth PL recovery patterns; in these cases, most of the increase of the signal occurs between 300-700 °C, with a taper-

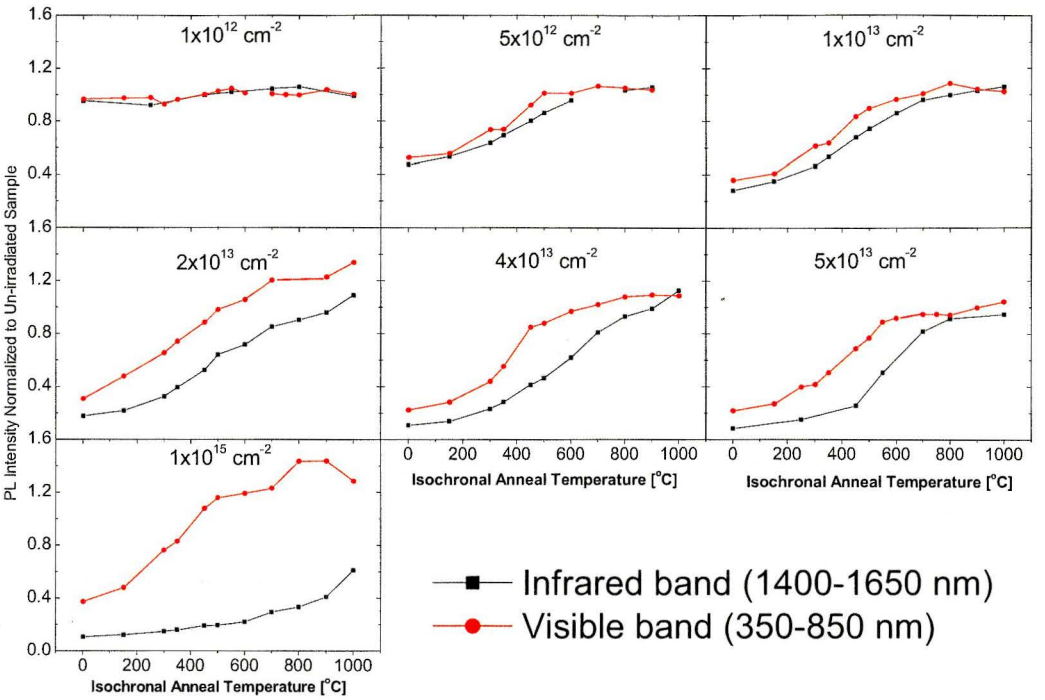

Figure 7.9 PART 2: Integrated PL intensities in both infrared (black curve) and visible (red curve) wavelength ranges. Each panel corresponds to a different irradiation fluence. All y-axes are synchronous.

ing at higher temperatures. In all cases, the final PL is very close to the value of the un-irradiated control sample. The major difference, however, occurs at the highest irradiation fluence ($1x10^{15}$ cm^{-2}). In this case, the PL recovers to only 61% of the control sample – even for annealing at 1000 °C. Interstingly, while the samples irradiated at $4x10^{13}$ and $5x10^{13}$ cm^{-2} exhibited an initial PL quenching to the same value as the highest fluence, these two samples exhibited close to a full recovery.

Comparing the recovery of the infared band PL to that of the visible band PL (Figure 7.9, Part 2), it is apparent that the basic recovery is dependent on the fluence, though to a lesser extent than the former. There is a trend with increasing irradiation fluence whereby the as-irradiated PL quenching becomes progressively more severe and the difference between the relative quenching/recovery of the PL

in the infrared versus the visible wavelength ranges becomes larger. The lowest fluence still causes almost no quenching and shows little change with annealing. The highest fluence is anomalous yet again, but as discussed above, in a manner that contradicts its behaviour in the infrared band. With the exception of this fluence, the similarity of both the annealing trends and shape of the recovery curves suggests that the PL near 1.54 μm and that near 410 nm must be related. This much is in agreement with the evidence of Chapter 6. The increasing difference between the PL recovery curves for the infrared and visible ranges suggests that increasing the fluence may have the effect of inflicting a progressive de-coupling of the oxide defects from the Er ions.

For the most part, the results are consistent with the annealing of standard non-radiative irradiation-induced electronic defects. In the case of the lowest fluence, it must either be that almost no non-radiative damage is introduced into the film, or there are sufficient sensitizing centres to overcome the few non-radiative defects that *are* introduced. While no luminescence lifetime measurements have been made on the visible defect PL in these films, it is possible that if they decay radiatively within an extremely short timescale, they may not couple effectively to nearby non-radiative defects. For example, the luminescence centre may radiate faster than an energy transfer can take place. The strong PL recovery observed for the intermediate fluences in the 300-700 °C range is consistent with a reduction of defects such as the E' centre, peroxy radical, and NBOHC. The continued recovery of these samples at even higher temperatures suggests that the damaged Er-O complexes repair themselves. However, it also suggests that there is damage introduced in the film which is rather more difficult to repair. This is why the results for the highest irradiation fluence are strange. Why does the Er-related PL at 1.54 μm quench so strongly without recovery while the visible defect PL recovers beyond its pre-irradiation value?

It is tempting to suggest that the irradiation has introduced further *radiative* electronic defects into the film which result in the observed enhancement of the oxide defect PL. However, this does not seem to be entirely feasible because the fundamental spectral shape of the PL in the region of enhancement (350-500 nm) is unchanged. It would seem overly coincidental that the irradiation would result in the introduction of radiative defects corresponding exactly to those present in the films as deposited. It appears, rather, that the irradiation has somehow allowed a population of defects, which were always present, to emit photons when they were inhibited from doing so before. This could very well be the set of oxide defects which couple as sensitizers to the Er ions. Indeed, there is a 60% reduction in the PL at 1.54 μm (relative to the pre-irradiation PL) for the 900 °C anneal of the $1x10^{15}$ cm^{-2} fluence. This corresponds with a 60% increase in the visible band PL (relative to the pre-irradiation PL) in the same sample at the same anneal temperature – which happens to be that at which the defect PL is a maximum. This strongly suggests that the *enhanced* oxide defect PL in the sample receiving the highest irradiation fluence is, in fact, due to the de-coupling of the sensitizing oxide defects from the Er^{3+}, and this de-coupling results in a concomitant *decrease* of the Er PL at 1.54 μm. Not only does this confirm the role of the oxide defects as sensitizers, but it also suggests that many of the sensitizing defects are normally dark; they do no not emit light when coupled to an Er^{3+} ion. This, in turn, suggests that the coupling is very strong, which means – within the framework of a Förster-Dexter transfer – that the defects must be located close to the Er^{3+} ions. That supports the earlier proposition that the Er incorporation, itself, forms the defects. Furthermore, it suggests that indeed, the observed oxide defect PL (as shown throughout Chapter 6) must typically correspond to centres not strongly coupled to an Er^{3+} ion. And this, finally, explains why the anneal-PL curves in the infrared and visible bands, depicted in Chapter 6 (Figure 6.4(a,b) and 6.11), have the same shape when the primary sensitization mechanism is related to defects instead of Si nano-clusters.

It is not immediately obvious why the high irradiation fluence is able to force a partial de-coupling between the Er ions and their sensitizers. It has been previously observed in the literature [239], in a thermal SiO_2 thin film, that an Er-doping implant fluence exceeding $1x10^{15}$ cm^{-2} produced a cathodoluminescence quenching at 1.54 μm relative to a lower implant dose that was apparently un-recoverable with annealing. This was ascribed to the presence of *persistent* defects (not detectable with EPR) resulting from the complete destruction of the SiO_2 network at the high implant dose, to the point that a complete regrowth at 1100 °C would be necessary to repair the structure.[279] This explanation does not seem to make sense in the films of the present study, however, because it contradicts with the extremely strong visible PL being emitted from the films. Figure 7.9 (Part 1(c)) suggests, quite strongly, that the irradiation introduces non-radiative defects which can quench the visible PL. If these defects were still present in large numbers at an anneal temperature of 800-900 °C, there should still be a quenching of the visible band PL. On the contrary, Figure 7.9 (Part 2) suggests that at the high irradiation fluence, there the film ultimately generates the same overall luminescence yield, but the relative PL yield in each spectral range has been shifted to favour the blue-violet emission. In other words, it is possible that the majority of irradiation-induced non-radiative damage has, in fact, been annealed, but the network itself has been permanently modified into some other reasonably stable confugration. Literature work on Ar^+ -irradiated Si-rich SiO_x films suggests that this structural modification of the network is open volume defects, which require annealing at 1100 °C to remove [236]. Indeed, this could explain why the present study only seems to observe the effect of this modification at the highest implant fluence.

To investigate this possibility concerning the formation of open-volume defects at the high irradiation fluence, in-situ annealing of two of the samples during a positron annihilation measurement has been carried out. The positron

[279] Although it was not addressed in the paper, one wonders if the reduced PL at the higher irradiation fluence might have been the result of concentration quenching.

energy was fixed to sample a single [mean] depth in the film (approximately 46.8 nm from the film surface) and the temperature was continuously ramped up to 600 °C over a period of hours. Following this, the full S-parameter spectrum was again measured at room temperature. The samples were then annealed to 800 °C (following the stepwise annealing scheme from 600-800 °C) and a final S-parameter spectrum was measured (at room temperature). Figure 7.10 depicts the recovery of the S-parameter as a function of the instantaneous anneal temperature for irradiation fluences of $1x10^{13}$ and $1x10^{15}$ cm^{-2}. The recovery itself has been normalized as a percentage of the difference between the [normalized] S-parameter at 46.8 nm for the sample as irradiated and the un-irradiated sample. The figure also depicts the recovery of the corresponding integrated PL intensity in the 1400-1650 nm band, normalized in exactly the same way as for the S-parameter.

It is clear that the S value in both samples ultimately underwent a full recovery to that of the un-irradiated sample (shown by the black scatter points). Before any attempt at a discussion of the correlation between PL yields and S-parameters, it is important to review the effect of temperature on Ps formation [240]. The in-situ measurement of the S-parameter is complicated by the enhancement of Ps formation (even in the presence of electronic defects) at elevated temperatures, which results from the tendency for thermal de-trapping of positrons from electronic defects. This produces an "artificial" enhancement of the S-parameter which is not necessarily related to the actual repair of electronic defects. The dashed red-line in Figure 7.10 attempts to portray the "real" S-parameter recovery *as it pertains to the recovery of electronic defects*, that is, with Ps thermal effects removed.

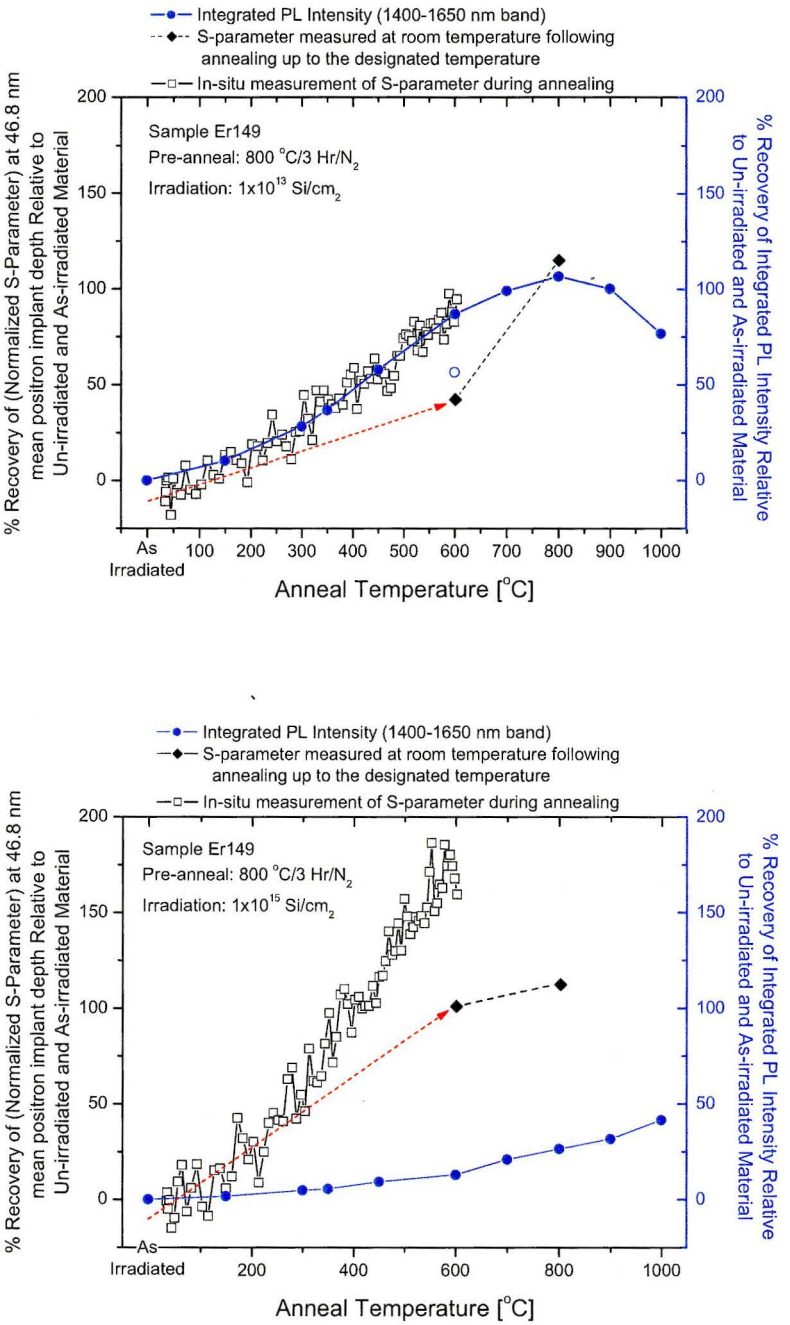

Figure 7.10: Integrated infrared PL intensity recovery plotted alongside the positron S-parameter recovery as a functional of anneal temperature. The upper panel depicts irradiation fluence $1x10^{13}$ cm^{-2}; the lower panel shows $1x10^{15}$ cm^{-2}. The dashed red line shows the effective S-parameter recovery without the effect of the enhanced thermal formation of Ps.

Figure 7.11 shows the difference spectra obtained, using the procedure described for Figure 7.6, which reveal the extent of (para) Ps formation at elevated temperature as compared to room temperature. Evidently, the red-curve shows the enhanced Ps formation at elevated temperature, while the green-curve shows the real enhancement in Ps formation which actually results from the repair of electronic defects. Note that there is enhanced Ps formation (both at room temperature and at 600 °C) in the sample receiving the highest fluence. This explains the exaggerated and much more rapid rise of the S-parameter with anneal temperature in Figure 7.10 as the result of the enhanced formation of Ps. However, because this occurs only at the highest irradiation fluence, it must be the result of vacancy-type open volume defects. This can be seen by considering that the lower fluence S-parameter shows only a 42% real recovery at 600 °C (compared with a 101% real recovery for the highest fluence), even though this

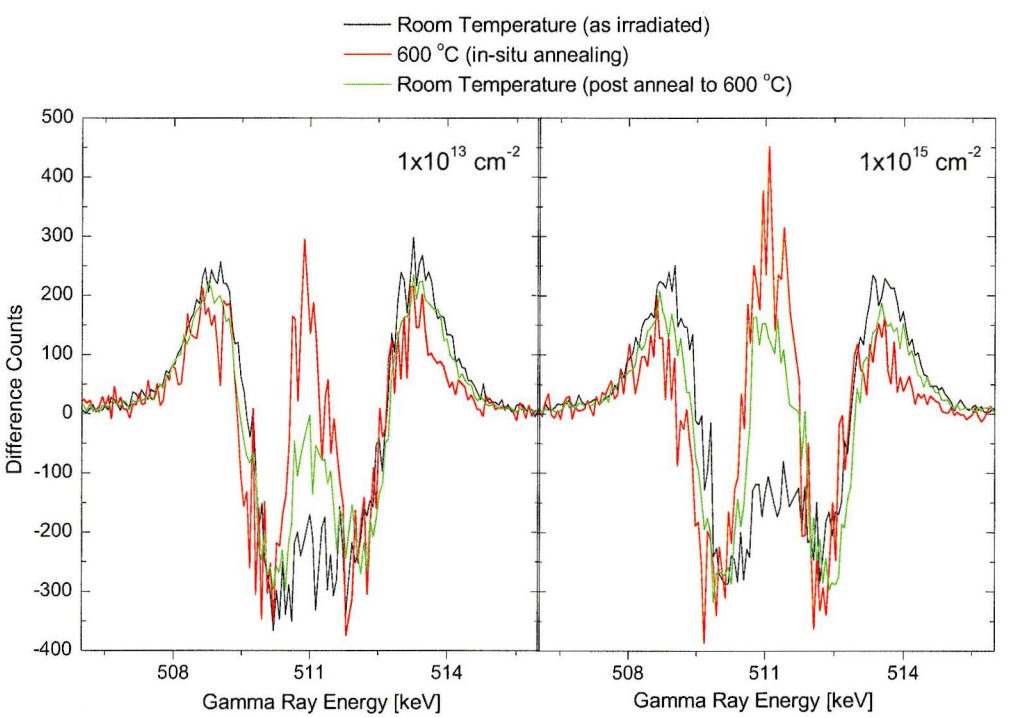

Figure 7.11: Difference spectra are shown for room temperature and elevated temperature positron measurements at two different implant fluences.

sample must necessarily contain fewer electronic defects. The positron trapping is dominated by the presence of open-volume defects in the film receiving the highest fluence.

The PL at 1.54 μm recovers faster than the S-parameter in the sample receiving the fluence of $1x10^{13}$ cm^{-2}, while it recovers much slower than the S-parameter in the sample receiving the highest fluence. Given that the Ps formation data in Figure 7.11 indicate that the vacancy-type defect population is the major difference between the two films, it seems that the Er^{3+} luminescence is severly quenched by those particular defects. Since these open-volume defects seem to be persistent to 900 °C, the fact that the PL for the sample receiving the lower implant fluence recovered completely means that this sample must have been dominated by electronic defects (which are fully expected to anneal out by 900 °C) with comparatively few vacancy defects. It is difficult to extend the correlation of the PL to any defects other than these.[280] This is because the electronic defects are driving the S-parameter down while the vacancies are driving the S-parameter up, the electronic defects and the vacancies don't anneal identically at a given temperature, and the PL near 1.54 μm has a particular sensitivity to the vacancies. Indeed, the opposing effects of coexistent paramagnetic and open volume defects on the S-parameter in silicon oxide films has been identified as a source of confusion, which is best remedied with a complementary positron liftetime measurement [241].

The question still remains as to whether the vacancy type defects are in fact forcing a de-coupling of defect and Er^{3+} PL centres. If this is indeed the case, it is difficult even to speculate at how this comes about.

---

[280] The NBOHC was isolated as a possible irradiation-induced defect in this chapter, especially in the sample receiving the highest fluence since it showed the broad PL band between 600-650 nm. This defect has also been cited in the literature, as being one that is probed by positrons. See: A. P. Knights, et. al., J. Appl. Phys. **79**, 9022 (1996). Thus, the strong recovery of the S-parameter correlates well with the reduction of NBOHC PL. Both effects were stronger in the sample receiving the higher fluence.

Figure 7.12 shows the full S-parameter spectra measured on the films after the various stages of annealing. The S values generally follow a flatter profile within the thickness of the film as the anneal temperature increases. The trends observed in Figure 7.10 appear to be the same throughout the film thickness. Although it is not shown in the figure, it is interesting to note that an anneal of 800 °C is required to repair the damage in the substrate for the sample receiving the lower implant fluence (annealing at 600 °C is nearly sufficient), whereas the substrate damage is not recovered at this temperature for the sample irradiated with the high fluence. [281]

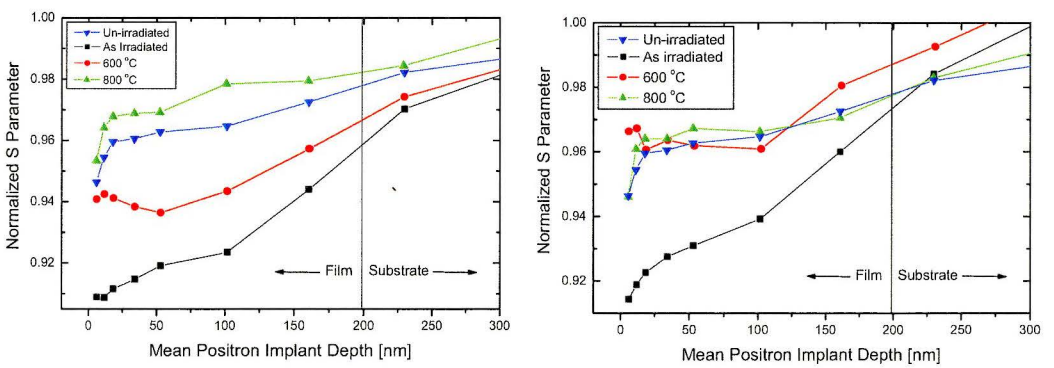

(a) (b)

Figure 7.12: S-parameter spectra for irradiation fluences of (a) $1x10^{13}$ cm^{-2} and (b) $1x10^{15}$ cm^{-2} as a function of mean positron implant depth for sample Er149; both as-irradiated and post-anneal spectra are shown. One spectrum for an un-irradiated specimen is provided for comparison.

[281] Although it is not shown here, there was a negligible change in the R parameter with annealing – and even between the $1x10^{13}$ and $1x10^{15}$ cm^{-2} irradiation fluences. This indicates that the relative balance of *o*-Ps to *p*-Ps is not significantly altered within this study.

Chapter 8

Conclusions and Future Work

8.1 Summary of the Thesis

This study investigated Er-doped Si-rich SiO_x thin films deposited by ECR-PECVD adapted for in-situ Er doping with a metalorganic precursor. There were two complementary objectives. The first objective was to map the deposition parameter and thermal processing space in order to optimize Er-related luminscence near a wavelength of 1.54 μm. The second was to understand the optimizing conditions in terms of both the dominant luminescence mechanisms and the self-assembly of the luminescent centres and thermally induced structural ordering in the films. Of particular interest was the ability of Si nano-clusters to act as sensitizing species for Er^{3+} ions. Luminescence characterization was carried out with single wavelength laser photoluminescence (PL) spectroscopy; compositional characterization was carried out with Rutherford backscattering spectrometry (RBS); defect characterization was carried out with Doppler broadening positron annihilation spectroscopy. In secondary work, RBS data analysis and simulation software has been compared and characterized, and a JetFirst 100 Rapid Thermal Processor was brought online and calibrated.

8.2 Review of Results and Conclusions

This research has revealed that the McMaster ECR-PECVD system has the ability to deposit Er-doped Si-rich SiO_x films at low temperature; a range of

compositions is possible including, but not limited to, excess Si concentrations from 32 atomic percent (at. %) to beyond 60 at. % (relative to O) and Er concentrations exceeding 4 at. %. The ratio of precursor gas flows imposes a coupling between the Er and excess Si incorporation and affects the extent to which C impurities from the $Er(tmhd)_3$ precursor, as well as residual H, enter the film. As a result, there is no simple relationship between the deposition parameters and the resulting composition. In conjunction, it is clear that film formation by thermal quenching during the ECR-PECVD process makes the as-deposited films sensitive to the plasma properties. The resulting structural response of the films to annealing was sensitive to the film composition as evidenced by a wide variability in the PL emission spectra. In fact, the luminescence properties were almost cusp-like in the vicinity of optimum concentrations. PL measurements revealed the apparent presence of three types of luminescent centres: Er^{3+} ions in O-based complexes luminescent at 1.54 μm with weak up-conversion luminescence observable in films with 36-40 at. % Si; Si nano-clusters emitting a broad, intense PL band peaked from 650-850 nm, exhibiting characteristic quantum size effects, optimized at low Er concentration for 39-40 at. % Si under an 1100 °C anneal in inert gas ambient; and oxide-defect centres exhibiting a more narrow PL band in the blue-violet wavelengths and optimized in films with Er concentrations exceeding 1 at. % but no excess Si. The PL at 1.54 μm is optimum when the Si concentration is 34-36 at. % and the Er doping is just below 2 at. %; an optimum thermal treatment is reached for annealing at 800-875 °C for 3 hours under inert gas ambient such as N_2 (or more preferably a gas mixture of 5% H_2 in Ar). It is evident that the ECR-PECVD system is, in general, able to *usefully incorporate* up to 2 at. % Er. It appears that the incorporation of the Er, during the ECR-PECVD process, simultaneously introduces radiative point defects in the vicinity of the Er^{3+} which are capable of providing some sensitization of the Er luminescence under 325 nm optical excitation. These defects seem to be partly the result of the incorporation of C in

the coordinating shell of the Er^{3+}, which has the added benefit of reducing the tendency for the formation of optically inactive Er clusters at anneal temperatures >900 °C. While these defects enable Er sensitized luminescence in the absence of excess Si, the PL at 1.54 μm can be increased by one order of magnitude with the addition of the small amount of excess Si noted above. This is the result of the formation of a small dense array of amorphous nano-clusters capable of sensitizing Er located near the cluster surface. The optimized anneal temperature near 800 °C is at least partly due to the simultaneous presence of a large Er-related oxide point defect population providing an Er-sensitization channel in addition to that of the Si nano-clusters. However, some coupling of these radiative point defects (associated with the Er-coordinating shell) to dangling bonds at the Si nano-cluster interface quenches most of the intrinsic defect PL. Er incorporation seems to inhibit the formation of Si nano-clusters, probably through a mechanism involving C, giving rise to a distribution of very small clusters which are capable of an enhanced Er sensitization. The exposure of the films (having little to no excess Si) to damaging ion irradiation (without introducing further doping) with Si^+ ions at a fluence of $1x10^{15}$ cm^{-2}, followed by subsequent annealing for 10 minutes at 800-900 °C can result in a de-coupling of the oxide defect sensitizing centres from the Er^{3+} ions. This results in a 25% enhancement of the blue-violet defect PL and a corresponding reduction in the Er-related emission near 1.54 μm. Positron annihilation spectroscopy confirms that post-irradiation annealing reduces most of the defects associated with the irradiation, however an apparently stable re-organization of the film bond network is possible which does not change significantly for anneal temperatures up to 1000 °C; this is thought to relate to the formation of vacancy complexes in the film. Finally, the PL emission in the films is stable against ion irradiation with 1 MeV Si^+ at a fluence of $1x10^{12}$ cm^{-2}; higher fluences induce a quenching of the PL in all wavelength ranges in the as-irradiated film.

8.3 Suggestions for Improvements to the ECR-PECVD System

The inclusion of metalorganic-based Er dopant into the ECR-PECVD Si-rich SiO_x system makes for a significantly more complex solid than the basic SiO_x film. Deposition repeatability requires enhanced process control over the Er precursor delivery than what exists now. In order to provide smooth and uniform gas flow from the Er cell into the deposition chamber, the carrier line should be fitted with custom heating sleeves designed to fit the line geometry exactly. The current Er cell should be replaced by a thin, flat chamber, the bottom of which is a uniform heating element. Several thermocouples should be firmly attached to the cell to map the temperature and lateral thermal gradients therein. The $Er(tmhd)_3$ powder should be completely pre-melted as part of the cell re-charging process to produce a thin, uniform layer of precursor with a smooth surface completely covering the floor in the dopant cell. The consistent solid precursor surface area should provide significantly enhanced control of the sublimation process.

The substrate stage should be fitted with multiple thermocouples in direct contact with the wafer so that the exact substrate temperature can be set prior to and measured throughout a deposition. Although such depositions will require that there be no substrate rotation, the deposition space should only need to be mapped out once to ascertain how the temperature varies in each case. After this has been completed, the thermocouples could be removed.

Finally, anticipating the fact that the current injection problem in Si-rich SiO_x films will probably necessitate devices employing very thin active layers or superlattice-type structures, the ECR-PECVD should be calibrated to operate at much lower gas flow rates. This should decrease the growth rate sufficiently to permit controllable deposition of high quality layers with a thickness of only a few nm.

8.4 Future Work

8.4.1 Continued Material Characterization

Synchrotron Radiation Study

Highly collimated beams of x-rays with sufficiently high energy to dislodge the innermost (*1s, 2s, 2p*) electrons from the atoms in a solid can be generated by synchrotron light sources. The use of x-rays whose energy is tuned to the absorption energy of a particular inner electron shell in a particular atom permits very specific site-selective investigation of the bond environment of the various film constituents. For example, one can differentiate between Si bonded to Si versus Si bonded to O because the bond environment perturbes the energy of the inner shell electrons; the same is true for the Er. Coordination numbers and radial distribution functions can be gained by analyzing the oscillations in the extended x-ray absorption fine structure (EXAFS) just beyond the initial x-ray absorption edge of the specific electron shell. Alternatively, studying both total [inner-shell] electron yield (TEY) of electrons emitted at the absorption edge as well as x-ray excited optical luminescence (XEOL) under the site-selective excitation can provide very specific information on the exact type and location of the different luminescent centres in the material. A study could be carried out for each elemental constituent in the films; film thicknesses of about 200 nm on Si substrates are good candidates for the study. The technique has been used relatively few times in the photonic device literature; this is probably because the required facilites are rare, however, Canada now has a Synchrotron Light Source at the University of Saskatchewan. A preliminary study has already been carried out using this facility on Si-rich SiO_x films grown at McMaster [242], including one of the films from the present study (Er149 annealed for one hour at 800 ^{o}C in flowing N_2). The XEOL excited at the O K-shell (1s) absorption edge (~546 eV) and Si K-shell (1s) edge for Si bonded to O (~1870 eV) are shown in Figure 8.1 (no XEOL was detected for excitation at the Si K-shell edge for Si bonded to Si).

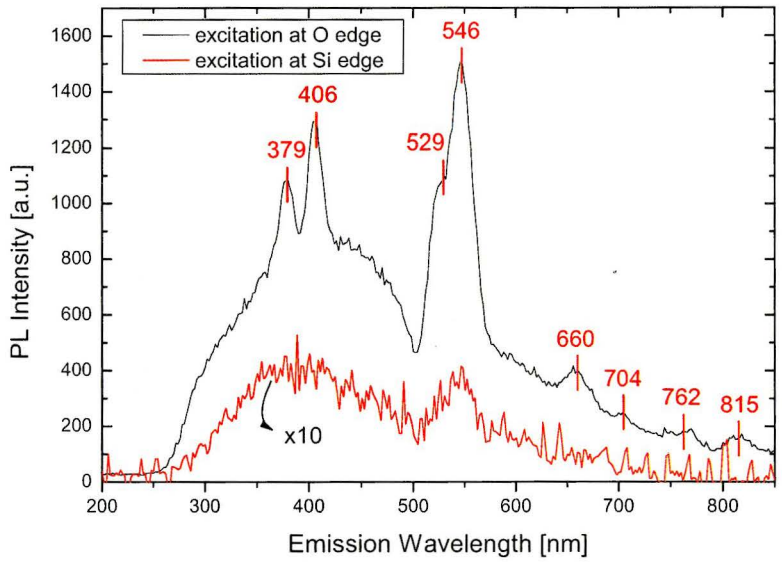

Figure 8.1: X-ray excited optical luminescence in film Er149 annealed for one hour at 800 °C in N_2 under excitation at O and Si absorption edges.

Mössbauer Spectroscopy

Mössbauer Spectroscopy is based on the recoil-less emission of gamma rays from excited state nuclei. Unfortunately, transmission Mössbauer spectroscopy using the 80.56 keV transition of excited state ^{166}Er is not feasible owing to the low gamma ray capture/emission cross sections for this istotope (prohibitively large amounts of material, not possible in thin film deposition, would be required). However, the technique *can* be used in the emission geometry by irradiating the films with slow neutrons. The irradiation transforms ^{168}Er (26.78% natural abundance) into radioisotope ^{169}Er by electron capture; the ^{169}Er decays, 42% of the time, by electron emission into excited state ^{169}Tm with a half-life of 9.4 days. The 8.40 keV gamma ray emitted during the relaxation of the ^{169}Tm nucleus can be measured directly. As a proof-of-concept measurement, a series of measurements were carried out in collaboration with the Mössbauer spectroscopy group at McGill University. Irradiation was carried out at the McMaster University nuclear reactor (duration of 48 hours at the high flux port) on film Er147 (4.32

atomic % Er relative to Si and O; and 35.1 atomic % Si relative to O) following an anneal at 800 °C for 1 hour in flowing N_2 gas; the film received a total slow neutron[282] flux of about $1x10^{19}$ $n°/cm^2$. At the current operating power of 3 MW, the high flux irradiation port provides $6x10^{13}$ *neutrons/cm²/s*; the Er should activate at a rate of 12 *mCi/hr/gram(Er)*. Reference standards of Tm_2O_3 (Alfa Aesar), $TmSi_2$ and TmB_{12} (boh fabricated at McGill) were measured in the transmission geometry by using a $^{168}Er_{10}Al_{90}$ foil as the source, following neutron irradiation of the source for a duration of 16 hours at the high flux port of the McMaster reactor. Measured spectra are shown in Figure 8.1. Note that the film required approximately 16 days of continuous gamma ray counting to obtain the statistics shown. The preliminary results suggest that the Er environment in the present samples is much different than the only other similar study in the literature, which analyzed Er-doped amorphous Si [243] (interestingly, the results of this previous study were never followed up). In order for this measurement to be made feasible, a one-hundred fold increase in the counts is required. This can realistically be achieved with two simultaneous improvements. First, films with a thickness of at least 2-3 μm should be grown.[283] Second, a higher flux neutron source is required, which can provide a total flux of at least $1x10^{20}$ $n°/cm^2$ within approximately one half-life (113 hours).[284] Such a flux will probably necessitate the use of a government operated reactor (eg. Chalk River Nuclear Reactor in Canada, or Argonne National Labs in the United States).

---

[282] Slow neutrons (near thermal energy of 0.01 eV) are used because they exhibit a high capture cross-section. Capture cross-section decreases with increasing neutron energy. Such slow neutron irradiation poses no threat of damaging the films under study since their energy is well below the relevant bond and displacement energies.

[283] The films should be thicker than this, if possible. This might be achievable by conducting the deposition in multiple steps; for example, 2 microns at a time.

[284] If the irradiation time is longer than this, the activation of the sample will be occurring at the same rate as the decay.

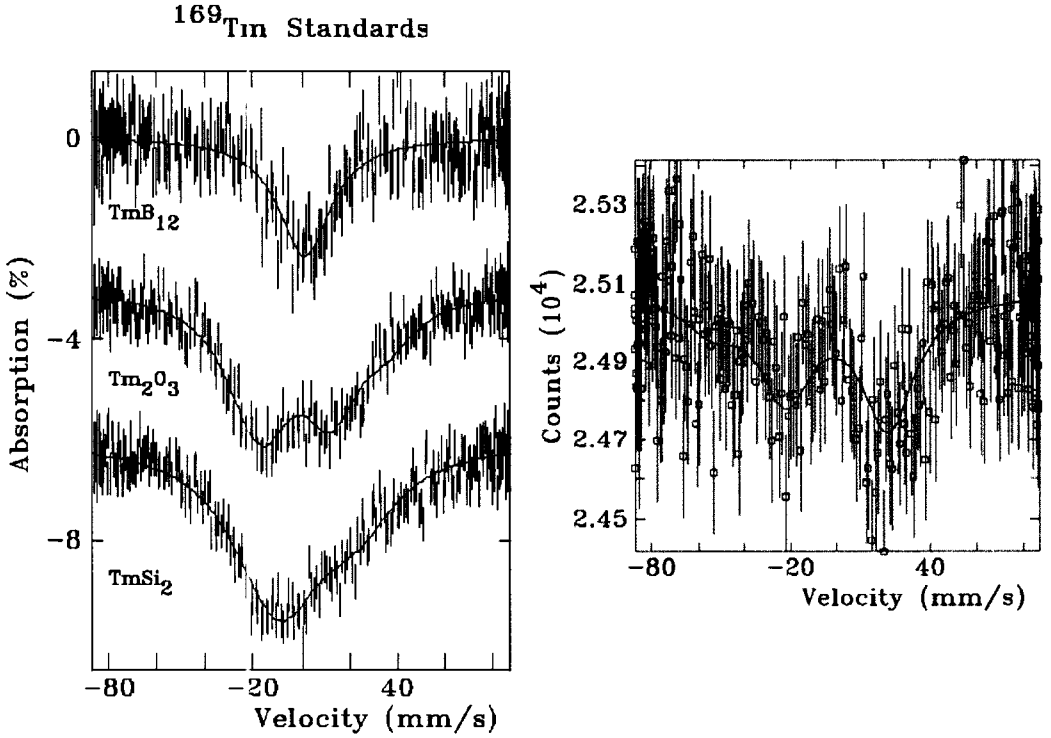

Figure 8.2: (a) ^{169}Tm Mössbauer spectra measured in the transmission geometry using Tm_2O_3, $TmSi_2$ and TmB_{12} standards as absorbers with a neutron-irradiated $Er_{10}Al_{90}$ source. (b) ^{169}Tm Mössbauer spectrum measured in the emission geometry using a neutron irradiated sample of film Er147 as the source (annealed at 800 °C for 1 hour in flowing N_2 gas). A Lorentzian fit of the data is shown.

Ultra-Violet Absorption and Photoluminescence Excitation Spectroscopies

These two measurements probably provide the most important simple luminescence characterization spectroscopies that should be undertaken. These would help to identify the luminescent defects (based on the UV absorption bands identified in Chapter 3) present in the films and could be used to identify whether or not they originate from the C co-doping/contamination.

8.4 Future Work

8.4.1 Continued Material Characterization

Synchrotron Radiation Study

Highly collimated beams of x-rays with sufficiently high energy to dislodge the innermost (*1s, 2s, 2p*) electrons from the atoms in a solid can be generated by synchrotron light sources. The use of x-rays whose energy is tuned to the absorption energy of a particular inner electron shell in a particular atom permits very specific site-selective investigation of the bond environment of the various film constituents. For example, one can differentiate between Si bonded to Si versus Si bonded to O because the bond environment perturbes the energy of the inner shell electrons; the same is true for the Er. Coordination numbers and radial distribution functions can be gained by analyzing the oscillations in the extended x-ray absorption fine structure (EXAFS) just beyond the initial x-ray absorption edge of the specific electron shell. Alternatively, studying both total [inner-shell] electron yield (TEY) of electrons emitted at the absorption edge as well as x-ray excited optical luminescence (XEOL) under the site-selective excitation can provide very specific information on the exact type and location of the different luminescent centres in the material. A study could be carried out for each elemental constituent in the films; film thicknesses of about 200 nm on Si substrates are good candidates for the study. The technique has been used relatively few times in the photonic device literature; this is probably because the required facilites are rare, however, Canada now has a Synchrotron Light Source at the University of Saskatchewan. A preliminary study has already been carried out using this facility on Si-rich SiO_x films grown at McMaster [242], including one of the films from the present study (Er149 annealed for one hour at 800 ^{o}C in flowing N_2). The XEOL excited at the O K-shell (1s) absorption edge (~546 eV) and Si K-shell (1s) edge for Si bonded to O (~1870 eV) are shown in Figure 8.1 (no XEOL was detected for excitation at the Si K-shell edge for Si bonded to Si).

8.4.2 Electroluminescent Devices

The central issue in the development of Si-rich SiO_x:Er thin film electroluminescent devices today is the current injection problem. Increasing the quantum efficiency and the power efficiency of the electroluminescence is an ongoing issue but will probably not be the factor that ultimately limits the feasibility. There are two parts to the current injection issue. The first is how to leverage the sensitizing effect of the Si nano-clusters to excite the Er.[285] The second is how to achieve efficient carrier injection (ideally bipolar injection) into the nano-clusters without risking dielectric breakdown.

Si nano-clusters can have a degrading effect on Er^{3+} impact excitation EL because they enable electrons to tunnel directly between clusters without entering the oxide conduction band as in Fowler Nordheim tunnelling. This prevents the electrons from being accelerated, by the applied field, to sufficient energies to excite the Er. The cluster spacing must be greater than 3 nm to reduce this effect [20]. While Si clusters can enhance current injection by providing conduction pathways through the oxide, they can decrease oxide reliability at high voltage because they create complex, inhomogeneous electric field concentration in their vicinity. Higher Er doping concentrations probably hinder efficient carrier energetics as well by introducing charge traps in their vicinity or by forming clusters. In fact, significant electron trapping by defects introduced in the vicinity of Er inclusions and Si nano-clusters is thought to reduce Er and Si cluster electron impact excitation by Coulomb scattering of hot (injected) electrons [244]. In effect, the charged defects and Si nano-clusters screen the Er^{3+} ion, repelling electrons which might provide an impact excitation. While these defects are thought to be the result of ion implantation steps, the PL data of the present study suggest that there are also defects introduced in the vicinity of Er and Si inclusions in ECR-PECVD films despite the 'soft' doping. In addition, ECR-

[285] Most EL devices to date rely on direct impact excitation of the Er. This is not intentional but it has proven difficult to efficiently excite the nano-clusters at electric field strengths lower than the oxide breakdown strength.

PECVD films employing metal-organic doping will probably be particularly prone to dielectric breakdown (at potentially low fields) because of the structural alterations relative to pure SiO_2 caused by a high concentration of impurity atoms.

The field effect electroluminescence mechanism that can be achieved in the transistor device geometry [22] should be investigated using ECR-PECVD Er-doped SiO_x containing Si nano-clusters or crystals as the floating gate oxide. This seems to offer the most efficient current injection to date.

An entirely different approach which could exploit a parallel-plate capacitor device geometry would involve the deposition of a superlattice film with layer thicknesses of a few nm. For example, the period could consist of a 2-3 nm layer of Si-rich SiO_x:Er followed by a 3-6 nm layer of SiO_2. Another example could be a 2-3 nm layer of SiO_2:Er followed by a 2-3 nm layer of Si-rich SiO_x. The electric field could then appear as a stepwise function through the film. This could permit a more uniform carrier tunnelling between layers and fewer regions of localized electric field concentration within a layer (since thin layers could be made much more uniformly than a single layer 100-200 nm thick film). In fact, superlattices seem to be the only way to produce controllable, mono-disperse size distributions of Si nano-clusters. These superlattices have been well researched in the literature (see for example [17,24,114,245,246]) and have been successfully implemented in a waveguide geometry [14]. The main problem with such a device structure is that it may not be manufactuable; the fabrication of the multiple layers may be too complex to fit into a typical CMOS-VLSI process flow.

Electrical contact to such capacitive LED[286] structures must maximize current spreading and injection efficiency. This usually necessitates that the contact completely cover the active region in the device. An efficient opaque electrode suitable for one side of the device consists of an Al ring deposited on a

[286] It should be noted that most EL devices based on SiO_x-type active layers are not actually "diodes" in the usual sense of the term as is commonly applied to *pn* junctions or III/V laser "diodes". However, the term is occasionally used in the Si photonics literature in the context of MOS capacitor structures.

gold current spreading layer. Another alternative is the use of transparent electrodes such at ITO (indium tin oxide) or a transparent conducting oxide (TCO) such as zinc oxide doped with aluminum.

Photonic crystals (photonic band gap structures) have only begun to be exploited in maximizing light extraction efficiency from Si nano-cluster LEDs. Interestingly, such a device has recently been fabricated [247] (using all optical lithography) with the claim that it is actually much simpler to manufacture than other devices engineered for enhanced light emission which rely on multi-layer structures or electron-beam lithography. It is claimed that the device is specifically compatible with current VLSI processing.

The appearance of the visible defect PL in these films presents the possibility of LEDs, including broad-band (nearly white) light emission, for solid-state lighting applications, providing the defects can be electrically pumped. It has been shown in the literature that these defects can be pumped by carrier tunnelling followed by impact excitation in simple MOS capacitor device structures [228]. Furthermore, it has been shown that at sufficiently high electric fields, Er^{3+} visible (green) EL can be generated due to the impact excitation by energetic carriers [20]. Since this EL does not appear to rely on an up-conversion mechanism, it may not be necessary to dope the films with excessively high Er concentrations. This EL should have a spectrum distinctly narrower in comparison with that of the oxide defects.

A final remark concerning EL devices should be made with respect to the potential use of thin film electroluminescence (TFEL) device geometries. Electroluminescence from insulating layers is the basis for various phosphor light emitters. The "sandwiching" of the active insulating layer between thin layers of higher dielectric constant allows an electric field clamping phenomenon and the intentional breakdown of the active layer leading to impact excitation of the phosphor under an AC field. This does not appear to have been investigated at all for Si-based LEDs. However, such a device could easily be grown on the ECR-

PECVD using an Er-doped Si-rich SiO_x active layer and SiO_xN_y "sandwich" layers with properly adjusted thickness. See [248].

8.5 Final Remarks

A fascinating shift of thinking seems to be currently underway with respect to Si based light emitter research and more specifically, optical interconnect. This is the development of *plasmonics*. From an optical device perspective, surface plasmon-polaritons[287] can enable light localization such that sub-wavelength (nano)-photonic devices could be realized[288] with features well into the deep submicron regime of current micro-electronics. In an optical interconnect scheme, this would enable the light from on-chip optical sources to couple into non-radiative surface plasmons in waveguides (made from noble metal nano-particles) with lateral dimensions less than 10% of the free space wavelength. A field of *silicon plasmonics* has even taken shape, as both Si nano-clusters and Er^{3+} ions have demonstrated an ability to couple to and excite surface plasmons in Ag or Au thin films [249,250]. Furthermore, the altered photonic environment (local optical density of states) caused by nearby metal can enhance Si nano-cluster emission efficiency and enable control of the Si nano-cluster/Er^{3+} energy transfer [251].

As this example illustrates, one of the fascinating aspects of the intense pursuit of a Si light emitter for optical interconnect has been its motivation for investigation of increasingly exotic optical phenomena, materials, and device structures. This has spawned new applications well beyond computer chip interconnect ranging from biophotonics to ultra-low cost Si-based solid state lighting. The financial motivation for Si-based technology seems to be good enough to cause man to think he can do anything with Si – or he should at least

---

[287] A surface plasmon is an electromagnetic wave localized at a metal/dielectric interface coupled to surface charge oscillations (J. Kalkman, et. al., Appl. Phys. Lett. **86**, 041113 (2005)).

[288] Such small optical devices have never been possible before because of limitations imposed by diffraction.

exhaust himself trying. It is thus the only material that could cause such an aggressive research initiative.

It is quite likely that photonics will eventually come to dominate everyday technology in the way micro-electronics dominates today; its resultant impact on society will probably be even greater. Whether a Si laser, or Si photonics in general, ever becomes a viable technology is somewhat beside the point. Its mere pursuit has been a tremendous catalyst for the development of new knowledge, exotic physics and some incredible ingenuity in device and materials engineering. It provides the researcher with an interesting context that seems to be characteristic of the new field of nano-technology; that is, the *engineering* of practical, manufacturable devices envisioned for mass consumption, directly from the obscurities of fundamental quantum mechanics.

Appendix A

Basic Physical Theory of Quantum Confinement

Quantum confinement effects require that a material is reduced in size along one or more of its dimensions. Three possible structures occur depending on whether the size is decreased along one spatial dimension (resulting in the familiar two-dimensional 'quantum well'), two spatial dimension (yielding a one-dimensional 'quantum wire') or three dimensions (yielding a zero dimensional 'quantum dot'). These are illustrated, conceptually, in Figure A.1.

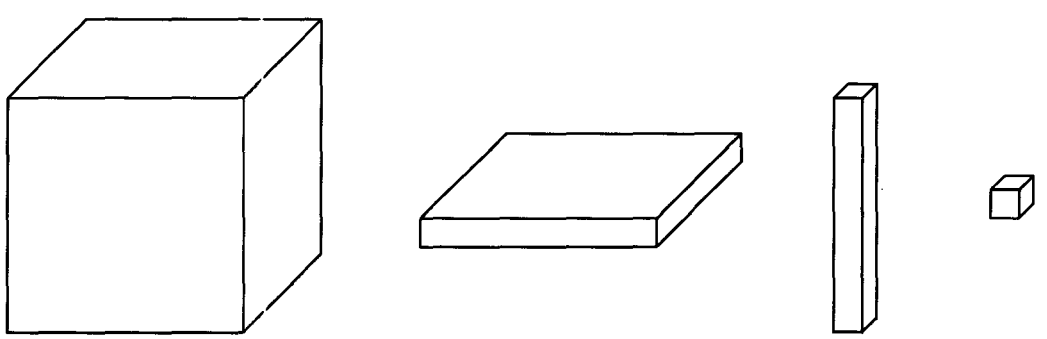

Figure A.1: Representation of the different dimensionalities of material structures discussed on quantum confinement theory. (a) bulk: no confinement; (b) thin film: quantum well, 2 dimensional confinement; (c) quantum wire, 1-dimensional confinement; (d) quantum dot, 0-dimensional confinement

Broadly speaking, quantum size effects can be identified experimentally as departures from the bulk behaviour of a solid. These effects become significant when the size of the sample becomes comparable to the wavelength of the important excitations in the solid [252]. Decreasing the size below this limit changes the nature of the excitations and any property based upon them. For example, phonon dispersion relationships change and cause the specific heat capacity to change; the electronic transition energies change and cause the optical absorption/emission curves to change. Another criterion for identifying the onset of quantum size effects is the point at which the energy level spacing exceeds kT (mean thermal energy of the Boltzmann distribution at temperature T). Notably, this onset occurs at a large size in semiconductors relative to metals or insulators.

The effect is most easily visualized with a two dimensional structure such as a thin film (see Figure A.2). Consider the material to be semi-infinite in the x and y directions ($L>>d$) and confined in the z direction. It is desired to calculate the single-electron wave functions and energy levels since these determine the optical properties. The electron can be treated as a free electron and the effect of the band structure absorbed in the appropriate effective mass for the solid under consideration (although in the confined direction this is an approximation because the effective mass depends on the potential seen by electron in a given direction). The now quasi-electron is free in the x and y directions and spatially confined in a one-dimensional infinite square well in the z direction (using a first order assumption of impenetrable barriers). The resultant wave function is a product of traveling Bloch waves along the x and y directions and a standing wave in the z direction originating from the reflection of the Bloch waves at the hard surfaces of the well. The energy ε corresponding to the total wave function is given by:

$$\varepsilon = \frac{\hbar^2 \vec{k} \bullet \vec{k}}{2m_e^*} = \frac{\hbar^2 (k_x^2 + k_y^2 + k_z^2)}{2m_e^*} \tag{A.1}$$

where $\hbar$ is the Dirac constant and m_e^* is the effective mass of the electron in the

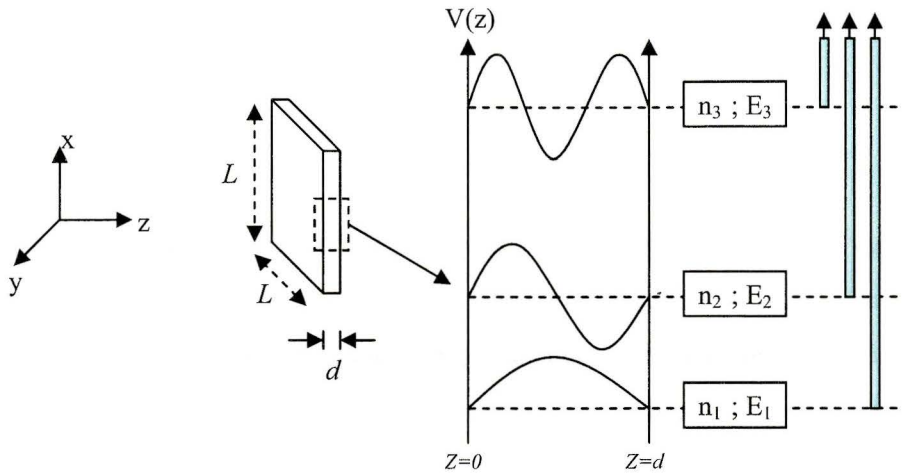

Figure A.2: In comparison with the quasi-continuous band of discrete states which the electron can occupy in the *xy* direction, the states corresponding to the *z*-motion are well separated since fewer wavefunctions satisfy the more stringent boundary conditions.

material of interest. The wave-vectors components,

$$k_x = \frac{2\pi p}{L_x}; p = 0,1,2,...$$
$$k_y = \frac{2\pi q}{L_y}; q = 0,1,2,... \qquad \text{(A.2)}$$
$$k_z = \frac{n\pi}{d}; n = 1,2,...$$

index the allowed Bloch waves (eigenfunctions).[289] This means that ε can be written as a sum of two terms, the first is the energy due to the motion of the electron in the *xy* plane, and the second is the energy due to motion in the *z* direction:

$$\varepsilon = E(L_x, L_y) + E_n(d) = \frac{\hbar^2}{2m_e^*}(p^2 + q^2) + \frac{\hbar^2 n^2 \pi^2}{2m_e^* d^2} \qquad \text{(A.3)}$$

[289] These quantities simply proceed from the application of the periodic boundary conditions (due to Born-von Kármán) in the *xy* plane and the zeroing of the wave function at the *z* boundaries.

with E_n defined to be:

$$E_n(d) = \frac{\hbar^2 n^2 \pi^2}{2m_e^* d^2} \tag{A.4}$$

The energy due to the motion in the z-direction is denoted E_n and is effectively the increase in energy of the level n relative to the unconfined case. For example, the quantity E_1 is the increase in the ground state energy of the electron relative to the unconfined case. This energy is therefore usually referred to as the *confinement energy* of the electron. E_1 is often denoted ΔE:

$$\Delta E \equiv E_1(d) = \left(\frac{\hbar^2}{2m_e^*}\right)\left(\frac{\pi^2}{d^2}\right) \tag{A.5}$$

It is clear that subsequent values of $n>1$ define excited states of the electron in the well and that their energy increase due to confinement can be written in terms of the [ground state] confinement energy:

$$E_n = n^2 \Delta E \tag{A.6}$$

Physically, the origin of the confinement energy lies in the Heisenberg uncertainty principle. Consider that the total energy of the electron can be written in terms of the crystal momentum $\vec{p} = \hbar\vec{k}$:

$$\varepsilon = \frac{\vec{p} \bullet \vec{p}}{2m_e^*} \tag{A.7}$$

According to the Heisenberg uncertainty principle, *both* the crystal momentum (or wave vector) and energy are precisely defined within equation A.7 only when the particle is infinitely delocalized. However, in the present case, the particle is spatially confined in the z-direction within a distance d. Therefore, by the uncertainty principle,

$$\Delta p_z \Delta z \geq \frac{\hbar}{2} \tag{A.8}$$

the uncertainty in the z-component of the particle's momentum p_z is increased by an amount of order $\hbar/d$. The corresponding increase in the particle's kinetic energy, considering equation A.7, due to confinement will also be of order $\hbar/d$ (compare with equation A.5). It is evident from this, that the energy gap between z-state levels increases as the confined length decreases. This can also be viewed as a Fourier transform effect.

It is not difficult to conceive of how this analysis would be extended to confinement in two and three dimensions. In the three dimensional (quantum dot) case the electron is confined in every direction so that the total energy levels ε are well separated with no intervening states due to unconfined motion. In all cases, filling of energy levels follows strictly from the Pauli Exclusion Principle (in the limit of zero temperature, corresponding to the absence of external excitations). The density of states (DOS) is based on counting those states corresponding to the quasi-continuous energy levels. The concept of DOS in the confined direction has little meaning with the vanishingly small differential element of energy used to define the DOS for the quasi-continuous levels. In fact, in the limit of a truly zero dimensional quantum dot, the density of states is a series of Dirac Delta functions at the precise energy levels. It is clear from Figure A.3 that as the structure becomes more confined, the states increasingly concentrate near the confined levels.

If one now considers real bounding media (see [253]), the potential well would be finite. In practice, this is usually achieved by bounding a material of band gap E_g by materials of band gap greater than E_g (eg. Si in SiO_2) thereby creating a confined system. In this way, one calculates the confinement of electrons and holes separately.[290] As in Figure A.4 (depicting a finite square

[290] This is because electrons and holes have different effective masses, valence and conduction and offsets will likely be different, and there are often spin-orbit coupling effects at the top of the valence band.

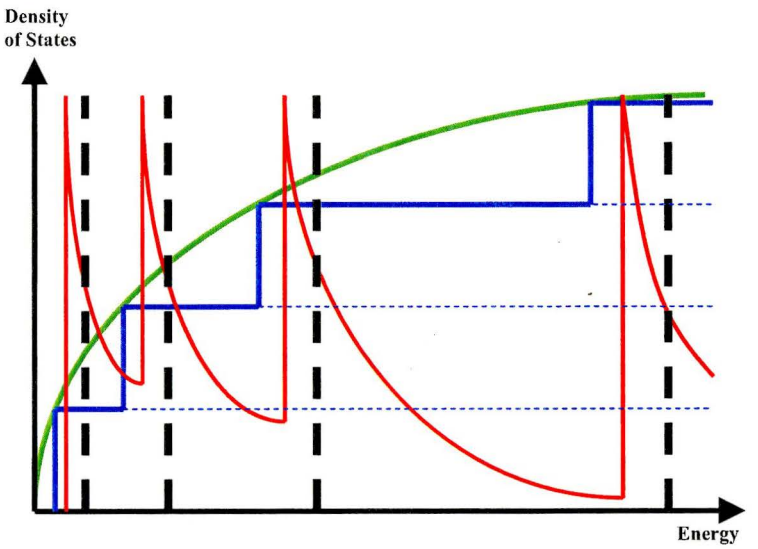

Figure A.3: Density of states function for different degrees of confinement. Green curve (bulk), blue (quantum well), red (quantum wire), black dash (quantum dot)

well), the energy level diagram depicts only a single point in k-space. Each level in the diagram therefore has its own associated $\varepsilon(k)$ structure. In this case, the energy eigenvalues corresponding to motion in the z-direction would be slightly altered from equation x and would not, in general, have an analytic form. The total energy of the conduction band states could be written in principle:

$$\varepsilon = E_c + E(L_x, L_y) + E_n(d) \tag{A.9}$$

The wave function could now penetrate the surface to some extent (evanescent wave), which is small if the barrier is large. This interaction of the wave function with the interface (which was not a factor in the case of the infinite well) introduces the 'real surface' properties as another important variable in quantum confined systems. The effect of impurity atoms, defects or irregular bonding geometries at the surface (including dangling bonds and strain) can introduce a non-square surface potential which further complicates the calculation of the wave function. Furthermore, because the confined dimension(s) has characteristic

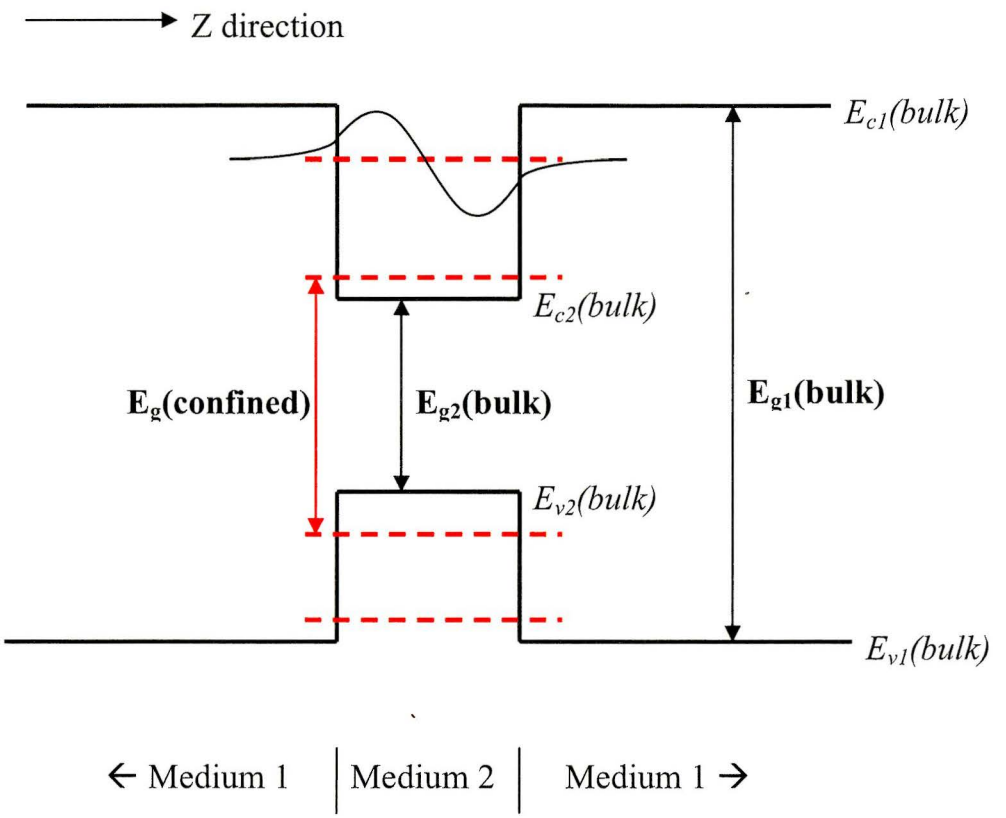

Figure A.4: Energy band edges depicted as a function of distance in the confinement direction of a 2D quantum well. The discretization of the energy levels is shown to lead to an effective enlargement of the band edge energy gap.

lengths of the order of the electron wavelength, the presence of the altered surface potential can significantly affect the structure of the wave function in the interior material. A defective surface may also introduce states localized at the surface which may be within the band gap of the confined material and therefore constitute charge traps. These surface effects become particularly important in the case of quantum dots where a typical dot may have a critical dimension of a few nanometres or less. In this case, the ratio of the dot surface area to its volume might be significant. In other words, a relevant fraction of the atoms constituting the dot might actually be on the surface, and therefore be subject to the aforementioned irregularities.

Appendix B

Er^{3+} 4f Electron Energy Levels

The following table provides a basic listing of the low-lying intra-4f Er^{3+} energy levels and the corresponding transition energies to the ground state (from [75]).

ENERGY LEVEL *[Term Symbol***]*	**ENERGY***		**WAVELENGTH**** *[nm]* *(transition to ground)*
	[eV]	*[cm^{-1}]*	
$^4I_{15/2}$ (ground state)	0	-	0
$^4I_{13/2}$	0.808	6515	1535
$^4I_{11/2}$	1.27	10236	978
$^4I_{9/2}$	1.53	12332	812
$^4F_{9/2}$	1.88	15153	661
$^4S_{3/2}$	2.25	18216	550
$^2H_{11/2}$	2.33	18860	531
$^4F_{7/2}$	2.53	20392	491
$^4F_{5/2}$	2.74	22165	452
$^4F_{3/2}$	2.79	22568	444
$^2H_{9/2}$	3.05	24583	407
$^4G_{11/2}$	3.23	26034	385
$^2G_{9/2}$	3.37	27162	369
$^2K_{15/2}$	3.41	27500	364
$^2G_{7/2}$	3.47	28000	358
$^2P_{3/2}$	3.89	31375	319
$^2K_{13/2}$	4.09	33000	303
$^4G_{7/2}$	4.21	33900	295
$^2D_{5/2}$	4.30	34675	289
$^4G_{9/2}$	4.50	36300	276
$^2I_{11/2}$	4.83	38900	257 *(three levels almost indistinguishable)*
$^4D_{7/2}$			
$^2L_{17/2}$			
$^2D_{13/2}$	5.06	40800	245
$^2I_{13/2}$	5.09	41000	244
$^4D_{3/2}$	5.11	41200	243

Table B.1: Er^{3+} 4f energy levels and term symbols

* Note: In general, the energy of a photon is calculated according to the equation $E = hc/\lambda$. However, the inverse relationship between E and λ is often inconvenient (eg. for graphical depiction of energy levels). Therefore, the expression of the energy in units of cm^{-1} (simply calculated as the inverse of the wavelength), which is actually the normalized quantity E/hc, is used. It is akin to plotting the linear function $E=E(1/\lambda)$.

** Wavelength measurements vary slightly from study to study depending on the exact host in which the Er is present, however this variation is almost invariably in the range of 2-5 nm. The transition wavelength should therefore rightly be defined as the central wavelength in the particular Stark manifold.

*** The term symbol is a notation that describes the electron configuration (through the angular momentum quantum numbers) for the optically active electron(s) of multi-electron atoms [72]. In this way, it descriptively indexes the energy levels of these electrons and identifies the angular momentum couplings (spin and orbital) occurring at each level. Hund's rules determine the possible angular momentum couplings arising from the residual Coulomb interaction (which represents a correction to the Hartree method for electronic structure calculations of muti-electron atoms) and the spin-orbit interaction (which represents the coupling of the electron spin angular momentum with the electron orbital angular momentum). The symbol has the form $^{2S+1}\mathbf{L}_{\mathbf{J}}$. The quantity **S** is the total spin of the atom/ion (so that **2S+1** is the number of possible spin orientations of the total spin of the atom/ion). The **L** quantity is the total orbital angular momentum of the atom/ion and is given by the sum of the orbital angular momenta of the individual electrons according to the Clebsch-Gordon series (notation: 0=**S**, 1=**P**, 2=**D**, **F**, **G**, **H**, **I**, etc.). The **J** quantity is the total angular momentum (**J=L+S**) of the atom/ion as determined by the Russell-Saunders coupling scheme (also known as the L-S coupling). The Russell-Saunders coupling refers to the determination of **S** (**L**) by the summation of the individual electron spins $\mathbf{s}_i$ (individual angular momenta $\mathbf{l}_i$) and is based on the assumption that the individual spins interact only with each other to generate the total spin (similarly for **L**). Under this assumption, the spin-orbit coupling is due mainly to the interaction of the total **L** and **S**. This breaks down in heavy atoms in which each orbital angular momentum $\mathbf{l}_i$ tends to combine with each individual spin angular momentum $\mathbf{s}_i$, to give individual total angular momenta $\mathbf{j}_i$; then $\mathbf{J}=\Sigma\ \mathbf{j}_i$ (this scheme is called jj coupling).

Appendix C

Positron Annihilation Spectroscopy

A positron (e^+) is the antiparticle of an electron (e^-) (see [254]). The positron/electron electromagnetic interaction brings about annihilation of e^+- e^- pairs through a reaction whose principle channel involves the emission of two gamma photons:

$$e^+ + e^- \rightarrow \gamma_1 + \gamma_2 \qquad \text{(C.1)}$$

In the centre of mass frame, conservation of energy and momentum dictate that each photon has energy equal to the rest mass energy of the electron (positron) $E_o=m_oc^2\approx 511\ [keV]$ (where m_o is the rest mass of the electron (positron) and c is the speed of light), and the photons are emitted in exactly opposite directions. In the laboratory frame of reference, only the positron is considered to be at rest, so that the photon energies are *Doppler shifted* to $E=E_o+\Delta E$ where $\Delta E\approx\pm cp_{-,L}/2$ and the photons are emitted in directions non-collinear by an angle $\Delta\theta\approx p_{-,T}/m_oc$ with $p_{-,L}$ *and* $p_{-,T}$ being the longitudinal and transverse momenta of the electron respectively. In this way, the gamma transition linewidth for two-photon positron annihilation is sensitive to the velocity (momentum) distribution of the electrons in a material.[291] Furthermore, the rate of annihilation is directly proportional to the effective electron density sampled by the positron prior to annihilation.

[291] Electron-positron annihilation at different sites (surfaces, vacancies, etc.) can be distinguished because each site has electrons with different momentum states.

Consider a positron which is implanted into a material with some intial kinetic energy $E \approx$ 0.1-1 MeV. The positron rapidly thermalizes ($\leq$10 ps) in penetrating the material.[292] The thermal positron then diffuses through the medium as a quantum mechanical wave. The depth distribution of thermalized positrons (ie. stopping profile of the implanted positrons) can be described by a Markovian distribution, giving the probability *P(z)* of finding the thermalized positron at a depth of z(Å).

$$P(z) = \frac{m z^{m-1}}{z_o^{\,m}} \exp\left\{-(z/z_o)^m\right\} \tag{C.2}$$

where

$$z_o = \frac{\bar{z}}{\Gamma\left[\frac{1}{m}+1\right]} \tag{C.3}$$

with m=2.0 and where $\bar{z}$ is the mean implant depth (at which the positron comes to rest) in units of Angstroms and is given by

$$\bar{z} = \frac{360}{\rho} E^n \tag{C.4}$$

with ρ the density of the solid (g/cm^3), in initial positron kinetic energy E in keV and n=1.6. As an example, Figure C.1 depicts the Markovian distribution for positrons implanted into SiO_2 at an energy of 2 keV.

The thermal positron interacts with its surroundings as it diffuses, with a mean free path ~10 nm, before annihilating with an environmental electron after a total diffusion length ~100 nm. If the medium contains no defects, then all of the positrons annihilate at the same [material-specific] rate λ_f.[293] The Coulomb repul-

---

[292] At the highest positron energies this energy loss occurs through excitation of core electrons in collisions with the host atoms (ionizations). At lower energies the energy is lost to electron-hole excitations and finally to phonon scattering once the kinetic energy drops well below 1 eV. The thermalized positron remains in thermal equilibrium by phonon emission/absorption.

[293] This is often referred to as the 'free-trapping rate' or 'bulk trapping rate'.

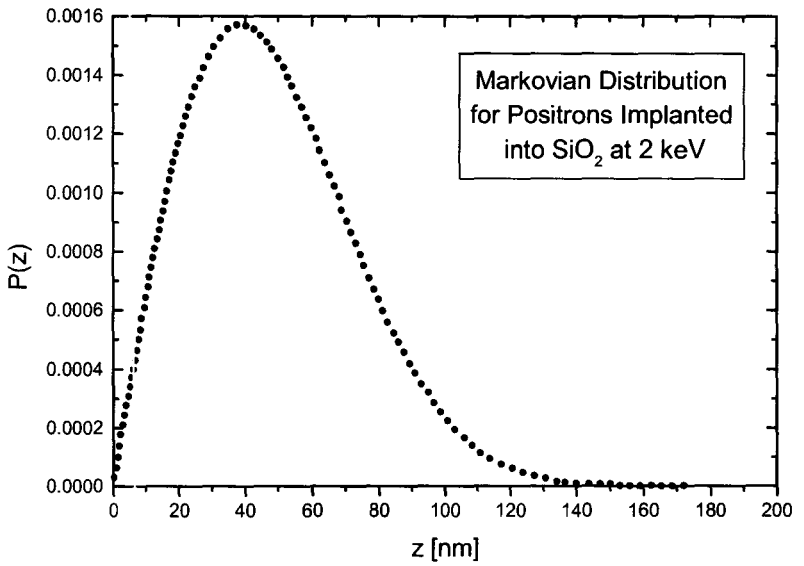

Figure C.1: Markovian distribution for positron implanted into SiO_2 at an energy of 2 keV. This is effectively the condition used to carry out the in-situ positron measurement while annealing.

sion exerted on the positron by the positive ion cores tends to force the positron into the inter-atomic space and/or open-volume defects (if they are present). Such regions constitute potential energy wells into which positrons may enter. The resulting localization of the positron wave function (dependent on the depth of the potential well) from its intial delocalized state is referred to as 'trapping'. Unless the well is shallow enough to permit thermal or phonon-assisted de-trapping, the positron remains in the trap until it annihilates with an electron. The reduced electron density in the trap tends to increase the positron lifetime relative to its value ($1/\lambda_f$) in the undefective bulk. The trapping of freely diffusing positrons at defects[294] produces an effective trapping rate λ_{eff}:

$$\lambda_{eff} = \lambda_f + \upsilon C \tag{C.5}$$

[294] Note that positrons are not sensitive to positively charged defects. Trapping defects may be netural, but are usually negatively charged.

where υ is the trapping rate of the defect(s) and C is the particular defect concentration. The trapping rate υ is specific to the exact type of defect.

There is an additional effect that occurs in many insulator materials (such as the films of this study), whereby the thermalized positron and an environmental electron may form a hydrogen-like bound state known as positronium (Ps).[295] The two possible spin orientations of the two particles mean that the Ps atom can exist in either the spin-antiparallel singlet state (parapositronium, p-Ps) or the spin-parallel triplet state (orthopositronium, o-Ps). While two-photon annihilation is a dipole allowed process between the positron and electron pair in p-Ps, it is not allowed in o-Ps. In o-Ps, self-annihilation only occurs by a three-photon process. The positron in o-Ps can only engage in two-photon annihilation by collision with an external electron of opposite spin (so-called 'pick-off annihilation'); this fast process tends to reduce the amount of three-photon self-annihilation observed. Table 8.1 summarizes the various positron states which can occur in a typical insulator, their lifetimes and dominant annihilation processes.

Positron State	**Annihilation Process**	**Characteristic Lifetime**
Free positron	2γ	0.1-0.4 ns
Trapped positron	2γ	0.2-0.5 ns
Parapositronium	2γ, self-annihilation	0.1 ns
	2γ, pick-off annihilation	>1 ns
Orthopositronium	3γ, self-annihilation[1]	140 ns
	2γ, pick-off annihilation	>1 ns

[1] These three photons occur with a continuous energy distribution ranging from 0 to about 511 keV.

Table C.1: Positron states and annihilation processes with characteristic lifetimes. Adapted from [254].

[295] Note that the Ps atom usually ends up repelled into void spaces within a material by the exchange interaction of the Ps electron with the environmental electrons. Ps is not really "trappable" by the Coulomb field since the Ps carries no net charge. In this way, there are two variations of Ps. The first corresponds to delocalized Ps in a solid, which typically has a diameter (i.e. coherent length) about $4\varepsilon a_o$ where ε is the dielectric constant and a_o is the bohr radius; any electron in the solid may be involved in this Ps atom so that its crystal momentum is not well defined. Alternately, Ps could become localized in a void. Such Ps is similar to Ps in a vacuum and has a definite crystal momentum.

In general, the ^{22}Na radioisotope is used as the positron source.[296] High resolution solid-state intrinsic Ge gamma ray detectors are used to measure the energy of each annihilation photon. There are various techniques which measure one of either positron lifetime, Doppler broadening of the anniliation line, angular correlation of annihilation photons, or age-momentum correlation, etc. In the present study, the Doppler broadening of the 511 keV gamma transition line is measured. The broadening is a function of the environment in which the positron annihilates. This is compared using a quantity known as the S-parameter, which is simply defined as the number of photon counts in the central region of the annihilation peak (510.27-511.73 keV) divided by the total counts in the peak (504.5-517.5 keV). A complementary value to the S-parameter known as the W-parameter is defined as the counts in the peak tails divided by the total counts in the peak. The measured S and W values in ion irradiated material are normalized against the corresponding values measured for unirradiated material.[297] The S value increases with the contribution of lower momentum electrons to the annihilation, such as occurs in an open volume defect due to the lack of high velocity core electrons; the S values are also increased by the presence of p-Ps because of the low centre of mass momentum in the p-Ps atom.[298] Evidently the W-parameter increases with increasing participation of high momentum core electrons in the annihilation. An additional parameter, known as the R-parameter can be defined which measures changes in the relative amount of o-Ps in the sample. It is based on the fact that the three-photon annihilation mode is the only such process capable of producing unscattered gamma gays with an energy below those contained in the 511 keV peak. It is defined as the difference between the

[296] The ^{22}Na radioisotope decays (90.4% of the time) by the emission of a 545 keV positron to produce excited state ^{22}Ne, which decays to stable ^{22}Ne within 3.7 ps by emission of a 1274 keV gamma ray. A ^{58}Co source is sometimes also used as an alternative, lower cost, positron source.

[297] In general, one attempts to fit the experimental line-shape parameter S(E) as a superposition of component line-shape parameters corresponding to the various annihilation mechansisms (bulk, trapping at defects, surface-based) weighted by the fraction of positrons which undergo each mechanism.

[298] Therefore, the suppression of the formation of Ps results in a decrease of the S-parameter.

total integrated count rate in the annihilation spectrum T and the integrated count rate in the 511 keV peak P, divided by P. A higher R value indicates increasing amounts of o-Ps.

Appendix D

List of Publications and Presentations

D.1 Journal Publications

D. E. Blakie, O. H. Y. Zalloum, J. Wojcik, E. A. Irving, A.P. Knights, and P. Mascher. *Sensitivity of Si and Er luminescence centers to annealing ambient in Er-doped Si_yO_{1-y} ($y \geq 1/3$).* Submitted to Appl. Phys. Lett. (2006).

D. E. Blakie, O. H. Y. Zalloum, J. Wojcik, E. A. Irving, A. P. Knights, and P. Mascher. *Si nano-clusters and Er-related centers as sensitizers for Er^{3+} luminescence in in-situ doped Si_yO_{1-y}:Er ($y \geq 1/3$) thin films.* Submitted to J. Appl. Phys. (2006).

D. E. Blakie, O. H. Y. Zalloum, J. Wojcik, E. A. Irving, P. J. Simpson, A. P. Knights, and P. Mascher. *Photoluminescence and positron annihilation spectroscopy of ion-irradiated Si_yO_{1-y}:Er ($y \geq 1/3$) thin films.* Submitted to J. Appl. Phys. (2006).

D.2 Conference Proceedings and Oral Presentations

D. E. Blakie, O. H. Y. Zalloum, J. Wojcik, E. A. Irving, A. P. Knights, and P. Mascher. *Erbium-doped silicon-rich silicon oxide luminescent thin films deposited by ECR-PECVD.* Presented at Photonics North 2005, article accepted for publication by SPIE (2005).

D. E. Blakie, O. H. Y. Zalloum, J. Wojcik, E. A. Irving, A. P. Knights, and P. Mascher. *Coupled luminescence centres in silicon-rich silicon oxide thin films.* Presented at Photonics North 2006, article accepted for publication by SPIE (2006).

D.3 Conference Poster Presentations

D. E. Blakie, O. H. Y. Zalloum, E. Irving, J. Wojcik, A. P. Knights, and P. Mascher. *Erbium-doped silicon rich silicon oxide thin films deposited by ECR-PECVD.* Annual General Meeting of the Canadian Institute for Photonic Innovations: Poster Session (2005). First Annual Showcase of the Ontario Photonics Consortium: Poster Session (2005).

D. E. Blakie, O. H. Y Zalloum, E. Irving, J. Wojcik, A. P. Knights, and P. Mascher. *Erbium-doped silicon rich silicon oxide thin films deposited by ECR-PECVD.* Second Annual Showcase of the Ontario Photonics Consortium: Poster Session (2006). Annual General Meeting of the Canadian Institute for Photonic Innovations: Poster Session (2006).

D. E. Blakie, O. H. Y. Zalloum, E. A. Irving, J. Wojcik, A. P. Knights, P. Mascher, and P. J. Simpson. *Positron annihilation in ion-irradiated erbium-doped photonic thin films.* 14^{th} International Conference on Positron Annihilation: Poster Session (2006).

References

[1] Lorenzo Pavesi and David J. Lockwood (Ed.), *Silicon Photonics*, Spring-Verlag, New York, NY, 2004.

[2] The National Technology Roadmap for Semiconductors 1997 Edition, SIA Semiconductor Industry Association (San Jose, CA 1997), pp. 1-196.

[3] L. Kimerling, "Silicon Microphotonics", *Appl. Surf. Sci.* **159-160**, 8 (2000).

[4] R. Soref, "Silicon-Based Optoelectronics", *Proc. IEEE* **81**, 1687 (1993).

[5] Graham T. Reed and Andrew P. Knights, *Silicon Photonics: An Introduction*, John Wiley & Sons Ltd., Etobicoke, ON, 2004.

[6] Sean Koehl, "Silicon Photonics Could Revolutionize Future Servers and Networks", *Market Dynamics*, Sept. 26, 2005.

[7] Craig Matsumoto, "Luxtera Chases Silicon Photonics", *Light Reading*, March 28, 2005.

[8] A. W. Fang, H. Park, R. Jones, O. Cohen, M. J. Paniccia, and J. E. Bowers, "A Continuous-Wave Hybrid AlGaInAs-Silicon Evanescent Laser", *IEEE Photonics Technology Letters* **18**, 1143 (2006).

[9] A. Liu, R. Jones, L. Liao, D. Samara-Rubio, D. Rubin, O. Cohen, R. Nicolaescu, and M. Paniccia, "A High-Speed Optical Modulator Based on a Metal-Oxide-Semiconductor Capacitor", *Nature* **427**, 615 (2004).

[10] P. J. Foster, J. K. Doylend, P. Mascher, A. P. Knights, and P. G. Coleman, "Optical attenuation in defect-engineered silicon rib waveguides", *J. Appl. Phys.* **99**, 073101 (2006).

[11] J. D. B. Bradley, P. E. Jessop, and A. P. Knights, "Silicon waveguide-integrated optical power monitor with enhanced sensitivity at 1550 nm", *Appl. Phys. Lett.* **86**, 241103 (2005).

[12] L. Pavesi, "Routes toward silicon-based lasers", *Materials Today*, p. 18, January (2005).

[13] L. Pavesi, L. Dal Negro, C. Mazzoleni, G. Franzò, and F. Priolo, "Optical gain in silicon nanocrystals", *Nature* **408**, 440 (2000).

[14] M. Cazzanelli, D. Navarro-Urriós, F. Riboli, N. Daldosso, L. Pavesi, J. Heitmann, L. X. Yi, R. Scholz, M. Zacharias, and U. Gösele, "Optical gain in monodispersed silicon nanocrystals", *J. Appl. Phys.* **96**, 3164 (2004).

[15] H. Rong, R. Jones, A. Liu, O. Cohen, D. Hak, A. Fang, and M. Paniccia, "A continuous-wave Raman silicon laser", *Nature* **433**, 725 (2005).

[16] L. Canham, "Silicon quantum wire array fabrication by electrochemical and chemical dissolution of wafers", *Appl. Phys. Lett.* **57**, 1046 (1990).

[17] V. Yu. Timoshenko, M. G. Lisachenko, O. A. Shalygina, B. V. Kamenev, D. M. Zhigunov, S. A. Teterukov, P. K. Kashkarov, J. Heitmann, M. Schmidt, and M. Zacharias, "Comparative study of photoluminescence of

undoped and erbium-doped size-controlled nanocrystalline Si/SiO_2 multi-layered structures", *J. Appl. Phys.* **96**, 2254 (2004).

[18] M. E. Castagna, S. Coffa, M. Monaco, A. Muscara, L. Caristia, S. Lorenti, and A. Messina, "High efficiency light emitting devices in silicon", *Mat. Sci. Eng. B* **105**, 83 (2003).

[19] S. Coffa, "Light From Silicon", *IEEE Spectrum* **NA**, 44 (2005).

[20] J. M. Sun, W. Skorupa, T. Dekorsky, M. Helm, A. N. Nazarov, and R. Rizk, "On the mechanism of electroluminescence excitation in Er-doped SiO_2 containing silicon nanoclusters", *Opt. Mater.* **27**, 1050 (2005).

[21] R. H. Fowler, and L. Nordheim, "Electron Emission in Intense Electric Fields", *Proc. Roy. Soc. Lon. A* **119**, 173 (1928).

[22] R. J. Walters, G. I. Bourianoff, and H. Atwater, "Field-effect electroluminescence in silicon nanocrystals", *Nat. Mater.* **4**, 143 (2005).

[23] M. Carrada, F. Gourbilleau, C. Dufour, M. Lavalois, and R. Rizk, "Influence of Er concentration on the emission properties of Er-doped Si-rich silica films obtained by reactive magnetron co-sputttering", *Opt. Mater.* **27**, 915 (2005).

[24] J.-H. Jhe, J. H. Shin, K. J. Kim, D. W. Moon, "The characteristic carrier-Er interaction distance in Er-doped *a*-Si/SiO_2 superlattices formed by ion sputtering", *Appl. Phys. Lett.* **82**, 4489 (2003).

[25] L. R. Tessler, J. L. Coffer, J. Ji, and R. A. Senter, "Erbium environment in silicon nanoparticles", *J. Non-Crystalline Sol.* **299-302**, 673 (2002).

[26] A. J. Kenyon, C. E. Chryssou, C. W. Pitt, T. Shimizu-Iwayama, D. E. Hole, N. Sharma, and C. J. Humphreys, "Luminescence from erbium-doped silicon nanocrystals in silica: Excitation mechanisms", *J. Appl. Phys.* **91**, 367 (2002).

[27] P. S. Andry, W. J. Varhue, F. Lapido, K. Ahmed, E. Adams, M. Lavoie, P. B. Klein, R. Hengehold, and J. Hunter, "Growth of Er-doped silicon using melalorganics by plasma-enhanced chemical vapour deposition", *J. Appl. Phys.* **80**, 551 (1996).

[28] J. H. Shin, W.-H. Lee, and H.-S. Han, "1.54 μm Er^{3+} photoluminescent properties of erbium-doped Si/SiO_2 superlattices", *Appl. Phys. Lett.* **74**, 1573 (1999).

[29] L. Brus, "Electronic Wave Functions in Semiconductor Clusters: Experiment and Theory", *J. Phys. Chem.* **90**, 2555 (1986).

[30] M. J. Kushner, "Plasma Chemistry of $He/O_2/SiH_4$ and $He/N_2O/SiH$ mixtures for remote plasma-activated chemical-vapour deposition of silicon dioxide", *J. Appl. Phys.* **74**, 6538 (1993).

[31] M. G. Boudreau, "SiO_xN_y Waveguides Deposited by ECR-PECVD", M.Eng. thesis, McMaster University, 1993.

[32] Francis F. Chen, *Introduction to Plasma Physics and Controlled Fusion, Volume 1: Plasma Physics* (2^{nd} Edition), Plenum Press, New York, NY, 1984.

[33] E. A. Irving, "Erbium-Doped SiO_xN_y Waveguides Produced by ECR-PECVD ", M.A.Sc. thesis, McMaster University, 2003.

[34] R. P. Tumminelli, B. C. McCollum, E. Snitzer, "Fabrication of high-concentration rare-earth doped optical fibres using chelates", *J. Lightwave Technol.* **8**, 1630 (1990).

[35] Rointan F. Bunsah (Ed.), *Handbook of Deposition Technologies for thin films and coatings: science, technology and applications* (2nd Edition), Noyes Publications, Park Ridge, New Jersey, 1994.

[36] J. Brown, "Characterization of Silicon Dioxide and Silicon Nitride Films Deposited by ECR-CVD", M.Eng. thesis, McMaster University, 1995.

[37] M. Flynn, J. Wojcik, S. Gujrathi, E. Irving, and P. Mascher, "The Impact of Deposition Parameters on the optical and Compositional Properties of Er Doped SRSO Thin Films Deposited by ECR-PECVD", *Mater. Res. Soc. Symp. Proc.* **866**, 163 V5.7/FF5.7 (2005).

[38] K. J. Price, L. E. McNeil, A. Suvkanov, E. A. Irene, P. J. MacFarlane, and M. E. Zvanut, "Characterization of the luminescence center in photo- and electroluminescent amorphous silicon oxynitride films", *J. Appl. Phys.* **86**, 2628 (1999).

[39] T. Roschuk, "Characterization of Amorphous Silicon (*a*-Si) and Silicon Rich Silicon Oxide (SiO_x) Materials Produced by ECR-PECVD", M.A.Sc. thesis, McMaster University, 2005.

[40] L. L. Hench and J. K. West, "Molecular Orbital Models of Silica", *Annual Review Materials Science* **25**, 37 (1995).

[41] Walter A. Harrison, *Electronic Structure and the Properties of Solids: the Physics of the Chemical Bond*, Dover Publications Inc., New York, 1989.

[42] J. R. Chelikowsky and M. Schlüter, "Electron states in alpha-quartz: A self-consistent pseudopotential calculation", *Phys. Rev. B* **15**, 4020 (1977).

[43] R. P. Gupta, "Electronic Structure of Crystalline and Amorphous Silicon Dioxide", *Phys. Rev. B* **32**, 8278 (1985).

[44] G. Wiech, H. O. Feldhütter, and A. Šimůnek, "Electronic Structure of Amorphous SiO_x:H Alloy Films Studied by x-ray Emission Spectroscopy: Si K, Si L, and O K Emission Bands", *Phys. Rev. B* **47**, 6981 (1993).

[45] C. Simionescu, "Characterization of Silicon Oxynitride Thin Films Deposited by Electron Cyclotron Resonance Plasma Enhanced Chemical Vapour Deposition", M.Eng. thesis, McMaster University, 2000.

[46] J. Brown, "Characterization of Silicon Dioxide and Silicon Nitride Films Deposited by ECR-CVD", M.Eng. thesis, McMaster University, 1995.

[47] X. Tan, "Study of the Optical Properties of Silicon Oxynitride Thin Films by Effective Medium Theories", M.A.Sc. thesis, McMaster University, 2004.

[48] E. Meeks, R. S. Larson, P. Ho, C. Apblett, S. M. Han, E. Edelberg, and E. S. Aydil, "Modeling of SiO_2 deposition in high density plasma reactors and comparisons of model predictions with experimental measurements", *J. Vac. Sci. Technol. A* **16**, 544 (1998).

[49] S. M. Han and E. S. Aydil, "Study of surface reactions during plasma enhanced chemical vapour deposition of SiO_2 from SiH_4, O_2, and Ar plasma", *J. Vac. Sci. Technol. A* **14**, 2062 (1996).

[50] G. Lucovsky and D. V. Tsu, "Plasma enhanced chemical vapour deposition: Differences between direct and remote plasma excitation", *J. Vac. Sci. Tehnol. A* **5**, 2231 (1987).

[51] G. Lucovsky, J. T. Fitch, D. V. Tsu, and S. S. Kim, "Atomic Structure in SiO_2 thin films deposited by remote plasma enhanced chemical vapour deposition", *J. Vac. Sci. Technol. A* **7**, 1136 (1989).

[52] D. Davazoglou and V. E. Vamvakas, "Arrangement of Si and O Atoms in Thermally Grown SiO_2 Films", *J. Electrochem. Soc.* **150**, F90 (2003).

[53] P. H. Citrin, P. A. Northrup, R. Birkhan, and A. J. Steckl, "Local structure and bonding of Er in GaN: A contrast with Er in Si", *Appl. Phys. Lett.* **76**, 2865 (2000).

[54] J. Du and A. N. Cormack, "The structure of erbium doped sodium silicate glasses", *J. Non-Crystalline Solids* **351**, 2263 (2005).

[55] J. Du and A. N. Cormack, "Structure Study of Rare Earth Doped Vitreous Silica by Molecular Dynamics Simulation", *Radiation Effects & Defects in Solids* **157**, 789 (2002).

[56] J. D. Carey, R. C. Barklie, J. F. Donegan, F. Priolo, G. Franzò, and S. Coffa, "Electron paramagnetic resonance and photoluminescence study of Er-impurity complexes in Si", *Phys. Rev. B* **59**, 2773 (1999).

[57] C. Maurizio, R. D'Acapito, F. Priolo, G. Franzò, F. Iacona, E. Borsella, S. Padovani, and P. Mazzoldi, "Site of Er ions in Er-implanted silica containing Si nanoclusters", *Opt. Mater.* **27**, 900 (2005).

[58] M. A. Marcus and A. Polman, "Local structure around Er in silica and sodium silicate glasses", *J. Non-Crystalline Solids* **136**, 260 (1991).

[59] D. L. Adler, D. C. Jacobson, D. J. Eaglesham, M. A. Marcus, J. L. Benton, J. M. Poate, and P. H. Citrin, "Local structure of 1.54-μm-luminescence Er^{3+} implanted in Si", *Appl. Phys. Lett.* **61**, 2181 (1992).

[60] Emmanual Desurvire, *Erbium-Doped Fiber Amplifiers: Principles and Applications*, John Wiley & Sons, Inc., New York, NY, 1994.

[61] J. Laegsgaard and K. Stokbro, "Pseudopotential description of rare earths in oxides: The case of $Er_2Si_2O_7$", *Phys. Rev. B* **63**, 075108 (2001).

[62] S. Kennou, S. Ladas, M. Grimaldi, T. A. Nguyen Tan, and J. Y. Veuillen, "Oxidation of thin erbium and erbium silicide overlayers in contact with silicon oxide films thermally grown on silicon", *Appl. Surf. Sci.* **102**, 142 (1996).

[63] J. R. Dean and D. Bloor, "Spectroscopy of rare earth oxide systems: II. Spectroscopic properties of erbium oxide", *J. Phys. C: Solid State Phys.* **5**, 2921 (1972).

[64] M. Ishii and Y. Komukai, "Theoretical prediction of local distortion in an ErO_6 cluster: Stabilization of a C_{4v} structure by a rack and pinion effect", *Appl. Phys. Lett.***79**, 934 (2001).

[65] D. Prezzi, T. A. G. Eberlein, R. Jones, J. S. Filhol, J. Coutinho, M. J. Shaw, and P. R. Briddon, "Electrical activity of Er and Er-O centers in silicon", *Phys. Rev. B* **71**, 245203 (2005).

[66] C. Piamonteze, A. C. Iñiquez, L. R. Tessler, M. C. Martins Alves, and H. Tolentino, "Environment of Erbium in *a*-Si:H and *a*-SiO_x:H", *Phys. Rev. Lett.* **81**, 4652 (1998).

[67] A. Kozanecki, B. J. Sealy, K. Homewood, S. Ledain, W. Jantsch, and D. Kuritsyn, "Sensitization of the 1.54 μm luminescence of Er^{3+} in SiO_2 films by Yb and Si-nanocrystals", *Mat. Sci. Eng. B* **81**, 23 (2001).

[68] A. J. Kenyon, "Recent developments in rare-earth doped materials for opto-electronics", *Progress in Quantum Electronics* **26**, 225 (2002).

[69] P. G. Kik and A. Polman, "Cooperative upconversion as the gain-limiting factor in Er-doped miniature Al_2O_3 optical waveguide amplifiers", *J. Appl. Phys.* **93**, 5008 (2003).

[70] J. E. Sicre, J. T. Dubois, K. J. Eisentraut, and R. E. Sievers, "Volatile Lanthanide Chelates. II. Vapour Pressures, Heats of Vaporization, and Heats of Sublimation", *J. Am. Chem. Soc.* **91**, 3476 (1969).

[71] J. L. Rogers, P. S. Andry, W. J. Varhue, E. Adams, and M. Lavoie, "Erbium-doped silicon films grown by plasma-enhanced chemical vapour deposition", *J. Appl. Phys.* **78**, 6241 (1995).

[72] Robert Eisberg and Robert Resnick, *Quantum Physics of Atoms, Molecules, Solids, Nuclei, and Particles* (2nd Edition), John Wiley & Sons Inc., New York, NY, 1985.

[73] G. Henderson, "How a Photon is Created or absorbed", *J. Chem. Edu.* **56**, 631 (1979).

[74] D. R. McMillin, "Fluctuating Electric Dipoles and the Absorption of Light", *J. Chem. Edu.* **55**, 7 (1978).

[75] Michael D. Lumb (Ed.), *Luminescence Spectroscopy*, Academic Press, London, U.K., 1978.

[76] L. D. Barron and C. G. Gray, "The multipole interaction Hamiltonian for time dependent fields", *J. Phys. A: Math., Nucl. Gen.* **6**, 59 (1973).

[77] David W. Oxtoby and Norman H. Nachtrieb, *Principles of Modern Chemistry* (2nd Edition), Saunders College Publishing, Philadelphia, PA, 1990.

[78] A. P. Alvisatos, "Perspectives on the Physical Chemistry of Semiconductor Nanocrystals", *J. Phys. Chem.* **100**, 13226 (1996).

[79] K. Imakita, M. Fujii, and S. Hayashi, "Spectrally resolved energy transfer from excitons in Si nanocrystals to Er ions", *Phys. Rev. B* **71**, 193301 (2005).

[80] S. Knief and W. von Niessen, "Disorder, defects, and optical absorption in *a*-Si and *a*-Si:H", Phys. *Rev. B* **59**, 12940 (1999).

[81] B. H. Augustine, E. A. Irene, Y. J. He, K. J. Price, L. E. McNeil, K. N. Christensen, and D. M. Maher, "Visible light emission from thin films containing Si, O, N, and H", *J. Appl. Phys.* **78**, 4020 (1995).

[82] M. A. Stevens Kalceff, "Cathodoluminescence microcharacterization of the defect structure of irradiated hydrated and anhydrous fused silicon dioxide", *Phys. Rev. B* **57**, 5674 (1998).

[83] S. Munekuni, T. Yamanaka, Y. Shimogaichi, R. Tohmon, Y. Ohki, K. Nasagawa, and Y. Hama, "Various types of nonbridging oxygen hole center in high-purity silica glass", *J. Appl. Phys.* **68**, 1212 (1990).

[84] M. A. Stevens Kalceff and M. R. Phillips, "Cathodoluminescence micro-characterization of the defect structure of quartz", *Phys. Rev. B* **52**, 3122 (1995).

[85] A. Paleari, N. Chiodini, D. Di Martino, and F. Meinardi, "Radiative decay of vacuum-ultraviolet excitation of silica synthesized by molecular precursors of Si-Si sites: An indicator of intracenter relaxation of neutral oxygen vacancies", *Phys. Rev. B* **71**, 075101 (2005).

[86] H. J. Fitting, A. N. Trukhin, T. Barfels, B. Schmidt, and A. V. Czarnowski, "Radiation Induced Defects in SiO_2", *Radiation Effects and Defects in Solids* **157**, 575 (2002).

[87] J. L. Shen, Y. C. Lee, Y. L. Lui, P. W. Cheng, and C. F. Cheng, "Blue-green photoluminescence in MCM-41 mesporous nanotubes", *J phys.: Condens. Matter* **15**, L297 (2003).

[88] C. Barthou, P. H. Duong, A. Oliver, J. C. Cheang-Wong, L. Rodríguez-Fernández, A. Crespo-Sosa, and T. Itoh, "Silicon nanocrystals and defects produced by silicon and silicon-and-gold implantation in silica", *J. Appl. Phys.* **93**, 10110 (2003).

[89] K. Raghavachari, D. Ricci, and G. Pacchioni, "Optical properties of point defects in SiO_2 from time-dependent density functional theory", *J. Chem. Phys.* **116**, 825 (2002).

[90] H. Nishikawa, E. Watanabe, D. Ito, Y. Sakurai, K. Nagasawa, Y. Ohki, "Visible photoluminescence from Si clusters in γ-irradiated amorphous SiO_2", *J. Appl. Phys.* **80**, 3513 (1996).

[91] J. R. Chavez, S. P. Karna, K. Vanheusden, C. P. Brothers, R. D. Pugh, B. K. Singaraju, W. L. Warren, and R. A. B. Devine, "Microscopic structure of the E'_δ center in amorphous SiO_2: A first principles quantum mechanical investigation", *IEEE Transactions on Nuclear Science* **44**, 1799 (1997).

[92] P. V. Sushko, S. Mukhopadyay, A. S. Mysovsky, V. B. Sulimov, A. Taga, and A. L. Shluger, "Structure and properties of defects in amorphous silica: new insights from embedded cluster calculations", *J. Phys.: Condens. Matter* **17**, S2115 (2005).

[93] Y. Sakurai and K. Nagasawa, "Correlation between the green photo-luminescence band and the peroxy radical in γ-irradiated silica glass", *J. Appl. Phys.* ***88,*** 168 (2000).

[94] A. Stirling, A. Pasquarello, J.-C. Charlier, and R. Car, "Dangling Bond Defects at *Si-SiO_2* Interfaces: Atomic Structure of the P_{b1} Center", *Phys. Rev. Lett.* ***85***, 2773 (2000).

[95] F. Meinardi and A. Paleari, "Native and radiation-induced photolumin-escenct defects in SiO_2: Role of impurities", *Phys. Rev. B* **58**, 3511 (1998).

[96] C. Delerue, M. Lannoo, G. Allan, and E. Martin, "Theoretical descriptions of porous silicon", *Thin Solid Films* **255**, 27 (1995).

[97] P. K. Choudhury and O. N. Singh (Ed.), *Frontiers in Optical Technology*, Nova Science Publishers Inc., New York, NY, 2006.

[98] A. Zunger and L.-W. Wang, "Theory of silicon nanostructures", *Appl. Surf. Sci.* **102**, 350 (1996).

[99] M. Nishida, "Calculations of the electronic structure of silicon quantum dots: oxidation-induced redshifts in the energy gap", *Semicond. Sci. Technol.* **21**, 443 (2006).

[100] Philip L. Taylor and Olle Heinonan, *A Quantum Approach to Condensed Matter Physics*, Cambridge University Press, Cambridge, UK, 2002.

[101] A. Puzder, A. J. Williamson, J. C. Grossman, and G. Galli, "Computational Studies of the Optical Emission of Silicon Nanocrystals", *J. Am. Chem. Soc.* **125**, 2786 (2003).

[102] N. Daldosso, M. Luppi, S. Ossicini, E. Degoli, R. Magri, G. Dalba, P. Fornasini, R. Grisenti, F. Rocca, L. Pavesi, S. Boninelli, F. Priolo, C. Spinella, and F. Iacona, "Role of the interface region on the optoelectronic properties of silicon nanocrystals embedded in SiO_2", *Phys. Rev. B* **68**, 085327 (2003).

[103] Z. Zhou, L. Brus, and R. Freisner, "Electronic Structure and Luminescence of 1.1- and 1.4-nm Silicon Nanocrystals: Oxide Shell versus Hydrogen Passivation", *Nano. Lett.* **3**, 163 (2003).

[104] M. V. Wolkin, J. Jorne, P. M. Fauchet, G. Allan, and C. Delerue, "Electronic States and Luminescence in Porous Silicon Quantum Dots: The Role of Oxygen", *Phys. Rev. Lett.* **82**, 197 (1999).

[105] M. Luppi and S. Ossicini, "*Ab initio* study on oxidized silicon clusters and silicon nanocrystals embedded in SiO_2: Beyond the quantum confinement effect", *Phys. Rev. B* **71**, 035340 (2005).

[106] M. Luppi and S. Ossicini, "Multiple Si=O bonds at the silicon cluster surface", *J. Appl. Phys.* **94**, 2130 (2003).

[107] L. Dal Negro, M. Cazzanelli, N. Daldosso, Z. Gaburro, L. Pavesi, F. Priolo, D. Pacifici, G. Franzò, and F. Iacona, "Stimulated emission in plasma-enhanced chemical vapour deposited silicon nanocrystals", *Physica E* **16**, 297 (2003).

[108] I. Sychugov, R. Juhasz, J. Valenta, and J. Linnros, "Narrow Luminescence Linewidth of a Silicon Quantum Dot", *Phys. Rev. Lett.* **94**, 087405 (2005).

[109] M. Zacharias, J. Heitmann, R. Scholz, U. Kahler, M. Schmidt, and J. Bläsing, "Size-controlled highly luminescent silicon nanocrystals: A SiO/SiO_2 superlattice approach", *Appl. Phys. Lett.* **80**, 661 (2002).

[110] D. Kuritsyn, A. Kozanecki, H. Przybylinska, and W. Jantsch, "Defect-mediated and resonant optical excitation of Er^{3+} ions in silicon-rich silicon oxide", *Appl. Phys. Lett.* **83**, 4160 (2003).

[111] A. Janotta, M. Schmidt, R. Janssen, and M. Stutzmann, "Photoluminescence of Er^{3+} -implanted amorphous hydrogenated silicon suboxides", *Phys. Rev. B* **68**, 165207 (2003).

[112] J. Linnros, N. Lalic, A. Galeckas, and V. Grivickas, "Analysis of the stretched exponential photoluminescence decay from nanometer-size silicon crystals in SiO_2", *J. Appl. Phys.* **86**, 6128 (1999).

[113] I. Sychugov, R. Juhasz, J. Linnros, and J. Valenta, "Luminescence blinking of a Si quantum dot in a SiO_2 shell", *Phys. Rev. B* **71**, 115331 (2005).

[114] M. Glover and A. Meldrum, "Effect of "buffer layers" on the optical properties of silicon nanocrystals superlattices", *Opt. Mater.* **27**, 977 (2005).

[115] F. Iacona, G. Franzò, V. Vinciguerra, A. Irrera, and F. Priolo, "Influence of the spatial arrangement on the quantum confinement properties of Si nanocrystals", *Opt. Mater.* **17**, 51 (2001).

[116] F. Priolo, G. Franzò, D. Pacifici, V. Vinciguerra, F. Iacona, and A. Irrera, "Role of the energy transfer in the optical properties of undoped and Er-doped interacting Si nanocrystals", *J. Appl. Phys.* **89**, 264 (2001).

[117] F. Iacona, C. Bongiorno, C. Spinella, S. Boninelli, and F. Priolo, "Formation and evolution of luminescent Si nanoclusters produced by thermal annealing of SiO_xfilms", *J. Appl. Phys.* **95**, 3723 (2004).

[118] D. Comedi, O. H. Y. Zalloum, E. A. Irving, J. Wojcik, T. Roschuk, M. J. Flynn, and P. Mascher, "X-ray diffraction study of crystalline Si nanocluster formation in annealed silicon-rich silicon oxides", *J. Appl. Phys.* **99**, 023518 (2006).

[119] A. R. Wilkinson and R. G. Elliman, "The effect of annealing environment on the luminescence of silicon nanocrystals in silica", *J. Appl. Phys.* **96**, 4018 (2004).

[120] H. Rinnert, M. Vergnat, and A. Burneau, "Evidence of light-emitting amorphous silicon clusters confined in a silicon oxide matrix", *J. Appl. Phys.* **89**, 237 (2001).

[121] G. Allan, C. Delerue, and M. Lannoo, "Electronic Structure of Amorphous Silicon Nanoclusters", *Phys. Rev. Lett.* **78**, 3161 (1997).

[122] G. Franzò, S. Boninelli, D. Pacifici, F. Priolo, F. Iacona, and C. Bongiorno, "Sensitizing properties of amorphous Si clusters on the 1.54-μm luminescence of Er in Si-rich SiO_2", *Appl. Phys. Lett.* **82**, 3871 (2003).

[123] F. Gourbilleau, R. Madelon, C. Dufour, and R. Rizk, "Fabrication and optical properties of Er-doped multilayers Si-rich SiO_2/SiO_2: size control, optimum Er-Si coupling and interaction distance monitoring", *Opt. Mater.* **27**, 868 (2005).

[124] J. Heitmann, M. Schmidt, M. Zacharias, V. Yu. Timoshenko, M. G. Lisachenko, and P. K. Kashkarov, "Fabrication and photoluminescence properties of erbium doped size-controlled silicon nanocrystals", *Mat. Sci. Eng. B* **105**, 214 (2003).

[125] K. Watanabe, M. Fujii, and S. Hayashi, "Resonant excitation of Er^{3+} by the energy transfer from Si nanocrystals", *J. Appl. Phys.* **90**, 4761 (2001).

[126] M. L. Brongersma, A. Polman, K. S. Min, and H. A. Atwater, "Depth distribution of luminescent Si nanocrystals in Si implanted SiO_2 films on Si", *J. Appl. Phys.* **86**, 759 (1999).

[127] E. Snoeks, A. Lagendijk, and A. Polman, "Measuring and Modifying the Spontaneous Emission Rate of Erbium near an Interface", *Phys. Rev. Lett.* **74**, 2459 (1995).

[128] D. Pacifici, G. Franzò, F. Iacona, S. Boninelli, A. Irrera, M. Miritello, and F. Priolo, "Er doped Si nanostructures", *Mat. Sci. Eng. B* **105**, 197 (2003).

[129] M. Fujii, M. Yoshida, S. Hayashi, and K. Yamamoto, "Photoluminescence from SiO_2 films containing Si nanocrystals and Er: Effects of nano-

crystalline size on the photoluminescence efficiency of Er^{3+}", *J. Appl. Phys.* **84**, 4525 (1998).

[130] N.-M. Park, T.-Y. Kim, K.-H. Kim, G. Y. Sung, B.-H. Kim, S.-J. Park, K. S. Cho, J. H. Shin, J.-K. Lee, and M. Nastasi, "Effect of Amorphous Si Quantum-Dot Size of 1.54 μm Luminescence of Er", *J. Electrochem. Soc.* **152**, G445 (2005).

[131] P. K. Kashkarov, B. V. Kamenev, M. G. Lisachenko, O. A. Shalygina, V. Yu. Timoshenko, M. Schmidt, J. Heitmann, and M. Zacharias, "High-efficiency erbium ion luminescence in silicon nanocrystal systems", Physics of the Solid State **46**, 104 (2004).

[132] A. J. Kenyon, C. E. Chryssou, C. W. Pitt, T. Shimizu-Iwayama, D. E. Hole, N. Sharma, and C. J. Humphreys, "Broad-band and flashlamp pumping of 1.53 μm emission from erbium-doped silicon nanocrystals", *Mat. Sci. Eng. B* **81**, 19 (2001).

[133] D. Kovalev, H. Heckler, G. Polisski, and F. Koch, "Optical Properties of Si Nanocrystals", *Phys. Stat. Sol. B* **215**, 871 (1999).

[134] M. Wojdak, M. Klik, M. Forcales, O. B. Gusev, T. Gregorkiewicz, D. Pacifici, G. Franzò, F. Priolo, and F. Iacona, "Sensitization of Er luminescence by Si nanoclusters", *Phys. Rev. B* **69**, 233315 (2004).

[135] D. Pacifici, L. Lanzanò, G. Franzò, F. Priolo, and F. Iacona, "Revealing the sequential nature of the Si-nanocluster-Er interaction by variable pulse duration excitation", *Phys. Rev. B* **72**, 045349 (2005).

[136] M. Falconieri, E. Borsella, F. Enrichi, G. Franzò, F. Priolo, F. Iacona, F. Gourbilleau, and R. Rizk, "Time dependence and excitation spectra of the

photoluminescence emission at 1.54 μm in Si-nanocluster and Er co-doped silica", *Opt. Mater.* **27**, 884 (2005).

[137] D. Pacifici, G. Franzò, F. Priolo, F. Iacona, L. Dal Negro, "Modelling and perspectives of the Si nanocrystals-Er interaction for optical amplification", *Phys. Rev. B* **67**, 245301 (2003).

[138] P. G. Kik and A. Polman, "Exciton-erbium energy transfer in Si nanocrystals-doped SiO_2", *Mat. Sci. Eng. B* **81**, 3 (2001).

[139] C. B. Layne, W. H. Lowdermilk, and M. J. Weber, "Multiphonon relaxation of rare-earth ions in oxide glasses", *Phys. Rev. B* **16**, 10 (1977).

[140] M. Fujii, K. Imakita, K. Watanabe, and S. Hayashi, "Coexistence of two different energy transfer processes in SiO_2 films containing Si nanocrystals and Er", *J. Appl. Phys.* 95, 272 (2004).

[141] C.-S. Son, S.-I. Kim, Y.-H. Kim, I.-K. Han, Y. T. Kim, A. Wakahara, I.-H. Choi, and H. C. Löpez, "Photoluminescence of Er-implanted GaN", *J. Korean. Phys. Soc.* **45**, 955 (2004).

[142] R. H. Birkhahn, R. Hudgins, D. S. Lee, B. K. Lee, A. J. Steckl, A. Saleh, R. G. Wilson, and J. M. Zavada, "Optical and Structural Properties of Er^{3+}-Doped GaN Grown by MBE", *MRS Internet J. Nitride Semicond. Res.* **4S1**, G3.80 (1999).

[143] M. J. A. de Dood, J. Knoester, A. Tip, and A. Polman, "Förster transfer and the local optical density of states in erbium-doped silica", *Phys. Rev. B* **71**, 115102 (2005).

[144] D. L. Dexter, "A Theory of Sensitized Luminescence in Solids", *J. Chem. Phys.* **21**, 836 (1953).

[145] A. J. Kenyon and F. Lucarz, "A critique of the existing model for excitation exchange between silicon nanoclusters and erbium ions in silica", *Electrochem. Soc. Proc.* **2004-13**, 255 (2005).

[146] B. Wieb Van Der Meer, George Coker III, and S.-Y. Simon Chen, *Resonance Energy Transfer Theory and Data*, VCH Publishers, New York, NY, 1994.

[147] F. Lucarz, "Silicon nanocrystals in erbium-doped silica for optical amplifiers", M.Sc. thesis, University College London, 2003.

[148] F. Priolo, G. Franzò, F. Iacona, D. Pacifici, V. Vinciguerra, "Excitation and non-radiative de-excitation processes in Er-doped Si nanocrystals", *Mat. Sci. Eng. B* **81**, 9 (2001).

[149] G. Franzò, V. Vinciguerra, and F. Priolo, "The excitation mechanism of rare-earth ions in silicon nanocrystals", *Appl. Phys. A* **69**, 3 (1999).

[150] P. Pellegrino, B. Garrido, J. Arbiol, C. Garcia, Y. Lebour, and J. R. Morante, "Site of Er ions in silica layers codoped with Si nanoclusters and Er", *Appl. Phys. Lett.* **88**, 121915 (2006).

[151] D. Kuritsyn, A. Kozanecki, H. Przybylińska, and W. Jantsch, "Energy transfer to Er^{3+} ions in silicon-rich-silicon oxide: efficiency limitations", *Phys. Stat. Sol (c)* **1**, 229 (2004).

[152] K. Imakita, M. Fujii, and S. Hayashi, "The mechanism of energy transfer from Si nanocrystals to Er ions in SiO_2", *Eur. Phys. J. D* **34**, 161 (2005).

[153] J. M . Sun, W. Skorupa, T. Dekorsy, H. Helm, L. Rebohle, and T. Gebel, "Bright green electroluminescence from Tb^{3+} in silicon metal-oxide semi-conductor devices", *J. Appl. Phys.* **97**, 123513 (2005).

[154] S.-Y. Seo and J. H. Shin, "Enhancement of the green, visible Tb^{3+} luminescence from Tb-doped silicon-rich silicon oxide by C co-doping", *Appl. Phys. Lett.* **84**, 4379 (2004).

[155] J. Thompson, R. I. R. Blyth, V. Arima, Y. Zou, R. Fink, E. Umbach, G. Gigli, and R. Cingolani, "4f energies in an organic-rare earth guest-host system: the rare-earth *tris*-8-hydroxyquinolines", *Mat. Sci. Eng. B* **105**, 41 (2003).

[156] A. Polman and F. C. J. M. van Veggel, "Broadband sensitizers for erbium-doped planar optical amplifiers: review", *J. Opt. Soc. Am. B* **21**, 871 (2004).

[157] J.-G. Kang, T.-J. Kim, K. S. Park, and S. K. Kang, "Structural and Optical Properties of Er(III) Complex with ODA and Phen (ODA=Oxydiacetate, Phen=1,10-Phenanthroline)", *Bull. Korean Chem. Soc.* **25**, 373 (2004).

[158] R. J. Curry and W. P. Gillin, "Electroluminescence of organolanthanide based organic light emitting diodes", *Current Opinion in Solid State and Materials Science* **5**, 481 (2001).

[159] H. R. Philipp, "Optical and bonding model for non-crystalline $SiO_x$and SiO_xN_y materials", *J. Non-Crystal. Sol.* **8-10**, 627 (1972).

[160] J. J. van Hapert, A. M. Vredenberg, E. E. van Faassen, N. Tomozeiu, W. M. Arnoldbik, and F. H. P. M. Habraken, "Role of spinodal decomposition in the structure of SiO_x", *Phys. Rev. B* **69**, 245202 (2004).

[161] W. D. Kingery, H. K. Bowen, and D. R. Uhlmann, *Introduction to Ceramics* (2nd Edition), John Wiley & Sons Inc., New York, NY, 1976.

[162] M. Flynn, O. H. Y. Zalloum, J. Wojcik, I. Calder, S. Gujrathi, S. Hill, and P. Mascher, "The impact of the rare-earth precursor on the composition, structure, and luminescence of Er-doped silicon-rich silicon oxide films", paper submitted to the 3rd International Conference on Group IV Photonics, Sept. 2005.

[163] D. J. Eaglesham, J. Michel, E. A. Fitzgerald, D. C. Jacobson, J. M. Poate, J. L. Benton, A. Polman, Y.-H. Xie, and L. C. Kimerling, "Microstructure of erbium-implanted Si", *Appl. Phys. Lett.* **58**, 2797 (1991).

[164] M. W. Sckerl, S. Guldberg-Kjaer, M. Rysholt Poulsen, and P. Shi, "Precipitate coarsening and self-organization in erbium-doped silica", *Phys. Rev. B* **59**, 13494 (1999).

[165] G.-Z. Ran, Y. Chen, Z.-C. Ma, W.-H. Zong, L.-Q. Xie, C.-G. Guo, and G.-G. Qin, "Dependence of 1.54 μm Photoluminescence on Excess-Si Degrees of Er-Doped Si-Rich SiO_2 Films Deposited by Magnetron Sputtering", *Chin. Phys. Lett.* **18**, 986 (2001).

[166] G.-Z. Ran, Y. Chen, W. C. Qin, J. S. Fu, Z.-C. Ma, W.-H. Zong, H. Lu, J. Qin, and G. G. Qin, "Room-temperature 1.54 μm electroluminescence from Er-doped silicon-rich silicon oxide films deposited on n^+-Si substrates by magnetron sputtering", *J. Appl. Phys.* **90**, 5835 (2001).

[167] A. Polman, "Erbium implanted thin film photonic materials", *J. Appl. Phys.* **82**, 1 (1997).

[168] T. D. M. Weijers, R. G. Elliman, and H. Timmers, "Heavy ion elastic recoil detection analysis of silicon-rich silica films", *Nucl. Inst. Meth. Phys. Res. B* **219-220**, 680 (2004).

[169] R. S. Brusa, C. Macchi, S. Mariazzi, G. P. Karwasz, W. Egger, P. Sperr, and G. Kögel, "Decoration of buried surfaces in Si detected by positron annihilation spectroscopy", *Appl. Phys. Lett.* **88**, 011920 (2006).

[170] David A. Porter and Kenneth E. Easterling, *Phase Transformations in Metals and Alloys*, CRC Press, Boca Raton, FL, 1992.

[171] B. Garrido Fernandez, M. López, C. Garcia, A. Pérez-Rodriguez, J. R. Morante, C. Bonafos, M. Carrada, and A. Claverie, "Influence of average size and interface passivation on the spectral emission of Si nanocrystals embedded in SiO_2", *J. Appl. Phys.* **91**, 798 (2002).

[172] T. Müller, K.-H. Heinig, and W. Möller, "Size and location control of Si nanocrystals at ion beam synthesis in thin SiO_2 films", *Appl. Phys. Lett.* **81**, 3049 (2002).

[173] Y. C. Fang, W. Q. Li, L. J. Qi, L. Y. Li, Y. Y. Zhao, Z. J. Zhang, and M. Lu, "Photoluminescence from SiO_x thin films: effects of film thickness and annealing temperature", *Nanotechnology* **15**, 494 (2004).

[174] C. Bonafos, B. Colombeau, M. Carrada, A. Altibelli, and A. Claverie, "Simulations of the ripening of 3D, 2D and 1D objects", *Mat. Sci. Eng. B* **88**, 112 (2002).

[175] C. Bonafos, B. Colombeau, A. Altibelli, M. Carrada, G. Ben Assayag, B. Garrido, M. Lopez, A. Pérez-Rodriguez, J. R. Morante, A. Claverie,

"Kinetic study of group IV nanoparticles ion beam synthesized in SiO_2", *Nucl. Inst. Meth. Phys. Res. B* **178**, 17 (2001).

[176] S. Boninelli, "Properties and Evolution of Si Nanoclusters studied by Energy Filtered Transmission Electron Microscopy", PhD thesis, University of Catania, 2004.

[177] L. A. Nesbit, "Annealing characteristics of Si-rich SiO_2 films", *Appl. Phys. Lett.* **46**, 38 (1985).

[178] A. M. Agarwal and S. T. Dunham, "Consistent quantitative model for the spatial extent of point defect interactions in silicon", *J. Appl. Phys.* **78**, 5313 (1995).

[179] Milton Ohring, *Materials Science of Thin Films: Deposition and Structure* (2nd Edition), Academic Press, San Diego, CA, (2002).

[180] D. Pacifici, E. C. Moreira, G. Franzò, V. Martorino, F. Priolo, and F. Iacona, "Defect production and annealing in ion-irradiated Si nanocrystals", *Phys. Rev. B* **65**, 144109 (2002).

[181] L. J. Zhuge, X. M. Wu, Q. Li, W. B. Wang, and S. L. Xiang, "Origin of violet photoluminescence in SiO_2 films co-doped with silicon and carbon", *Physica E* **23**, 86 (2004).

[182] M. L. Brongersma, A. Polman, K. S. Min, E. Boer, T. Tambo, and H. A. Atwater, "Tuning the emission wavelength of Si nanocrystals in SiO_2 by oxidation", *Appl. Phys. Lett.* **72**, 2577 (1998).

[183] X. D. Pi, P. G. Coleman, R. Harding, G. Davies, R. M. Gwilliam, and B. J. Sealy, "Positron annihilation spectroscopy of the interface between nano-crystalline Si and SiO_2", *Physica B* **340-342**, 1094 (2003).

[184] X. D. Pi, P. G. Coleman, R. Harding, G. Davies, and R. M. Gwilliam, "Characterization of the interface region during the agglomeration of silicon nanocrystals in silicon dioxide", *J. Appl. Phys.* **95**, 8155 (2004).

[185] G. Dalba, N. Daldosso, P. Fornasini, R. Grisenti, L. Pavesi, F. Rocca, G. Franzò, F. Priolo, F. Iacona, "Chemical composition and local structure of plasma enhanced chemical vapour-deposited Si nanodots and their embedding silica matrix", *Appl. Phys. Lett.* **82**, 889 (2003).

[186] A. Kenyon, P. F. Trwoga, C. W. Pitt, and G. Rehm, "The origin of photoluminescence from thin films of silicon-rich silica", *J. Appl. Phys.* **79**, 9291 (1996).

[187] Private communication with Dr. Michael Flynn (2005).

[188] Private communication with Dr. Jacek Wojcik (2006).

[189] R. Henda, E. Scheid, and D. Bielle-Daspet, "Investigation of the Thermal Behaviour of a RTP Furnace", *IEEE Trans. Semicond. Manufact.* **8**, 362 (1995).

[190] C. Y. Chang and S. M. Sze, *ULSI Technology*, The McGraw-Hill Companies, Inc., New York, NY, 1996.

[191] C.-J. Han and C. R. Helms, "Parallel Oxiation Mechanism for Si Oxidation in Dry O_2", *J. Electrochem. Soc.: Solid-State Sci. and Technol.* **134**, 1297 (1987).

[192] H. Z. Massoud, J. D. Plummer, and E. A. Irene, "Thermal Oxidation of Silicon in Dry Oxygen Growth-Rate Enhancement in the Thin Regime: I. Experimental Results and II. Physical Mechanisms", *J. Electrochem. Soc.: Solid-State Sci and Technol.* **132**, 2685 (1985).

[193] H. Z. Massoud, J. D. Plummer, and E. A. Irene, "Thermal Oxidation of Silicon in Dry Oxygen: Accurate Determination of the Kinetic Rate Constants", *J. Electrochem. Soc.: Solid-State Sci. and Technol.* **132**, 1745 (1985).

[194] B. E. Deal and A. S. Grove, "General Relationships for the Thermal Oxidation of Silicon", *J. Appl. Phys.* **36**, 3770 (1965).

[195] O. H. Y. Zalloum, M. Flynn, T. Roschuk, J. Wojcik, E. Irving, and P. Mascher, "Laser photoluminescence spectrometer based on charge-coupled device detection for silicon-based photonics", *Rev. Sci. Inst.* **77**, 023907 (2006).

[196] R. Ferre, B. Garrido, P. Pellegrino, M. Perálvarez, C. Garcia, J. A. Moreno, J. Carreras, and J. R. Morante, "Optical-geometrical effects on the photoluminescence spectra of Si nanocrystals embedded in SiO_2", *J. Appl. Phys.* **98**, 084319 (2005).

[197] P. J. Schultz, "A variable-energy positron beam for low to medium energy research", *Nucl. Inst. Meth. Phys. B* **30**, 94 (1988).

[198] J. A. Moreno, B. Garrido, P. Pellegrino, C. Garcia, J. Arbiol, J. R. Morante, P. Marie, F. Gourbilleu, and R. Rizk, "Size dependence of refractive index of Si nanoclusters embedded in SiO_2", *J. Appl. Phys.* **98**, 013523 (2005).

[199] Private communication with Dr. Michael Flynn (2006).

[200] A. Pérez-Rodriguez, O. González-Varona, B. Garrido, P. Pellegrino, J. R. Morante, C. Bonafos, M. Carrada, and A. Claverie, "White luminescence from Si^+ and C^+ ion-implanted SiO_2 films", *J. Appl. Phys.* **94**, 254 (2003).

[201] L. Rebohle, T. Gebel, H. Fröb, H. Reuther, and W. Skorupa, "Ion beam processing for Si/C-rich thermally grown SiO_2 layers: photoluminescence and microstructure", *Appl. Surf. Sci.* **184**, 156 (2001).

[202] C. Y. Chen, W. D. Chen, S. F. Song, Z. J. Xu, X. B. Liao, G.-H. Li, L. F. Bian, K. Ding, "Correlation between Er^{3+} emission and Si clusters in erbium-doped a-SiO_x:H films", *Physica E* **27**, 21 (2005).

[203] C. Y. Chen, W. D. Chen, S. F. Song, and C. C. Hsu, "Photoluminescence of Er-doped SiO_2 films containing Si nanocrystals and Er", *J. Crys. Growth.* **253**, 10 (2003).

[204] D. Pacifici, "Erbium doped silicon nanoclusters for microphotonics", PhD thesis, University of Catania, 2003.

[205] D. E. Blakie, O. H. Y. Zalloum, J. Wojcik, E. A. Irving, A. P. Knights, and P. Mascher, "Coupled luminescence centres in silicon-rich silicon oxide thin films", to be published in SPIE conference proceedings for Photonics North 2005 (Toronto, Canada).

[206] X. D. Pi, O. H. Y. Zalloum, T. Roschuk, J. Wojcik, A. P. Knights, and P. Mascher, "Light emission from Si nanoclusters formed at low temperature", *Appl. Phys. Lett.* **88**, 103111 (2006).

[207] D. E. Blakie, O. H. Y. Zalloum, J. Wojcik, E. A. Irving, A. P. Knights, and P. Mascher, "Si nano-clusters and Er-related centers as sensitizers for Er^{3+} luminescence in in-situ doped Si_yO_{1-y}:Er ($y \geq 1/3$) thin films", submitted to the Journal of Applied Physics, 2006.

[208] M. Fujii, A. Mimura, S. Hayashi, K. Yamamoto, C. Urakawa, and H. Ohta, "Improvement in photoluminescence efficiency of SiO_2 films containing Si nanocrystals by P doping: An electron spin resonance study", *J. Appl. Phys.* **87**, 1855 (2000).

[209] A. P. Knights, P. J. Simpson, L. B. Allard, J. L. Brebner, and J. Albert, "Si ion implantation-induced damage in fused silica probed by variable-energy positrons", *J. Appl. Phys.* **79**, 9022 (1996).

[210] D. Comedi, O. H. Y. Zalloum, and P. Mascher, "H-sensitive recombination path in Si nanoclusters embedded in SiO_2" *Appl. Phys. Lett.* **87**, 213110 (2005).

[211] H.-J. Fitting, T. Ziems, R. Salh, A. von Czarnowski, and B. Schmidt, "Luminescent defect dynamics in amorphous SiO_2:H", *Phys. Stat. Sol. (c)* **2**, 693 (2005).

[212] L. Skuja, M. Hirano, H. Hosono, and K. Kajihara, "Defects in oxide glasses", *Phys. Stat. Sol. (c)* 2, 15 (2005).

[213] J. A. García, R. Plugaru, B. Méndez, J. Piqueras, and T. J. Tate, "Resonant excitation of Er ion luminescence in a nanocrystalline silicon matrix", *Eur. Phys. J. Appl. Phys.* **27**, 75 (2004).

[214] R. Plugaru, J. Piqueras, E. Nogales, B. Méndez, J. A. García, and T. J. Tate, "Cathodo- and photo-luminescence of erbium ions in nano-crystalline

silicon: mechanism of excitation energy transfer", *J. Optoelectron. Adv. Mater.* **4**, 883 (2002).

[215] Private communication with Dr. David Comedi (2005).

[216] G. Ghislotti, B. Nielsen, P. Asoka-Kumar, K. G. Lynn, A. Gambhir, L. F. Di Mauro, and C. E. Bottani, "Effect of different preparation conditions on light emission from silicon implanted SiO_2 layers", *J. Appl. Phys.* **79**, 8660 (1996).

[217] R. Khatri, P. Asoka-Kumar, B. Nielsen, L. O. Roelling, and K. G. Lynn, "Kinetics of hydrogen interaction with SiO_2-Si interface trap centers", *Appl. Phys. Lett.* **65**, 330 (1994).

[218] D. K. Yu, R. Q. Zhang, and S. T. Lee, "Structural properties of hydrogenated silicon nanocrystals and nanoclusters", *J. Appl. Phys.* **92**, 7453 (2002).

[219] A. R. Wilkinson and R. G. Elliman, "Passivation of Si nanocrystals in SiO_2: Atomic versus molecular hydrogen", *Appl. Phys. Lett.* **83**, 5512 (2003).

[220] N.-M. Park, T.-Y. Kim, K.-H. Kim, G.-Y. Sung, K. S. Cho, J. H. Shin, B.-H. Kim, S.-J. Park, J.-K. Lee, and M. Nastasi, "Hydrogenation Effect on the Er Luminescence in Amorphous Silicon Quantum Dot Films", *Electrochemical and Solid-State Letters* **8**, G63 (2005).

[221] J. S. Biteen, N. S. Lewis, H. A. Atwater, and A. Polman, "Size-dependent oxygen-related electronic states in silicon nanocrystals" *Appl. Phys. Lett.* **84**, 5389 (2004).

[222] X. D. Pi, O. H. Y. Zalloum, J. Wojcik, A. P. Knights, P. Mascher, A. D. W. Todd, and P. J. Simpson, "Formation and oxidation of Si nanoclusters in Er-doped Si-rich SiO_x", *J. Appl. Phys.* **97**, 096108 (2005).

[223] J.F. Ziegler, J.P. Biersack, and U. Littmark, *The Stopping and Range of Ions in Solids*, Pergamon Press, New York, NY, 1985.

[224] Joseph R. Tesmer and Michael Nastasi, *Handbook of Modern Ion Beam Analysis*, Materials Research Society, Pittsburg, PA, 1995.

[225] W. N. Lennard, Notes on Ion Beam Techniques, Department of Physics and Astronomy, University of Western Ontario (2004). Available online at publish.uwo.ca/~wlennard/.

[226] Private communication with Dr. Andrew Knights (2006).

[227] M. Fujinami and N. B. Chilton, "Ion implantation induced defects in SiO_2: The applicability of the positron probe", *Appl. Phys. Lett.* **62**, 1131 (1993).

[228] C.-J. Lin and G.-R. Lin, "Defect-Enhanced Visible Electroluminescence of Multi-Energy Silicon-Implanted Silicon Dioxide Film", *IEEE J. Quant. Electron.* **41**, 441 (2005).

[229] G.-R. Lin, C.-J. Lin, C.-K. Lin, L.-J. Chou, and Y.-L. Chueh, "Oxygen defect and Si nanocrystals dependent white-light and near-infrared electroluminescence of Si-implanted and plasma-enhanced chemical-vapour deposition-grown Si-rich SiO_2", *J. Appl. Phys.* **97**, 094306 (2005).

[230] G.-R. Lin, C.-J. Lin, and K.-C. Yu, "Time-resolved photoluminescence and capacitance-voltage analysis of the neutral vacancy defect in silicon implanted SiO_2 on silicon substrate", *J. Appl. Phys.* **96**, 3025 (2004).

[231] T. Gebel, L. Rebohle, J. Sun, and W. Skorupa, "Electroluminescence from thin SiO_2 layers after Si- and C-coimplantation", *Physica E* **16**, 366 (2003).

[232] L. Rebohle, J. von Borany, R. A. Yankov, W. Skorupa, I. E. Tyschenko, H. Fröb, and K. Leo, "Strong blue and violet photoluminescence and electroluminescence from germanium-implanted and silicon-implanted silicon-dioxide layers", *Appl. Phys. Lett.* **71**, 2809 (1997).

[233] A. Uedono, T. Kawano, S. Tanigawa, and H. Itoh, "Defects in electron-irradiated vitreous SiO_2 probed by positron annihilation", *J. Phys.: Condens. Matter* **6**, 8669 (1994).

[234] A. Uedono, L. Wei, S. Tanigawa, R. Suzuki, H. Ohgaki, T. Mikado, T. Kawano, and Y. Ohji, "Positronium formation in SiO_2 films grown on Si substrates studied by monoenergetic positron beams", *J. Appl. Phys.* **75**, 3822 (1994).

[235] A. Rivera, I. Montilla, A. Alba Garcia, R. Escobar Galindo, C. V. Falub, A. van Veen, H. Schut, J. M. M. de Nijs, and P. Balk, "Native and Irradiation-Induced Defects in SiO_2 Structures Studied by Positron Annihilation Techniques", *Mater. Sci. Forum* **363-365**, 64 (2001).

[236] R. S. Brusa, G. P. Karwasz, G. Mariotto, A. Zecca, R. Ferragut, P. Folegati, A. Dupasquier, G. Ottaviani, and R. Tonini, "Structural evolution in Ar^+ implanted Si-rich silicon oxide", *J. Appl. Phys.* **94**, 7483 (2003).

[237] R. S. Brusa, S. Mariazzi, and A. Dupasquier, "Buried surfaces, open volumes decoration and positronium formation in He and He+H implanted Si studied by depth profiling positron annihilation spectroscopies", 14th International Conference on Positron Annihilation, Poster 108 (2006).

[238] P. J. Simpson, M. Spooner, H. Xia, and A. P. Knights, "Enhanced depth resolution in positron analysis of ion irradiated SiO_2 films", *J. Appl. Phys.* **85**, 1765 (1999).

[239] K. Hirata, H. Arai, A. Kawasuso, T. Sekiguchi, Y. Kobayashi, and S. Okada, "Defects in 30 keV Er^{3+}-implanted SiO_2/Si studied by positron annihilation and cathodoluminescence", *J. Appl. Phys.* **90**, 237 (2001).

[240] A. P. Mills, Jr., "Positronium Formation at Surfaces", *Phys. Rev. Lett.* **41**, 1828 (1978).

[241] R. S. Yu, K. Ito, W. Zheng, and Y. Kobayashi, "Effects of coexistent pores and paramagnetic defects on positron annihilation in silicon oxide thin films", *J. Appl. Phys.* **93**, 3340 (2003).

[242] D. Comedi, O. H. Y. Zalloum, D. E. Blakie, J. Wojcik, and P. Mascher, "Formation of and Light Emission from Si nanocrystals Embedded in Amorphous Silicon Oxides", submitted to the 210th ECS Conference Proceedings (2006).

[243] V. F. Masterov, F. S. Nasredinov, P. P. Seregin, V. Kh. Kudoyarova, A. N. Kuznetsov, and E. I. Terukov, "Local environment of erbium atoms in amorphous hydrogenated silicon", *Appl. Phys. Lett.* **72**, 728 (1998).

[244] A. Nazarov, J. M. Sun, W. Skorupa, R. A. Yankov, I. N. Osiyuk, I. P. Tjagulskii, V. S. Lysenko, and T. Gebel, "Light emission and charge trapping in Er-doped silicon dioxide films containing silicon nanocrystals", *Appl. Phys. Lett.* **86**, 151914 (2005).

[245] L. Khriachtchev, S. Novikov, and J. Lahtinen, "Thermal annealing of Si/SiO_2 materials: Modification of structural and photoluminescence emission properties", *J. Appl. Phys.* **92**, 5856 (2002).

[246] T. Ouisse, V. Ioannou-Sougleridis, D. Kouvatsos, and A. G. Nassiopoulou, "Electrical modelling of Si/SiO_2 superlattices", *J. Phys. D: Appl. Phys.* **33**, 2691 (2000).

[247] C. D. Presti, A. Irrera, G. Franzò, I. Crupi, F. Priolo, F. Iacona, G. Di Stefano, A. Piana, D. Sanfilippo, and P. G. Fallica, "Photonic-crystal silicon-nanocluster light-emitting device", *Appl. Phys. Lett.* **88**, 033501 (2006).

[248] M. Flynn, "Luminescence from cadmium processed $Zn_{1-x}Ga_2O_{4-x}$:Mn", Phd thesis, McMaster University, 2000.

[249] J. Kalkman, H. Gersen, L. Kuipers, and A. Polman, "Excitation of surface plasmons at a SiO_2/Ag interface by silicon quantum dots: Experiment and theory", *Phys. Rev. B* **73,** 075317 (2006).

[250] J. Kalkman, L. Kuipers, A. Polman, and H. Gersen, "Coupling of Er ions to surface plasmons on Ag", *Appl. Phys. Lett.* **86**, 041113 (2005).

[251] T. Nakamura, M. Fujii, K. Imakita, and S. Hayashi, "Modification of energy transfer from Si nanocrystals to Er^{3+} near a Au thin film", *Phys. Rev. B* **72**, 235412 (2005).

[252] J. R. Hook and H. E. Hall, *Solid State Physics* (2nd Edition), Wiley & Sons, New York, NY, 1991.

[253] P. Yu and M. Cardona, *Fundamentals of Semiconductors: Physics and Material Properties* (3rd Edition), Springer-Verlag, Berlin, Germany, 2001.

[254] I. Procházka, "Positron Annihilation Spectroscopy", *Materials Structure* **8**, 55 (2001).